Project Final Report

Research and Development of Fuel Cells for Stationary and Transportation Applications
DE-EE0005667

Project Title:

"High Performance, Durable, Low Cost Membrane Electrode Assemblies for Transportation Applications"

Company: 3M Company

Technical POC: Andrew J. Steinbach | Specialist Materials Science | 3M Fuel Cell Components Program | 3M Center, Building 201-2N-19 | St. Paul, MN 55144-1000 | Office: 651 737 0103 | Fax: 651 575 1187 | ajsteinbach2@mmm.com
Contract POC: Steven L. Kays | Contract Manager | Government R&D Contracts Department | 3M Center, Building 0224-02-S-25 | St. Paul, MN 55144-1000 | Office: 651 737 0853 | Fax: 651 736 4777 | slkays@mmm.com

Major Participants: 3M Company, Michigan Technological University, Lawrence Berkeley National Laboratory, Johns Hopkins University, Oak Ridge National Laboratory, General Motors Company

Project Period of Performance: September, 2012 – August, 2016.

Acknowledgment: This material is based upon work supported by the Department of Energy under Award Number DE-EE0005667.

Table of Contents

Executive Summary

The primary project objective was development of improved polymer electrolyte membrane fuel cell (PEMFC) membrane electrode assemblies (MEAs) which address the key U.S. Department of Energy (DOE) barriers of performance, durability and cost. Additional project objectives were to address commercialization barriers specific to MEAs comprising 3M nanostructured thin film (NSTF) electrodes, including a larger-than-acceptable sensitivity to operating conditions, an unexplained loss of rated power capability with operating time, and slow break-in conditioning. Significant progress was made against each of these barriers, and most DOE 2020 targets were met or substantially approached.

Over the course of the project, significant improvements in performance were realized. In single cell testing, the final project MEA exceeded the DOE 2020 ¼ power target (60% improvement over baseline) and achieved 89% of the rated power target ($1W/cm^2$) and 85% of the specific power target (kW/g_{PGM}). Total platinum group metal (PGM) content was reduced 13% from 0.151 to $0.131mg/cm^2$, which is 4.8% above the target of $0.125mg_{PGM}/cm^2$. The improved performance and cost were largely due to improvements in the cathode catalyst processing (dealloying), minimization of anode electrocatalyst PGM content, and the first successful integration of next generation, low equivalent weight perfluorosulfonic acid (PFSA) PEMs with mechanical support.

The final project MEA cost was estimated to be $8.62/kW when produced at 500k systems per year, 23% higher than the target cost of $7/kW. The projected cost of automotive stacks would be reduced by between 19.2 and 28.2% ($/kW) compared to stacks incorporating the baseline NSTF MEA. Cost estimates were conducted by Argonne National Laboratory (ANL) and Strategic Analysis, Inc. (SA), using experimental 3M performance data. The path to achieving all DOE 2020 MEA PGM content and performance targets was identified, largely requiring only an improvement in the mass activity of the cathode electrocatalyst. Additionally, a key component to cost is manufacturability; all final project MEA components were fabricated using continuous pilot scale production equipment with reasonable yields, indicating good prospects for scalability of the material sets.

Operating condition sensitivity (operational robustness) was also improved and the project approach was largely validated. As compared to the baseline project MEA, the final project MEA demonstrated an approximate 2x gain in steady performance at 40°C temperature. Additionally, the final project MEA was able to successfully operate under rapid load transient operation between 40 and 80°C cell temperature, a much wider and improved operating window than the 70 to 80°C window for the pre-project baseline. The final project MEA approached, but did not achieve, the operational robustness target of transient and steady state operation at 30°C cell temperature. In short stack testing, the project approach of using optimized anode diffusion media and cathode interlayers to improve NSTF MEA operational robustness was substantially validated. When the optimized anode diffusion media and cathode interlayer were matched with a baseline NSTF catalyst coated membrane (CCM), successful load transients down to 30°C stack temperature were demonstrated. A likely key mechanism of the improved operational robustness imparted by the anode diffusion media was determined through extensive

characterization and development of a novel integrated MEA model, which included both a pore network model and a continuum model.

The final project MEA, when evaluated in short stacks at a project partner, yielded performance and operational robustness below expectation based on single cell results. While several factors were possibly explanatory, diagnostic experiments revealed that one large factor was the exceptionally large and unanticipated sensitivity of the final project MEA performance and operational robustness to break-in conditioning extent of the MEA anode electrode. Such sensitivity appeared to be largely tied to the final pilot-production CCM, as laboratory scale CCMs were less sensitive to anode break-in conditioning extent. Extensive development work was conducted to develop accelerated MEA conditioning protocols, which indicated the possibility of break-in conditioning of ca. 10 hours or less in single cell. When implemented in short stack, the recommended accelerated conditioning protocol resulted in improved operational robustness, but overall performance and robustness remained below expectation.

The durability of the final project MEAs and components achieved some but not all of the DOE 2020 targets. The final project MEA achieved the DOE 2020 MEA chemical durability target. The cathode electrocatalyst similar to the final project best of class (BOC) MEA passed the DOE Support AST, but failed the DOE electrocatalyst accelerated stress test (AST). Development of an improved durability, manufacturable cathode electrocatalyst, which occurred outside the project, did not materialize in the project timeframe. When evaluated under the DOE support cycle AST, the cathode interlayer maintained its operational robustness and the MEA performance improved. The cathode interlayer was also reasonably durable against the DOE Electrocatalyst AST, maintaining robustness through a majority of the AST test.
The final project MEA's durability with cycling was estimated to be between 656-1864 hours to 10% voltage loss, substantially below the DOE 2020 target of 5000 hours. Extensive experimental and modeling work was conducted to identify the root cause of the rated power loss. A key correlation correlated rated power loss to cathode catalyst activity, and that cathode catalyst activity decay correlated with the extent of decomposition of the PEM PFSA ionomer. Two primary mitigation pathways were identified based on these analyses. One mitigation approach resulted in an improvement, but absolute rated power performance was insufficient for inclusion in the final project MEA. The positive mitigation result provides a validation of the possibility for materials-based approaches for rated power durability improvements with NSTF MEAs.

Key Project Accomplishments

MEA Performance and Cost Improved (Specific Power Improved to 6.8kW/g, a 54% Improvement vs. Pre-Project Status).

- ***NSTF Anode PGM Minimization****:* Studies to understand influences of anode NSTF PGM content allowed anode PGM minimization and provides direction for further possible reduction. A hydrogen oxidation reaction (HOR) kinetic model was developed and provided insight into PGM sensitivity of NSTF anodes.
- ***NSTF Cathode Dealloying Development****:* An improved, scalable PtNi/NSTF dealloying process was developed. Dealloying development work also identified the apparent limits of this and similar "simple" free-corrosion approaches, which resulted in development initiation of alternative and improved methods.
- ***Development of Cathode Catalyst Process/Structure/Response Correlations***: Cathode annealing and dealloying optimization work has provided key data and insights, likely allowing further gains in a new cathode catalyst DOE-funded project.
- ***3M Supported Membrane Integration****:* Key factor identified which prevented integration of NSTF with supported 3M PEMs, which allowed allows higher performance and improved MEA mechanical durability. Finding is helping commercial product development.
- ***Path to Achieve All DOE 2020 PGM Content and Performance Identified:*** Studies indicated that achievement of the DOE 2020 PGM content and performance targets could be realized with the final project MEA if an improved mass activity cathode catalyst was integrated.
- ***Components and Processes Scalability:*** All components were fabricated with continuous, pilot-scale manufacturing processes. In limited work, very good trial-trial reproducibility was established. Process scalability and yields are key factors influencing true cost of components.

NSTF MEA Operational Robustness Operating Window Improved (Robust Down to 40°C Cell Temperature vs. 70°C Pre-Project)

- ***Anode Gas Diffusion Layer (GDL)****:* Optimization of low electrical resistance anode backing key to allow improved robustness *and* high rated power performance. Identification and extensive characterization and modeling of key anode GDL structural factors which enabled improved MEA water management. Insight developed may lead to development of structurally-tailored anode GDLs to further enhance robustness.
- ***Novel GDL Characterization Method Developed:*** An X-ray computed tomography method was developed which allowed direct imaging of liquid permeation in gas diffusion layers, allowing direct validation of several hypotheses.
- ***Integrated MEA Model Development:*** A novel MEA model was developed which successfully integrated a GDL pore network model and CCM continuum model. The integrated model was validated experimentally, and provides unique insight into the mechanisms by which diffusion media can influence performance in saturatable electrodes.
- ***Cathode Interlayer****:* Developed understanding of the key influential material factors of the cathode interlayer, resulting in development of durable tolerance to load transients with "floodable" electrodes. Will aid in next generation NSTF MEA development.

NSTF MEA Rated Power Degradation Mechanism Identified.

- ***Rated Power Correlation to Cathode Oxygen Reduction Reaction (ORR) Activity:*** A significant correlation revealed that NSTF MEA rated power may depend solely on the cathode absolute ORR activity (mA/cm^2_{PLANAR}). The correlation, which held for 53 MEAs and over 200 data points taken at beginning of life and after decay, is highly indicative that degradation of the cathode activity alone is the primary factor for NSTF MEA rated power loss.
- ***Cathode ORR Activity Correlation to PFSA Decomposition****:* In a study conducted by ANL and 3M, ORR activity loss correlated directly with the cumulative F^- ion generation extent, a measure of PFSA decomposition.
- ***Key Material Factors Identified:*** Diagnostic studies revealed exceptionally strong sensitivities to PFSA PEM variables, such as equivalent weight and presence of PFSA decomposition mitigation additive.
- ***Rated Power Loss Mitigation Successful:*** A first novel material-based mitigation resulted in improved retention of ORR activity and kinetic performance. Performance improvement need.
- ***NSTF MEA Durability Model Development:*** ANL model was developed based on experimental performance and PFSA decomposition extent data, taken at several operating conditions. The model predictions reasonably matched experimentally-determined NSTF MEA lifetimes, and provided key quantified recommendations for mitigation.

Project Status towards Targets

Table 1 summarizes final project status again the DOE 2020 targets. The final project MEA achieved the DOE 2020 Q/ΔT and Performance @ 0.8 V targets. The final project MEA was within 15% of the DOE 2020 targets for Performance @ rated power, PGM total content (both electrodes), and PGM total loading. MEA cost was projected to be 23% higher than the 7 $/kW target, based on a model by Strategic Analysis, Inc. Durability with cycling was below the DOE 2020 5000 hour target, achieving between 13 and 37% of that target.

Table 1. Project Final Status Against Representative DOE 2020 Targets

Characteristic	Units	2020 Targets	3M 2016 Status*
Q/ΔT	kW / °C	1.45	1.45
Cost	$ / kW	7	8.62**
Durability with cycling	hours	5000	656-1864
Performance @ 0.8 V	mA/cm^2	300	310
Performance @ rated power	mW/cm^2	1000	891
Platinum group metal total content (both electrodes)	g / kW (rated)	0.125	0.147
Platinum group metal (PGM) total loading	mg PGM / cm^2 electrode area	0.125	0.131

***3M Status with 2015 (September) Best of Class MEA: 0.019 mg_{PGM}/cm^2 PtCoMn/NSTF anode electrode, 0.096 mg_{PGM}/cm^2 Pt_3Ni_7 (TREATED) /NSTF + 0.016 mg_{PGM}/cm^2 Pt/C interlayer cathode electrode, 14 µm 725EW 3M supported PEM, 3M "X3"/2979 Anode/Cathode GDLs, "FF2" Flow Fields. Performance assessed at 90°C, 150 kPa H_2/Air (outlet), 2.0/2.5 H_2/Air Stoichiometry, 84°C Dewpoints (J > 0.4 A/cm^2) or 68°C Dewpoints (J < 0.4 A/cm^2); rated power defined at 0.692 V, which achieves Q/ΔT = 1.45 kW/°C.**

"Best of Class" refers to the currently-determined optimal combination of components.

Durability with cycling evaluated in single 50cm^2 cell under 3M 80°C Load/RH cycle and assessed at 0.8A/cm^2, 1.5 atmA H_2/Air.

****: MEA cost estimated by Strategic Analysis, Inc. at 500k systems/year volume, DOE 2016 AMR [1].**

Table 2 summarizes project status against project goals 1-13. Goals 1, 4, 5, 11, 12, and 13 were achieved. Goal 3 status was 4.8% above target. Goals 7 and 8 were not evaluable with the final project MEA. For Goal 10, 2 of 3 metrics were achieved.

Table 2. Project Performance, Cost, and Durability Goals and Current Project Status			
Goal ID	*Project Goals (units)*	*Goal Value*	*Status*
Performance at ¼ Power, Performance at rated power, and Q/DT Targets			
1	Performance at 0.80V (A/cm^2); single cell, ≥80ºC cell temperature at 50,100,150kPag, respectively.	0.300 NA NA	0.310 [A] NA NA
2	Performance at Rated Power, Q/ΔT : Cell voltage at 1.41A/cm^2 (Volts); single cell, ≥88ºC cell temperature, 50kPag[*]	0.709	0.679[A]
Cost Targets			
3	Anode, Cathode Electrode PGM Content (mg/cm^2)	≤ 0.125	0.131[A]
4	PEM Ionomer Content (effective ion. thickness, microns)	≤ 16	12[A]
Transient response (time from 10% to 90% of rated power), Cold start time to 50% of rated power at -20°C, +20°C), and Unassisted start.			
5	Transient response (time from 10% to 90% of rated power); single cell at 50°C, 100% RH (seconds)	≤ 1	PASS (0%RH)[A]
6	Cold start time to 50% of rated power at +20°C; evaluated as single cell steady state J at 30°C (A/cm^2)	0.8	0.7[A]
7	Cold start time … at -20°C; short stack (seconds)	≤ 30	Not Determined
8	Unassisted start from -40°C (pass/fail); short stack	Pass at -40°C	Not Determined
MEA Durability with cycling, Electrocatalyst Cycle, Catalyst Support Cycle, MEA Chemical Stability, and Membrane Mechanical Targets			
9	Cycling time under 80°C MEA/Stack Durability Protocol with ≤ 30mV Irreversible Performance Loss (hours)	≥ 5000	656-1864[A]
10	Table D-1 Electrocatalyst Cycle and Metrics Mass activity % loss mV loss at 0.8A/cm^2 % initial area loss	 ≤-40 ≤-30 ≤-40	 -40±0.8 -28±1.4 -14±0.2 [F]
11	Table D-2 Catalyst Support Cycle and Metrics Mass activity % loss mV loss at 1.5A/cm^2 % initial area loss	 ≤-40 ≤-30 ≤-40	 -40±7 -11±3 (0.8) -19±3[E]
12	Table D-3 MEA Chemical Stability: 500 hours (H_2 crossover (mA/cm^2); OCV loss (% Volts); Shorting resistance (ohm-cm^2))	 ≤2 ≤-20 >1000	 PASS -4 PASS[B]
13	Table D-4 Membrane Mechanical Cycle: 20k Cycles (H_2 crossover (mA/cm^2); Shorting resistance (ohm-cm^2))	≤2 >1000	20.1k[A (PEM ONLY)]

A: Mean values for duplicate 3M 2015(Sept.) Best of Class NSTF MEAs: Anode=0.02PtCoMn/NSTF, Cathode= 0.095Pt_3Ni_7/NSTF + 0.016Pt/C IL, (0.131m_{PGM}/cm^2 total), 3M-S 725EW 14µ PEM, X2/2979+IL Anode/Cathode, 3M "FF2" flow fields, operated at 90ºC cell temperature with subsaturated inlet humidity and anode/cathode stoichs of 2.0/2.5 and at stated anode/cathode reactant outlet pressures, respectively.
B: Mean value for duplicate 3M 2015(Mar.) Best of Class MEAs. Analogous result for 2015(Sept.) MEAs is expected.
C: OEM Stack testing results with 3M NSTF MEAs: Anode=0.10PtCoMn/NSTF, Cathode=0.15PtCoMn/NSTF, (0.25mg_{PGM}/cm^2 total), 3M ionomer in supported PEM, Baseline 2979/2979 GDLs. OEM-specific enabling technology.
E: Value for Replicate 3M NSTF MEAs. Anode: 0.05PtCoMn/NSTF. Cathode=0.107 or 0.125 Pt_3Ni_7/NSTF(Dealloy+SET), 3M 825EW 24µ PEM w/ or w/o additive, Baseline 2979/2979 GDLs, w/ or w/o Edge Protection, Quad Serpentine Flow Field.
E: Value for Replicate 3M NSTF MEAs. Anode: 0.05PtCoMn/NSTF. Cathode: "M", 0.091mg_{PGM}/cm^2, 3M 825EW 24µ PEM w/ or w/o additive, Baseline 2979/2979 GDLs, w/ or w/o Edge Protection, Quad Serpentine Flow Field.
*: Cell performance of 0.709V at 1.41A/cm^2 with cell temperature of ≥88ºC simultaneously achieves the Q/ΔT and rated power targets of 1.45kW/ºC and 1000mW/cm^2, respectively.
**: Single sample result. MEA failed prematurely due to experimental error.

Statement of Project Objectives

Final version, revised Oct. 2013.

PROJECT OBJECTIVES

The objective of this project is development of a durable, low-cost, and high performance membrane electrode assembly (MEA) for transportation applications, characterized by: a) total Platinum (Pt) group metal loadings of ≤ 0.125mg/cm^2 of MEA area, b) performance at rated power of ≥ 1000mW/cm^2, c) performance at ¼ power (0.8V) of ≥ 0.3A/cm^2, d) durability of ≥ 5000 hours under cycling conditions, e) Q/ΔT of ≤ 1.45 kW/°C, and f) cost of 5-9 $/kW, projected at high volume, thereby meeting or exceeding the targets outlined in Table 7 – Technical Targets: MEAs for Transportation in DE-FOA-0000360. Additionally, the MEA must be operationally robust, characterized by a) Transient response, b) Cold start time to 50% of rated power, and c) Unassisted start from low temperature.

PROJECT SCOPE

While significant progress has been made, state-of-the-art Proton Exchange Membrane (PEM) fuel cell (FC) membrane electrode assemblies (MEAs) utilized in today's prototype automotive traction fuel cell systems continue to suffer from limitations due to high cost, insufficient durability, and low robustness to off-nominal operating conditions. Many of these limitations are due directly and indirectly to the properties of the conventional precious metal supported nanoparticle catalysts incorporated into the MEA anode and cathode electrodes. State-of-the art MEAs based on conventional catalysts currently incorporate precious metal loadings which are above that needed to achieve MEA cost targets; as precious metal content of these conventional catalysts is reduced towards the requisite loadings, performance, durability and/or robustness decrease significantly.

The focus of this project is integration of 3M's state-of-the-art nanostructured thin film (NSTF) anode and cathode catalyst technology platform with 3M's state-of-the-art polymer electrolyte membranes, advanced and low-cost gas diffusion layers, and robustness-enhancing interfacial layers. At notably lower precious metal content, the NSTF catalyst technology platform has several demonstrated performance, durability, and cost benefits over conventional catalysts. Integration of these components to achieve the ultimate performance, cost, and durability targets will require an improved understanding of the interactions between MEA components, especially towards optimization of water management to minimize oxygen mass transport limitations at rated power, cold-start and freeze-start operating regimes.

TASKS TO BE PERFORMED

Task 1. Integration Activities Toward ¼ Power, Performance @ rated power, Q/ΔT, and Cost Targets

The work under Task 1 emphasizes component integration towards achievement of the ¼ power, rated power, and Q/ΔT targets, with a focus on 50cm^2 single cell MEA evaluation of anode and cathode catalysts, PEMs, and anode and cathode gas diffusion layers (GDLs) with the potential for performance and durability improvements towards meeting the targets. In addition, subtask 1.5 will evaluate the impact of flow field land and channel geometry to potentially further improve performance towards the above targets. Initially, testing will occur with a common baseline material set, where the specific component under evaluation replaces the same component in the baseline material set.

Subtask 1.1. Improved Mass Activity, Durable, and Rated-power Capable NSTF Cathode Oxygen Reduction Reaction (ORR) Catalysts

Subtask 1.1's focus is evaluation of MEAs incorporating advanced NSTF cathode ORR catalysts with varying compositions, loadings, and post-process treatments, with initial focus on the 3M Pt_3Ni_7 material system. Subtask 1.1 also includes specific work towards optimizing the dealloying post-process method, optimizing the surface energetic treatment (SET) post-process method, and advanced transmission electron microscopy (TEM)characterization of materials.

Subtask 1.2. Durable, Ultra-Low PGM NSTF Anode Catalyst

The work on subtask 1.2 is evaluation of NSTF anode catalysts, including durable materials developed under current award DE-EE0000456; a key initial focus will be Platinum group metal (PGM) loading minimization < 0.05mg$_{PGM}$/cm^2.

Subtask 1.3. Durable, Improved Conductivity PEMs

Subtask 1.3 is evaluation of advanced 3M membranes, including expected available variations of ionomer chemistry, ionomer equivalent weight, thickness, support variables, and durability-enhancing additive type and level; other commercially available PEMs may be evaluated based on literature reports.

Subtask 1.4. Low-Cost, High Performance GDLs

Subtask 1.4 involves evaluation of advanced, low-cost, and high performance anode and cathode GDLs available at 3M, subcontractors, and commercially available materials.

Subtask 1.5. Rated Power Sensitivity to Flow Field Geometry

Subtask 1.5 involves evaluation of the interaction of basic flow field geometry (land and channel widths) with the anode and cathode GDLs evaluated in subtask 1.4 to optimize rated power response. With few exceptions, 3M NSTF MEA single cell test results generated at 3M have been with a single standardized flow field design. Limited results at 3M have shown dramatic changes in rated power response with change in land and channel geometries, and it is believed that further improvement in rated power response could be realized with modest effort. The work would involve a very modest flow field design effort, consisting of selection of a range of basic flow field land and channel dimensions, simple computational fluid dynamic (CFD) modeling to select proper channel depth to ensure even reactant flow distribution, flow field fabrication via milling of standard 3M flow field graphite plates, followed by 50cm^2 single fuel cell evaluation. Initial fuel cell evaluation would consist of evaluating different flow field geometries with the baseline MEA component set for rated power, cold start, and load transient

responses, a second round of evaluation would occur with the interim best of class MEA(s), and a final round with the final down selected best of class MEA.

Milestone 1.1: Demonstration of Interim Best of Class MEA component set candidates which meet Go/No-Go Value Goals 1-4 from Table D.2 (section D) by project Q7.
Milestone 1.2: Demonstration of Final Best of Class MEA component set candidates which meet Target Value Goals 1-4 from Table D.2 by project Q11.

Task 2. Integration Activities Toward Transient Response, Cold Start Time to 50% of Rated Power, and Unassisted Start from Low Temperature Targets

Task 2 involves evaluation of 50cm^2 MEAs comprising new anode and cathode GDLs and interfacial layer candidates with the potential to aid in meeting the cold start time and transient response transportation system targets.

Subtask 2.1 GDL Optimization for Cold Start

The primary objective of subtask 2.1 is optimization of anode gas diffusion layers for cold start response. The work will first involve screening of different GDL backings with or without standard hydrophobization and no microporous layer (MPL) for cold start and rated power response. Due to durability concerns with bare GDL backings, MPLs are needed to minimize backing fiber protrusion through the membrane. Work will also include evaluation of experimental backing materials developed at a vendor with input from 3M. Optimally-performing backing candidates will be downselected and then MPL loading and composition will be optimized, again towards the key factors of improved cold start and rated power with minimization of electronic shorting to acceptable levels. The experimental plan of evaluating backings without MPL first and optimizing the MPL second is based on 3M's experience that utilization of a non-optimized MPL can quench the cold start response, potentially causing exclusion of promising backing candidates.

Subtask 2.2 Interfacial Layer Optimization for Kinetic, Transient Response

Subtask 2.2 involves optimization of interfacial layers for load transient response and kinetic optimization. Load transients are rapid (~1s) step increases in load from idle to high levels (e.g. 0.02 to 1.0A/cm^2). Previous results at 3M have shown the capability of "standard" NSTF MEAs to withstand the load transient is not as robust as needed under all conditions, especially cooler and wetter conditions. Previous work had also shown that addition of a modestly low-loaded (0.015-0.05mg$_{Pt}$/cm^2) conventional carbon-supported electrode between the NSTF cathode electrode and cathode GDL greatly improved the load transient response. However, initial efforts to minimize or eliminate the PGM content of the interfacial layer suppressed the activity of the NSTF cathode. Along with the unacceptable PGM content of the interfacial layer, durability of the carbon-supported interfacial layer Pt catalyst is of concern.

The work under subtask 2.2 will involve: 1) identification of the most durable supported conventional catalyst based on existing 3M and subcontractor data; 2) incorporation of top 2-5 candidates into interfacial layers with ~0.01mg$_{PGM}$/cm^2 and 2-5 variations of layer composition; 3) single cell fuel cell evaluation for load transient, rated power, and kinetic response. If any interfacial layers show acceptable benefit in load transient response while either maintaining or improving the overall mass activity, the downselected 1-2 interfacial layers will be evaluated for durability via DOE electrocatalyst and support durability protocols.

Milestone 2.1: Demonstration of Interim Best of Class MEA component set candidates which meet Go/No-Go Value Goals 5-8 from Table D.2 by project Q7.

Milestone 2.2: Demonstration of Final Best of Class MEA component set candidates which meet Target Value Goals 5-8 from Table D.2 by project Q11.

Task 3. Water Management Modeling for Cold Start

The primary objective of Task 3 is to determine the key material properties and mechanisms influencing cold start with ultra-thin electrode NSTF MEAs, focusing on the demonstrated benefit of the anode GDL. The expected outcome of Task 3 is a mechanistic understanding of specific GDL material properties needed for optimal cold start with existing materials and a design tool to enable further improvement.

Subtask 3.1 Material Property and Segmented Cell Measurements

Subtask 3.1 involves material property measurements and specialized fuel cell testing to provide data to the modeling efforts which occur in subtasks 3.2-3.4.

Subtask 3.2 GDL Modeling for Cold Start

Subtask 3.2's objective is incorporation of anode GDLs into an existing subcontractor GDL network model to generate mechanistic understanding of the specific material properties of the anode GDLs which have demonstrated such significant improvement on cold start. The subcontractor will develop network models for 3-5 anode GDLs, identified by the team and which have demonstrated large variation in low temperature response.

Subtask 3.3 MEA Modeling for Cold Start

Subtask 3.3's objective is incorporation of MEA material properties into an existing subcontractor PEMFC model, with the express goal of determining the primary causal factors responsible for the wide variation in cold start response with differing anode GDLs from an overall MEA perspective, including thermal and water transport. It is expected that 3-5 MEA component sets will be incorporated into the model.

Subtask 3.4 GDL, MEA Model Integration

Due to the computational demands of these models, the GDL and PEMFC models cannot be directly integrated within the same computational cluster, and as such some work is needed to integrate results between the GDL and MEA level models; subtask 3.4 involves iterated runs of the respective models with results from one fed into the other, until the models are well integrated for each component set.

Subtask 3.5 Model Validation

Subtask 3.5 consists of periodic fuel cell evaluations to validate model predictions and provide feedback for further model optimization.

Milestone 3.1: Experimental validation of the GDL model with 2 or more 3M anode gas diffusion layers by project Q7.
Milestone 3.2: Experimental validation of integrated MEA cool start model with 2 or more 3M MEAs by project Q12.

Task 4. Best of Class MEA Integration Activities

The overall objective of Task 4 is development of an overall Best of Class MEA, utilizing top component candidates identified in subtasks 1.1-1.5, 2.1, 2.2, 5.1, and 5.5, and to develop improved mechanistic understanding of component interactions which cause performance change.

Subtask 4.1 Best of Class Component Integration

In subtask 4.1, components will be integrated into a series of experiments to identify synergistically beneficial interactions, if any, between particular component sets, leading to identification of a few top performing MEA candidates with improved performance, durability, and cold start capabilities; evaluation will consist primarily of 50cm^2 single cell tests.

Subtask 4.2 Component Interaction Diagnostic Studies

Subtask 4.2 involves experimental work aimed at developing mechanistic understanding of component interactions leading to particular performance response, particularly water management and cathode reactant utilization; experimental work will include segmented cell studies, AC impedance spectroscopy, no-gradient cell testing, and product water distribution measurements.

Milestone 4.1: Demonstration of Interim Best of Class MEA which meets Go/No-Go Value Goals 1-13 from Table D.2 by project Q7.
Milestone 4.2: Demonstration of Final Best of Class MEA which meets Target Value Goals 1-13 from Table D.2 by project Q11.

Task 5. Durability Evaluation and Performance Degradation Mitigation

Subtask 5.1 Candidate Component Evaluation and Ex-situ Characterization Subtask 5.2 Baseline MEA Evaluation and Ex-situ Characterization

Subtask 5.3 Interim Best of Class MEA Evaluation and Ex-situ Characterization

Subtask 5.4 Best of Class MEA Evaluation and Ex-situ Characterization

Subtask 5.5 Mitigation of Irreversible and Reversible Rated Power Performance Degradation

A first overall objective of Task 5 is evaluation of components and integrated MEAs towards achieving the MEA durability targets, evaluated via 50cm^2 single cell accelerated stress tests. The primary objectives of sub-tasks 5.1-5.4 are fuel cell evaluation under specified accelerated stress tests (1-4, 6, U.S. DRIVE Partnership Fuel Cell Technical Team "Cell Component Accelerated Stress Test and Polarization Curve Protocols for Polymer Electrolyte Membrane Fuel Cells, Rev. Dec. 16, 2010) with periodic in-situ diagnostics to evaluate performance as the MEA ages and ex-situ diagnostics to determine the root-cause component material changes responsible for any significant performance loss.

A second objective of Task 5, addressed in subtask 5.5, is mitigation of reversible and irreversible modes of rated power loss. As background, reduction in rated power output is known to occur in the literature via several well-documented modes, including cathode catalyst mass activity degradation, membrane conductivity degradation, and gas diffusion layer reactant transport degradation; the mechanisms by which these component degradations result in rated power loss are relatively well-understood. However, at least one additional rated power loss mode has been observed to occur in both conventional supported nanoparticle and extended-

surface area catalyst systems, such as 3M NSTF, which appears to be caused by an entirely new and not-fully-understood mechanism. The loss is manifested as a reduction in peak current density and is correlated to cathode catalyst Pt surface area per unit MEA area (cm^2_{Pt}/cm^2_{planar}) below a critical level, SA_{CRIT}, which depends upon the cathode catalyst support, loading, and composition. SA_{CRIT} for 3M NSTF Pt alloy cathodes occurs at loadings near or below the cathode PGM loadings necessary to achieve the 2017 targets (~0.075-10mg_{PGM}/cm^2_{planar}); based on literature reports, the loading at which this issue occurs with conventional supported Pt nanoparticle cathodes can be significantly higher (onset at ~0.3mg_{Pt}/cm^2).

This SA_{CRIT}-related rated power loss mode has both irreversible and reversible components, both related due to decrease of active cathode surface area. *Irreversible* rated power loss, due to this mode, is caused by irreversible decrease of the cathode Pt surface area below SA_{CRIT}, such as induced by well-documented catalyst degradation modes such as Pt dissolution and agglomeration. *Reversible* rated power losses are believed to occur by reversibly adsorbed catalytic contaminants (such as Cl^- ions), and the rated power loss is recovered by removing the adsorbed contaminants. The mechanism(s) by which the above physical causes induce the rated power loss is not known with certainty, but hypotheses exist which provide direction for initial study.

The work under subtask 5.5 will begin with internal and external literature review to gather data to support or refute our existing hypotheses and if warranted, generation of new hypotheses. The team will then design specific 50cm^2 fuel cell experiments, coupled with in-situ and ex-situ diagnostics, to further refine mechanistic understanding and narrow in on a few specific likely root causes. If identified, these root causes will provide experimental direction towards specific material modifications to reduce rated power loss.

Milestone 5.1: Demonstration of Interim Best of Class MEA component set candidates which meet Go/No-Go Value Goals 9-13 from Table D.2 by project Q7.
Milestone 5.2: Demonstration of Final Best of Class MEA component set candidates which meet Target Value Goals 9-13 from Table D.2 by project Q11.

Task 6. Short Stack Beginning of Life Performance, Power Transient, and Cold Start Evaluation

Subtask 6.1 Baseline MEA Evaluation

Subtask 6.2 Interim Best of Class MEA Evaluation

Subtask 6.3 Best of Class MEA Evaluation

The work under Task 6 consists of evaluation of 1 stack with the interim best of class MEAs determined from subtask 4.1 (subtask 6.2), and in the final year, 1 stack containing Best of Class Integrated MEA candidates from subtask 4.1 (subtask 6.3). Short stack evaluation is a necessary benchmark to validate improvements observed in the single cell MEA development work done under other tasks, especially improvements towards cold start and power transient, as well as to demonstrate freeze start. The results of subtask 6.3, combined with the durability testing results from subtask 5.4, will be used to determine the final Best of Class Integrated MEA to be incorporated into the final short stack deliverable.

Short stack evaluation in Subtask 6.2 and 6.3 is to occur at General Motors, contingent upon passage of three MEA robustness criteria in 50cm^2 MEA testing at 3M (Table 3). Delivery of the final project short stack is also contingent upon passage of the Table C.1 criteria.

Table 3. Robustness Criteria

Demonstration of the three robustness criteria to occur in subscale (e.g. 50cm^2) hardware with stack candidate materials. Evaluation to occur at 3M.

Criteria name	Description	Value
Cold Operation	Stack voltage at 30°C as a fraction of the stack voltage at 80°C operation at 1.0 A/cm^2, measured using the protocol for a polarization curve found in Table C.2. A 25°C dew point is used only for 30°C operation.	>0.3
Hot Operation	Stack voltage at 90°C as a fraction of the stack voltage at 80°C operation at 1.0 A/cm^2, measured using the protocol for a polarization curve found in Table C.2. A 59°C dew point is used for both 90°C and 80°C operations.	>0.3
Cold Transient	Stack voltage at 30°C transient as a fraction of the stack voltage at 80°C steady-state operation at 1.0 A/cm^2, measured using the protocol for a polarization curve found in Table C.2. A 25°C dew point is used only for 30°C operation. 30°C transient operation is at 1 A/cm^2 for at least 15 minutes then lowered to 0.1 A/cm^2 for 3 minutes without changing operating conditions. After 3 minutes, the current density is returned to 1 A/cm^2. The voltage is measured 5 seconds after returning to 1 A/cm^2.	>0.3

Milestone 6.1: Completion of beginning of life short stack performance evaluation of Baseline MEA by project Q2. *CANCELLED.*
Milestone 6.2: Completion of beginning of life short stack performance evaluation of Interim Best of Class MEA(s) by project Q7.
Milestone 6.3: Completion of beginning of life short stack performance evaluation of Final Best of Class MEA(s) by project Q12.

Task 7. Project Management

Task 7 incorporates overall project management tasks, including project-related meetings, correspondence between team members, and report generation.

3M will be primarily responsible to prepare the technical and financial reporting. 3M will provide reports and other deliverables in accordance with the Federal Assistance Reporting Checklist following the instructions therein. In addition, a draft project management plan, which includes the project schedule and milestones, will be provided to DOE within 30 days of the start of the project. The project management plan should be approved by 3M and DOE within 60 days of the start of the project, and will updated as necessary.

Towards the goal of optimizing the MEA, 3M will generate, collect, and analyze fuel cell testing data. 3M will provide appropriate representative data to the National Renewable Energy Laboratory using data templates as agreed to between 3M and NREL.

3M will participate in the DOE Hydrogen Program Annual Merit Review and prepare and present detailed briefings of plans, progress, and results of the technical effort to DOE personnel, as requested by DOE. 3M will also participate in Fuel Cell Tech Team meetings as requested by DOE.

Task 8. Relative Cost and Manufacturing Assessment of Technology

In Task 8, 3M will provide relative cost savings data of the downselected MEA relative to current baseline MEA using existing models for MEA cost at ~500k/year volume.

Milestone 8.1: Completion of relative cost savings report of Final Best of Class MEA relative to 2012 Best of Class MEA by project Q12.

Technical Summary

Task 1. Integration Activities Toward ¼ Power, Performance at rated power, Q/ΔT, and Cost Targets

- *Subtask 1.1. Improved Mass Activity, Durable, and Rated-power Capable NSTF Cathode Oxygen Reduction Reaction (ORR) Catalysts*
- *Subtask 1.2. Durable, Ultra-Low PGM NSTF Anode Catalyst*
- *Subtask 1.3. Durable, Improved Conductivity PEMs*
- *Subtask 1.4. Low-Cost, High Performance GDLs*
- *Subtask 1.5. Rated Power Sensitivity to Flow Field Geometry*

The work under Task 1 emphasizes component integration towards achievement of the ¼ power, rated power, and Q/ΔT targets, with a focus on 50cm^2 single cell MEA evaluation of anode and cathode catalysts, PEMs, and anode and cathode gas diffusion layers (GDLs) with the potential for performance and durability improvements towards meeting the targets. In addition, subtask 1.5 will evaluate the impact of flow field land and channel geometry to potentially further improve performance towards the above targets. Initially, testing will occur with a common baseline material set, where the specific component under evaluation replaces the same component in the baseline material set.

Subtask 1.1. Improved Mass Activity, Durable, and Rated-power Capable NSTF Cathode Oxygen Reduction Reaction (ORR) Catalysts

Subtask Overview

Subtask 1.1's focus is evaluation of MEAs incorporating advanced NSTF cathode ORR catalysts with varying compositions, loadings, and post-process treatments, with initial focus on the 3M Pt_3Ni_7 material system.

Subtask High Level Work Summary

The work in this subtask focused on optimization of annealing and dealloying post processes. A set of 4 annealing experiment series were conducted, and the annealed catalysts were evaluated in fuel cell, by X-ray diffraction (XRD), and by transmission electron microscopy with energy-dispersive X-ray spectroscopy (TEM+EDS). New dealloying methods were assessed, consisting of four classes of free corrosion and one electrochemical method. 63 catalysts with new dealloying methods were generated. One free corrosion method was downselected and optimized for potential scale-up. Three 50' sections of dealloyed catalyst were ultimately produced for the short stack deliverable. Catalysts were evaluated for beginning of life (BOL) performance, activity, and break-in conditioning rate, as well as limited durability studies.

Subtask Key Results

PtNi Annealing Optimization

In previous work, the mass activity of PtNi/NSTF was found to improve dramatically with annealing (Figure 1). Limited work had indicated that annealing of "P4" PtNi/NSTF (multiple Pt and Ni layers) resulted in substantial mass activity gains, increasing from ca. 0.25 to in excess of 0.6A/mg. Limited work with "P1" PtNi/NSTF (fabricated from an alloy target, homogenous) had shown more modest gains.

The objective of the work within this project was to further optimize the annealing for improved mass activity, performance, and potentially durability.
Four series of annealing studies were conducted, all using "P1" Pt_3Ni_7 at ca. 0.12mg_{Pt}/cm^2 loading. All used the "SET" process for annealing, akin to that disclosed in U.S. patent US8748330, which discloses using radiation annealing. Catalysts were typically evaluated for change in bulk crystalline properties by XRD, mass activity and surface area by XRD, and a subset were evaluated via TEM and EDS.

Figure 3 summarizes the key activity and XRD results from this study. Without treatment, the mass activity of the P1 Pt_3Ni_7 was ca. 0.38-0.40A/mg. Annealing often resulted in modest gains in activity, with several exceeding 0.44A/mg and one exceeding 0.50A/mg. Specific area was found to increase from ca. 15 to as high as 19m^2/g. Annealing resulted in significant changes in detected grain size and lattice constant, with (111) grain sizes increasing as much as 2.5x and the lattice constant decreasing from 3.69 to 3.67Å, similar to that reported for annealed bulk alloys. This figure suggests a possible correlation between mass activity and/or specific area to the bulk crystalline properties.

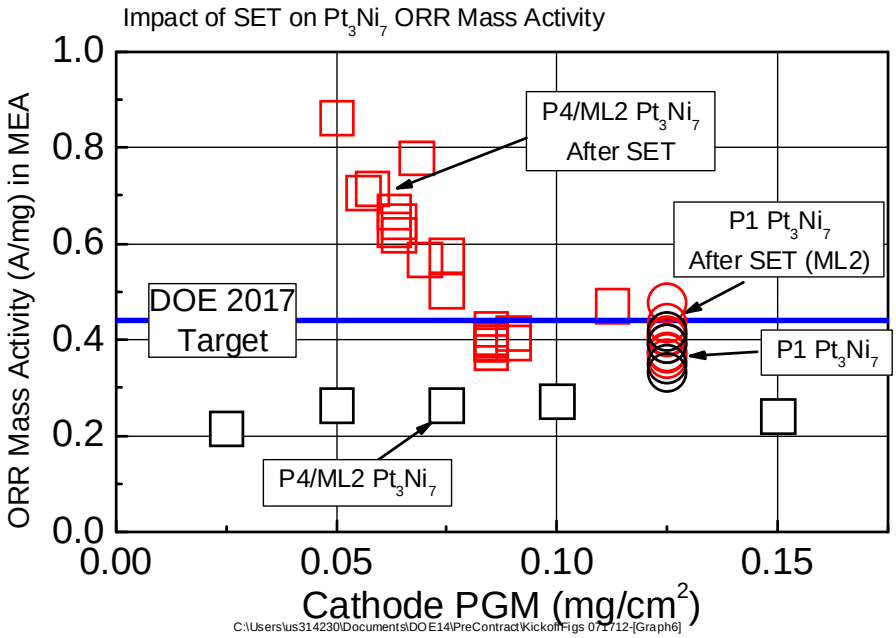

Figure 1. Impact of annealing on PtNi/NSTF mass activity (pre-project).

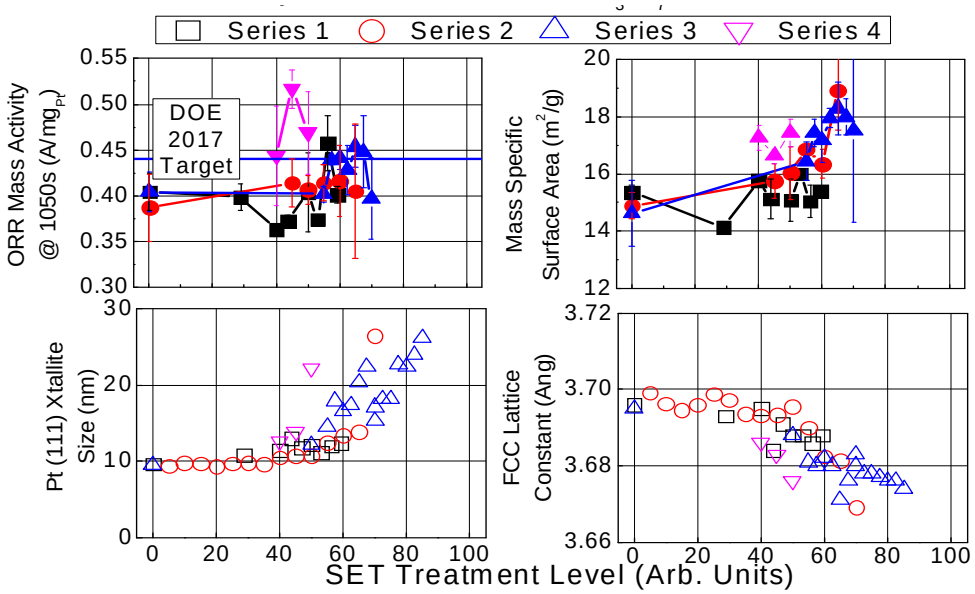

Figure 2. Impact of SET treatment level on mass activity, surface area, (111) grain size, and FCC lattice constant.

Figure 3 directly plots specific area against the grain size and lattice constant. Specific area increases monotonically with grain size between 10nm (as deposited) and 20nm, after which no further gains are noted. The specific area may also correlate with FCC lattice constant.

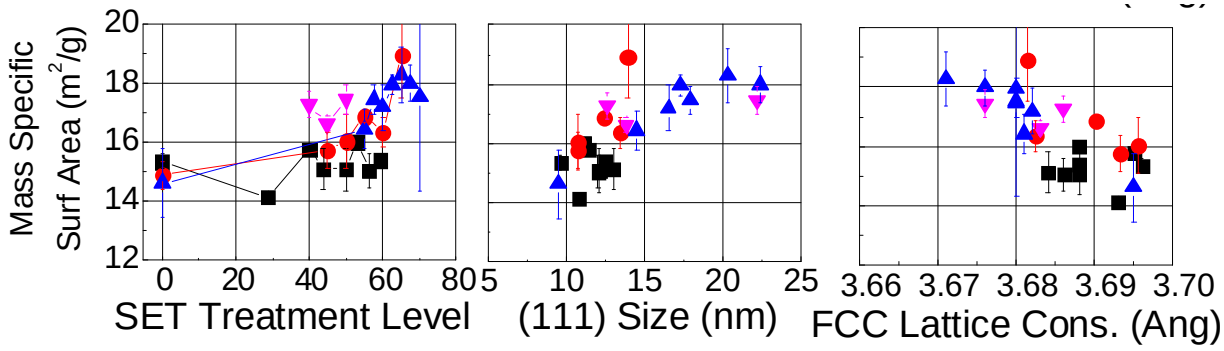

Figure 3. Correlation of specific area to SET treatment level, XRD grain size, and XRD lattice constant.

Representative samples were analyzed by TEM, to understand bulk morphological changes before and after annealing, and how annealing influences ultimate structure and composition after MEA break-in conditioning, which effectively dealloy the catalyst in-situ via electrochemical cycling. Figure 5 shows that annealing increased crystallinity, as evidenced by development of relatively large surface facets embedded into the thin film matrix. Figure 5 shows that after MEA conditioning, the Pt_3Ni_7 transforms into a nanoporous thin film coating. The annealed sample, with higher specific area, had qualitatively better defined nanopore structure and slightly higher Ni content.

While annealing was found to be effective at increasing the activity and specific area of Pt_3Ni_7, there were two issues which ultimately lead to us not utilizing annealed Pt_3Ni_7 within this project. The first issue was that annealed materials were more difficult to dealloy than non-annealed. Figure 6 (left) shows that after dealloying using the standard 3M chemistry and time, the dealloying successfully removed ca. 25% of the original Ni content, and this fraction tended

to decrease as the annealing extent increased. Our assessment was that developing a dealloying method for annealed catalyst was not feasible in the 1st project year when this work was done.

The second primary issue with annealing was that in general, it slowed the break-in conditioning rate. Figure 6 (right) shows that early in conditioning, the annealed catalyst's performance was highly suppressed relative to the as-made, unannealed catalyst over the first 10 hours.

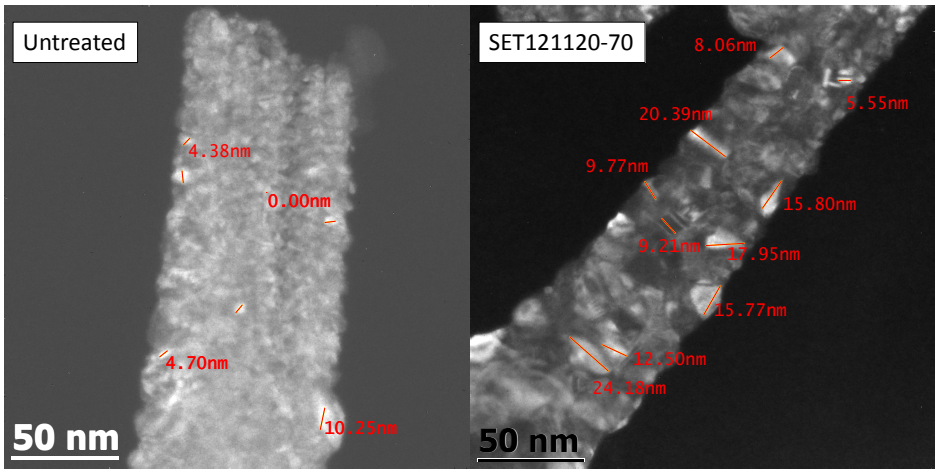

Figure 4. TEM of as deposited vs. SET annealed Pt_3Ni_7.

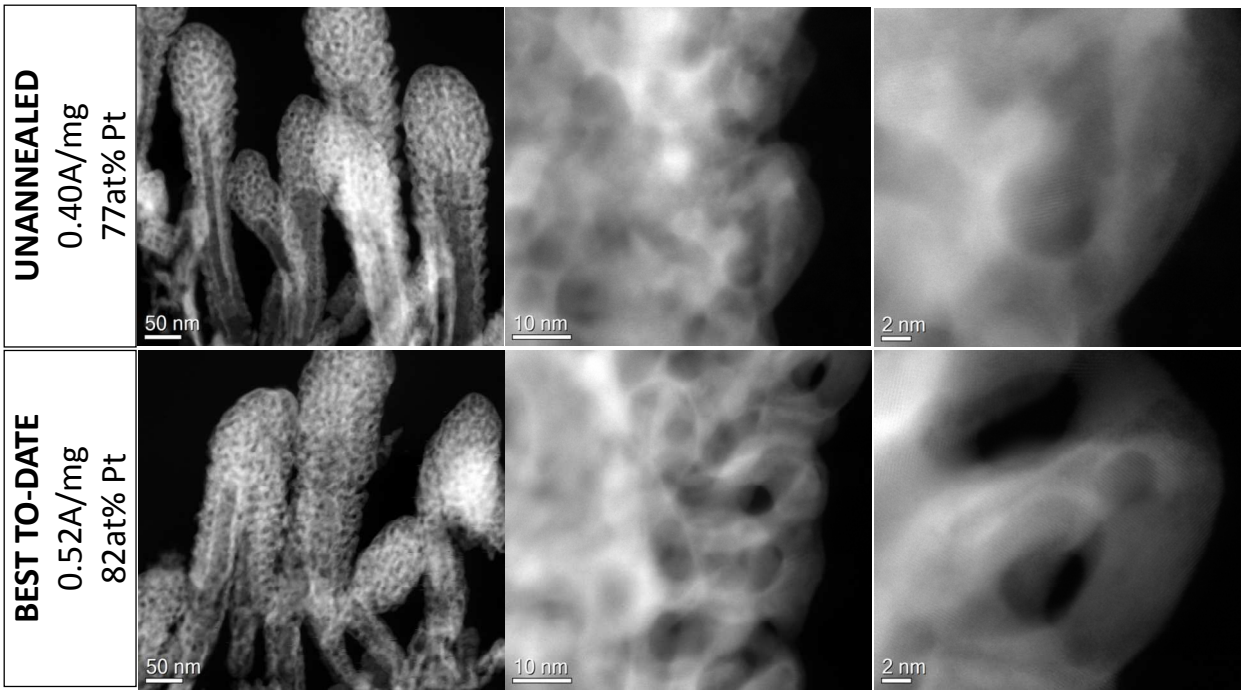

Figure 5. TEM of as deposited vs. SET annealed Pt_3Ni_7, after break-in conditioning.

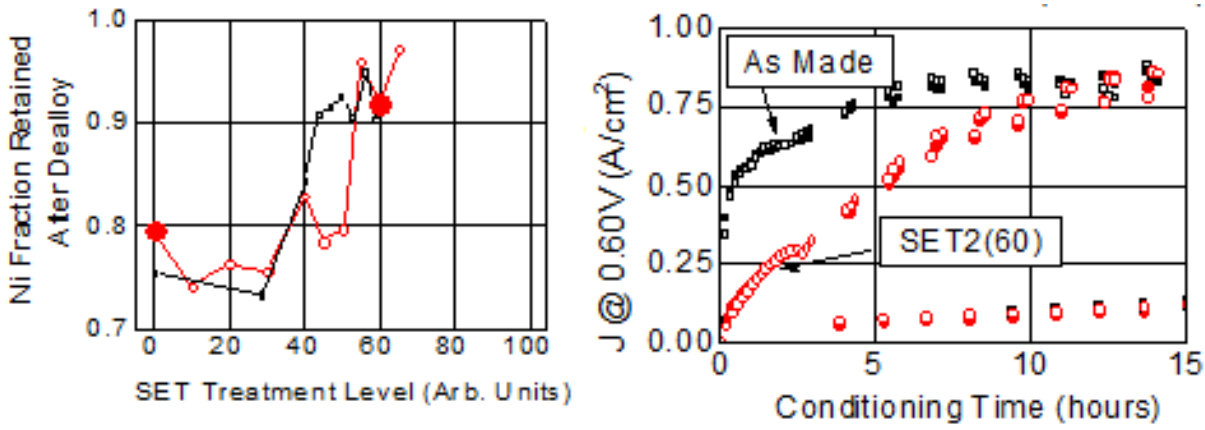

Figure 6. Impact of annealing on dealloyability (left) and break-in conditioning rate (right).

PtNi Dealloying Optimization – Free Corrosion Chemistry Optimization

Initial dealloying optimization focused largely on development of free corrosion methods for rapidly dealloying Pt_3Ni_7/NSTF catalyst via optimization of the free corrosion bath chemistry. Several new chemistries were initially proposed and evaluated by Johns Hopkins University (JHU). The primary screening criteria were the dealloying rate, dealloying extent, and compatibility with proposed pilot-scale continuous processing at 3M. Figure 7 compares the dealloying extents vs. treatment time for the 4 general classes of dealloying chemistry evaluated. Chemistries 1 and 2 were found to increase the Pt mole fraction from ca. 0.3 to 0.4 without further increase. Chemistries 3 and 4 were found to rapidly achieve Pt mole fractions exceeding 0.50 within a few minutes.

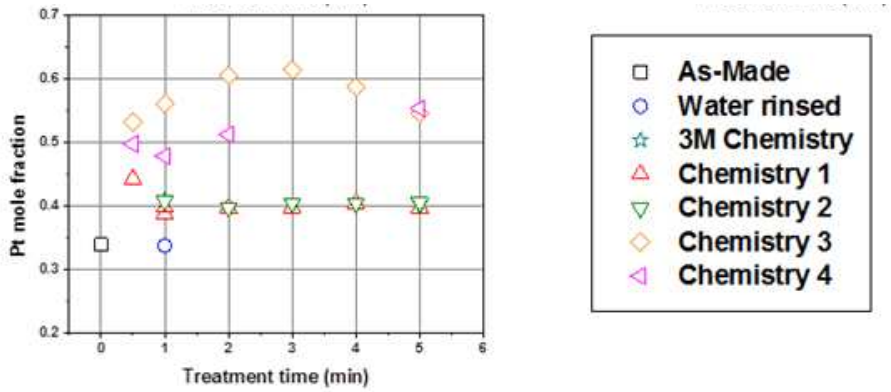

Figure 7. Impact of dealloying chemistry type and treatment time on resultant dealloyed composition.

Proposed methods which met these initial criteria were then typically analyzed for performance and activity in fuel cell. 83 individual fuel cell samples were fabricated and a substantial fraction were evaluated in fuel cell. Figure 8 provides an overview of a representative number of samples. In general, the JHU dealloying methods had strong impacts on mass activity, specific area, and H_2/Air performance. Several samples had generally improved H_2/Air performance compared to the 3M baseline method, but often the improved performance came with the tradeoff of marginally-to-severely reduced mass activity.

Figure 9 compares performance, activity, and ECSA from the most promising methods from the JHU development. The "best" JHU free corrosion method yielded significantly improved H_2/Air performance as compared to the baseline dealloying method, and similar mass activity. Electrochemical (EC) dealloying yielded the best overall performance, but was deemed out of scope for this project where stack quantities of catalyst would be needed. EC dealloying as practiced here required long treatment times and was perceived to have complicated equipment and process development needed.

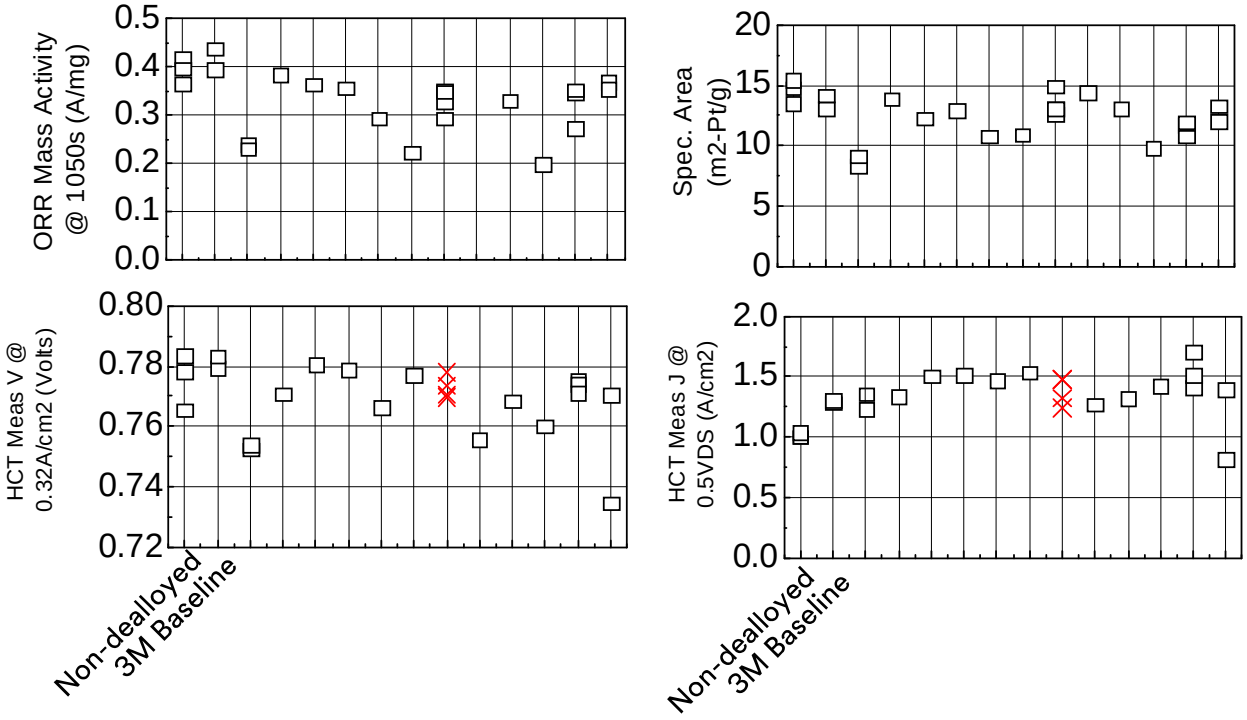

Figure 8. Comparison of experimental JHU dealloying treatments to non-dealloyed (1st column) and 3M pre-project baseline dealloying method (2nd column). All with 0.125mg$_{Pt}$ Pt_3Ni_7/NSTF. (Top right): Mass activity. (Top left): Specific area. (Bottom left): HCT H_2/Air cell voltage at 0.32A/cm^2. (Bottom right): HCT H_2/Air current density at 0.50V.

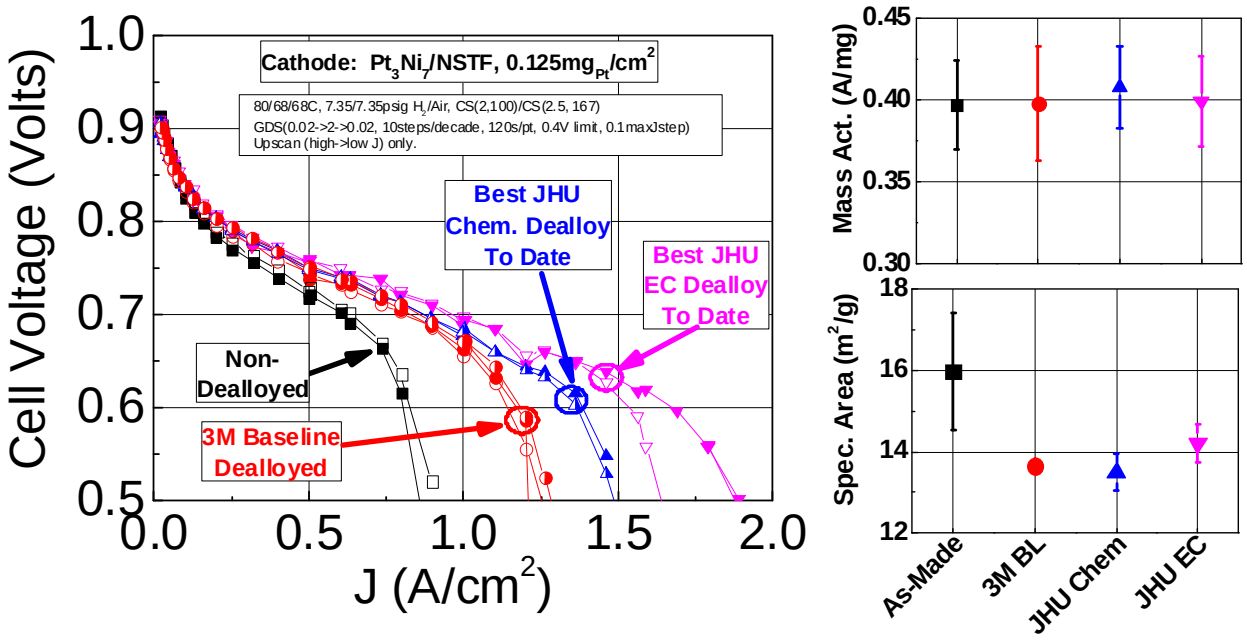

Figure 9. Comparison of JHU free corrosion and EC dealloying to baseline 3M dealloying method. (Left): HCT H_2/Air performance. (Top right): Mass activity. (Bottom right): Specific area.

Two methods which yielded promising fuel cell results and rapid dealloying were then evaluated for pilot-scale compatibility with pilot-scale trials. One method involved treatment in warm, concentrated sulfuric acid, which was quickly discarded due to degradation of and acid retention within the catalyst liner, as well as concerns about process safety. The other method was evaluated and found to be compatible, and was downselected for performance and process optimization.

PtNi Dealloying Optimization – Performance Sensitivity to Dealloying Conditions

As noted above, the downselected dealloying method experiments were conducted to determine the impact of dealloying time and temperature on resultant MEA mass activity and H_2/Air performance. 4x4" pieces of Pt_3Ni_7/NSTF catalyst were treated with the downselected chemistry at three temperatures (T1 < T2 < T3) and for various treatment times. Catalysts were evaluated in fuel cell and for post-dealloy composition. Figure 10 summarizes the results. As time increased at T1 temperature, mass activity decreased slightly, specific area decreased slowly, and H_2/Air performance increased. As temperature increased to T2 and T3, the rate of mass activity and specific area loss increased. At T2 and T3, H_2/Air performance generally increased with short treatment times then decreased.

Figure 11 shows that the variations of activity, area, and H_2/Air performance are largely just a function of the Pt mole fraction after dealloying. Mass activity and specific area decreased as the post-dealloy Pt mole fraction increased above ca. 0.40, but H_2/Air performance generally was maximized above 0.43. The assessment was that dealloying too aggressively does not allow nanoporosity to develop, which limits specific area and thereby mass activity.

Based on these results, it was determined that for dealloying process optimization, the post-dealloy Pt mole fraction should target 0.40-0.42 to co-optimize the mass activity and H_2/Air performance.

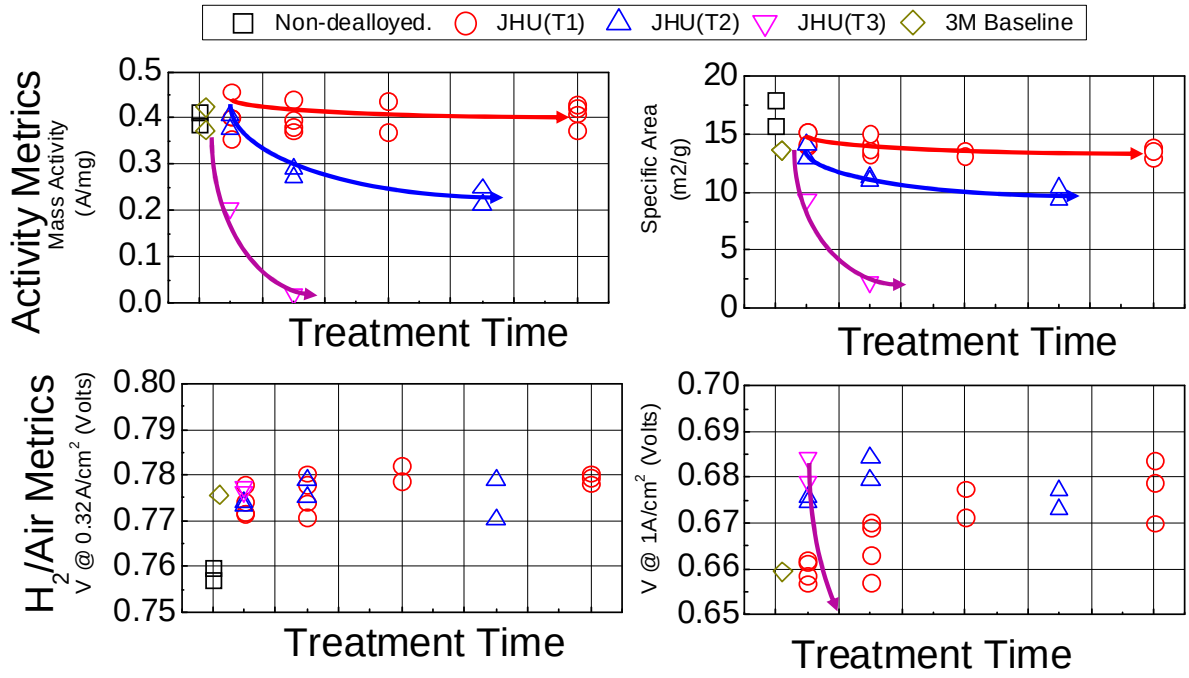

Figure 10. Impact of dealloying temperature and time. (Top left): Mass activity. (Top right): Specific Area. (Bottom left, right): HCT H_2/Air cell voltage at 0.32A/cm^2 and 1A/cm^2.

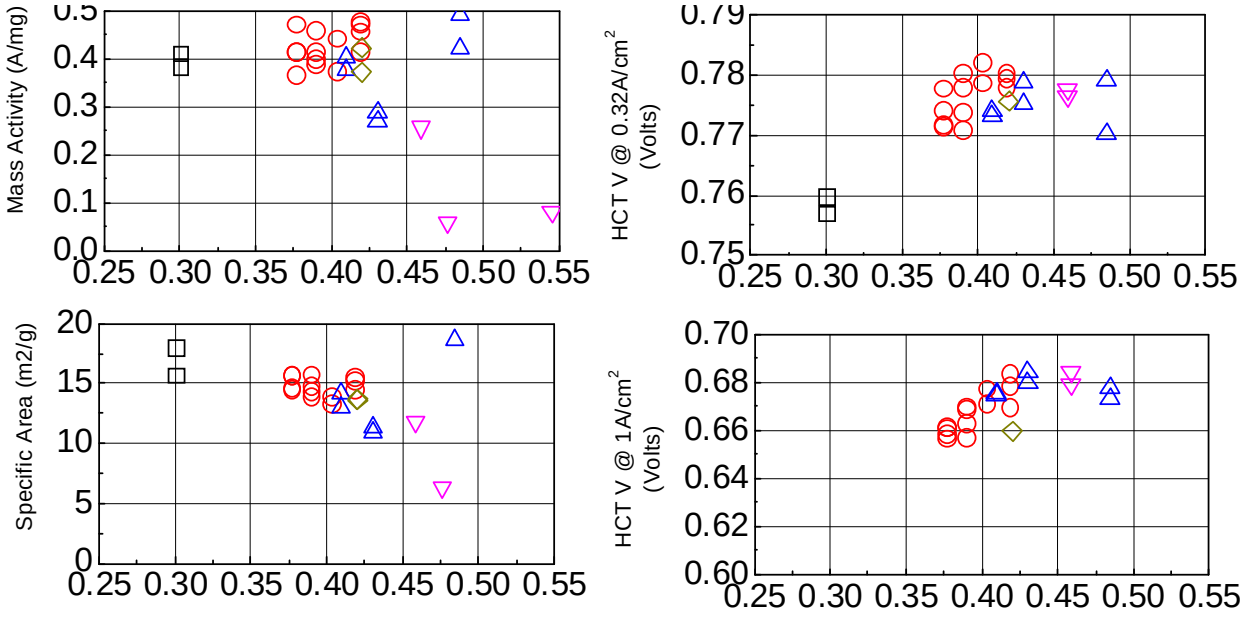

Figure 11. Impact of post-dealloy mole fraction. (Top left): Mass activity. (Top right): Specific Area. (Bottom left, right): HCT H_2/Air cell voltage at 0.32A/cm^2 and 1A/cm^2.

PtNi Dealloying Optimization – Structural and Compositional Characterization of Downselected Dealloying Chemistry

Pt_3Ni_7/NSTF which was dealloyed with JHU conditions were evaluated for structure and composition by TEM+EDS at Oak Ridge National Laboratory (ORNL). Figure 12 compares

pre- and post-dealloyed. After dealloying, the bulk Pt mole fraction increased from 30 to 42at% Pt, but the surface was further dealloyed to ca. 53at%. Dealloying resulted in formation of pores between whiskerettes and perhaps some nanoscale pores, but did not result in the typical well defined ordered pore structure obtained with MEA conditioning, i.e. *in-situ electrochemical dealloying.* It is believed that an optimal ex-situ free corrosion method would ultimately allow the same composition and structure as obtained with MEA conditioning.

Bulk vs. surface Pt (at.%) in Pt_3Ni_7/NSTF

	$Bulk_{(STEM)}$	$Surface_{(XPS)}$	Surface Layer
No Dealloy	30	20	Ni Oxide
JHU Chem.	42	53	Pt-rich

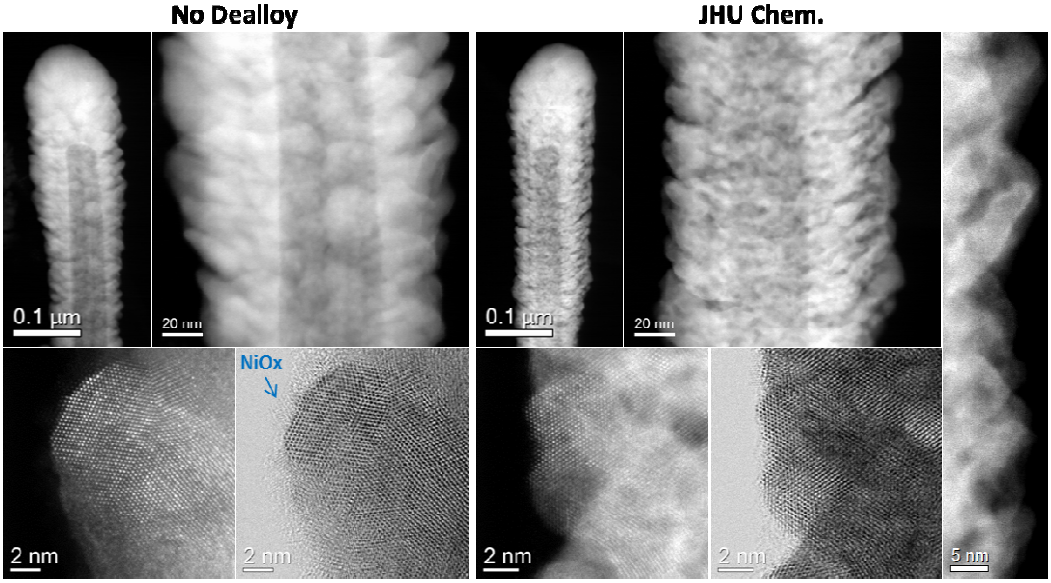

Figure 12. TEM structural and EDS composition analysis of JHU dealloyed Pt_3Ni_7.

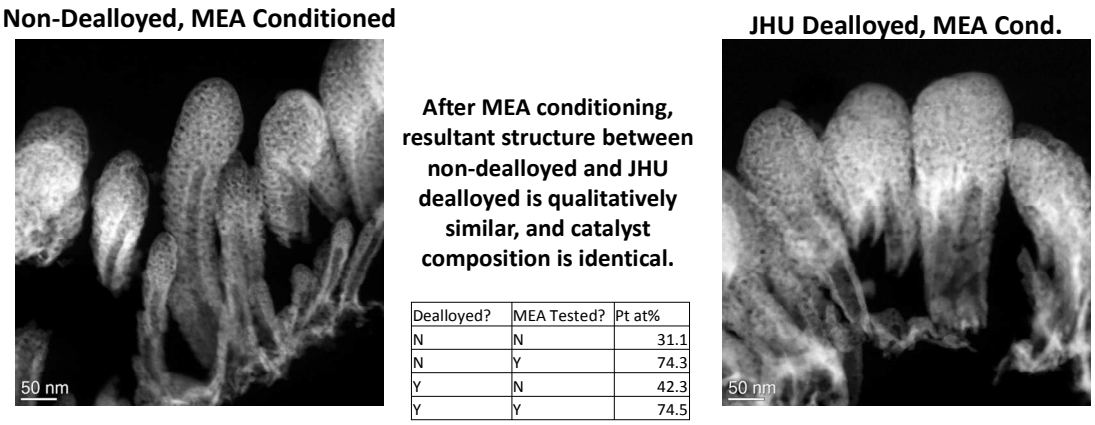

After MEA conditioning, resultant structure between non-dealloyed and JHU dealloyed is qualitatively similar, and catalyst composition is identical.

Dealloyed?	MEA Tested?	Pt at%
N	N	31.1
N	Y	74.3
Y	N	42.3
Y	Y	74.5

Figure 13. Comparison of MEA-conditioned PtNi/NSTF with and without JHU dealloying.

PtNi Dealloying Optimization – Downselected Chemistry Optimization

One challenge with the downselected chemistry was that at room temperature, the dealloying rate was too slow to enable reasonable continuous processing rates (e.g. a few minutes). Work was conducted to determine if the rate could be increased through increased dealloying temperature. 1x1" pieces of catalyst were exposed to the JHU chemistry for times ranging from seconds to several minutes, then evaluated for post-dealloy composition by XRF. The post-dealloy Pt mole fraction at a given temperature was found to be well represented by a semi-log relationship with time, and the semi-log slope generally increased with increasing temperature. An effective activation energy was found to analyzing the slope vs. 1000/T.

One concern with the temperature-accelerated method was that MEA performance and catalyst activity may be negatively impacted. For example, it is conceivable that higher temperature could change the composition profile through the coating thickness. To test this, larger catalyst pieces were treated and evaluated for composition by XRF and in fuel cell for mass activity and surface area. A summary of three experiments is shown in Table 4. Experiment 1 consisted of a less aggressive dealloying conditions, with relatively lower treatment temperature and long treatment time. Experiment 2 was moderate aggressive and Experiment 3 was relatively very aggressive, using relatively high dealloying temperature and short dealloying time. XRF analysis shows that in the more aggressive Experiment 3, the dealloying resulted in a Pt mole fraction higher than targeted. Mass activities generally remained close to the 0.4A/mg benchmark.

Table 4. Time/Temp Optimization, Targeting 0.41 Final Pt Mole Fraction

Experiment	Final Pt Loading (mg/cm^2)	Pt Mole Fraction	Specific Area (m^2/g)	Mass Activity (A/mg)
1	0.121	0.43	13.4	0.37
2	0.129	0.42	13.0	0.39
3	0.119	0.46	12.9	0.37

PtNi Dealloying Optimization – Lab-scale continuous process development.

Several experiments were conducted to evaluate the feasibility of dealloying using the downselected chemistry in a continuous, roll-to-roll process, summarized in Table 5. In the initial experiments, 10' sections of catalyst were treated by immersion in baths containing the dealloying chemistry, followed by DI rinsing and drying.
Trial 2 focused on mapping the batch to continuous process, via evaluating at different dwell times. Trial 3 focused on evaluating the dealloying model-determined times and temperatures which aimed to yield ca. 0.40-0.42 final Pt mole fractions, which was largely successful.

Trial 4 was a first attempt at producing an extended quantity (50') suitable for making dealloyed NSTF CCMs on continuous roll to roll CCM fabrication processing for stack testing. The resultant Pt mole fraction was slightly higher than targeted, at 0.435 on average. Based on the trial 4 results, re-optimization for dwell time was needed (Trial 5).

Trial 6 and 7 were the second and third attempts at producing 50' batches of dealloyed catalyst for stack testing. Resultant Pt mole fractions were 0.40 and 0.41, slightly below and just at the targeted 0.40-0.42 mole fraction.

Table 5. Summary of Pilot-scale process trials

Phase	Run	Purpose	Chemistry	Run Date	**Cathode ID**	Dwell Time (arb.)	Temp (arb.)	Cat. Length (ft.)	Mean Post Dealloy Pt Load ($\mu g/cm^2$)	Mean Post Dealloy Pt Fraction
1	1	Validate new set up with old 3M chemistry	3M	11/11/2014	**NB161304-21-A**	1.0	RT	10	105.8	0.383
2	1	Eval. JHU chem. @ different dwell times	JHU	11/24/2014	**NB161304-21-B**	5.0	T1	10	108.7	0.405
	2			11/24/2014	**NB161304-21-C**	15.0	T1	10	105.9	0.424
	3			11/24/2014	**NB161304-21-D**	30.0	T1	10	98.6	0.444
3	1	Eval. opt. temp/speed w/ JHU chem.	JHU	1/19/2015	**NB161304-26-A**	10.4	T2	10	105.4	0.429
	2		JHU		**NB161304-26-B**	4.1	T3	10	108.7	0.414
	3		JHU		**NB161304-26-C**	2.0	T3	10	109.9	0.409
4	1	Final BOC Stack – 1st CCM Batch	JHU	7/20/2015	**NB161304-63**	2.0	T3	50	103.2	0.435
5	1	50°C Dwell Time Exp	JHU	8/14/2015	**NB161304-70_1**	0.5	T3	3	101.3	0.414
	2				**NB161304-70_2**	1.0		3	102.3	0.427
	3				**NB161304-70_3**	1.5		3	101.2	0.442
	4				**NB161304-70_4**	2.0		3	99.0	0.433
	5				**NB161304-70_5**	2.5		3	97.3	0.451
	6				**NB161304-70_6**	0.5		3	104.7	0.410
	7				**NB161304-70_7**	2.0		3	100.2	0.445
6	1	Final BOC Stack – 2nd CCM Batch	JHU	9/9/2015	**NB161304-76**	0.8	T3	50	105.65	0.399
7	1	Final BOC Stack – 2nd CCM Batch	JHU	9/23/2015	**NB161304-79**	1.3	T3	50	102.70	0.412

Figure 14 summarizes resultant activity, area, and H_2/Air performance for the Trial 4 – 7 catalysts, plotted as a function of Pt mole fraction. Near the targeted 0.40-0.42 Pt mole fraction, mass activities were on average above 0.30A/mg, with large decreases at higher Pt fractions,

consistent with the previous lab-scale work. On average, the mass activities were modestly lower than those obtained with the laboratory dealloying (~0.38A/mg, Table 4).

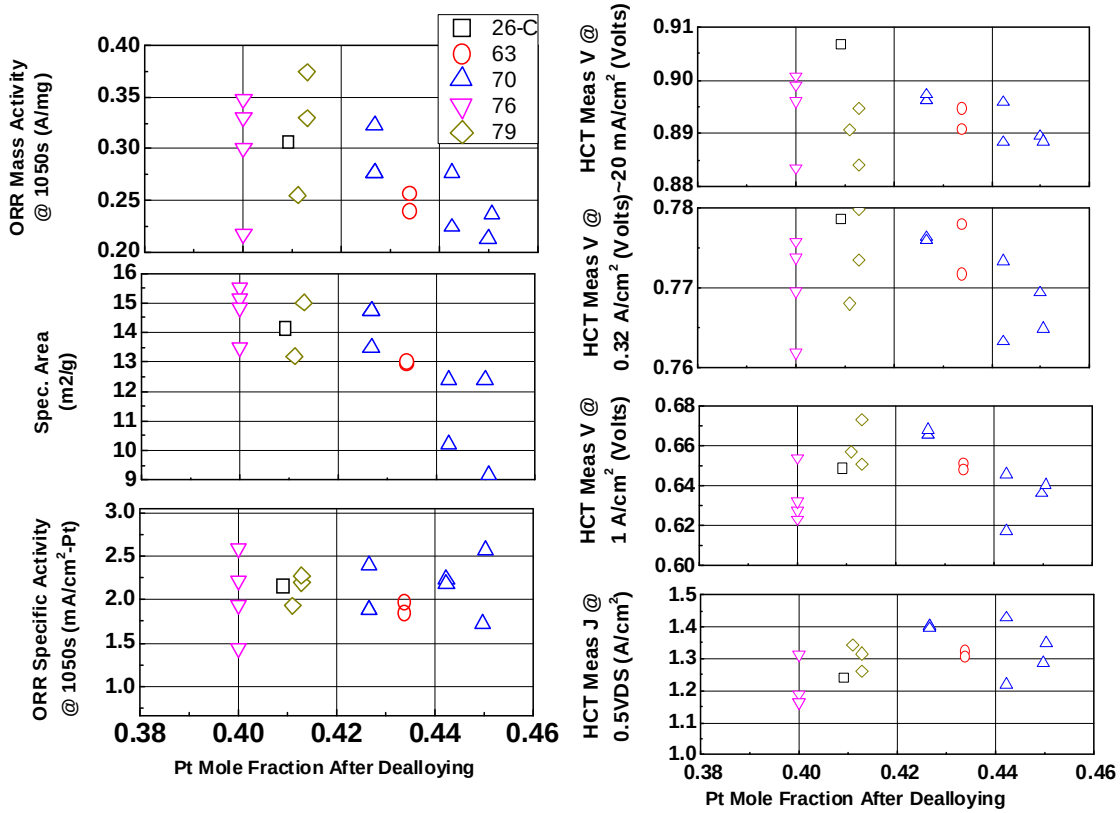

Figure 14. Activity, area, and H_2/Air performance of trial 4-7 dealloyed cathode catalysts.

In addition to the catalyst performance metrics, the rate of break-in conditioning was also assessed. Figure 15 shows that break-in was substantially complete in less than 10 hours with lab-scale CCMs (not best of class construction).

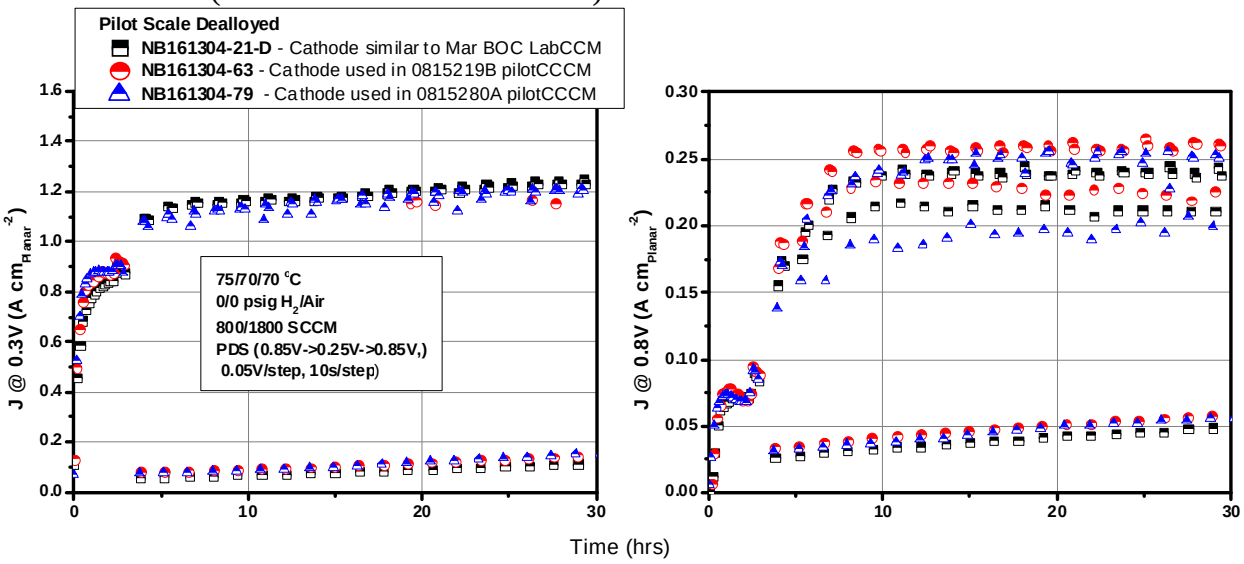

Figure 15. Break-in conditioning of lab CCMs utilizing roll-to-roll dealloyed PtNi.

PtNi Optimization – Durability

A subset of electrocatalysts were evaluated for durability under the DOE Electrocatalyst AST (30k cycles between 0.6-1.0V). Figure 16 summarizes beginning of life and post-AST metrics, measured in fuel cell. Annealing resulted in substantial activity improvements, but did not improve the durability. Mass activity losses ranged from 60 to 70% after 30k cycles, and the post-AST mass activity was independent of annealing extent.

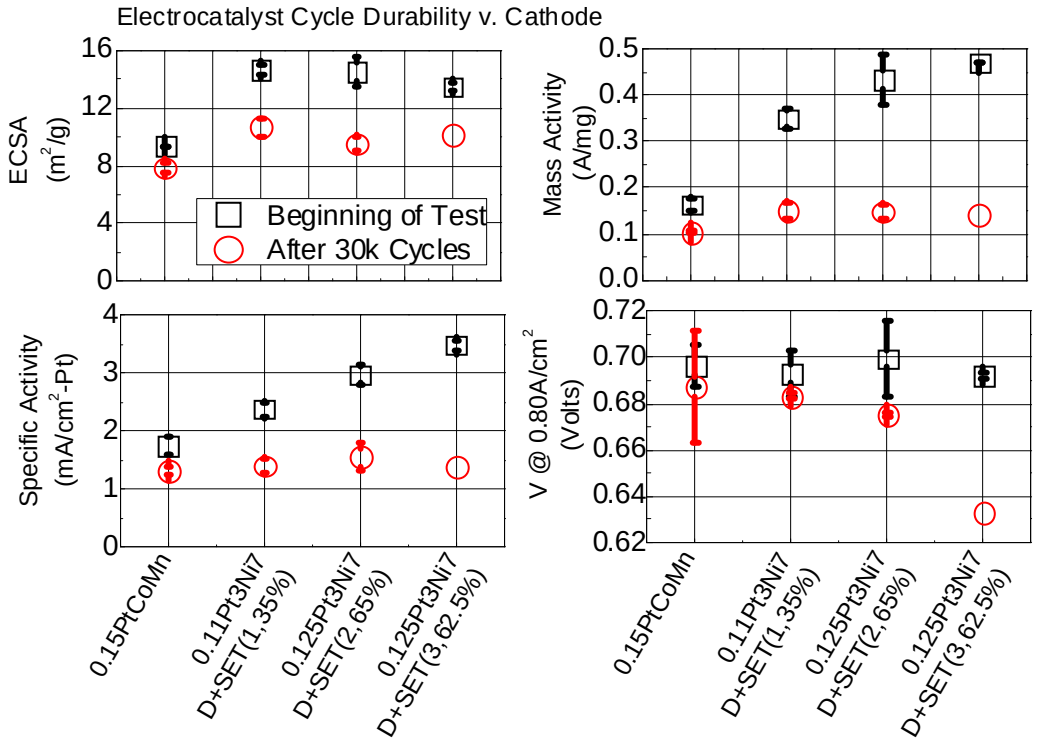

Figure 16. Electrocatalyst Durability of Select Annealed + Dealloyed PtNi/NSTF Catalysts

Work was initiated to improve the durability of PtNi/NSTF, outside the project. That work identified that incorporation of small amounts of additives into Pt_3Ni_7 greatly improved mass activity and specific area retention, from which four patent applications were ultimately filed. Optimization of this approach for BOL activity and durability is continuing.

Subtask Conclusions

This subtask has focused on optimization of annealing and dealloying processes for P1 Pt_3Ni_7/NSTF catalyst.

Annealing was found to modestly increase the mass activity and specific area of P1 Pt_3Ni_7 up to ~ 20% vs. unannealed. The improved specific area correlated with increased grain size with annealing, detected by XRD and TEM. Annealed P1 catalyst was not downselected for incorporation into the project best of class MEAs due to increased difficulty in dealloying and reduced startup rate.

Significant work was conducted towards development of a scalable dealloying process which resulted in improved performance relative to the 3M baseline method. 4 classes of dealloying chemistry were evaluated, and one was downselected which yielded improved high current density performance and was compatible with continuous processing. Time and temperature

sensitivity of the dealloying method was assessed, and a process map identified. 6 continuous roll to roll process trials were conducted on lab-scale equipment, and 3 50' rolls of catalyst were produced for use in continuous CCM fabrication for the final project stack deliverable. Roll-to-roll catalysts were found to yield slightly suppressed mass activity as compared to laboratory batch dealloyed. Break-in conditioning was relatively rapid, achieving largely complete performance within 10 hours.
Durability of representative PtNi catalysts was assessed using the DOE Electrocatalyst AST. The dealloyed catalysts generally had relatively poor mass activity durability, losing 60-70% after the AST, and the end of test activity was largely independent of annealing or dealloying.

Future Directions

Additional work towards optimization of annealing and dealloying of nanoporous NSTF catalysts is warranted. In the limited work here, annealing was found to increase the mass activity above the DOE 2020 target. Work to develop effective dealloying processes for annealed PtNi catalysts could enable high activity and high performance.
Electrochemical dealloying shows significant promise towards improving the rated power capability. The key question to address is scalability.
Durability of nanoporous catalysts is of key concern, but incorporation of durability additives has been shown to be effective.
Such work is currently in progress at 3M under another DOE-funded project, and is showing good prospects of achieving the DOE mass activity and durability targets in the near term.

Subtask 1.2. Durable, Ultra-Low PGM NSTF Anode Catalyst

Subtask Overview

The work on subtask 1.2 is evaluation of NSTF anode catalysts, including durable materials developed under current award DE-EE0005667; a key initial focus will be PGM loading minimization < $0.05 mg_{PGM}/cm^2$.

Subtask High Level Work Summary

Several experimental NSTF anode catalyst candidates were fabricated and evaluated for BOL performance, with the objective of determining minimum PGM loading. The influence of different NSTF support geometries (number density, loading) were also evaluated.
A study conducted with ANL evaluated the HOR kinetics of NSTF electrodes, resulting in an understanding of the loading/surface area/performance sensitivity of NSTF HOR anodes.

Subtask Key Results

Table 6 summarizes the catalysts generated and evaluated. Catalysts consisted of 5 different compositions, including reversal tolerance catalysts, with areal loadings ranging from 5 to 30 $\mu g_{PGM}/cm^2$. Compositions included pre-project baseline Pt and PtCoMn, as well as new candidates including PtNi and a subset of the above base catalysts with an OER additive to enable improved reversal tolerance.

Figure 17 summarizes the impact of composition and loading on the H_2/Air performance, as compared to baseline PtCoMn/NSTF anode catalyst with 0.05 mg_{Pt}/cm^2. All compositions were able to reach loadings as low as 20 $\mu g/cm^2$ without significant performance impact. As loadings were reduced further, significant performance losses were observed, which depended upon the

composition. For pure Pt, PtCoMn, and PtNi, the performance losses occurred at loadings of 10, 5, and 5 μg/cm^2, respectively.

Table 6. NSTF Anode Compositions and Target Loadings		
Composition	NSTF Support	Anode PGM (mg_{PGM}/cm^2)
Pt	Standard	0.01, 0.02, 0.03
$Pt_{69}Co_{28}Mn_3$	Standard	0.005, 0.01, 0.02
Pt_3Ni_7	Standard	0.005, 0.01, 0.02
$Pt_{69}Co_{28}Mn_3$+OER	Standard	0.018
Pt_3Ni_7+OER	Standard	0.018

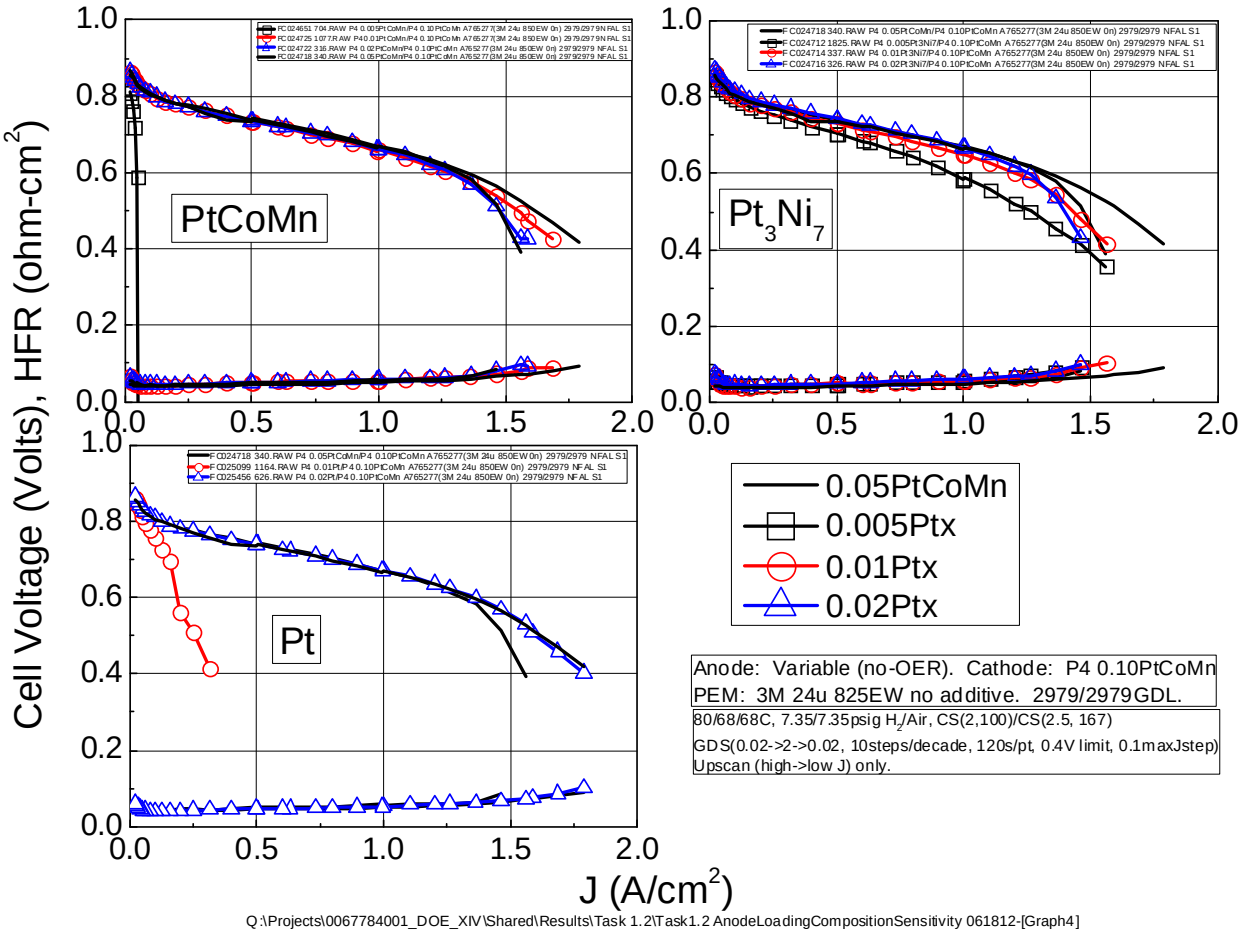

Q:\Projects\0067784001_DOE_XIV\Shared\Results\Task 1.2\Task1.2 AnodeLoadingCompositionSensitivity 061812-[Graph4]

Figure 17. Influence of Anode NSTF Catalyst Composition and Loading on Performance

Figure 18 summarizes performance at 1A/cm under H_2/Air for the experimental anode catalysts. For OER-free catalysts (left), the onset of performance loss occurred at µg/cm^2. Catalysts with OER generally followed the same trends as OER-free.

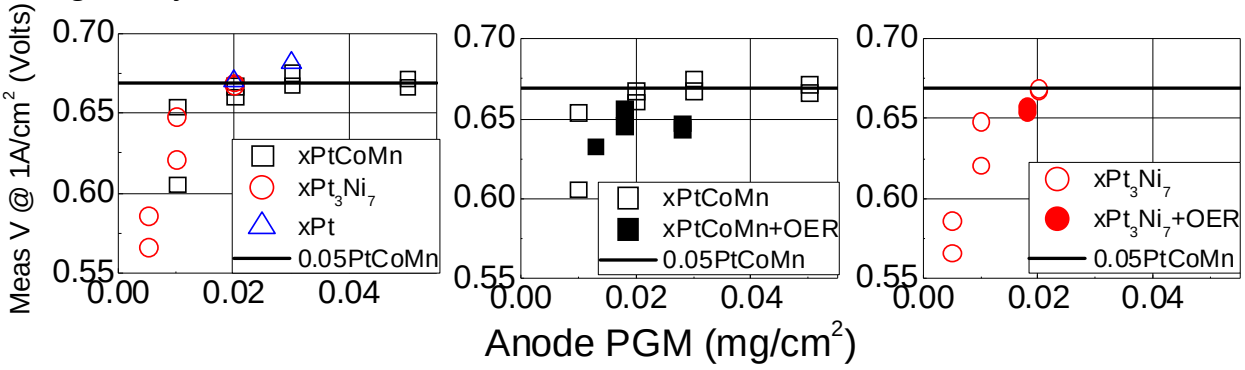

Figure 18. Summary of H_2/Air Performance vs. Anode Loading and Composition

Figure 19 summarizes performance evolution during break-in conditioning for MEAs with the experimental anodes. Break-in rate also depended strongly on composition and loading. Break-in times ranged from ca. 20 hours for the baseline and 20 µg/cm^2 loaded electrodes to hundreds of hours with the lowest loaded electrodes.

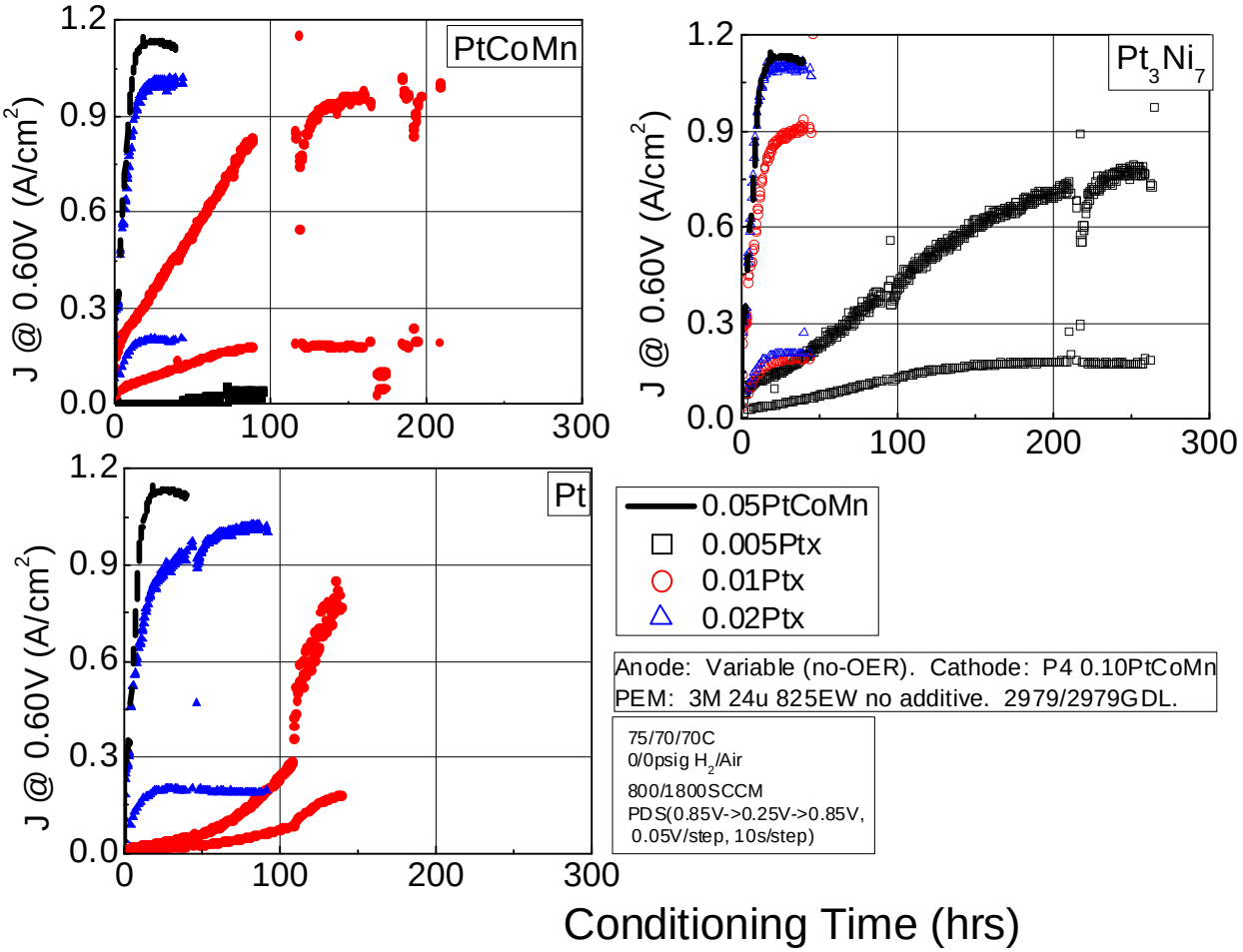

Figure 19. Influence of Anode NSTF Catalyst Composition and Loading on MEA Break-in Conditioning.

A study was conducted with Argonne National Laboratory (Ahluwalia, Wang) to characterize and model the HOR/HER kinetics. Figure 20 summarizes H_2 pump polarization curves as a

function of temperature and conditioning state, taken with symmetric electrode NSTF MEAs with 0.02mgPt/cm^2. Measurements were taken either after standard MEA conditioning ("NFAL", cathode electrode specifically conditioned) or after both electrodes were conditioned ("NFAL+RFAL"). Significant reductions in hydrogen oxidation reaction/hydrogen evolution reaction (HOR/HER) overpotential were observed after anode specific conditioning was applied.

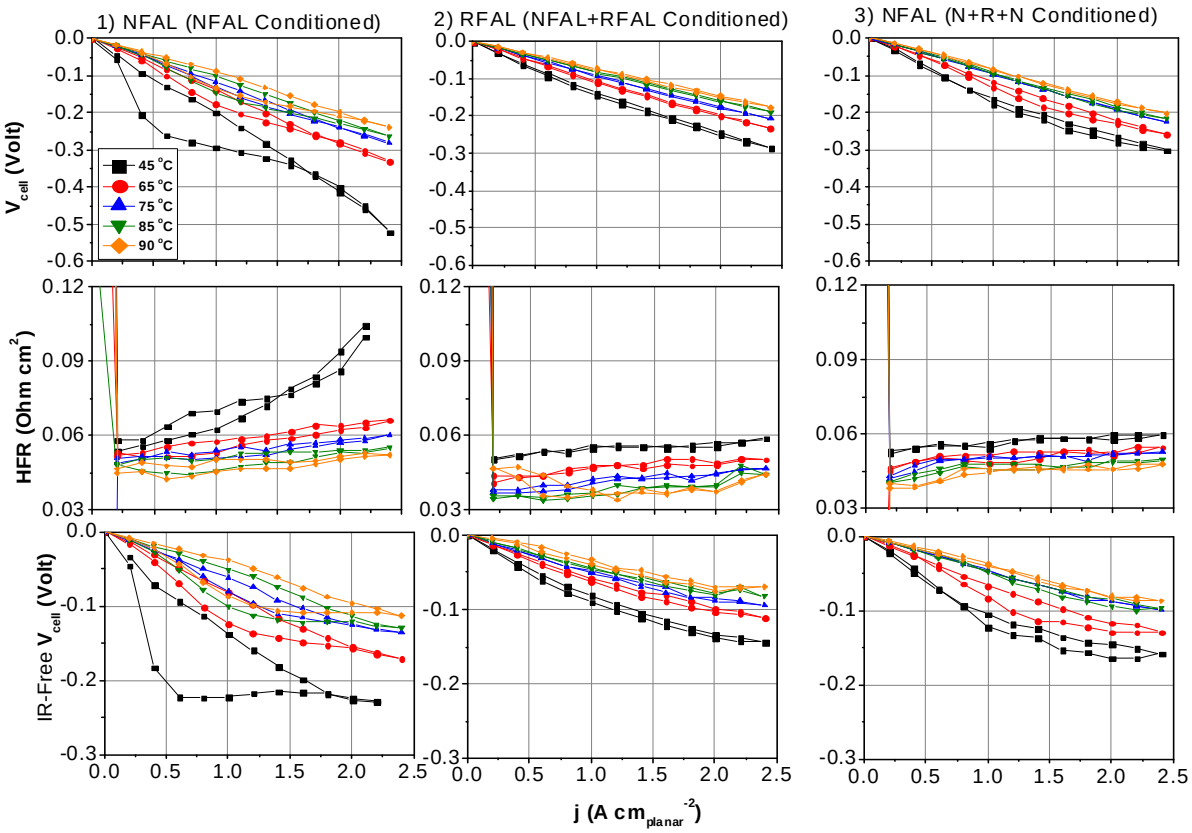

Figure 20. HOR/HER Kinetic Study w/ 0.02 mgPt/cm^2 PtCoMn/NSTF Anode/Cathode MEA

Table 7 summarizes the ANL analysis of the HOR activity for NSTF and Pt/C electrodes. The NSTF electrodes had comparable or higher HOR specific activity as the Pt/C electrodes, but the overall determined activity depends upon conditioning state. With fully conditioned 0.02PtCoMn/NSTF anodes, the HOR exchange current density, i_0, was either 226 or 473mA/cm^2 depending upon the fitting parameters used.

Model predictions indicate a ca. 25mV performance loss at 1.5A/cm^2 as the NSTF anode loading is reduced from 0.05 to 0.02mg/cm^2. This differs from the experimental Figure 18 results, which suggests the anode loading would need to be reduced from 0.05 to 0.01mg/cm^2 for a similar loss.

Table 7. Estimated HOR Kinetics Extracted from Experimental data

Catalyst / Support	Pt Loading $mg.cm^{-2}$	Catalyst Conditioning	Anode SEF $cm_{Pt}^{-2}.cm^{-2}$	T ^{o}C	E_{HOR} $kJ.mol^{-1}$	α	n	γ	i_0 $mA.cm_{Pt}^{-2}$
PtCoMn / NSTF[1]	0.02 (a) 0.02 (c)	PCA	2.3	80	30.2	0.305	2	1.25	215
PtCoMn / NSTF[2]	0.02 (a) 0.02 (c)	CCA	2.3	80	30.2	0.673	2	1.25	226
PtCoMn / NSTF[1]	0.05 (a) 0.1 (c)	PCA	5.9	80	30.2	0.305	2	1.25	450
PtCoMn / NSTF[2]	0.05 (a) 0.1 (c)	CCA	5.9	80	30.2	0.673	2	1.25	995
PtCoMn / NSTF[2]	0.02 (a) 0.02 (c)	CCA	2.3	80	22.7	0.527	1	1.25	473
5 wt% Pt / Carbon[3]	0.003 (a) 0.4 (c)		2.9	80	Not Measured	0.5	2	Not Measured	235-300

1. Partially-conditioned anode
2. Completely-conditioned anode
3. J. Electrochem. Soc., 154 (7), B631 (2007)

Subtask Conclusions

Performance and break-in conditioning rate depended strongly on the NSTF catalyst composition and loading. Minimum anode electrode PGM loadings to obtain acceptable performance ranged from 10-20 $\mu g/cm^2$, being largely dependent upon the specific area of the electrocatalyst. At further reduced loading, performance decreased precipitously and break-in conditioning rate slowed.

HOR kinetic measurement experiments and analysis were conducted. The analysis indicates that NSTF PtCoMn HOR catalysts have comparable or higher specific activity as Pt/C, but the ca. 10x lower specific area of NSTF will impart HOR kinetic losses can lead to 10s of mV loss at high current density at sufficiently low loading.

Future Directions

The underlying mechanism for the impact of anode catalyst loading on break-in conditioning warrants further study. Such work could provide key insight into the reasons for the relatively slower break-in of NSTF based MEAs than comparative dispersed electrode MEAs.

Subtask 1.3. Durable, Improved Conductivity PEMs

Subtask Overview

Subtask 1.3 is an evaluation of advanced 3M membranes, including expected available variations of ionomer chemistry, ionomer equivalent weight, thickness, support variables, and durability-enhancing additive type and level; other commercially available PEMs may be evaluated based on literature reports.

Subtask High Level Work Summary

Work focused on developing performance relationships vs. key PEM variables for two electrode types and optimization of 3M PEMs for integration with NSTF electrodes. Several dozen experimental PEMs were fabricated and evaluated in fuel cell. Key PEM material and process factors, which limit performance of low surface area electrodes, were identified. New PEMs with appropriate factors were generated which yielded good performance. Durability evaluations were primarily conducted in Task 5.

Subtask Key Results

PEM Sensitivity Studies with Dealloyed PtNi/NSTF

In this study, several MEAs comprising dealloyed PtNi/NSTF cathodes were evaluated for performance sensitivity to membranes with differing ionomer type, equivalent weight, additives, thicknesses, and supports, summarized in Table 8. The primary objective of the study was to determine how these variables influence the high current density performance of electrodes which have large amounts of leachable transition metals.

Table 8. PEM variables evaluated in study

Series	Ionomer	EW	Additive (Arb. Level)	Support (Arb. Level)	Thickness (micron)
EW	3M	**825**	0	0	20
EW	3M	**825**	0	0	20
EW	3M	**734**	0	0	20
EW	3M	**1000**	0	0	20
Ionomer	**Nafion**	9xx	0	0	20
Additive	3M	825	**0**	0	20
Additive	3M	825	**1**	0	20
Support	3M	825	1	**0**	20
Support	3M	825	1	**1**	20
Thickness	3M	734	1	1	**24**
Thickness	3M	734	1	1	**20**
Thickness	3M	734	1	1	**16**

Figure 21 compares H_2/Air polarization curves taken from the ionomer/EW study (left) and the impact of thickness with supported membranes (right). Unsupported 20um PEMs with ionomers with EW > 825EW lead to severe performance reduction. Supported 734EW PEMs led to much lower performance than unsupported PEMs, even as the thickness was reduced.

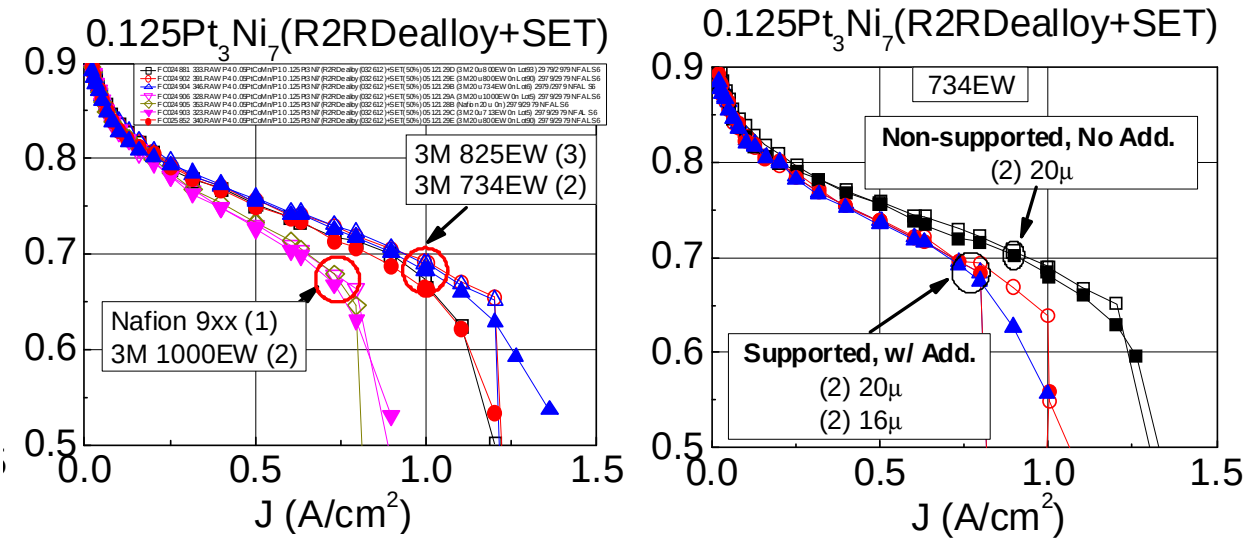

Figure 21. (Left): Impact of Ionomer Type. (Right): Impact of Support Type

Figure 22 (left) summarizes the limiting current density (J @ 0.50V) for numerous MEAs comprising PtCoMn and PtNi NSTF cathode electrodes, as a function of calculated "effective" equivalent weight of the membrane. The PEM effective EW takes into account ion exchange capacity lost due to dissolution into transition metals from the cathode, and depends upon the ionomer equivalent weight, PEM thickness, and the presence of support. High limiting current densities were generally achievable if the effective EW was 900 g/mol or less.

Figure 22 (right) summarizes how the calculated effective equivalent weight is related to the post-dealloyed Pt mole fraction of the cathode. With a 734EW, 20 µm thick supported PEM, the effective equivalent weight varied from ca. 800 to ca. 1600 g/mol, depending upon the initial Pt mole fraction in a 0.125mg/cm^2 Pt_xM_{1-x} alloy, where x varied from 0.30 (non-dealloyed) to highly dealloyed (x=0.65). The analysis indicated that the composition after dealloying, ca. x=0.40, would result in an ~1100 EW_{EFF} and suppressed performance. Achievement of x=0.55 would result in 900 EW_{EFF} and would be predicted to provide good high current density performance.

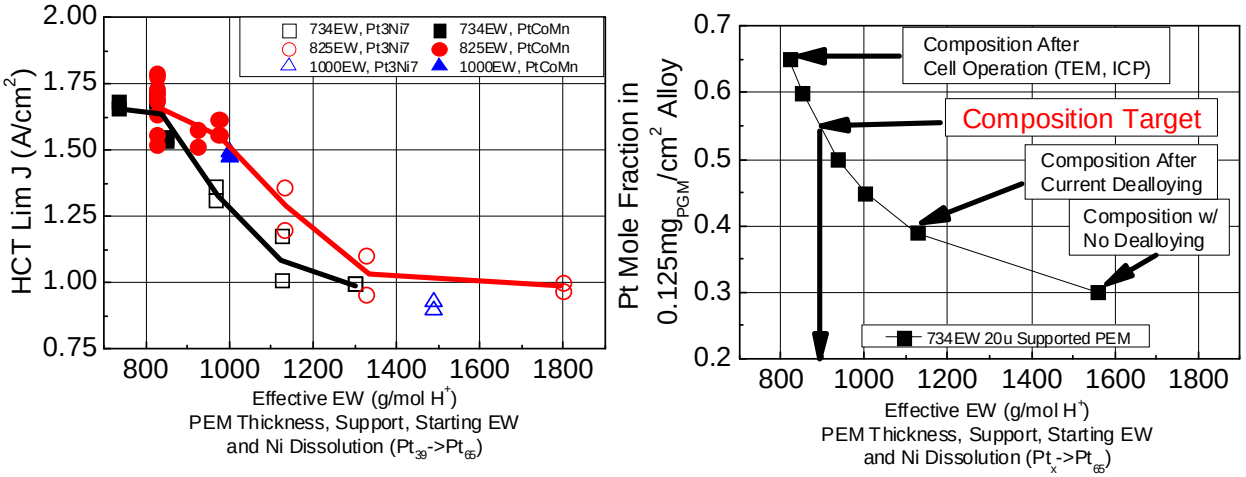

Figure 22. (Left): Limiting current densities vs. calculated effective PEM equivalent weight. (Right): Estimation of Effective EW for PtNi with differing initial Ni mole fractions.

PEM Sensitivity Studies with PtCoMn

Figure 23 summarizes the impact of ionomer equivalent weight and the presence of support with PtCoMn/NSTF cathode electrodes. Similar performances were obtained with 734 or 825EW neat 20 µm thick PEMs, and performance decreased as EW increased (Left). For 20 µm thick 734EW PEMs, 2 supported PEMs yielded equivalent performance as unsupported PEMs, but surprisingly, a thinner supported PEM yielded much worse performance.

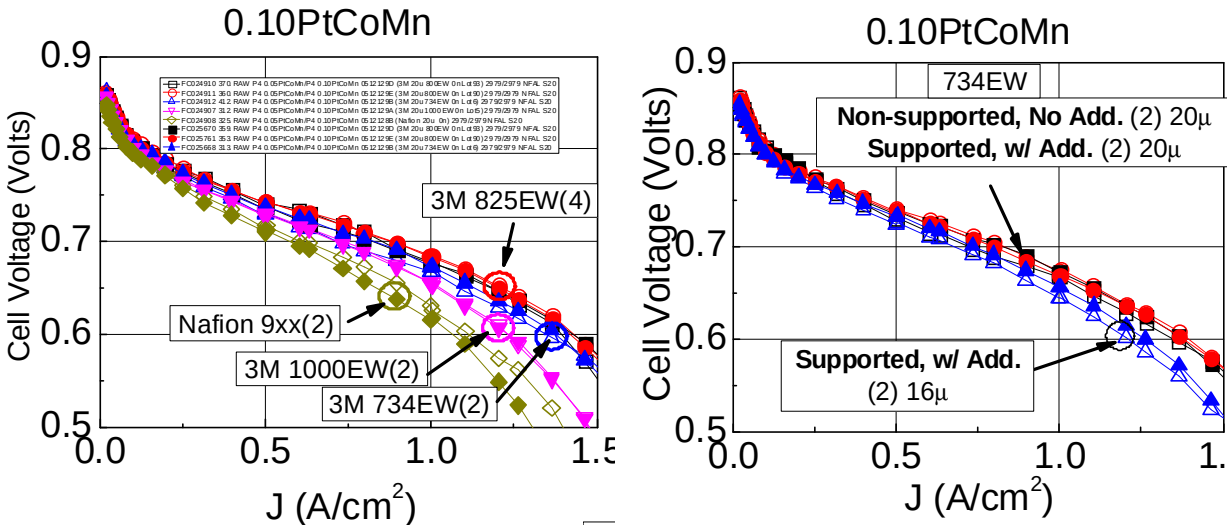

Figure 23. (Left): Impact of Ionomer Type. (Right): Impact of Support Type

The unexpected variation in performance with PEM variables was assessed. Figure 24 summarizes measured cell voltage, HFR, and IR-Free voltage at 1.46A/cm^2 for the MEAs with various PEMs. In most cases, MEAs with suppressed measured performance had modestly higher HFR. However, correction for HFR was not sufficient to account for the severe performance losses. As discussed below, the performance variation may be explained by assessing the MEA area utilization or Pt utilization of the cathode.

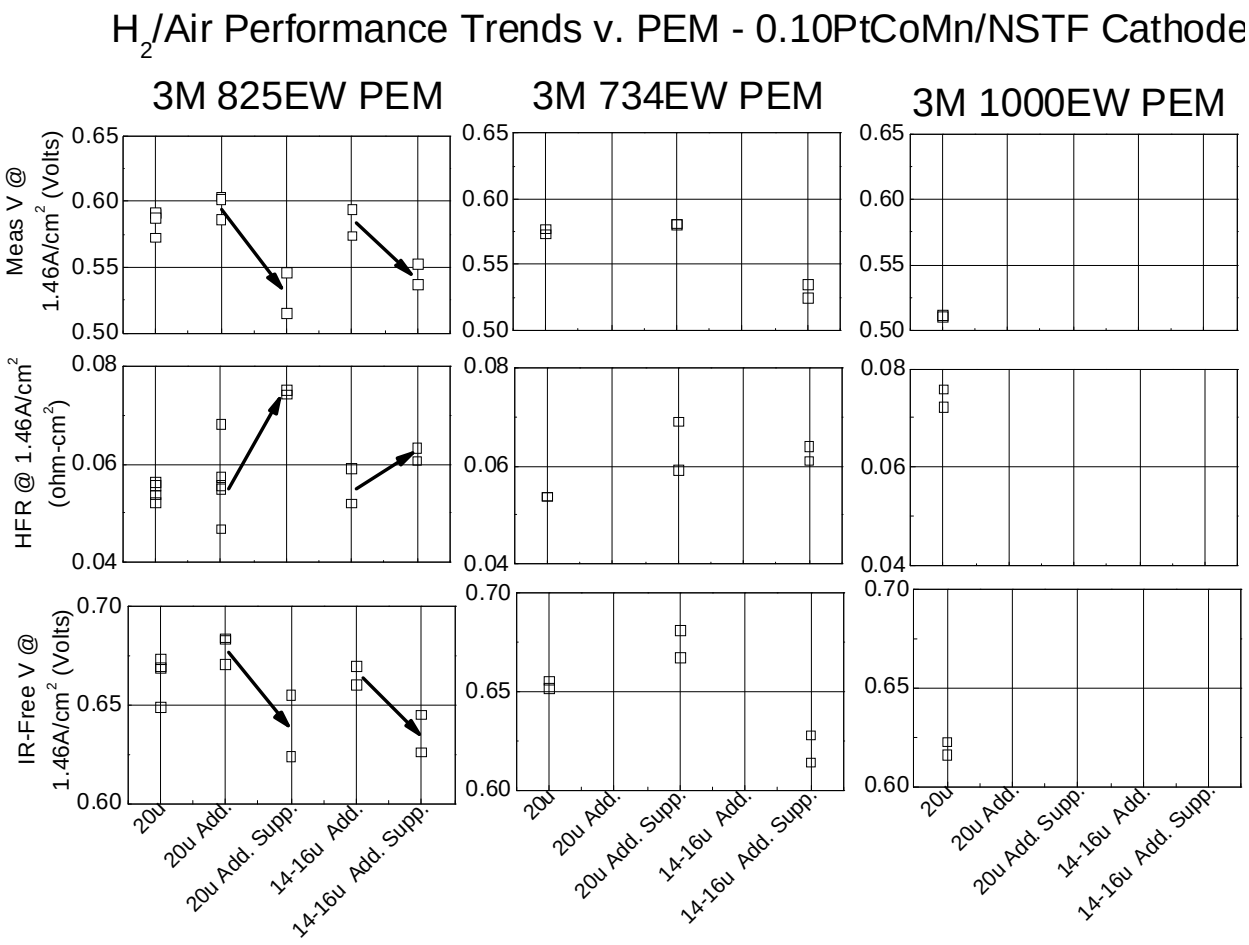

Figure 24. Ohmic analysis of PEM-induced performance losses

Electrode Utilization Analysis of Performance with PtCoMn

In previous work, it was determined that the performance variation is often not accounted for with HFR alone, especially under hot and dry conditions (see Steinbach et. al, "Polymer Electrolyte Membrane Fuel Cell Active Area Utilization Dependence on Relative Humidity Measured via AC Impedance High Frequency Resistance", *ECS Trans*. **2013** volume 58, issue 1, 1589-1600). The previous analysis indicated that the performance variation with reduced RH can be accounted for if one assumes that the HFR variation reflects variation in active area, rather than the ionomer bulk conductivity.

Equation 1

$$U(J)_{ACTIVE} = \frac{R_{REF}}{R(J)_{MEAS}} = \frac{\left(\frac{\rho l}{A}\right)_{REF}}{\left(\frac{\rho l}{A}\right)_{MEAS}(J)} = \frac{A(J)_{MEAS}}{A_{REF}}$$

Equation 2

$$I_{NORM} = \frac{J_{MEAS}}{U(J_{MEAS})_{ACTIVE}}$$

Equation 1 and Equation 2 were applied to the current study MEAs (supported vs. unsupported 734 and 825EW PEMs), and the area normalized results are shown in the bottom row of Figure 25. After area normalization, the performance curves largely overlapped, suggesting the primary source of performance variation with the differing PEM types was area utilization.

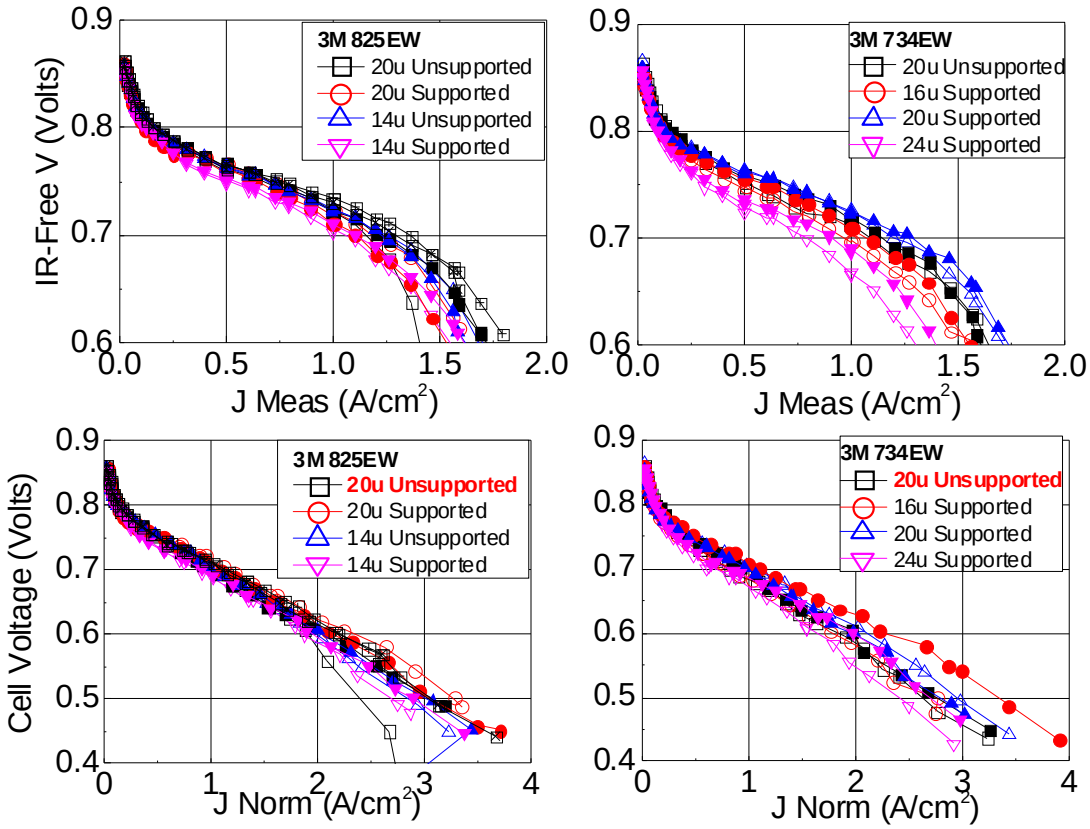

Figure 25. Performance variation breakdown by area utilization analysis.

The experimental data was also analyzed by ANL. Their analysis indicated that the differing H_2/Air performances could be explained by differing Pt utilizations, determined by Equation 3. In essence, the Pt utilization, U_{Pt}, was defined as the measured IR-Free current density at 0.80V divided by the best performance in the set. The right side of Figure 26 summarizes the results after Pt utilization correction, where a large majority of the polarization curves overlapped extremely well.

Equation 3

$$U_{Pt} = \frac{J(0.8V_{IR-FREE})_{MEAS}}{J(0.8V_{IR-FREE})_{BEST}}$$

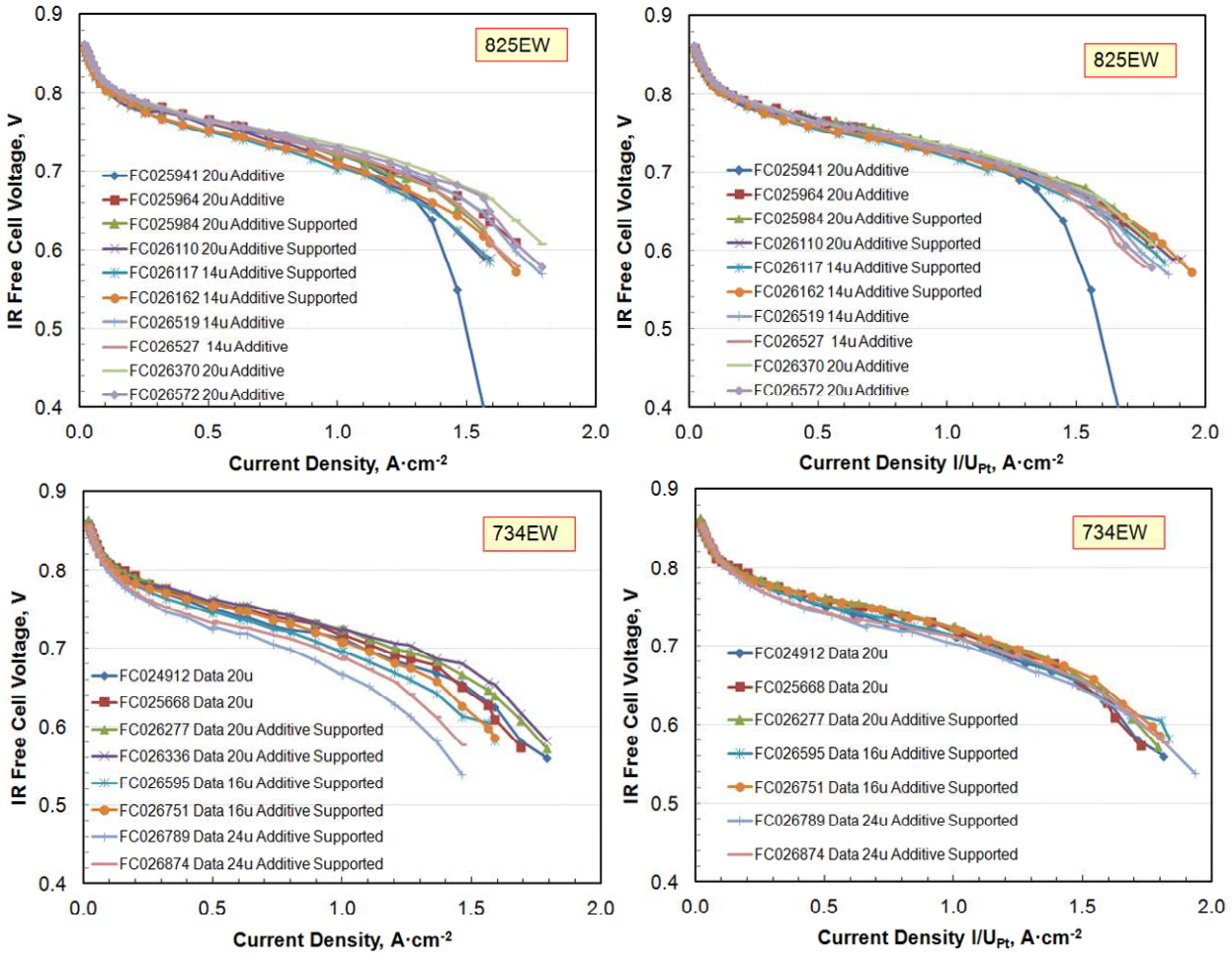

Figure 26. Pt utilization analysis by Argonne National Laboratory.

In summary, two methods were shown to be successful in accounting for the measured performance variation. Both methods indicate that performance depended upon a measured utilization factor. It is likely that both methods are assessing a similar underlying mechanism that a PEM factor is influencing the extent of the electrode used.

Root Cause Diagnoses

Experiments were conducted to understand the root cause of the unexpected performance variation and area/Pt utilization and to resolve the issue. Figure 27 summarizes measured H_2/Air performance variation for several 3M 725-734EW PEMs, unsupported or with varying support lots. Performance obtained with supported PEMs ranged from comparable to unsupported to 140mV deactivation.

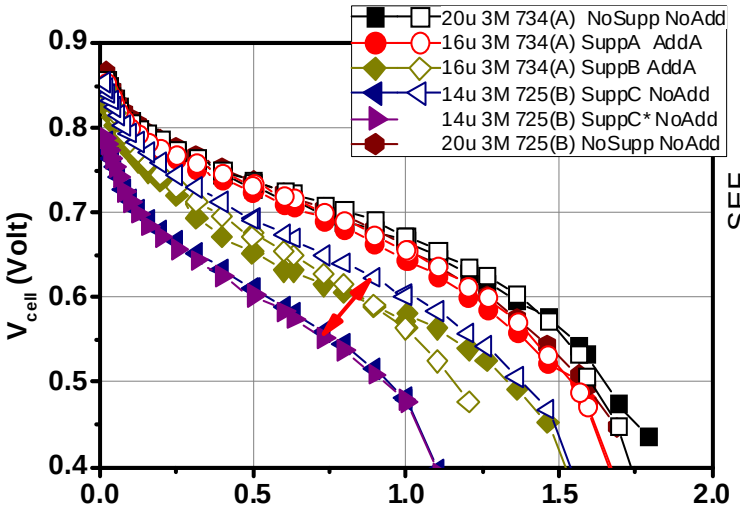

Figure 27. Performance variation with experimental PEMs with various supports.

The variation in high current density performance was found to correlate with cathode catalyst surface area and absolute ORR activity. Figure 28 summarizes cathode surface area roughness factor (SEF), absolute activity, and limiting current densities as a function of 13 different PEM lots. PEM lot had a strong influence on the performance. Figure 29 directly compares the relationship between limiting current density and SEF, absolute activity, and specific activity. The H_2/Air performance at 0.50V appeared to be well correlated by decreases in the cathode catalyst activity / area metrics.

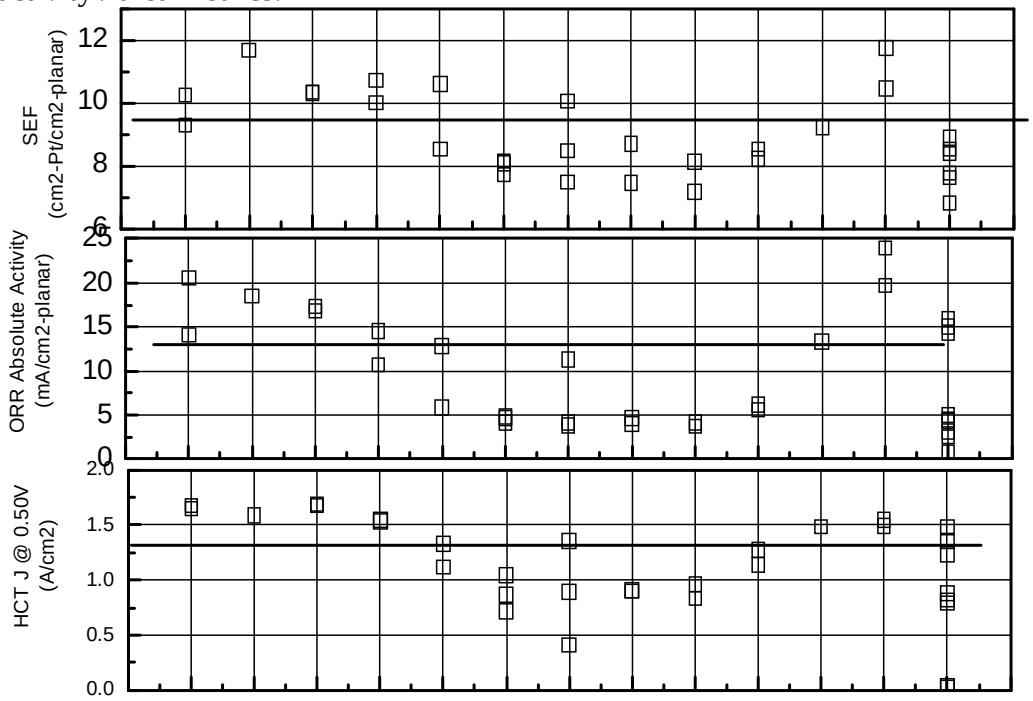

Figure 28. Measured surface area, ORR absolute activity, and limiting current density for 13 different PEM lots.

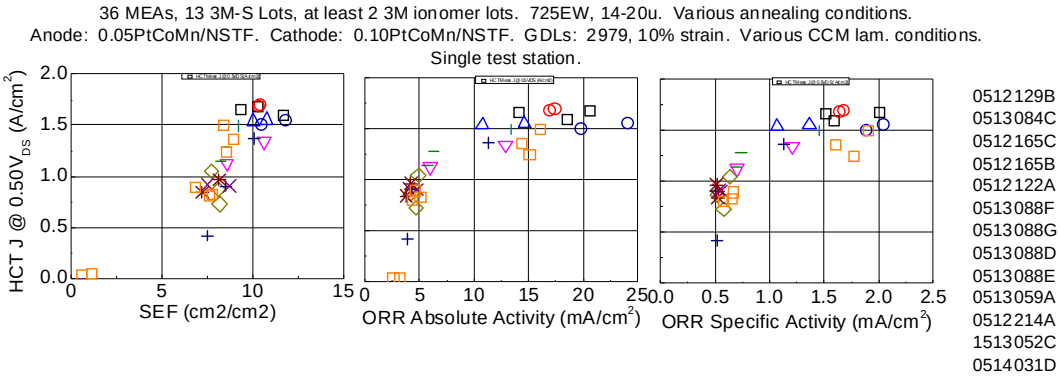

Figure 29. Relationship between limiting current density and cathode catalyst activity/area metrics.

Such strong impact of PEM lot had not been observed before with NSTF MEAs. Due to the strong activity/performance relationships with differing PEM lots, one suspicion was that the PEM support was perhaps involved in the performance variation. Experiments were conducted to evaluate the impact of the supported PEM thermal history, including annealing conditions. Figure 30 shows that the limiting current density performance depended monotonically on support type and annealing conditions.

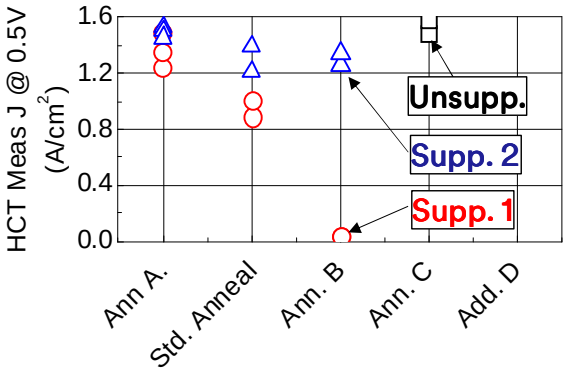

Figure 30. Impact of annealing conditions on H_2/Air performance with two supported PEM lots.

Using the insight from the above experiments, two PEM lots were generated with the improved support type and the appropriate annealing conditions. Figure 31 shows that the replicate lots yielded comparable performance to each other and the unsupported control. This PEM construction, which yields relatively high performance and no deactivation, was downselected for BOC MEA integration.

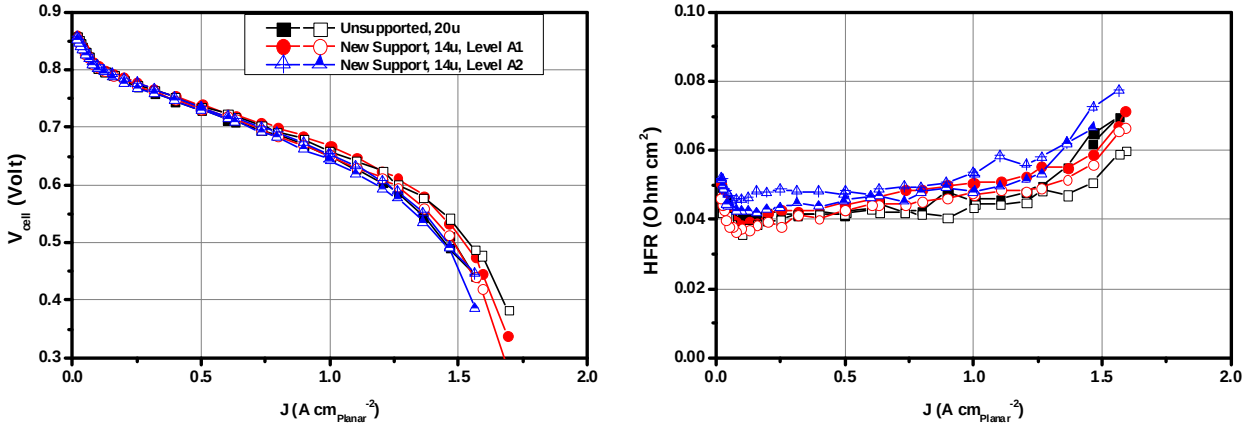

Figure 31. Replication of downselected PEM for BOC integration with two PEM lots.

It is important to note that such large performance variation was not observed when such PEMs were tested with high area Pt/C electrodes at 3M. Evaluation of internal proprietary data indicated relatively small performance impacts, which did have some correlation to the observations with the 0.10PtCoMn/NSTF electrodes here. As noted in the first section, the impact was also modest with the PtNi/NSTF electrodes, which had nearly 2x higher absolute surface area than the PtCoMn/NSTF electrodes.

Alternative Ionomer Studies

Limited experiments were conducted evaluating non-3M PFSA ionomer PEMs and next generation 3M PFIA ionomer PEMs. Figure 32 shows that an unsupported alternative PFSA ionomer PEM yielded lower performance than 3M PFSA PEM. Figure 33 shows that, as received, the experimental 3M PFIA yielded much lower performance than the 725EW PFSA. It was suspected that the experimental PFIA contained contaminants. After a laboratory cleaning procedure, the performance had increased dramatically and was comparable to the unsupported 725EW PFSA PEM.

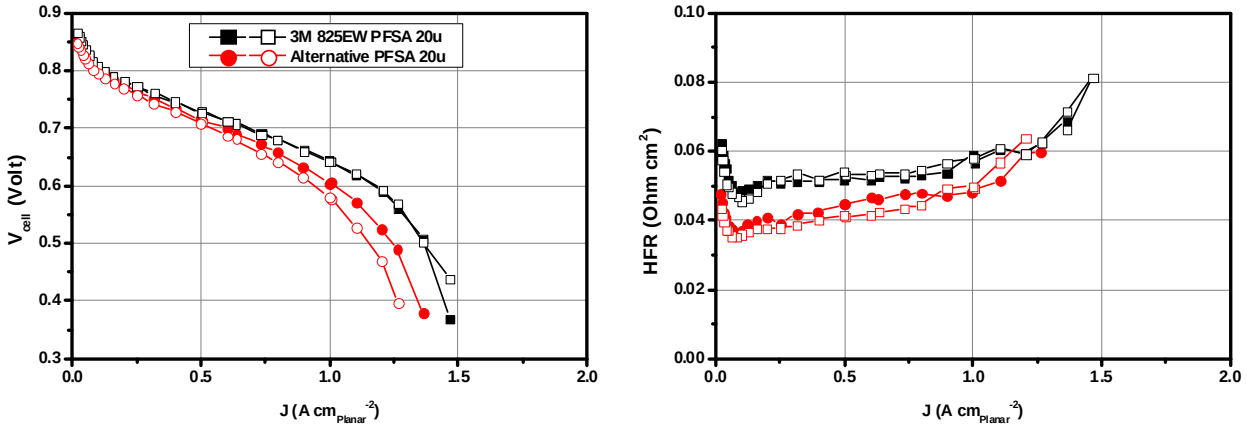

Figure 32. H_2/Air performance of 3M 825EW PFSA vs. Aquivion Ionomer PEMs.

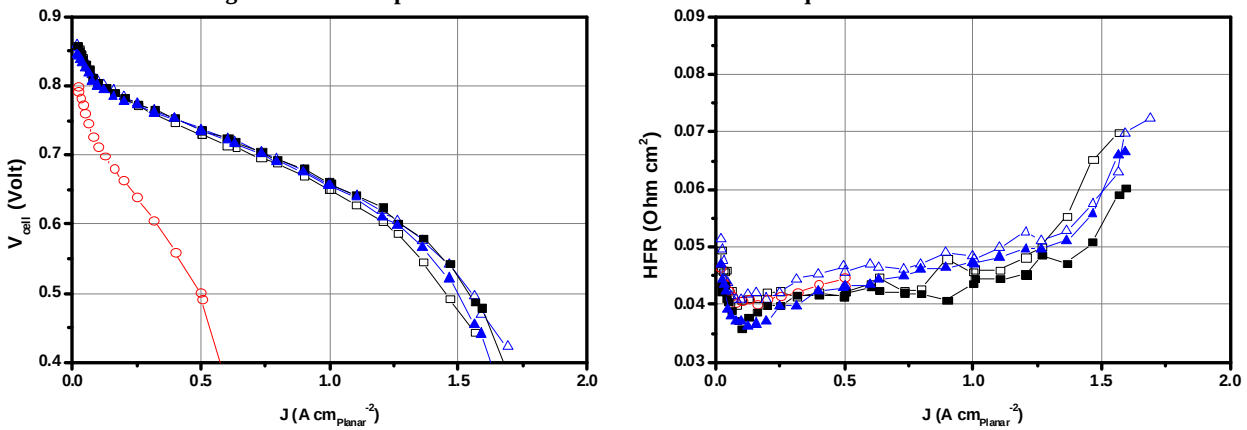

Figure 33. H_2/Air performance of 3M 725EW PFSA and 3M PFIA PEMs. Black: 3M 725EW PFSA. Red: 3M PFIA, as received. Blue: 3M PFIA, cleaned.

Subtask Conclusions

A relationship was determined between performance and the PEM effective equivalent weight, which accounted for the ion exchange capacity lost due to transition metal dissolution from the PtNi electrode into the PEM. This relationship was used to set targets for the degree of dealloying needed to achieve high performance in MEA.

Extensive work was conducted to determine and resolve an integration issue between 3M supported PEMs and NSTF cathodes. Performance was found to depend strongly upon support type and PEM thermal history. Unoptimized support and thermal history lead to severe performance degradation, which correlated to cathode ORR activity and surface area. Optimized composition and process lead to a downselected PEM with high performance.

PEMs comprised of an alternative PFSA ionomer and a next generation experimental ionomer were evaluated. Performance was below that obtained with comparable 3M PFSAs.

Future Directions

The work above provides key insight into the challenges the industry will face as cathode PGM loadings and absolute surface areas decrease. Use of low loading, low area electrodes will likely help PEM developers to identify possible contaminants and decrease their concentration in PEMs.

Subtask 1.4. Low-Cost, High Performance GDLs

Subtask Overview

Subtask 1.4 involves evaluation of advanced, low-cost, and high-performance anode and cathode GDLs available commercially, at 3M, and at General Motors (GM).

Subtask High Level Work Summary

Four commercial and one 3M proprietary GDL were evaluated for general performance characteristics.

Subtask Key Results

Four GDL candidates were obtained from Freudenberg and evaluated for general performance characteristics, including H_2/Air performance and two operational robustness tests. For all tests, the anode GDL was 3M 2979, the CCM was a roll-good NSTF CCM (0.05PtCoMn/NSTF anode, 0.15PtCoMn/NSTF cathode, 20u 825EW unsupported PEM). A control MEA with 3M 2979 cathode GDL was also evaluated.

Figure 34 (left) shows that at a high level, all GDLs yielded qualitatively similar H_2/Air performance at 80°C with similar limiting current density. Figure 34 (right) shows that one cathode GDL type, H2315 C2, yielded improved low temperature performance over all others.

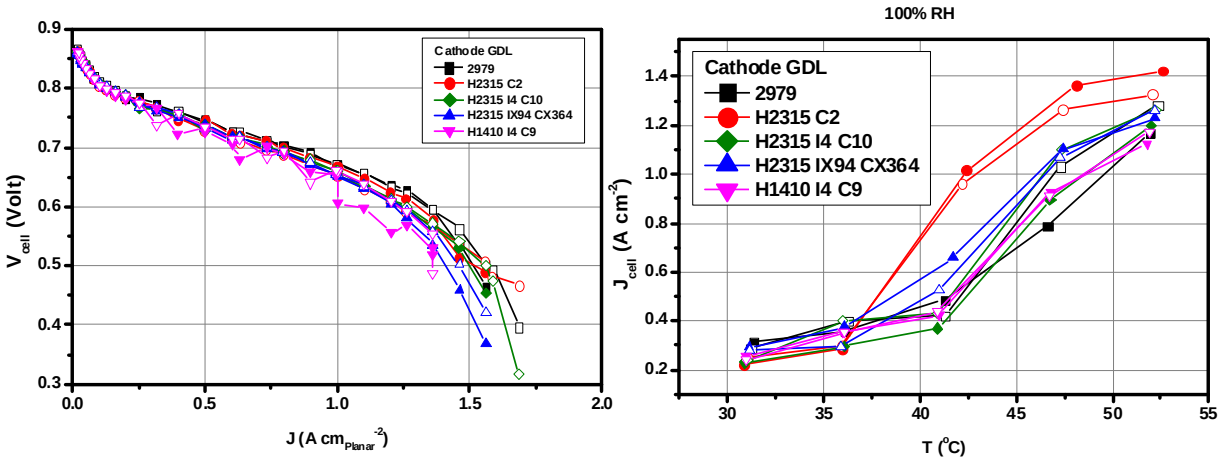

Figure 34(Left): HCT H_2/Air performance. (Right): CoolPSS temperature sensitivity.

Figure 35 compares several performance and robustness metrics directly. The various Freudenberg cathode GDLs generally had lower performance and higher HFR than 3M 2979. As noted above, H2315 C2 yielded higher steady state 40°C performance by nearly 2x over 2979. Additionally, H2315 C2 yielded an improved steady state performance under load transient than the other GDLs.

Due to the 10-20mV reduction in H_2/Air performance with commercial GDLs, the incumbent 3M 2979 was downselected for project cathode GDL.

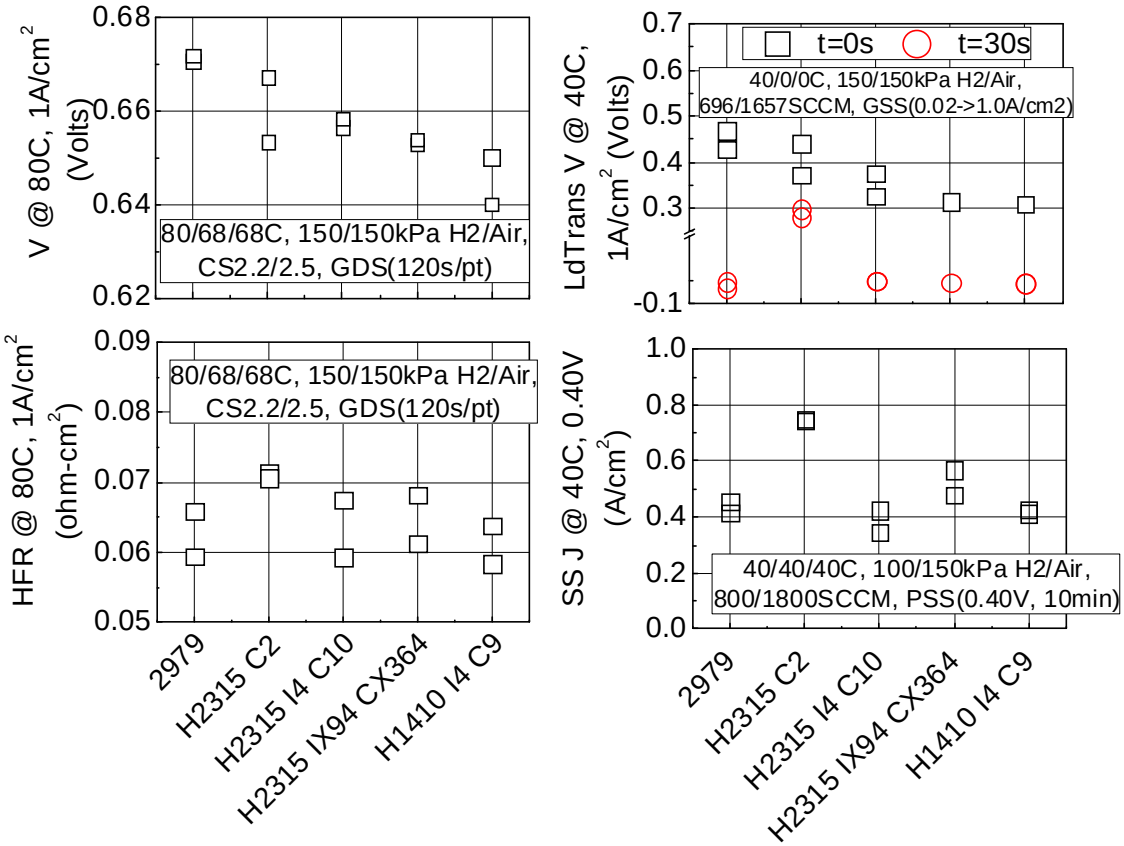

Figure 35. (Top left, bottom left): HCT H_2/Air cell voltage and HFR at 1A/cm^2. (Top right): Performance under load transients at 40°C. (Bottom right): CoolPSS performance at 40°C.

Subtask Conclusions

Limited evaluations of commercial cathode GDLs indicated that the incumbent cathode GDL yields the best H_2/Air performance under a limited set of testing conditions.

The cathode GDL can also positively influence low temperature performance. One type yielded nearly a 2x gain in 40°C steady state performance.

Future Directions

One type of cathode GDL, Freudenberg H2315 C2, yielded improved low temperature performance and operational robustness. Work to understand the mechanism of this improvement could potentially lead to more operationally robust MEAs.

Subtask 1.5. Rated Power Sensitivity to Flow Field Geometry (3M)

Subtask Overview

Subtask 1.5 involves evaluation of the interaction of basic flow field geometry (land and channel widths) with the anode and cathode GDLs evaluated in subtask 1.4 to optimize rated power response. The proposed work would involve a very modest flow field design effort and initial fuel cell evaluation of different flow field geometries with the baseline MEA component set for rated power, cold start, and load transient responses. A second round of evaluation would occur with the interim best of class MEA(s), and a final round with the final downselected best of class MEA.

Subtask High Level Work Summary

A limited study on the impact of flow field type was assessed on two types of NSTF MEAs.

Subtask Key Results

Based on previous work, flow field geometry had a strong influence on rated power performance in MEA. The previous work found that “FF2”, which had relatively narrower lands and channels than the baseline Fuel Cell Technologies “quad serpentine” flow field, yielded higher rated power performance with pre-project MEAs.

Figure 36 summarizes H_2/Air performance curves for baseline NSTF MEAs with 0.10PtCoMn/NSTF cathodes with three flow field types, FF2, FF5 (quad serpentine), and FF1 which had 0.5, 0.8, and 2.0mm channels, respectively. Performance increased with decreasing channel width at all pressures.

The different flow fields had different pressure drops, which can influence performance. Among other factors, the average reactant pressure will change. Figure 37 summarizes a simple analysis. The left plot shows 0.60V current density at 1.0 atmA outlet pressure for various flow fields, and the middle plot shows the average pressure. The right figure is the current density divided by average pressure. FF2, with narrow lands and channels, yields the highest pressure-independent performance, ~33% higher than quad serpentine with 0.8 mm lands and channels.

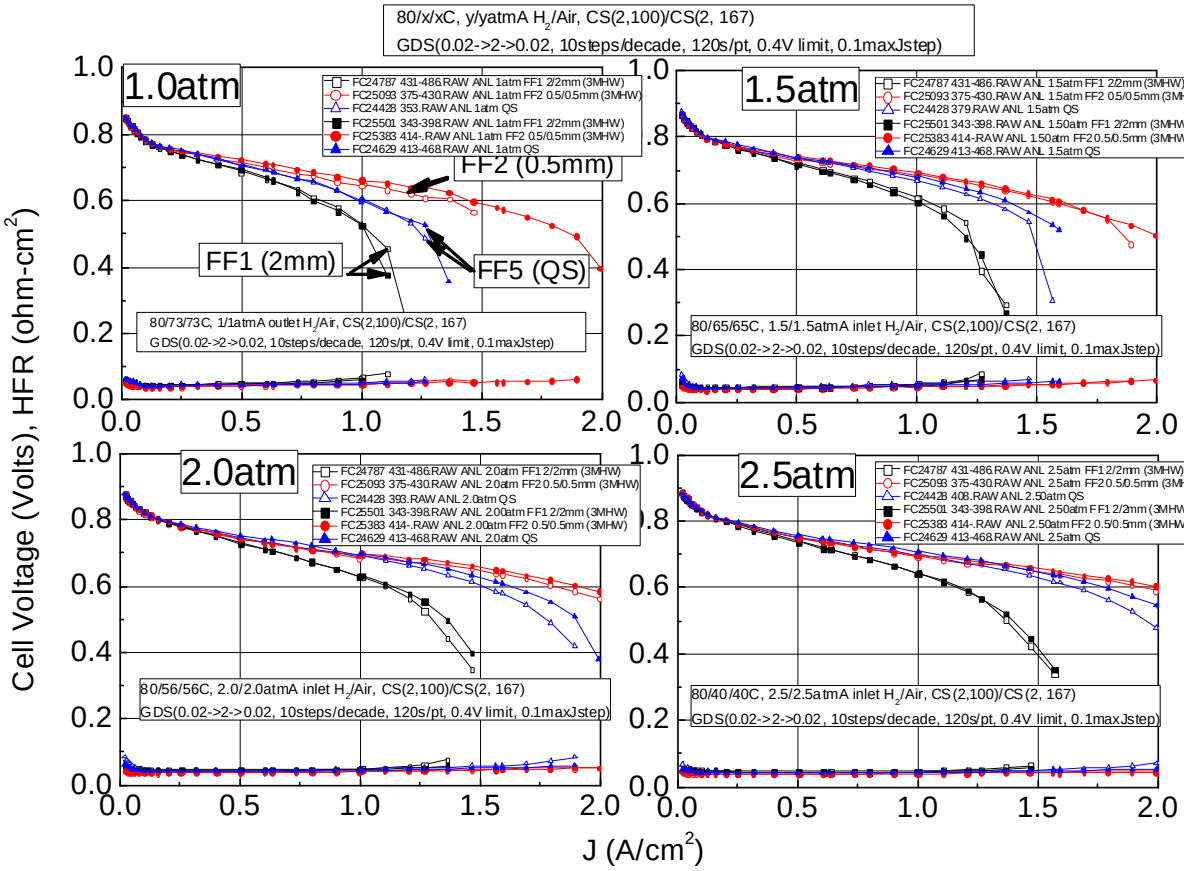

Figure 36. Influence of FF type on H_2/Air performance at several pressures.

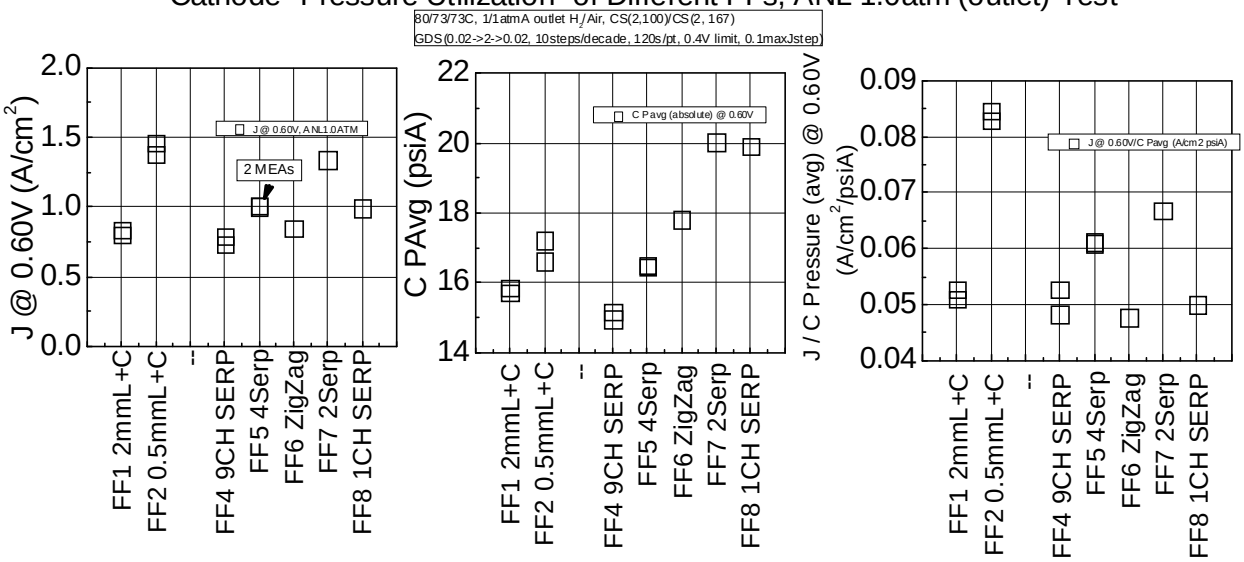

Figure 37. Performance, pressure drop, and performance/pressure

Representative flow fields from above were selected for study with project electrocatalysts. Figure 38 shows that while FF2 yields large performance improvements over FF5 with PtCoMn, the impact is more modest with dealloyed PtNi. It is likely that with PtNi, the still relatively large amount of Ni dissolution into the PEM impacted the limiting current density.

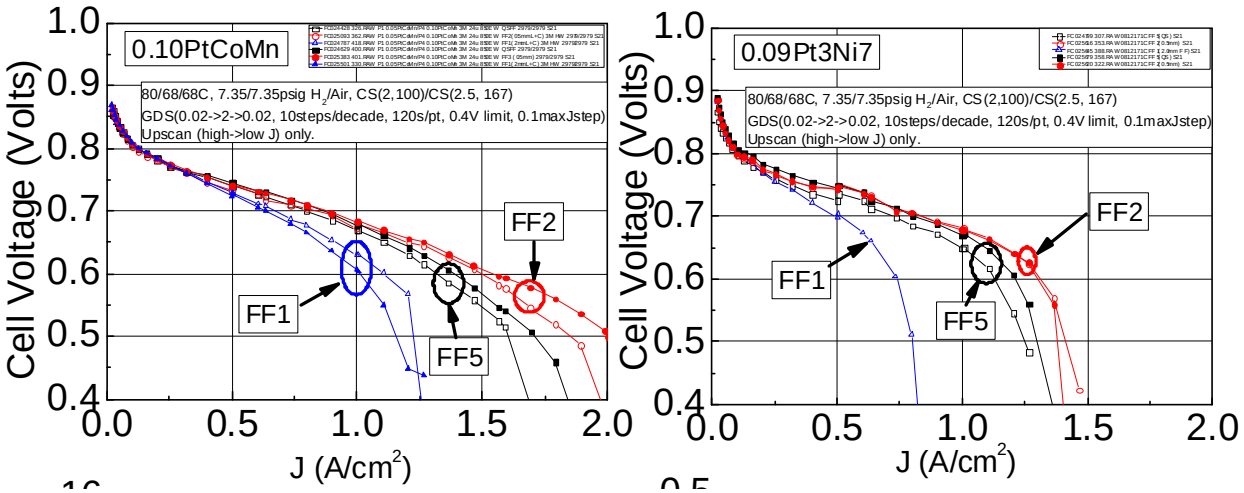

Figure 38. Impact of flow field type on HCT H_2/Air performance. (Left): 0.10PtCoMn/NSTF cathode. (Right): Dealloyed 0.09PtNi/NSTF cathode.

Several flow field designs were modeled to probe the influence of land and channel widths with NSTF MEA, summarized in Table 9. Land and channel widths ranged from 0.3 to 2.0 mm, and depths were set to approximately yield similar pressure drops. One FF, C0.5L0.5, was fabricated, but initial testing resulted in unexpectedly poor performance. Additional flow fields were not generated due to the poor initial results and program prioritization.

Table 9. Flow Field Designs Considered

"Name"	Channel Width (mm)	Land width (mm)	# Parallel Channels
FF5 (Quad Serp)	0.8	0.8	4
FF2 (prop.)	NA	NA	NA
C0.5L0.5	0.5	0.5	24
C0.5L0.5 - deeper	0.5	0.5	14
C0.5L0.5 - deeper2	0.5	0.5	10
C0.3L0.5	0.3	0.5	30
C0.4L0.5	0.4	0.5	26
C0.6L0.5	0.6	0.5	13
C0.8L0.5	0.8	0.5	11
C1.0L0.5	1	0.5	9
C1.5L0.5	1.5	0.5	7
C2.0L0.5	2	0.5	4
C0.5L0.3	0.5	0.3	18
C0.5L0.4	0.5	0.4	26
C0.5L0.6	0.5	0.6	21
C0.5L0.8	0.5	0.8	18
C0.5L1.0	0.5	1	16
C0.5L1.5	0.5	1.5	12
C0.5L2.0	0.5	2	9

The impact of FF was again evaluated towards the end of the project. Figure 39 shows that the BOC MEA performance was strongly sensitive to FF type. Performance at 0.60V increased 66% with FF2 vs. quad serpentine. It is possible that the narrower land/channel pitch with FF2 helps mitigate some of the losses associated with MEAs with relatively high levels of transition metal (TM) contamination.

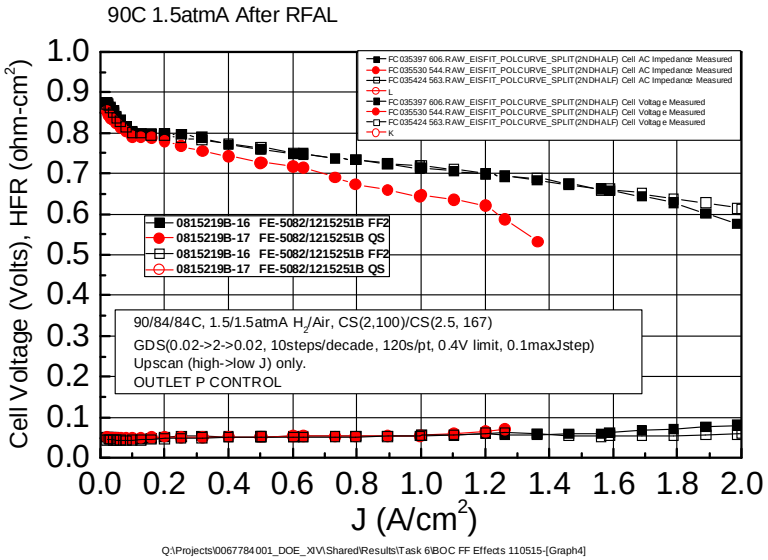

Figure 39. Impact of flow field type on final project BOC MEA performance. Black: FF2. Red: Quad serpentine.

Subtask Conclusions

Flow field type was found to be influential for rated power performance with NSTF MEAs. Narrow lands and channels substantially improve rated power performance, even after accounting for differences in pressure drop. Narrow lands and/or channels may also help mitigate effects of TM contamination.

Future Directions

A systematic study of the influence of flow field land and channel geometry is highly warranted from a fundamental perspective. Based on the results here, further specific power gains would be likely. Such work would benefit from being conducted with a flow field/stack manufacturer to help assess cost tradeoffs of various designs.

Task 2. Integration Activities Toward Transient Response, Cold Start Time to 50% of Rated Power, and Unassisted Start from Low Temperature Targets

- *Subtask 2.1 GDL Optimization for Cold Start*
- *Subtask 2.2 Subtask 2.2 Interfacial Layer Optimization for Kinetic, Transient Response*

Task 2 involves evaluation of 50cm^2 MEAs comprising new anode and cathode GDLs and interfacial layer candidates with the potential to aid in meeting the cold start time and transient response transportation system targets.

Subtask 2.1. GDL Optimization for Cold Start

Subtask Overview

The primary objective of subtask 2.1 is optimization of anode gas diffusion layers for cold start response. The work will involve screening of different GDL backings with or without standard hydrophobization and no MPL for cold start and rated power response. Due to durability concerns with bare GDL backings, microporous layers (MPLs) are needed to minimize backing fiber protrusion through the membrane.

Optimally-performing backing candidates will be downselected, and then MPL loading and composition will be optimized, again towards the key factors of improved cold start and rated power with minimization of electronic shorting to acceptable levels.

Subtask High Level Work Summary

Fuel cell experiments were conducted to evaluate the impact of several relevant anode GDL parameters on NSTF MEA performance and operational robustness. Parameters evaluated include backing structure, backing thickness, backing hydrophobic treatment level, MPL basis weight, MPL porosity, and MPL formulation. Optimized parameters were downselected and a ~30m roll was produced.

Subtask Key Results

Pre-project Background

Figure 40 and Figure 41 summarize key results from pre-project work, which provided the initial direction for the project. Figure 40 (left) shows that the anode GDL type can have large influence on performance; replacement of baseline 3M 2979 anode GDL with an experimental MRC paper increased the performance at 35°C more than 3x. While low temperature performance with this anode backing was substantially improved, the GDL was to resistive to allow good high current density performance under rated power conditions. Figure 40 (right) summarizes another key finding. Freudenberg H2315, without MPL, yielded a ca. 2x gain in low temperature performance over the baseline 3M 2979, but addition of MPL, needed to prevent electronic shorting, tended to quench the response.

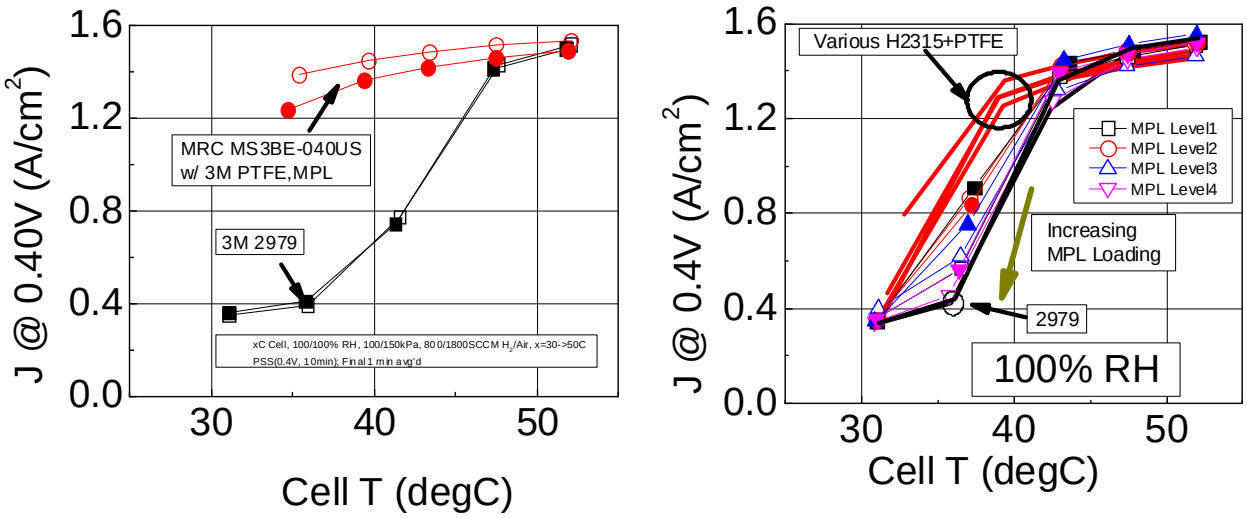

Figure 40. (Left): Impact of anode GDL substrate type on temperature sensitivity. (Right): Impact of MPL on temperature sensitivity.

Figure 41 summarizes additional pre-project work, which showed that two experimental Freudenberg backings, X0154 and X0155, had improved 40°C performance compared to baseline 2979 and reasonably low resistance in MEA.

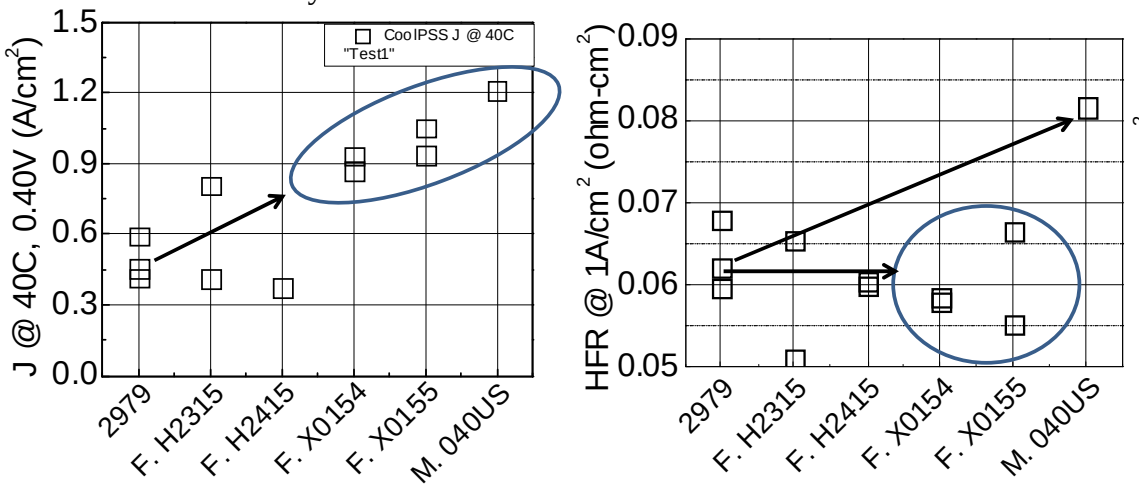

Figure 41. Impact of base substrate on 40°C limiting current density (left) and MEA resistance (right).

Anode GDL Optimization – Initial backing downselection

Initial project work focused on optimization of X0154 and X0155 for low temperature performance via first optimizing the MPL coating level. Experiments were conducted generally with a baseline NSTF CCM (anode: PtCoMn/NSTF, 0.05mg$_{Pt}$/cm^2; cathode: PtCoMn/NSTF, 0.15mg$_{Pt}$/cm^2; 3M 825EW 20µm thick PEM) and a baseline cathode GDL (3M 2979). All were tested in 50cm^2 cells, and the MEAs did not incorporate edge protection.

Figure 42 summarizes temperature sensitivity for baseline NSTF MEAs where the anode GDL was either 3M 2979 or one of a series of experimental anode GDLs, comprised of either X0154 or X0155 backing, hydrophobic treated at a standard level, with a range of MPL coating thicknesses ranging from 0.00 (no MPL) to 1.25x standard thickness. For both X0154 and X0155, addition of MPL reduced low T performance compared to no MPL, but the extent of loss was relatively insensitive to MPL coatings between 0.75-1.25 of standard.

Figure 43 summarizes several performance characteristics. Figure 43 (top left) shows that in general, X0155 anode GDLs with MPL generally yield higher performance at 80°C cell temperature than X0154 anode GDLs. Figure 43 (top right) shows that at 40°C, X0155 generally yielded higher performance than X0154. Figure 43 (bottom right) shows that in general, the X0154 and X0155 with MPL had higher electronic shorting than the baseline 2979, but was considered acceptable (1-3 mS/cm^2) in light of the lack of edge protection in these screening experiments. Based on these results, Freudenberg X0155 was downselected for further optimization. 1.00 MPL level was also downselected, to minimize risks of potential electronic shorting.

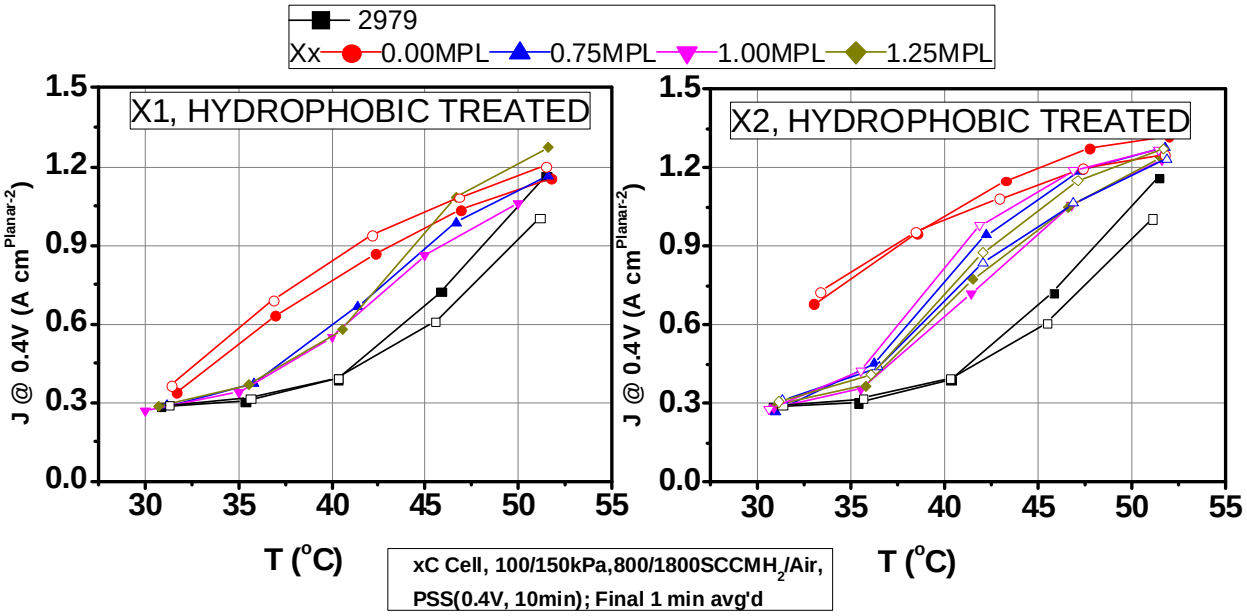

Figure 42. Impact of backing type and MPL coating level on NSTF MEA temperature sensitivity. X1 is X0154, X2 is X0155.

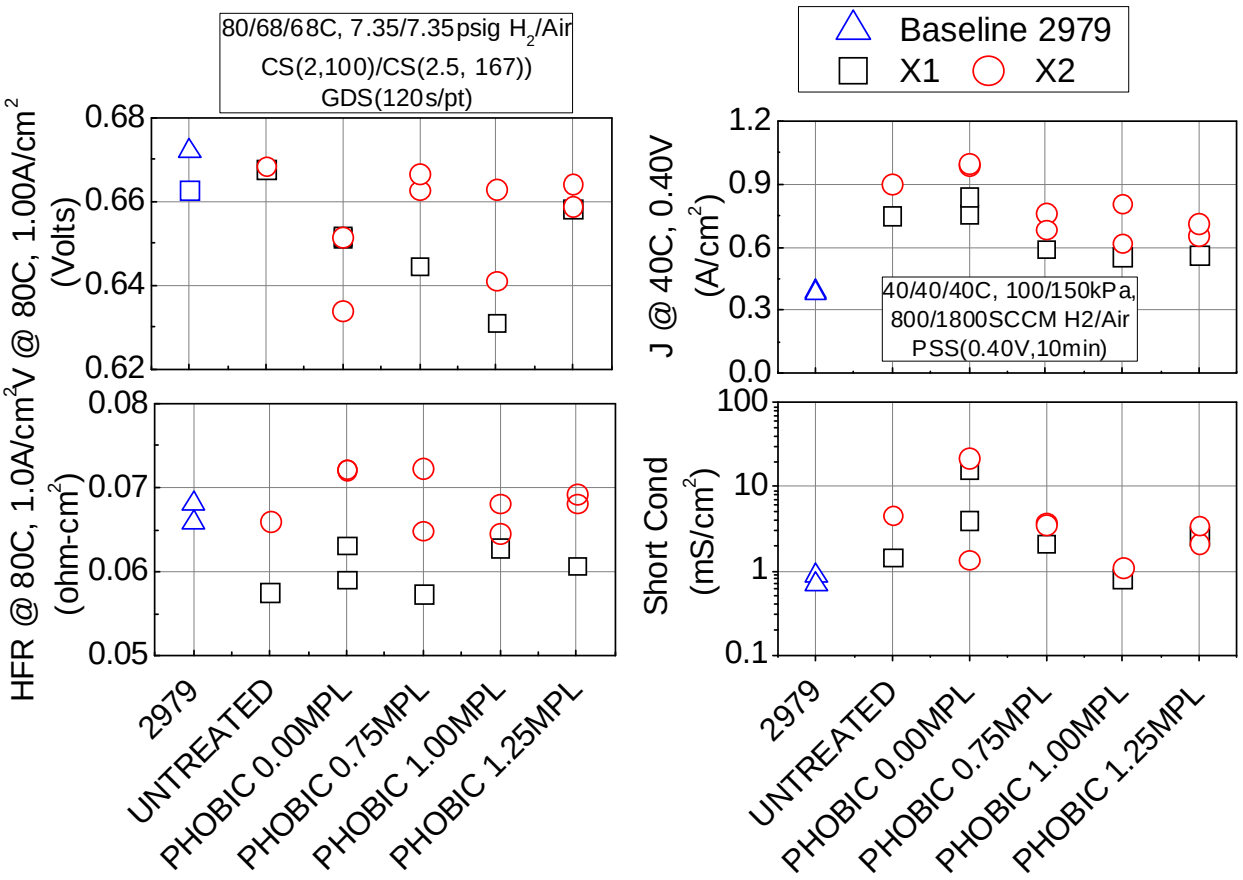

Figure 43. Summary of H_2/Air performance and resistance at 80C, 1A/cm^2 (left), 40°C limiting current density (top right), and electronic shorting conductivity (bottom right). X1 is X0154, X2 is X0155.

Anode GDL Optimization – Impact of Backing Thickness/Stacking

In this work, the impact of backing thickness was evaluated. The motivation was to determine if there was a critical thickness dependence on the temperature sensitivity response of NSTF MEAs. Since backings of interest with different thicknesses were not available, experiments were conducted where the number of anode backings installed into the cell were varied. Figure 44 (left) compares the temperature sensitivity of either 1 or 2 layers of X0155 backing (hydrophobic treated, no MPL) to 3M 2979. Very surprisingly, the low temperature performance with 2 layers was substantially improved over a single layer, with limiting current densities exceeding 1.2A/cm^2 at 35°C, a more than 4x gain over the baseline 2979. Results were reported to the Task 3 modeling team and this phenomenon was modeled. While very intriguing from a fundamental understanding perspective, it was not deemed practical as a downselect MEA candidate due to unacceptably high electronic resistance (Figure 44 right).

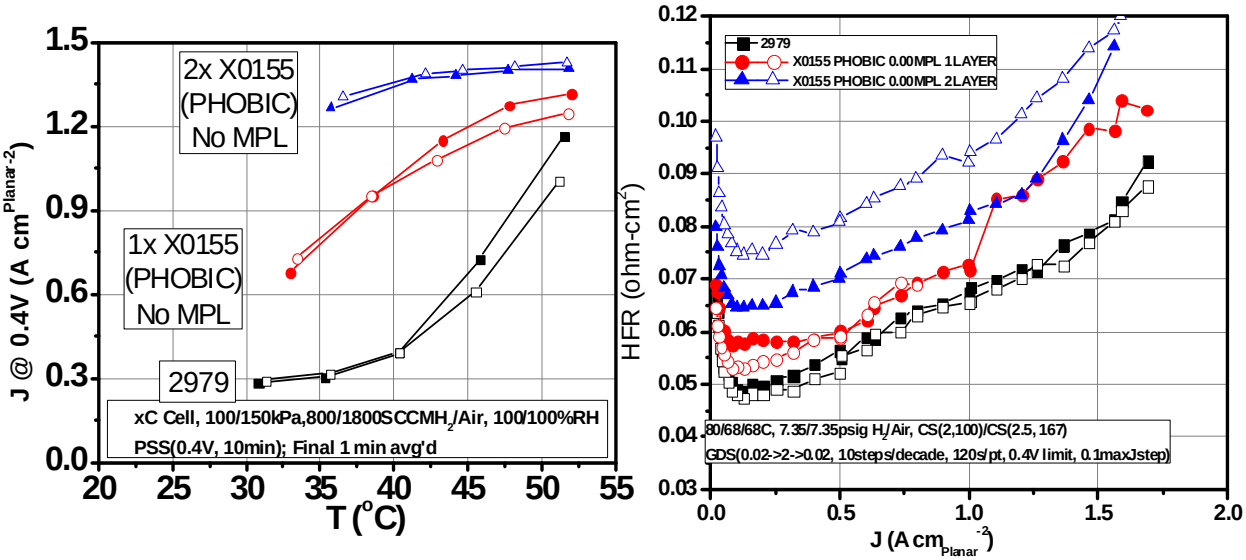

Figure 44. Comparison of low temperature performance and MEA resistance for 2979 and either one or two layers of X0155 backings. (Left): Temperature sensitivity. (Right): 80°C H_2/Air HFR.

Anode GDL Optimization – Experimental Freudenberg Backings

In Task 3, characterization of backing materials provided insight into how the backing type may influence low temperature performance. The key observation was that among materials evaluated, those with improved low temperature performance tended to have regions of relatively low fiber density.

In this work, the objective was to evaluate the impact of the backing structure using backing materials with controlled structural variations. Relevant Freudenberg materials consists of regions of relatively higher and lower fiber density (fiber "bars" and "channels", respectively). Three classes of experimental rolls of backing were generated where the relative fiber bar and channel content were varied (six total rolls, two for each structure type).

Figure 45 shows magnified transmitted light images of the various experimental backings, V25, V41, and V31. The lighter regions of the images indicate lower density regions where light is able to penetrate through the backing more readily. Qualitative differences are observed between X0155, V25, and V41.

Figure 45. Transmitted light images of untreated, experimental backings.

The experimental backings were received by 3M, where standard hydrophobic treatment and MPLs were applied. Figure 46 shows that the various backings had only modest impacts on

80°C H_2/Air performance, 40°C performance, and shorting conductivity. Based on this result, development work continued with further optimization of X0155.

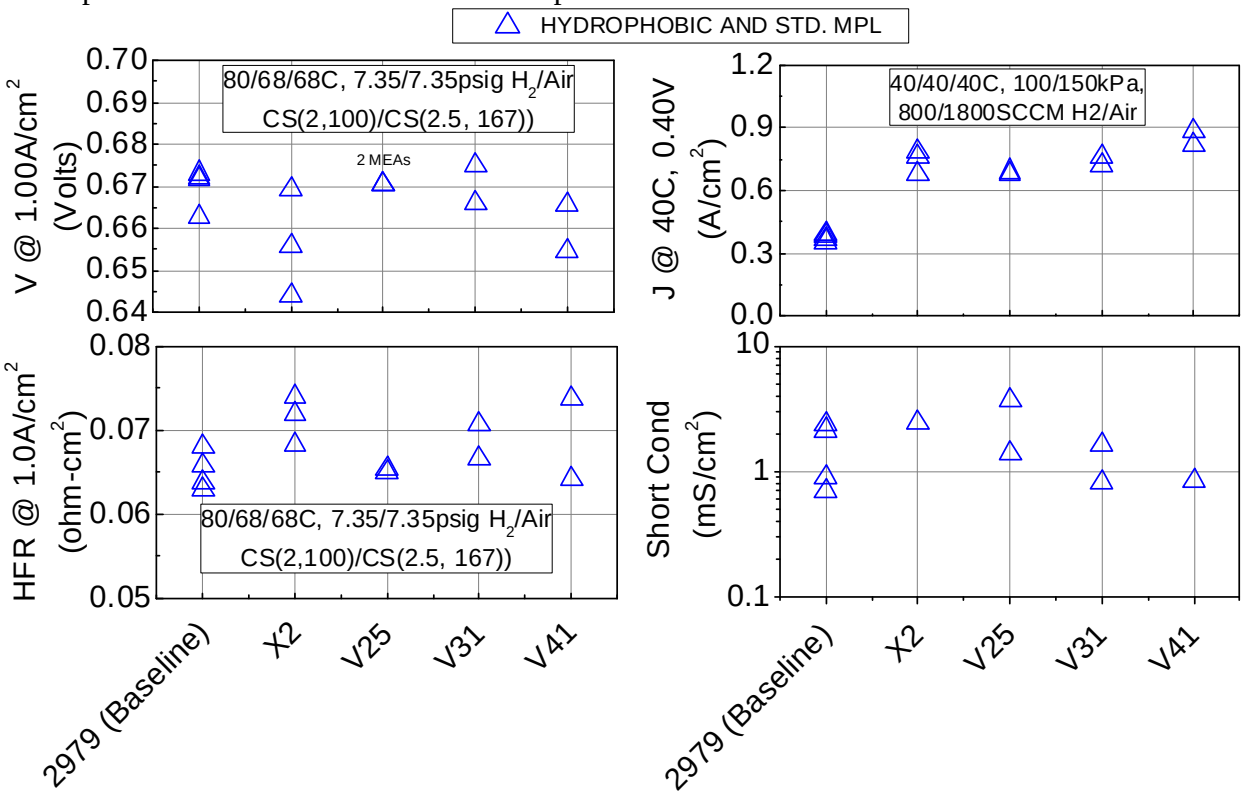

Figure 46. Impact of experimental Freudenberg backing structure on 80°C H_2/Air performance and resistance (left), 40°C limiting current density (top right), and shorting conductivity. X2 is X0155.

Anode GDL Optimization – MPL Optimization

In collaboration with Freudenberg, a variety of experimental MPLs were generated and evaluated. X0155 backing was hydrophobic treated at 3M and then coated with experimental MPLs at Freudenberg, outlined in Table 10. The MPLs consisted of a design of experiments based on different MPL coating weights and MPL porosity. The coated backings were evaluated at 3M for performance and operational robustness, summarized in Figure 47. Several Freudenberg backings yielded comparable 80°C H_2/air performance as the 3M MPL, but all yield sub-par low temperature limiting current densities. Based on this result, the 3M MPL was downselected.

Table 10. Summary of Freudenberg MPL DOE.

Trial Number	Raw GDL type	Impregnation	Material	MPL recipe	MPL weight [g/m²]	Additional pore volume	Number of A3 sheets
LV15-01-1+2	X0155	3M	X0155 3M CX578	1	20	medium	2
LV15-01-4+5	X0155	3M	X0155 3M CX579	1	20	high	2
LV15-01-7+8	X0155	3M	X0155 3M CX580	1	13	medium	2

LV15-01-10+11	X0155	3M	X0155 3M CX581	1	13	high	2
LV15-01-13+14	X0155	3M	X0155 3M CX582	2	20	medium	2
LV15-01-17+18	X0155	3M	X0155 3M CX583	2	20	high	2
LV15-01-19+20	X0155	3M	X0155 3M CX584	2	13	medium	2
LV15-01-22+24	X0155	3M	X0155 3M CX585	2	13	high	2

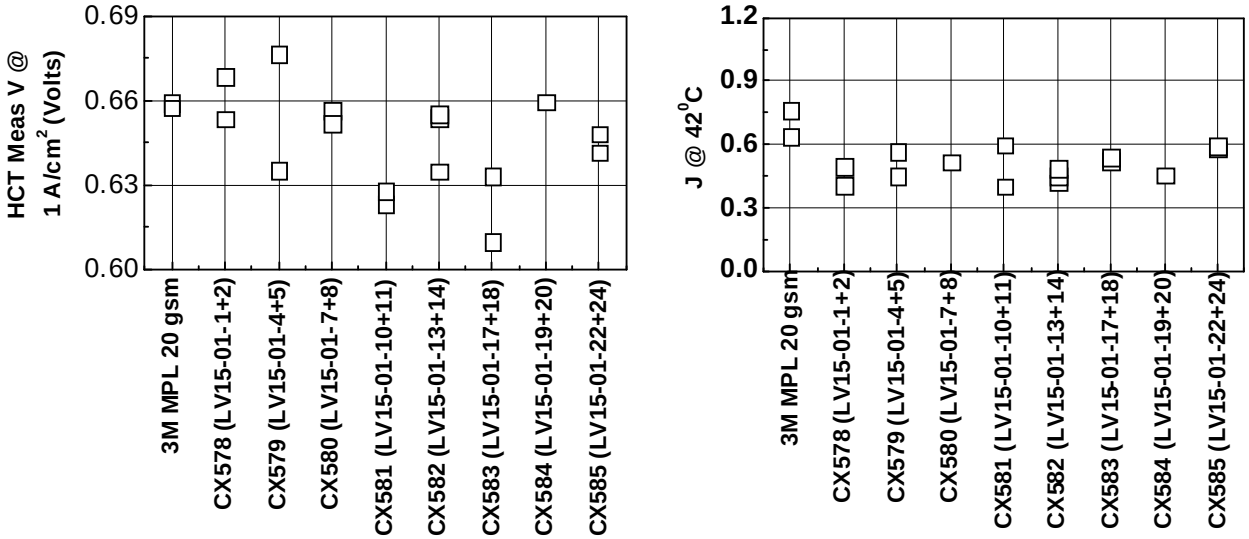

Figure 47. Comparison of 3M MPL to Freudenberg Experimental MPLs. (Left): 80°C H_2/Air performance. (Right): 42°C Limiting current density.

Anode GDL Optimization – Hydrophobic treatment level optimization

Experiments were conducted to determine the sensitivity to backing hydrophobic treatment level. X0155 GDLs were treated with a variety of hydrophobic treatment levels, above and below the baseline, and a subset were subsequently coated with a standard MPL. Figure 48 shows that either with or without MPL, improved low temperature performance correlated with lower hydrophobic treatment level. The minimum hydrophobic treatment level evaluated was downselected.

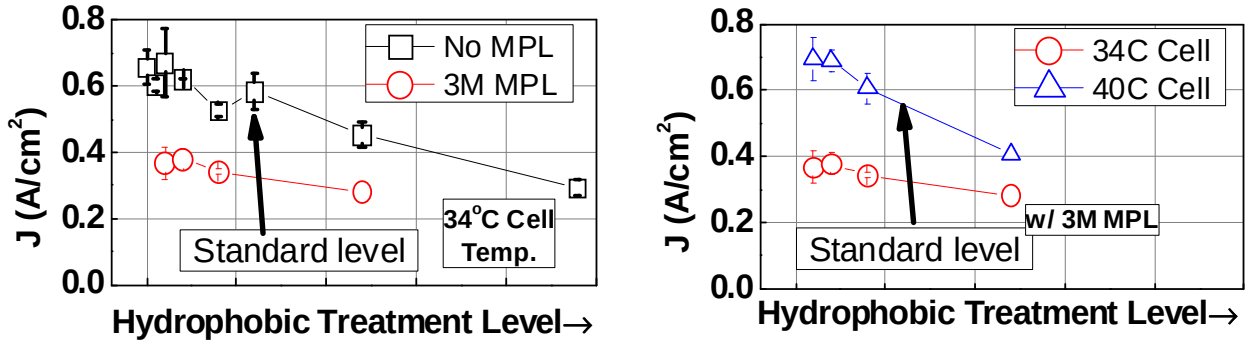

Figure 48. Impact of hydrophobic treatment level on low temperature limiting current density. (Left): Comparison with and without MPL. (Right): Comparison of sensitivity at 34 and 40C.

Anode GDL Optimization – Rollgood production for Project Deliverable

~30m of the project downselected GDL was produced, using X0155 backing, standard MPL, and low hydrophobic treatment level. Evaluation of the downselected GDL, "X3", produced a modest gain over previous "X2" (same, but standard hydrophobic treatment level). The final X3 GDL yielded better than a 2x gain in 40°C limiting current density than the project baseline 2979 (Figure 49).

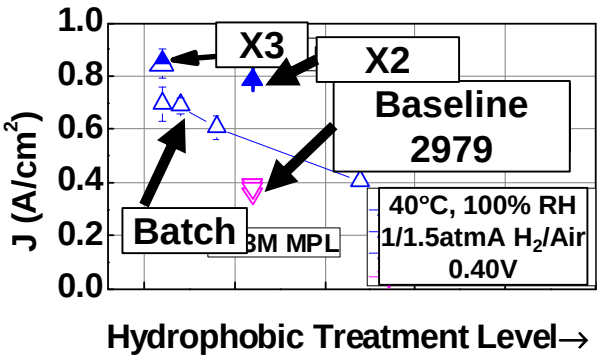

Figure 49. 40°C limiting current density with project downselect GDL.

Subtask Conclusions

An improved anode GDL was developed which yielded a 2x gain in low temperature limiting current density over the baseline 2979. Experiments which evaluated the impact of six backing fiber density variations did not yield improvement over the downselected X0155. Experiments which evaluated experimental MPLs yielded worse low temperature performance than downselected 3M MPL. Evaluations of the impact of backing thickness revealed that low temperature performance may improve with increased backing thickness and/or having an interfacial region between multiple layers, but resistance will need to be improved.

The downselected GDL construction is producible at pilot scale with expected improved low temperature performance.

Future Directions

Material development towards implementing thicker and/or multi-interface anode backings is warranted. In the limited work above, such material yielded dramatic improvement which would seemingly resolve a key aspect of operational robustness with NSTF MEAs.

Subtask 2.2 Interfacial Layer Optimization for Kinetic, Transient Response

Subtask Overview

Subtask 2.2 involves optimization of interfacial layers for load transient response and kinetic optimization. Load transients are rapid (~1s) step increases in load from idle to high levels (e.g. 0.02 to 1.0A/cm^2).

The work under subtask 2.2 will involve: 1) identification of the most durable supported conventional catalyst based on existing data; 2) incorporation of top 2-5 candidates into interfacial layers with ~0.01mg$_{PGM}$/cm^2 and 2-5 variations of layer composition; 3) single cell fuel cell evaluation for load transient, rated power, and kinetic response. If any interfacial layers

show acceptable benefit in load transient response while either maintaining or improving the overall mass activity, the downselected 1-2 interfacial layers will be evaluated for durability via DOE electrocatalyst and support durability protocols.

Subtask High Level Work Summary

Several new cathode interlayers were generated and evaluated for their impact on rated power performance, mass activity, and load transient operational robustness. A subset were evaluated for durability. Approximately 50m of downselected interlayer was produced on pilot scale equipment.

Subtask Key Results

Pre-Project Background

In pre-project work, cathode interfacial layers ("interlayers" or "ILs") were found to generally improve one aspect of operational robustness, load transients. Cathode interlayers are low-loaded Pt/C electrodes which are interspersed between the NSTF cathode electrode and the cathode GDL. Figure 50 (left) shows that without interlayer, a baseline NSTF MEA cannot withstand a rapid increase in load from 0.02 to 1.0A/cm^2 under condensing conditions, such as those expected at 60°C, 100% RH. Immediately after the load increase (t=32s), the cell voltage was negative, indicating that the cathode electrode was evolving hydrogen rather than reducing oxygen. Inclusion of the interlayer with either 0.016 or 0.05mg$_{PGM}$/cm^2 resulted in maintenance of positive cell voltage throughout the duration of the test.

One issue with pre-project interlayers was that a suppression of H_2/Air performance was observed at low current density (Figure 50 right). With a variety of interlayer formulation (denoted by different color symbols), the cell voltage at 20mA/cm^2 decreased as the interlayer loading was decreased.

An additional question with the interlayers was durability. Interlayers are constructed from carbon-supported Pt nanoparticle catalysts, which have significant durability concerns in terms of carbon corrosion and Pt dissolution.

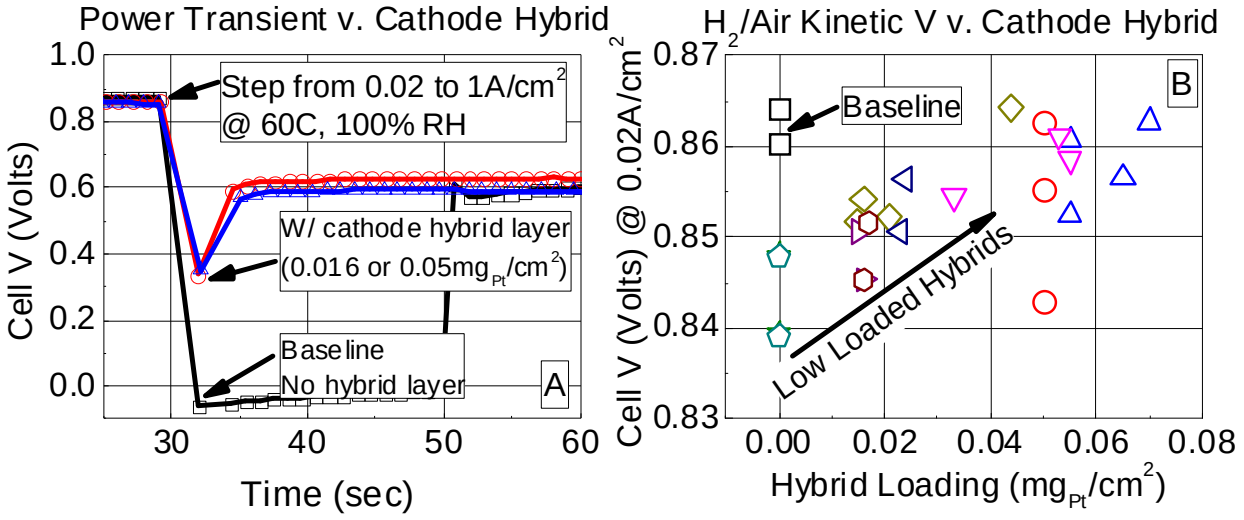

Figure 50. Impact of interlayer on load transient performance (left) and H_2/Air kinetic performance (right).

Impact of Primary Interlayer Formulation Variables

Initial project work focused on determining the sensitivity of several performance and robustness attributes on key interlayer formulation variables, with a primary focus on the type of carbon-supported Pt nanoparticle catalyst. Variables evaluated included the Pt wt% on carbon, the impact of catalyst heat treatment, the interlayer Pt loading, carbon type and the interlayer electrocatalyst formulation (Pt, Pt alloy, or Au). Performance attributes evaluated included the composite mass activity of the combined NSTF + Pt/C cathode electrode, the specific area, 80°C HCT H_2/Air performance, and load transient performance, evaluated between 30-80°C cell temperatures. Experiments were conducted primarily in 50cm^2 test cells with baseline NSTF CCM (0.05PtCoMn/NSTF anode, 0.15PtCoMn/NSTF cathode, 3M 8250EW 20µm PEM) and an X0155 based anode GDL (with baseline hydrophobic treatment and baseline 3M MPL).

A summary of key results is shown in Figure 51. A key overall conclusion was that good load transient performance could be achieved with very low interlayer Pt loadings as low as ca. 6ugPt/cm^2. Within the range of variables explored, little difference was observed between interlayers comprised of 30 vs. 40 wt% Pt on carbon and type "A" vs. "B" carbon. Heat-treated catalyst induced large performance loss relative to non-heat treated.

Experiments were conducted to understand the influence of heat treatment on the load transient performance. Analysis summarized in Figure 52 indicates that the primary loss mechanism was loss of interlayer Pt surface area with heat treatment. Passing load transient (positive cell voltage) was obtained when the total cathode Pt SEF was > 20cm^2_{Pt}/cm^2_{planar}, corresponding to an interlayer SEF of about 8 cm^2/cm^2.

Figure 53 summarizes the impact of interlayer Pt loading, Pt wt%, and heat treatment on general performance characteristics. As Pt/C interlayer loading increased from 10 to 50µg/cm^2, the mass activity generally decreased and absolute surface area increased, and no appreciable change in 80°C HCT H_2/Air performance was observed at either 0.02 or 1.46A/cm^2. The decrease in mass activity was due to the intrinsically lower specific activity of the Pt/C catalyst vs. PtCoMn/NSTF. The relative insensitivity of interlayer loading on H_2/Air performance was an important improvement as compared to pre-project status, where low-loaded interlayers suppressed performance at 20mA/cm^2.

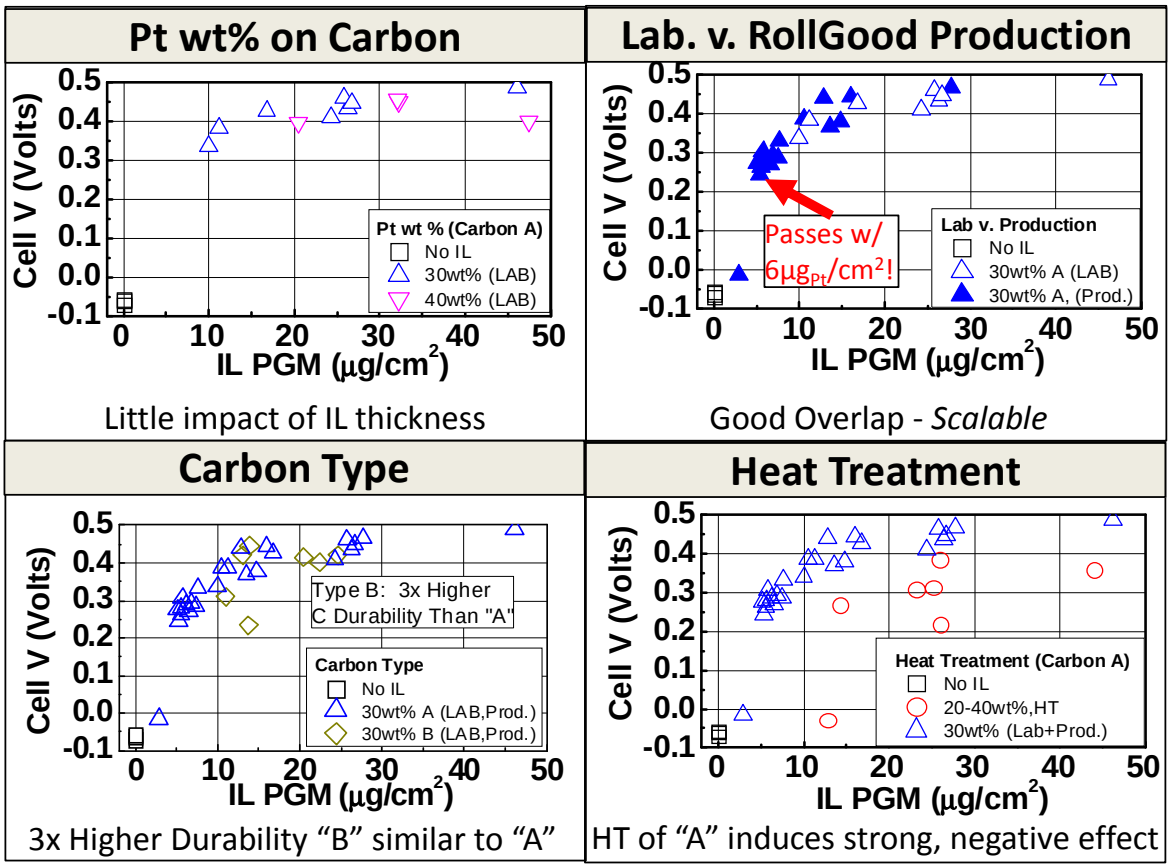

Figure 51. Impact of key interlayer variables on load transient performance, measured at 60°C cell temperature, 100% RH. (Top left): Impact of Pt wt% on carbon. (Top right): Comparison of laboratory vs. pilot-scale fabricated interlayers. (Bottom left): Impact of carbon type. (Bottom right): Impact of catalyst heat treatment.

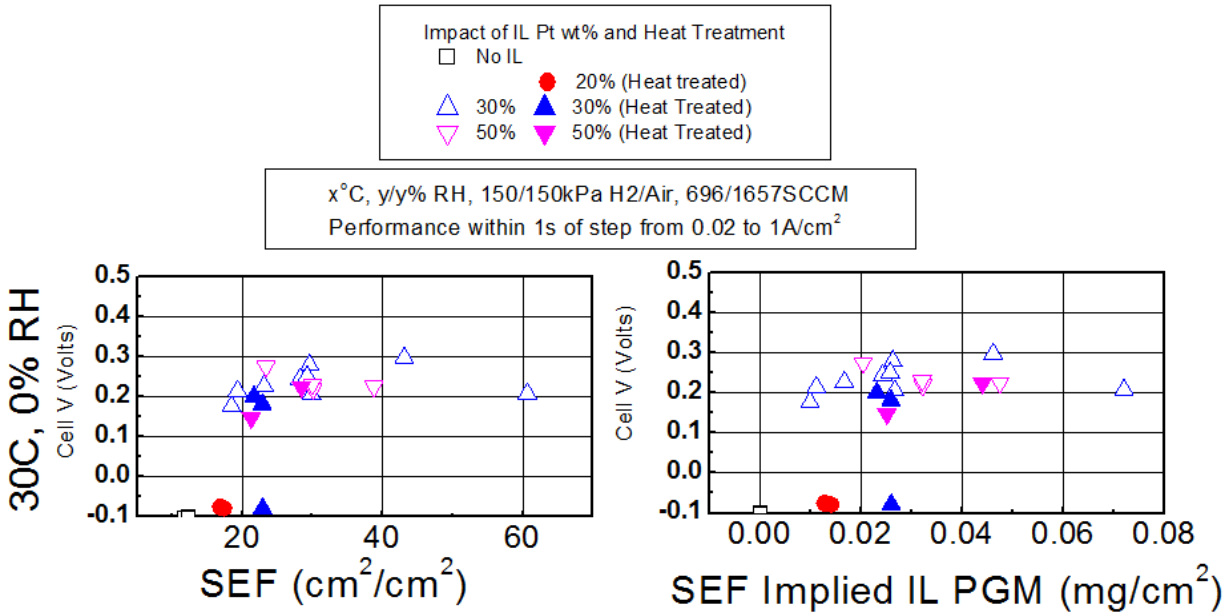

Figure 52. Analysis of heat-treatment impact on 30°C, 0% RH load transients. (Left): Load transient cell voltage vs. cathode absolute Pt surface area. (Right): Load transient cell voltage vs. cathode interlayer Pt loading.

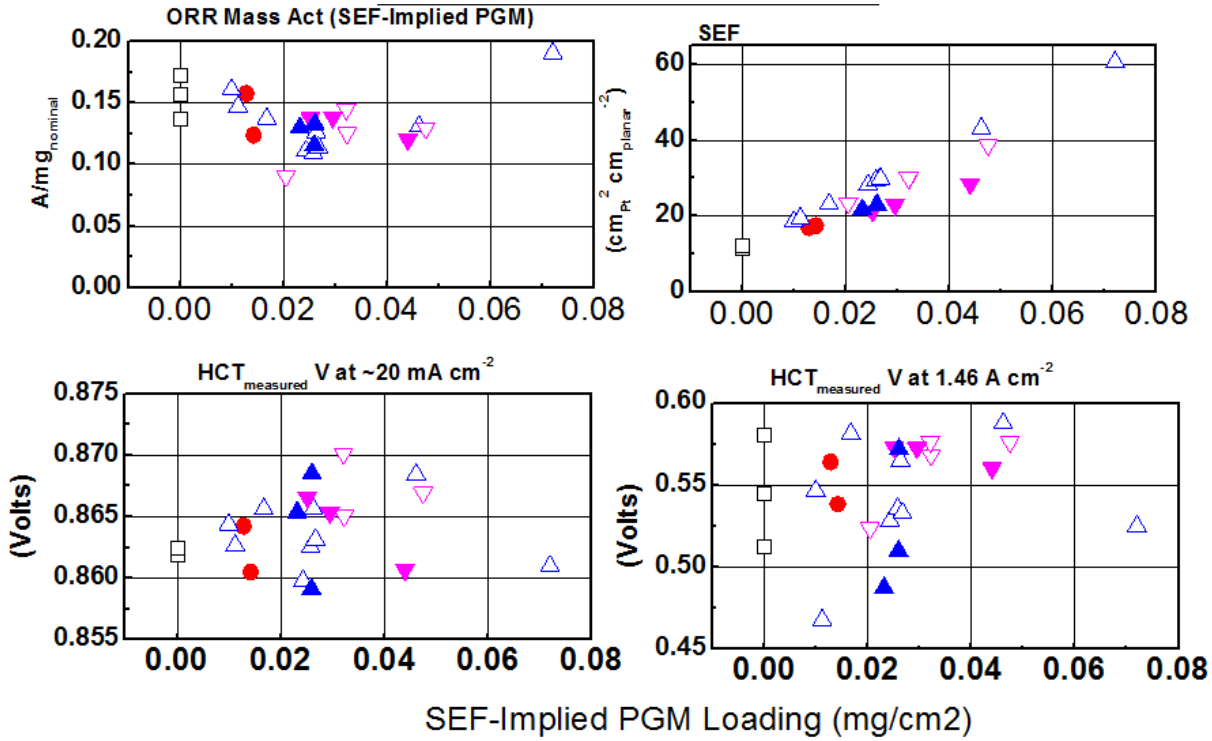

Figure 53. Impact of interlayer loading, Pt wt% on carbon, and heat treatment on general performance characteristics. (Top left): Mass activity (NSTF + IL Pt content). (Top right): Total cathode SEF. (Bottom left): HCT H_2/Air performance at 20mA/cm^2. (Bottom right): HCT H_2/Air performance at 1.46A/cm^2.

The impact of interlayer electrocatalyst composition was evaluated in limited experiments. Figure 54 (left) shows that a higher activity Pt alloy catalyst yielded equivalent load transient performance as Pt.

An experiment was also conducted with Au/C electrocatalyst, to probe if ORR activity was needed for good load transient performance. Figure 54 (right) shows that relatively high-loaded Au interlayers are not effective for improving load transient of NSTF MEAs, and as such some ORR activity is needed.

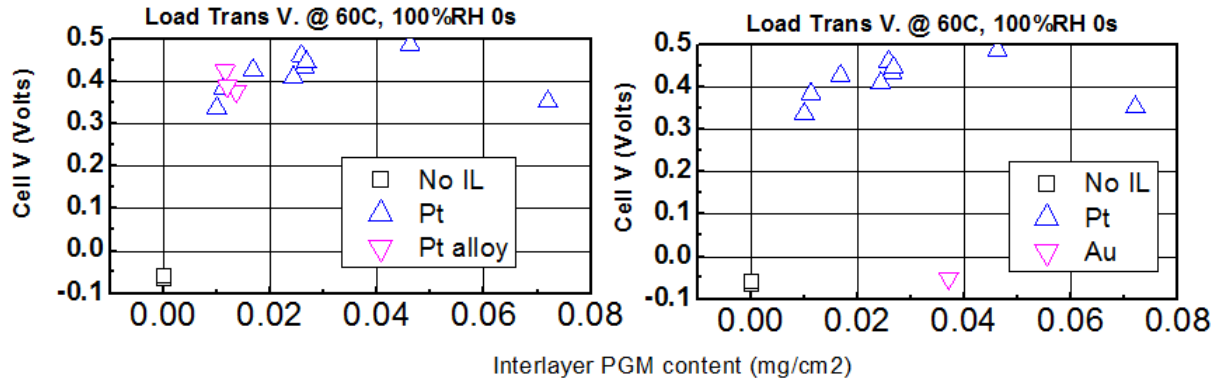

Figure 54. Impact of interlayer electrocatalyst composition. (Left): Pt vs. Pt alloy. (Right): Pt vs. Au.

Interlayer Durability Evaluations

One key concern with the interlayer approach was that the Pt/C electrocatalyst incorporated will be insufficiently durable to allow maintenance of high operational robustness. Figure 55 summarizes durability assessments of NSTF MEAs containing an interlayer with non-heat treated catalyst on a relatively less stable carbon ("type "A" from above). The durability was assessed by using the then-current DOE electrocatalyst cycle (0.6-1.0V, 30k cycles) and the previous DOE support AST (400 hour hold at 1.2V).

After the electrocatalyst cycle, MEA 80°C performance and cathode mass activity were substantially stable, with a modest H_2/Air performance improvement and 15% mass activity loss, both of which pass the DOE 2020 durability targets. However, the load transient performance degraded after 10k cycles, and ultimately failed after 20k cycles.

During the support AST cycle (1.2V hold), H_2/Air performance and mass activity was also stable through 90 hours. Performance at 1.5A/cm^2 increased 50mV, and mass activity loss was about 10%. Again, load transient performance failed after about 50 hours of hold time.

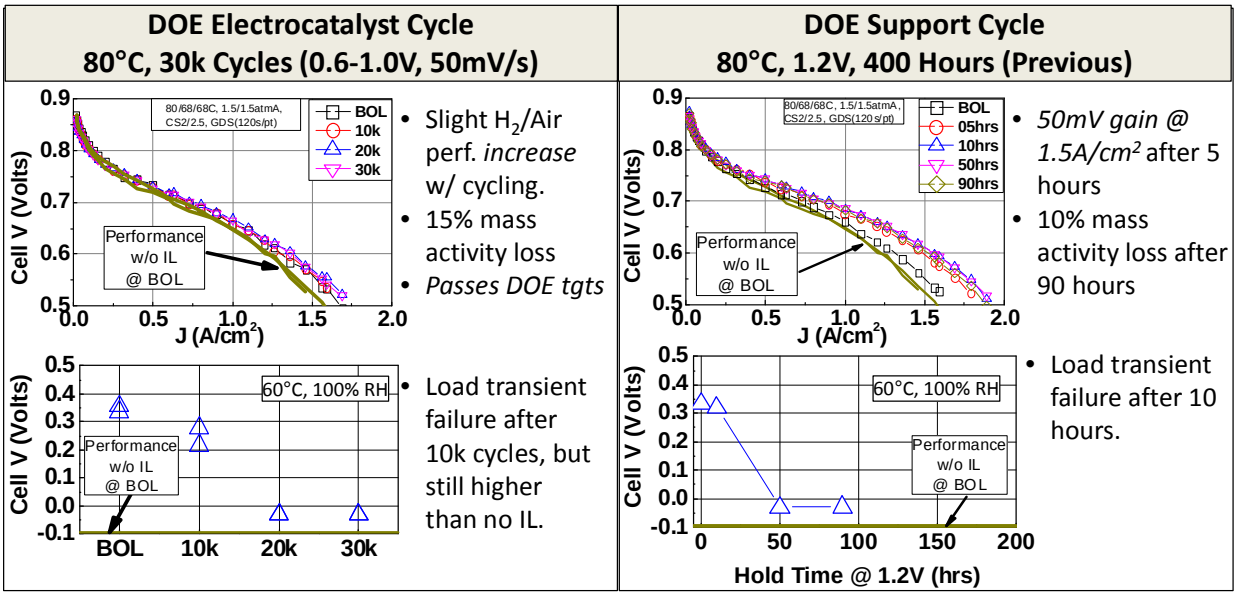

Figure 55. Performance and load transient durability of type "A" carbon interlayers during the DOE Electrocatalyst AST and the (Previous) Support Cycle (400 hour 1.2V hold).

Due to the inadequate durability of the interlayer's operational robustness, development effort focused on incorporation and evaluation of interlayers with type "B" carbon, known to be more stable based on 3M internal assessment. Figure 56 summarizes the key durability results. Under the electrocatalyst AST, NSTF MEAs with type "B" interlayers yielded relatively stable mass activity (~30% loss after 20k cycles) and improved H_2/Air performance at 1.5A/cm^2. Load transient durability of type "B" improved relative to type "A", but failed between 20 and 30 thousand cycles.

Under the current support AST (5000 cycles between 1-1.5V), NSTF MEAs with type "B" interlayer passed all relevant metrics. The improved H_2/Air performance observed with type "B" interlayer was also observed with an interlayer-free NSTF MEA, indicating that the intrinsic NSTF MEA performance was responsible.

Based on this improved durability, interlayers with type "B" carbon were downselected, targeting 15-20µg$_{Pt}$/cm^2 loading.

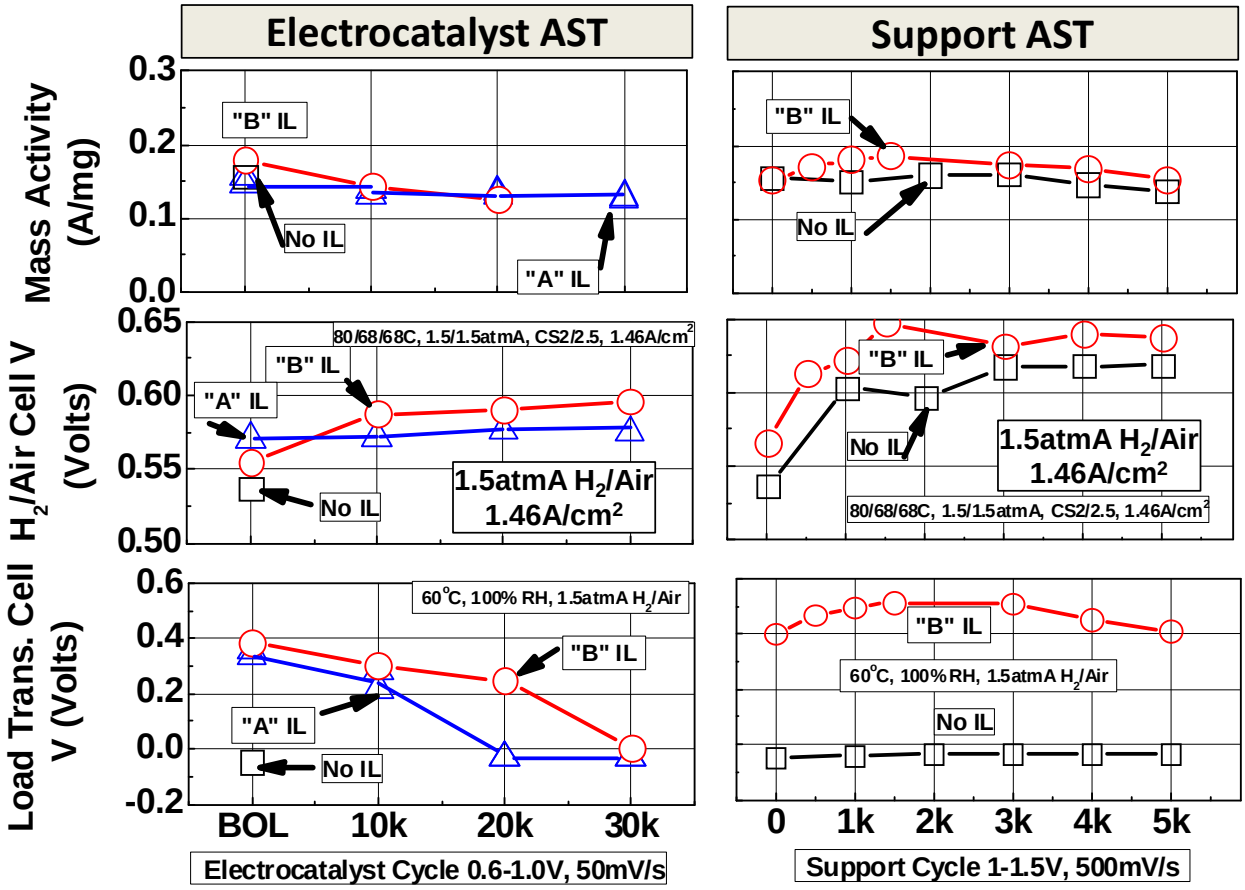

Figure 56. Evolution of mass activity, H2/Air performance, and load transient for NSTF MEAs without interlayer or with type "A" or "B" carbon interlayers.

Downselected Cathode Interlayer Fabrication

Approximately 50m of the downselected cathode interlayer were produced. A loading analysis by XRF indicated that the loading was 16 ± 3 µg$_{PGM}$/cm^2. Figure 57 shows that the load transient performance of the final production lot agreed well with previous lots.

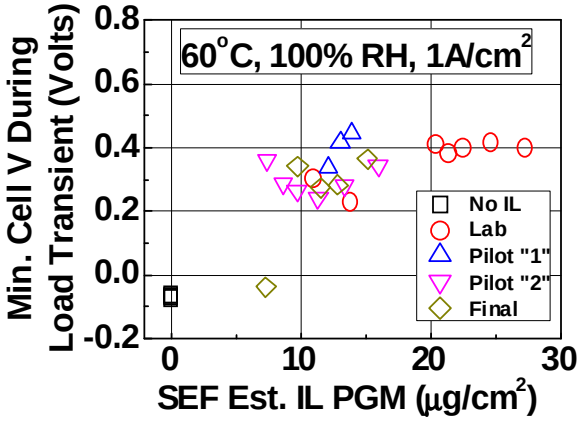

Figure 57. Load transient performance comparison between type "B" interlayers produced in laboratory and three pilot-scale lots.

Subtask Conclusions

Cathode interlayers can provide substantially improved operational robustness to NSTF MEAs at relatively low PGM contents and can be reasonably durable. When coupled with the project downselected anode GDL, successful load transients up to 1A/cm^2 were demonstrated too for cell temperatures between 30 and 80°C. Interlayers developed in this project had relatively small impacts on beginning of life rated power performance.

Through the work conducted here, the performance of cathode interlayers depends predominantly on interlayer Pt absolute surface area, directly proportional to loading. Modest changes in key Pt/C variables, including Pt wt% on carbon and carbon type, had little effect on load transient performance. Heat treated catalysts were less effective at a given Pt loading due to their lower specific Pt surface area.

Retention of operational robustness appears to depend upon maintenance of Pt surface area. When relatively stable carbon supports are used, the operational robustness and MEA performance are retained after 5,000 support AST cycles between 1.0-1.5V. However, degradation of Pt surface area, via the electrocatalyst AST, resulted in failure of operational robustness after 20k cycles vs. the 30k target.

Future Directions

The key remaining development work is incorporation of interlayer catalysts with improved electrocatalyst stability. It is suspected that a Pt electrocatalyst which is modestly more stable than that used in the downselected interlayer would allow adequate retention of the operational robustness.

Task 3. Water Management Modeling for Cold Start

- *Subtask 3.1 Material Property and Segmented Cell Measurements*
- *Subtask 3.2 GDL Modeling for Cold Start*
- *Subtask 3.3 MEA Modeling for Cold Start*
- *Subtask 3.4 GDL, MEA Model Integration*
- *Subtask 3.5 Model Validation*

The primary objective of Task 3 is to determine the key material properties and mechanisms influencing cold start with ultra-thin electrode NSTF MEAs, focusing on the already demonstrated significant experimental effect of the anode GDL. The expected outcome of Task 3 is a mechanistic understanding of specific GDL material properties needed for optimal cold start with existing materials and a design tool to enable further improvement.

Subtask 3.1 Material Property and Segmented Cell Measurements

Subtask Overview

Subtask 3.1 involves material property measurements and specialized fuel cell testing to provide data to the modeling efforts which occur in subtasks 3.2-3.4.

Subtask High Level Work Summary

Project GDLs were analyzed for physical structure, static and dynamic wetting properties, and thermal conductivity.

Subtask Key Results

Background

Prior to project initiation, 3M had identified that the anode gas diffusion layer can have significant influence on the low temperature performance with typical NSTF MEAs (Figure 58). A primary objective of task 3.1 is to measure material properties of the anode gas diffusion layer materials of interest, which are to be used as inputs to the Michigan Technical University (MTU) GDL model and Lawrence Berkeley National Laboratory (LBNL) MEA model.

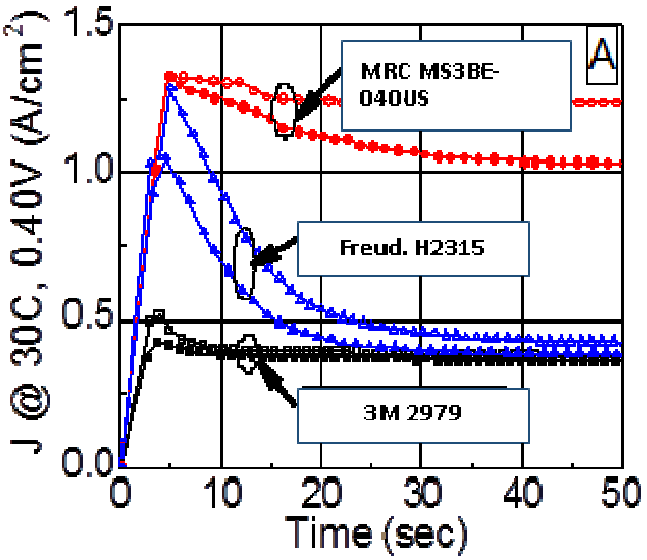

Figure 58. Single cell cold start with various anode backings s with 3M PTFE and MPL. 30/30/30C, 1.0/1.5atmA H_2/Air, 800/1800SCCM, PSS (0.40V).

Several initial GDL sample materials were provided to MTU and LBNL. The material sets included Freudenberg H2315 and MRC MS3BE-040US, both as received or with a 3M PTFE treatment. The backing used in the baseline 3M anode 2979 GDL was also provided.

GDL Static Wetting Analysis

Initial MTU work in Subtask 3.1 focused on measurement of GDL contact angle measurement, microscopy, and liquid water percolation measurements. Table 11 lists the measured static contact angles for the various relevant anode backings, with or without PTFE treatment.

Table 11. Static Contact Angles of Anode Backings w/ and w/o PTFE treatment and w and w/o MPL.

No	Sample	Contact Angle (°)
1	Freudenberg H2315 – As Received	129.0 ± 12
2	Freudenberg H2315 – PTFE	141.4 ± 6
3	Freudenberg H2315 – PTFE + MPL	142.7 ± 6
4	MRC MS3BE-040US – As Received	140.9 ± 5
5	MRC MS3BE-040US – PTFE	151.3 ± 5
6	MRC MS3BE-040US – PTFE + MPL	156.9 ± 6
7	2979 Bare Paper – Untreated	Wicking
8	2979 Bare Paper - PTFE	130.6 ± 7
9	2979 Bare Paper - PTFE + MPL	149.3 ± 9
10	Freudenberg X0155 – PTFE	141.8 ± 3
11	Freudenberg X0155 – PTFE + MPL	143.4 ± 3

GDL Water Percolation Analysis

Water transport is characterized via liquid water percolation testing. Percolation testing is conducted over a range of flow rates, and the data collected is time-dependent percolation pressure and wetted area. Figure 59 (left) summarizes injection pressure data obtained with the Freudenberg H2315 backing. Figure 60 summarizes the recorded water percolation images and wetted area analysis, used to generate the wetted area data shown in Figure 59 (right).

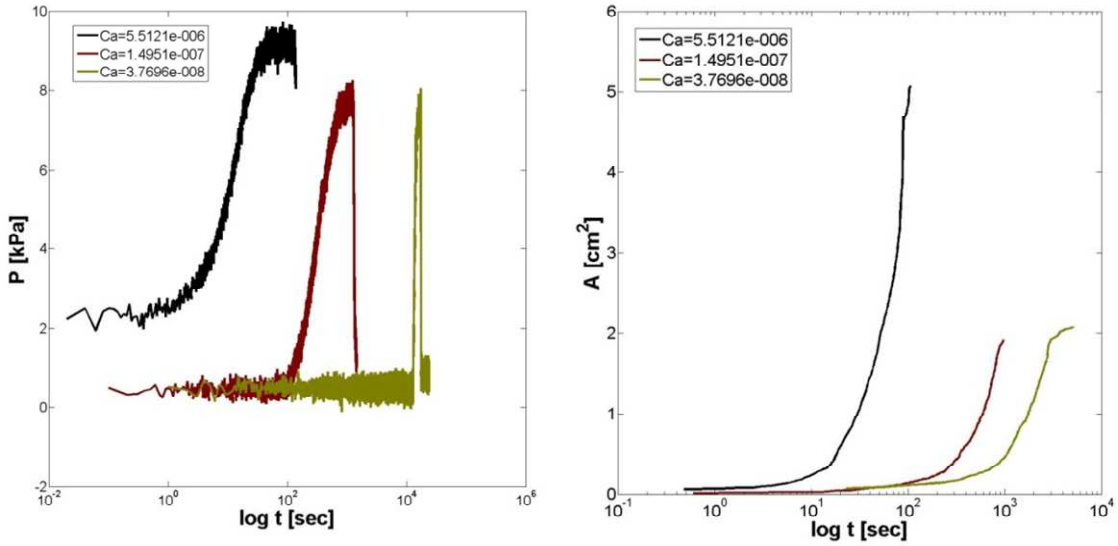

Figure 59. Experimental liquid water percolation data for Freudenberg H2315 at three water injection rates. (Left): Injection pressure. (Right): Wetted area.

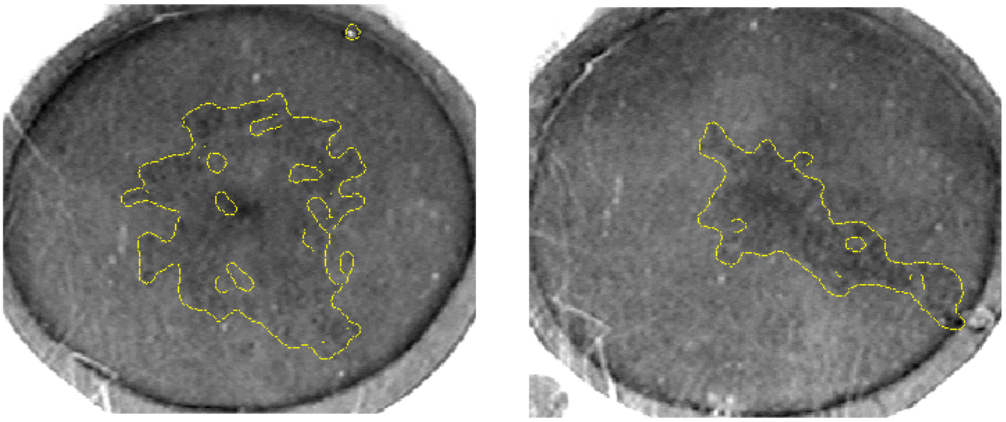

Figure 60. Analysis of wetted areas of porous transport layers.

The peak, or plateau, percolation pressures and capillary number for the tested samples are shown in Table 12. The highest capillary number (far right column) resulted in a stable displacement (SD) flow regime in which the percolation pressure does not plateau.

Table 12. Percolation pressures for the samples listed, measured in kPa, at different capillary numbers. SD represents stable displacement.

Sample	Percolation Pressure (kPa) @ Capillary Number			
	3.7696e-8	1.4951e-7	5.5121e-6	3.8737e-5
Freudenberg-H2315-Untreated	5	5-5.25	5.5	SD
Freudenberg-H2315-PTFE	5.1-5.4	5.3-5.5	5.95	SD
Freudenberg-H2315-PTFE-MPL*	5.6-5.8	5.4-5.6	6.2-6.5	SD

2979-Bare-Paper-Untreated	5.1-6.4	5.7-6.3	7.1-7.5	SD
2979-Bare-Paper-PTFE	7.2-7.5	7.3	8.1	SD
MRC-MS3BE-040US-PTFE	6.1-6.3	6.2	6.6-6.9	SD
MRC-MS3BE-040US-PTFE, Sample 2*	5.9-6.1	6.2-6.5	6.5-6.7	SD
MRC-MS3BE-040US-Untreated*	5.3-5.4	5.4-5.5	5.5-5.7	SD

Work was also conducted to evaluate the force by which GDLs hold onto water droplets as they grow and detach into the flow field channels. Measurements were made at LBNL by placing the GDL next to a flow channel and make a droplet by pushing water underneath and then see at what velocity it detached, summarized in Figure 61. Significant differences were observed between PTFE coated and untreated backings. PTFE tended to decrease the velocity (proportional to force) needed for detach the droplets. Backing type was also influential – higher performing MRC MS3BE-040US yielded lower detachment velocities than MRC U105.

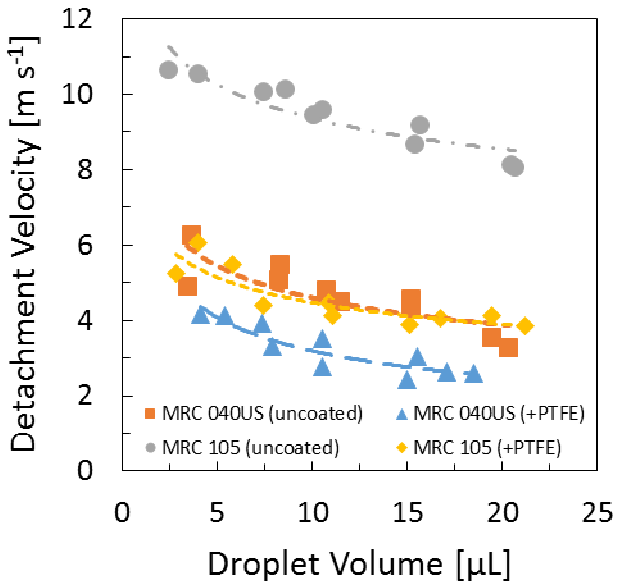

Figure 61. Measurements of velocity needed to detach droplets as a function of droplet volume.

GDL Structural Characterization

Figure 62 shows backlit optical micrograph images of the three anode backings at three magnification levels. One of the striking differences, not previously observed, is that the improved anode GDL materials, Freudenberg H2315 and MRC MS3BE-040US, show an apparent modulation in fiber thickness or density at an approximate 1mm scale. This is not visible with the 3M 2979 backing, and so far appears to *qualitatively* correlate with the low temperature performance variation observed in Figure 58. This modulation is even more pronounced in the MRC MS3BE-040US, where the light from the backlighting is visible, indicating extraordinarily low density/thickness in these regions. It is posited that these lower density regions act as lower resistance conduits for liquid water transport. This finding was

examined in modeling trials at MTU and LBNL, discussed later in this section. Other observed differences include fiber type and degree of binder content.

X-ray computed tomography was also used to evaluate the structure of backings as a function of compression as well as with liquid water injection. Figure 63 compares tomography images and analyses of the highest performance MRC backing to the lowest performing 2979 baseline backing.

The top row shows the measured tomography images, where the lower density region of the MS3BE-040US paper is fairly evident. The middle and bottom rows show image processed versions of the top row datasets, with the middle row being the image-processing-determined solid phase and the bottom row the void phase. With the 2979 backing, the void phase is of reasonably uniform size and is relatively uniformly distributed. The density modulation is clearly evident with the MRC MS3BE-040US, with a very large void region surrounded by a region of low void density (high solid phase density).

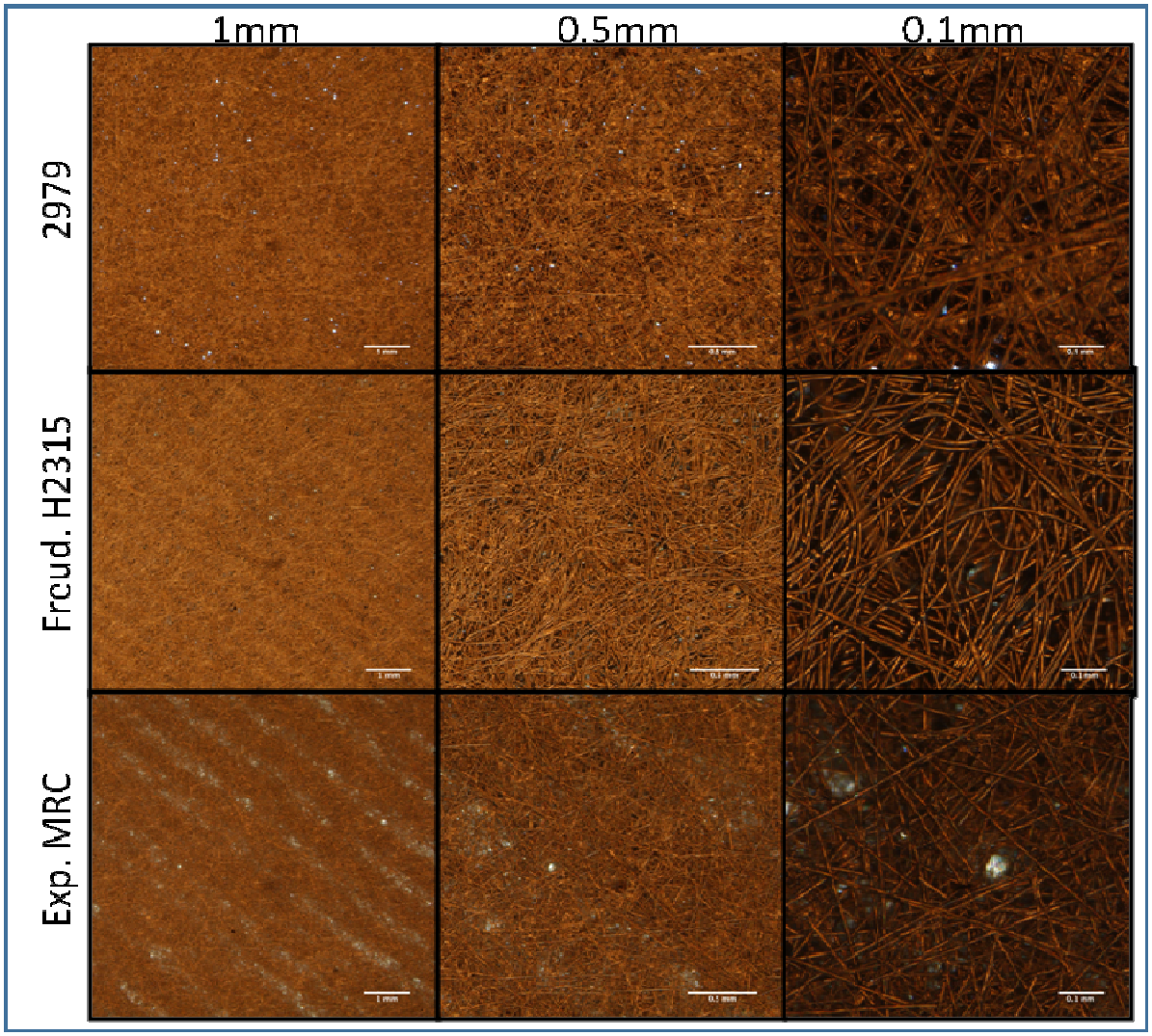

Figure 62. Optical Micrographs of Initial Set of 3M Anode GDL Backings w/ PTFE Treatment (rows). Labels at top correspond to dimensions of scale bars.

Additional tomography was conducted on the MRC MS3BE-040US backing with 3M MPL coating (Figure 64). The analysis confirmed that the MPL penetrates significantly into the backing. The portion of the MPL on top of the backing is ca. 40 microns, and the MPL penetrates into the backing as much as an additional 50 microns. The MPL surface was also determined to be relatively rough, consisting of a ridged structure of ca. 20 microns high. This tomographic analysis could potentially provide a much richer analysis of the pore structure of the GDLs than the typical pore size distribution determined by porosimetry, as the porosimetry does not capture the through-plane variation. The possibility was assessed and is discussed below.

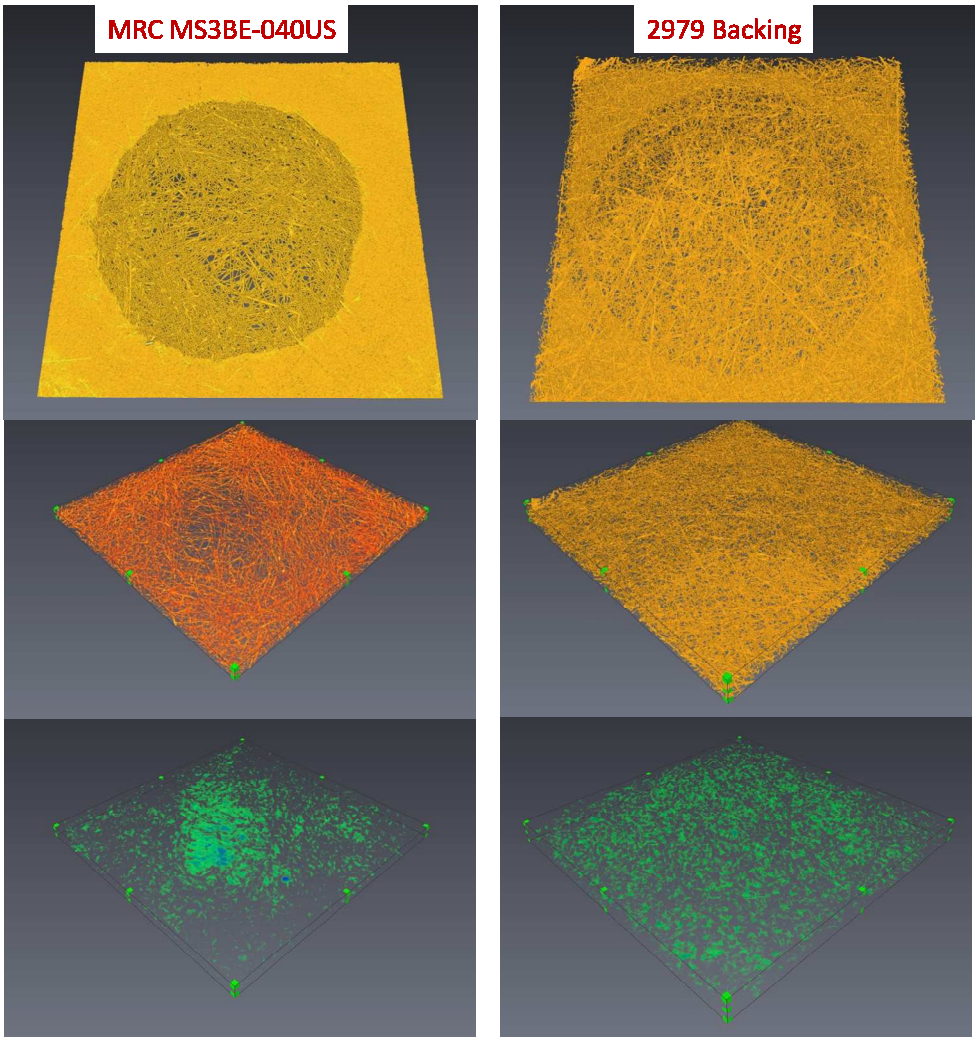

Figure 63. X-Ray Tomography of Project Backings. Top row: Raw images. Middle row: Image-processed solid phase. Bottom row: Image-processed void phase.

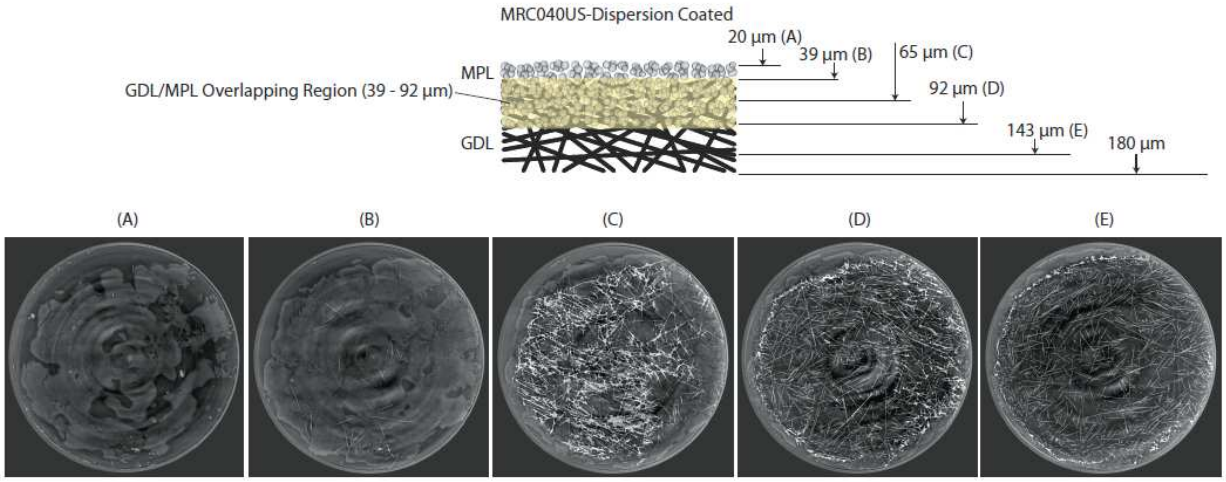

Figure 64 Tomographic analysis of MRC MS3BE-040US, with 3M hydrophobic treatment and MPL.

Thermal Conductivity Analysis of GDLs

Thermal conductivity of backings is known to strongly influence the water saturation levels in GDLs. Low thermal conductivity can allow generation of thermal gradients through the GDL between the CCM and flow field. This can also enable enhanced water removal in the vapor phase.

Experiments were conducted to evaluate backing thermal conductivity at LBNL, as a function of backing type and liquid saturation level. Exemplary data and analysis for 3M GDLs based on H2315 ("FE-01577) and X0155 ("FE-02316") is shown in Figure 65.

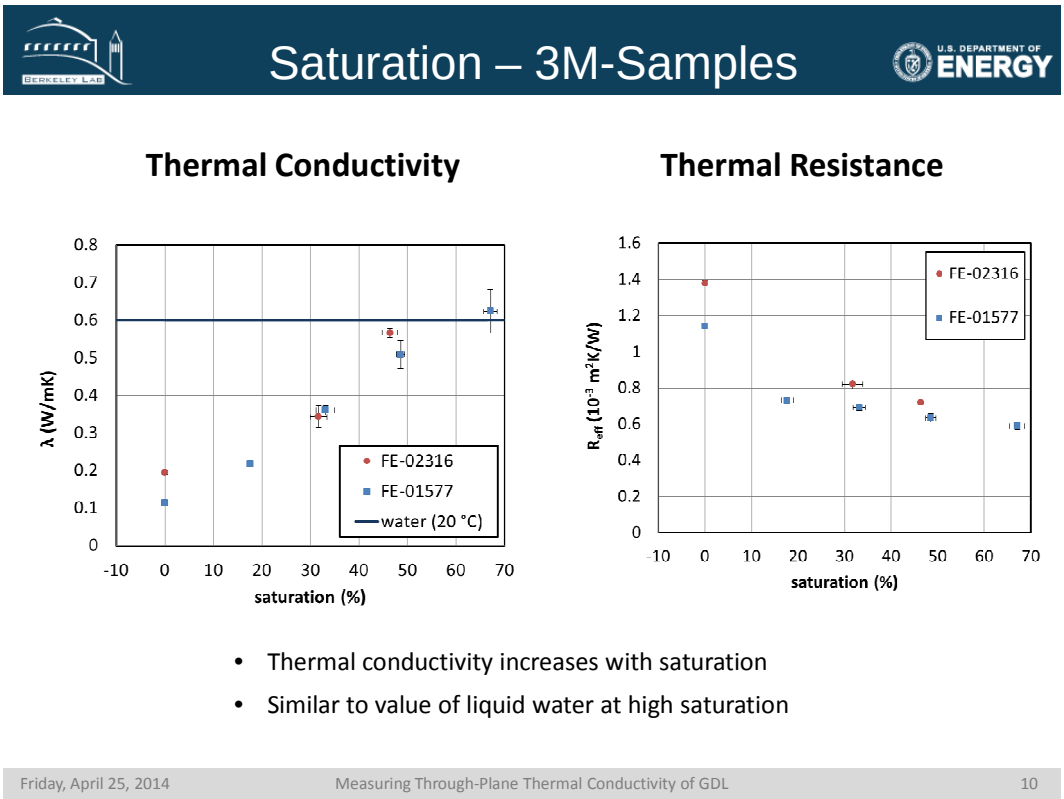

Figure 65. Influence of water saturation on thermal conductivity.

Analysis of stacked anode GDLs

In subtask 2.1, a significant and surprising observation was made. Significantly improved low temperature performance was enabled when two layers of X0155 anode GDL were installed in the fuel cell, as compared to the typical single layer. Figure 66 (left) shows that the performance at 40°C increased from ca. 0.7 to 1.2A/cm^2 as the number of anode GDLs layers increased from one to two. Figure 66 (right) shows that the limiting anode water removal rate also increased as the number of anode X0155 layers increased from one to two.

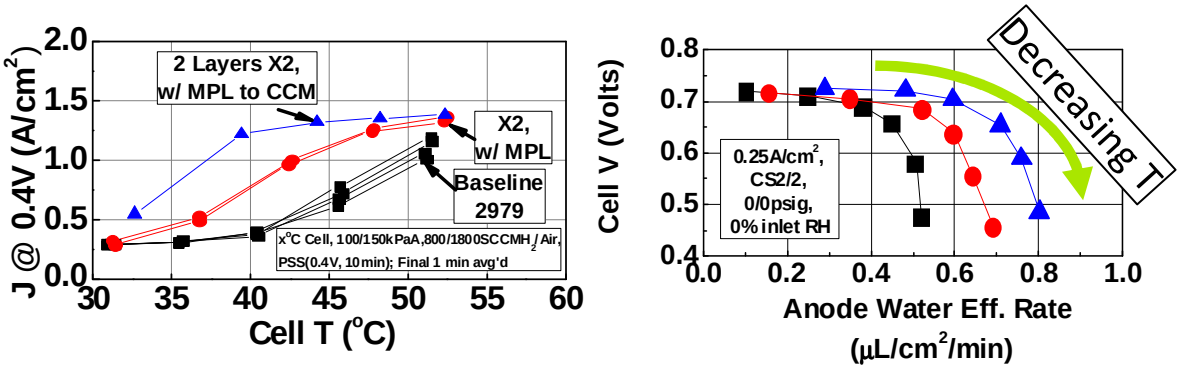

Figure 66. Impact of stacked GDLs on low temperature performance (left) and MEA water balance (right).

While impractical from a cost and rated power performance perspective (too electronically resistive), the strong effect warranted further study from a mechanistic perspective. To understand the performance gain observed by 3M for stacked GDLs, LBNL stacked these GDLs in different configurations and analyzed by X-ray CT (XCT) to determine possible underlining physical mechanisms that are believed to be of interfacial nature. Figure 67 summarizes porosity

analysis for either one or two stacked X0155 w/ GDLs, treated with PTFE but not MPL. Through-thickness GDL porosity is highly non-uniform. The decrease of porosity (significantly pronounced for 1x X0155 sample shown by red) is attributed to application of PTFE as indicated by in-plane tomographs shown as insets in the figure. Stacking two Freudenberg X0155 increased the porosity of the PTFE region.

The experiment for stacking experimental Freudenberg samples included the uncompressed and compressed GDL builds with four GDLs each to represent all possible configurations. As shown for Freudenberg V41 samples in Figure 68, the porosity sharply increased at all the interface for uncompressed samples. Whereas, for compressed samples the interfacial porosity peaks decreased and the through GDL porosity has remained unchanged. Comparing PTFE-treated V41 samples (red and blue) to untreated (black) a major observation is made of sharp dips in porosity near the interface for PTFE-treated samples. The untreated sample did not show decrease in porosity.

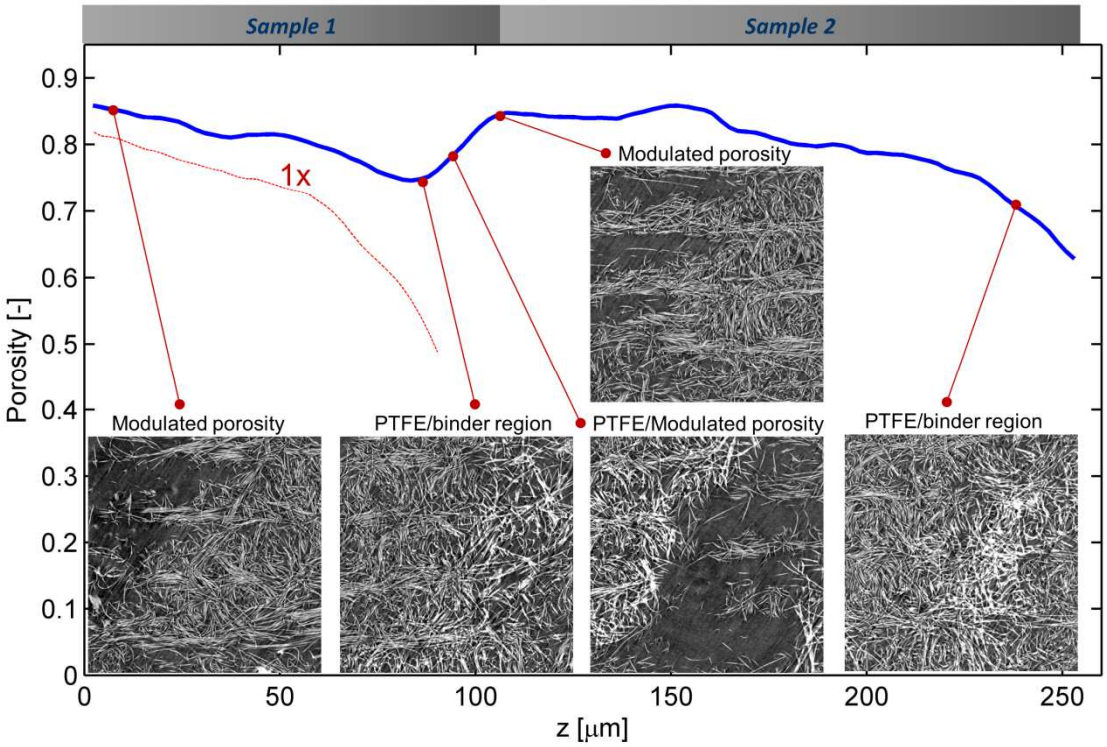

Figure 67. Porosity analysis by XCT.

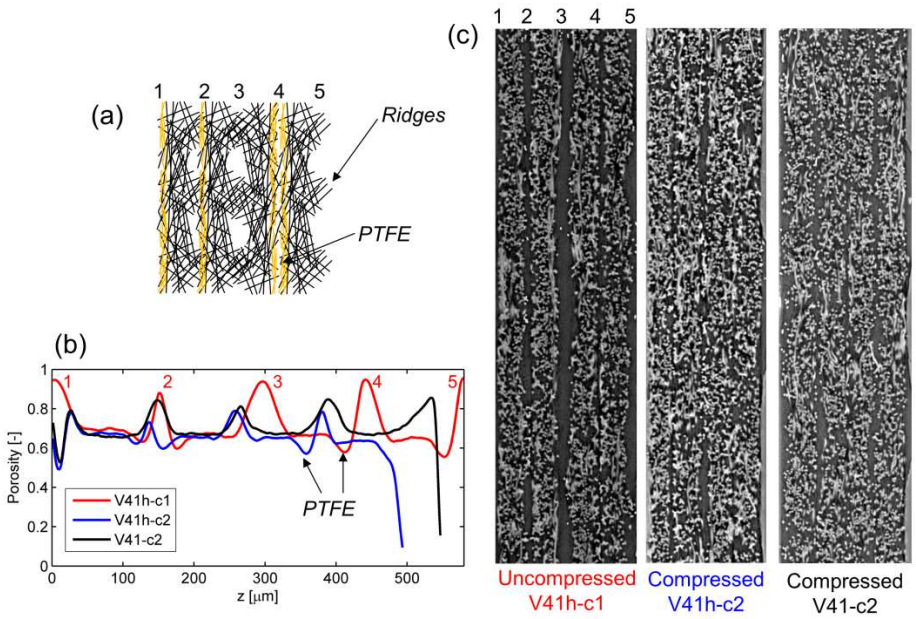

Figure 68. Influence of compression on stacked GDL porosity.

X-ray CT was used to study water distribution under constant applied liquid pressure for 1x vs. 2x X0155 GDLs. Figure 69 shows spatial porosity and saturation distributions at different liquid pressures. At higher pressures (> 2 kPa) water fills the low fiber-density (high porosity) regions, whereas at lower pressures the water front is more uniform. In these experiments hydrophobic plug was used on top of the sample to contain water within the sample. The figure on the right compares liquid-saturation distributions for 1x vs. 2x X0155 GDLs. Higher porosity is observed for two layers because interface was at much higher porosity (0.9). Area-averaged saturation was lower for 2x because of larger volume. We hypothesize that additional interfacial porosity between the two layers allows for water redistribution and improves the overall water-removal capability of these GDLs as compared to single layer GDLs.

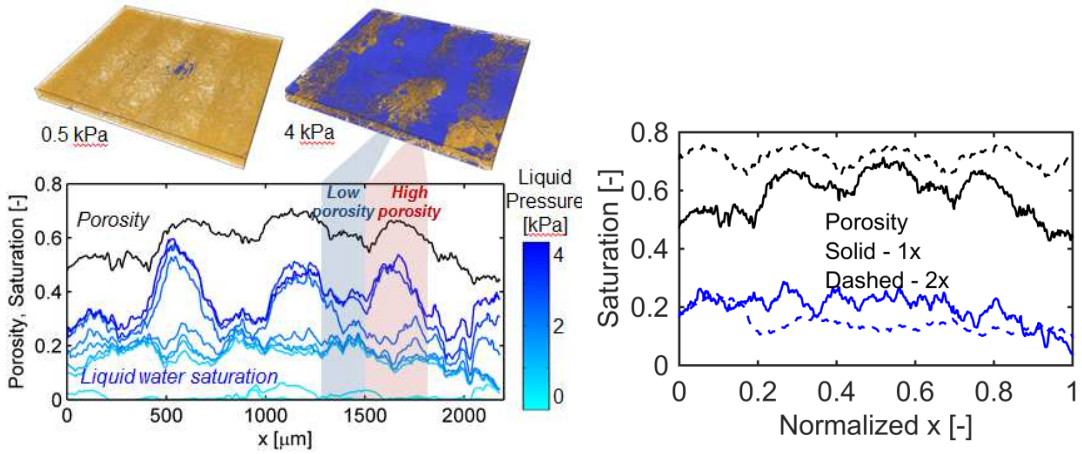

Figure 69. Area-averaged porosity and saturation for 1x X0155 for different liquid pressures. On the right: spatial-distribution of saturation and porosity for PL = 2.5 kPa, where dashed lines show the results for 2x and solid for 1x X0155 GDLs.

GDL pore size distribution analysis from XCT

Traditionally, pore size distributions are determined through porosimetry measurements which analyze the injection pressure vs. injection volume of highly wetting and/or largely non-wetting fluids. The pore size distribution is an important input parameter for GDL models. 3M had data for two of the baseline materials (H2315 and 2979), but not the highest performing baseline MRC MS3BE-040US, or the improved X0155 material used for project downselect. Attempts to obtain porosimetry data for the new GDLs were made through a test house, but results were poor. Few alternative vendors were identified. As such, motivation existed for determining if X-ray CT could be used to generate useful pore size distributions.

LBNL quantified previously-imaged 1x and 2x X0155 GDLs in terms of pore-size distributions (PSDs) using 3D imaged volumes. Figure 70 shows results for 1x X0155 GDL, where plot 'a' shows segmented image and a schematic of fitted spherical kernels. To extract PSD these spherical kernels were fit to the entire GDL domain starting from the largest possible sphere and then radii of these have been tabulated as a histogram. The segmented volume was divided into two sub-volumes (B1-2 and B2-2) to better quantify PSDs' variation through the thickness. In this case, B1-2 was the volume enclosing fiber-density modulations. Figure 69b shows PSDs for full volume, B1-2 and B2-2 subvolumes, where the figure on the left shows the results of subtracting B1-2 and B2-2 from the full volume. B1-2 has many more pores larger than 20 μm compared to the full volume, whereas B2-2 has many more pores smaller than 20 μm. This is more clearly seen in Figure 69c, where B1-2 segment has a large distribution tail, corresponding to larger voids that are due to fiber-density modulation. On the other hand, the B2-2 volume has most of the pores lower than 20 μm because in this region porosity is reduced by PTFE treatment.

Figure 71 shows PSDs for two layers of X0155 (2x X0155). Figure 71a shows that most of the large pores are located at the interface between the two layers in B2-3 domain. This is also confirmed by the PSDs in Figure 71b and Figure 71c, where it is clearly seen a large tail in PSD in region B2-3. The distribution of B2-3 region is similar to that of B1-2 of 1x X-1055, however the major difference is in its location within the GDL. It is believed that this extra region with large pores in the middle of the GDL is responsible for water redistribution from cooler lands to channels.

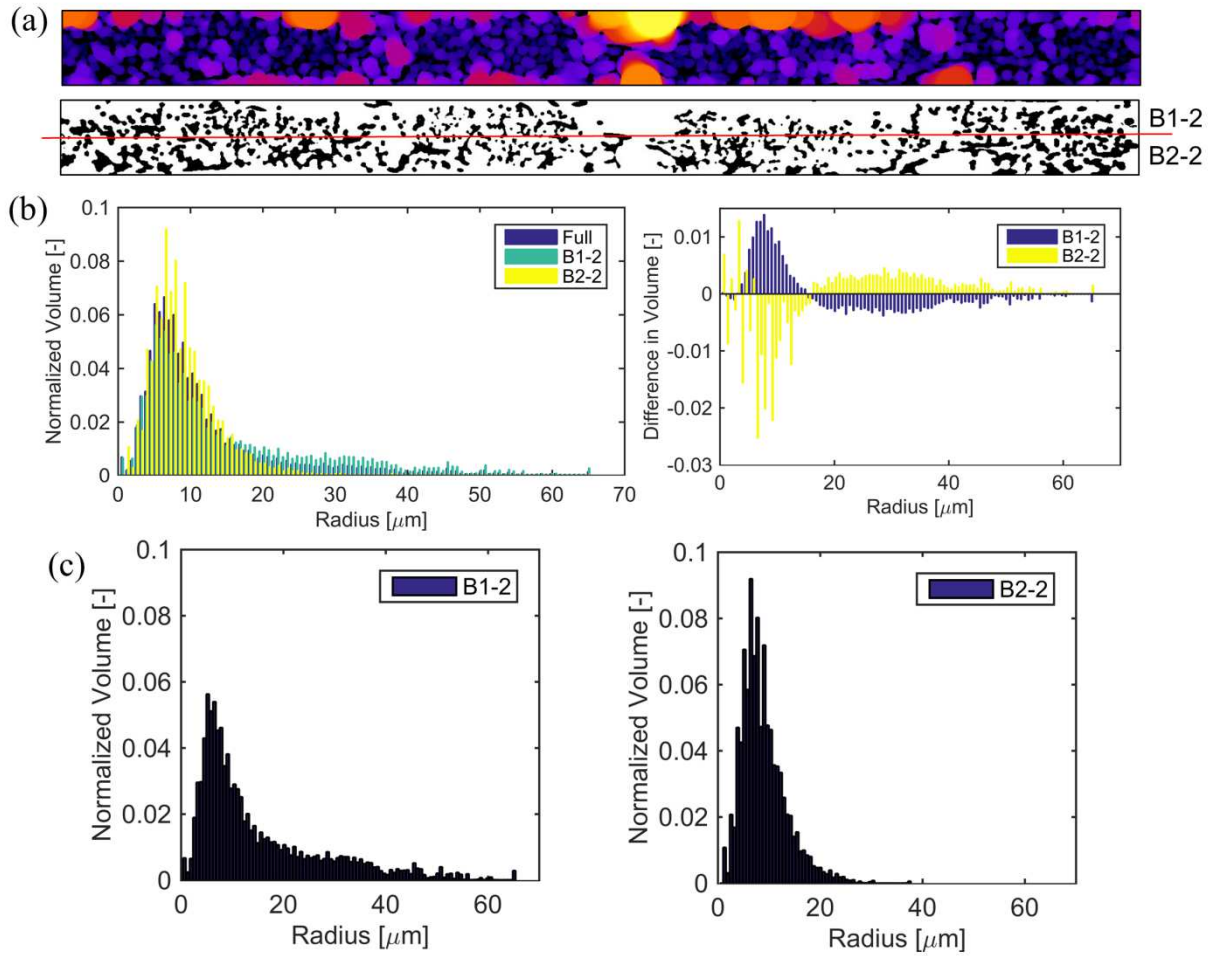

Figure 70. a) A 2D tomograph of dry 1x X0155 GDL and a schematic of fitted spherical kernels, where sub-volumes B1-2 and B2-2 are shown too. b) The PSD of full, and sub-volumes on the right and on the left the difference in PSD between the full and B1-2, B2-2 sub-segments. c) PSDs plotted separately for sub-volumes B1-2 and B2-2.

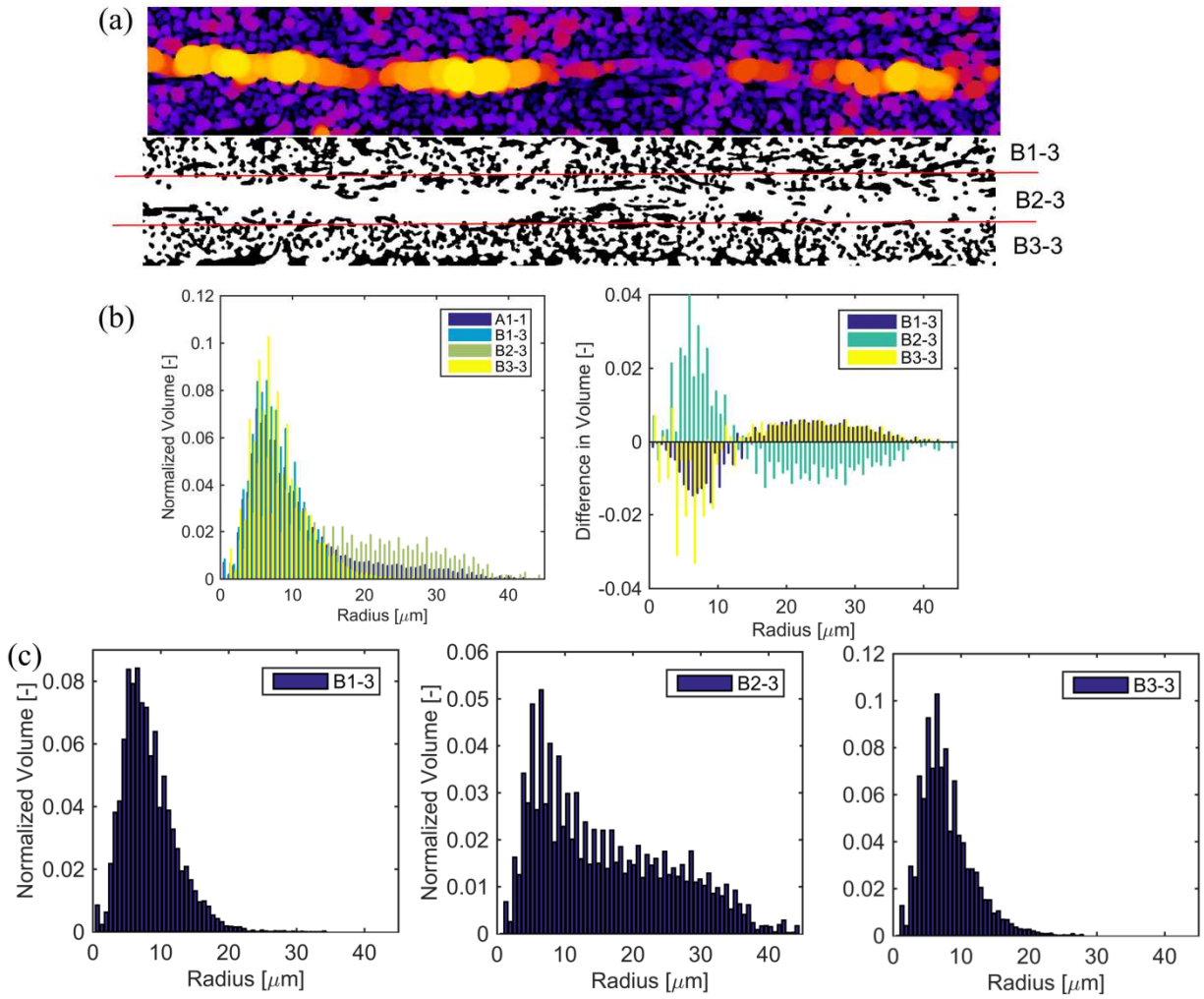

Figure 71 a) A 2D tomograph of dry 2x X0155 GDL and a schematic of fitted spherical kernels, where sub-volumes B1-3, B2-3 and B3-3 are shown too. b) The PSD of full, and sub-volumes on the right and on the left the difference in PSD between the full and B1-3, B2-3, B3-3 sub-segments. c) PSDs plotted separately for the three sub-volumes.

Subtask Conclusions

Analysis of physical structure identified that modulation of in-plane backing fiber density was a key first predictor of low temperature NSTF MEA performance. GDLs with qualitatively larger modulation yielded improved low temperature performance.

New methods of X-ray computed tomography on GDLs were developed and found to be highly insightful into the influences of anode GDL compression, fiber density modulation, and stacked GDLs, all found to be significant influences on MEA performance. A new method for generating pore size distributions from XCT data was also investigated.

Future Directions

Validation of the XCT method for pore size distribution into the MTU-LBNL pore network model (PNM)-continuum models and comparing experimental vs. model predictions of low temperature MEA performance.

Subtask 3.2 GDL Modeling for Cold Start (MTU)

Subtask Overview

Subtask 3.2's objective is incorporation of anode GDLs into the existing MTU GDL network models to generate mechanistic understanding of the specific material properties of the anode GDLs, which have demonstrated such significant improvement on cold start. MTU will develop network models for 3-5 anode GDLs identified by the team and demonstrated significant variation in low temperature response.

Subtask High Level Work Summary

Experimental GDL properties, such as liquid water permeation, thermal conductivity, and pore size distributions were incorporated into a pore network model. The model was enhanced to account for observed experimental factors, such as spatially-varying properties. Model validation occurred by comparing experimental and modeled liquid water percolation.

Subtask Key Results

Modeling Approach and Validation

For each liquid water injection flow rate (proportional to capillary number, Ca), the injection pressure, and wetted area v. time data is reconfigured into scaled energy and time ratios, as shown in Figure 72. C_e is a measure of the input energy dissipated due to viscous stresses and the energy used to generate interfacial area. C_e is larger when higher pressure is required to wet a certain area at a given water injection rate. t^* is a non-dimensional time ratio which demarks the transition from capillary fingering water transport ($t^* > 1$) at low injection flow rates to stable displacement ($t^* < 1$) at high injection flow rates.

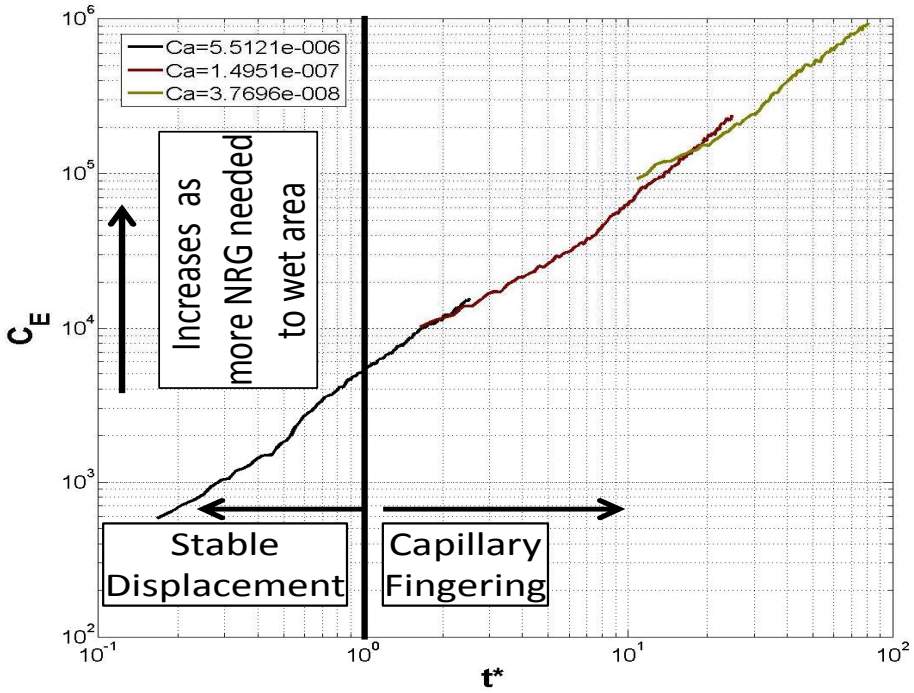

Figure 72. Energy and time scaling of liquid water percolation.

Figure 73 is an energy/time scaling analysis of three project backings. At a given water injection flow rate (proportional to Ca), the energy ratio C_e is higher for the Freudenberg backing with hydrophobic treatment than as received. The treated 2979 backing has a higher energy ratio than

the treated H2315 backing. All three backings transitioned from stable displacement to capillary fingering as Ca decreased from $5.5x10^{-6}$ to $1.5x10^{-7}$.

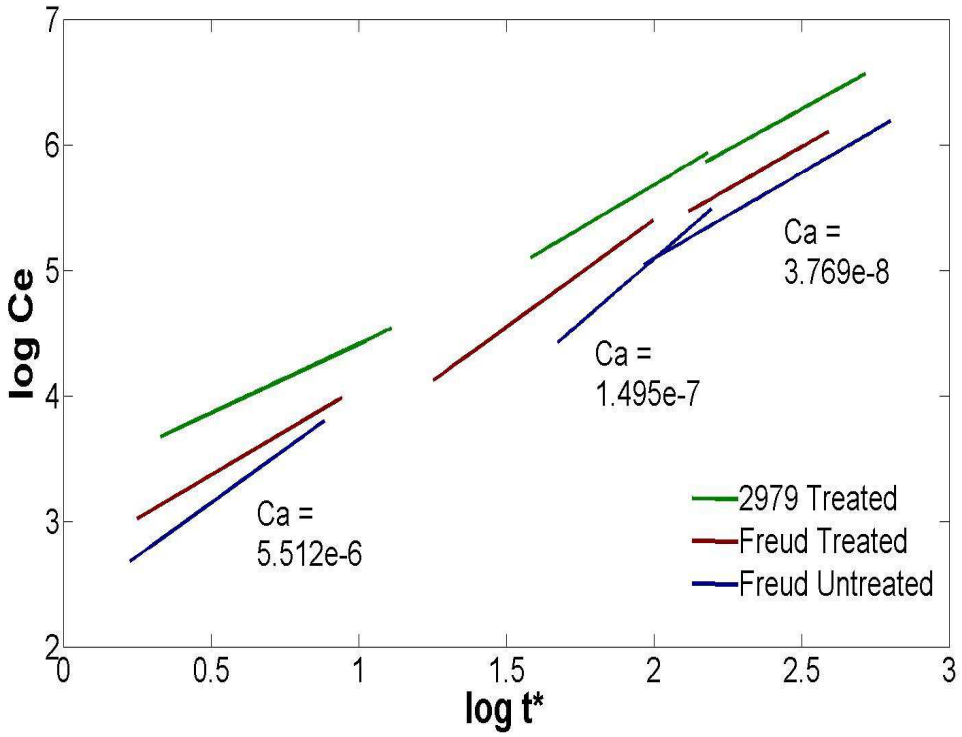

Figure 73. Summary of PTL Percolation Analysis of Subset of Project Anode GDLs

In addition to the scaling analyses, the physical pore size distribution of the anode backing is needed to allow accurate representation in the model. Measured pore size distributions are functionally captured using porosity distribution functions, as shown in Figure 74.

Figure 75 summarizes model vs. experimental liquid water percolation in Freudenberg H2315 GDL at three water injection rates. Excellent agreement was observed over the three orders of magnitude of scaled energy and time. This result served as the Subtask 3.2 model validation.
Continuing the validation effort of the pore network model, a series of two dimensional simulations with no evaporation or condensation were performed using the material properties of the Freudenberg 2315 and the 2979 GDLs. The numerical simulations were performed with boundary and initial conditions found on the percolation tests. The results of the simulations were compared against the experimental data obtained in the percolation tests using the C_e versus t* as shown in Figure 77. A good agreement was obtained between the experiment and simulations for both materials. The slight differences in the Ca for the corresponding numerical and experimental plots are due to the computational limitations on the simulated sample size, which is smaller than the experimental sample size. However, this difference in Ca does not change the slope or the shift of C_e-t* curve for the any of the GDL tested. The computational limitations have been resolved with a new machine. The code is being ported to this machine to run the 2D simulations on similar size domains as found in the experiment.

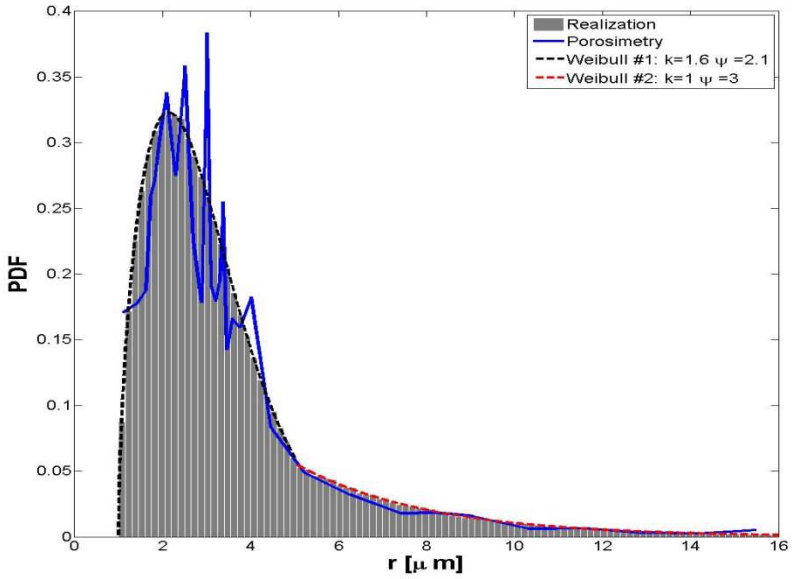

Figure 74. Modeled and experimental pore size distribution of Fruedenberg porous transport layer.

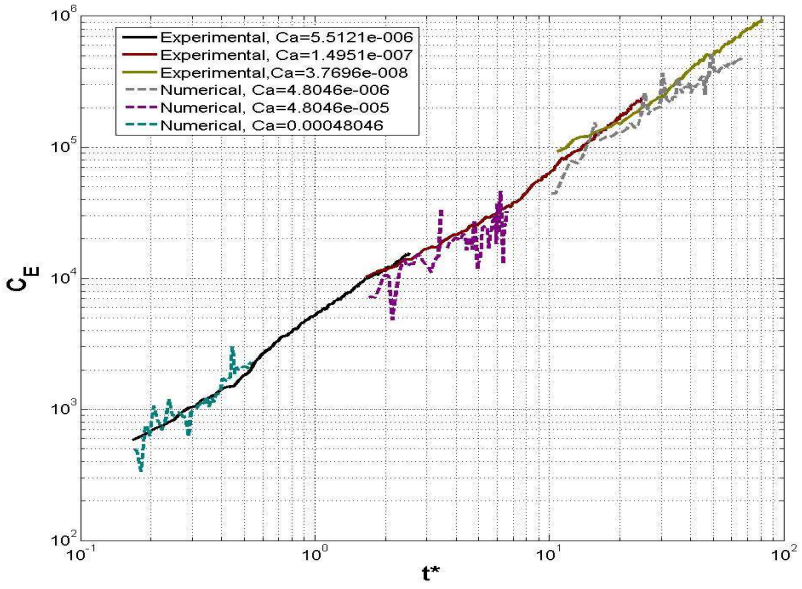

Figure 75. Modeled vs. experimental liquid water wetting dynamics of Freudenberg H2315.

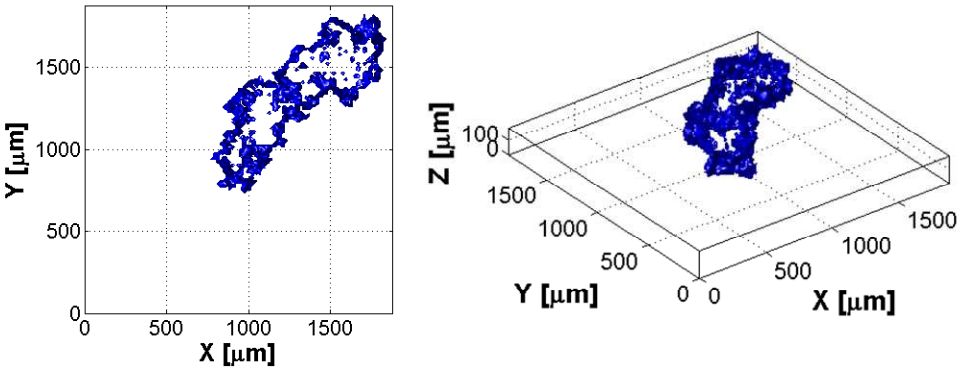

Figure 76. Modeled water distribution in porous transport layer.

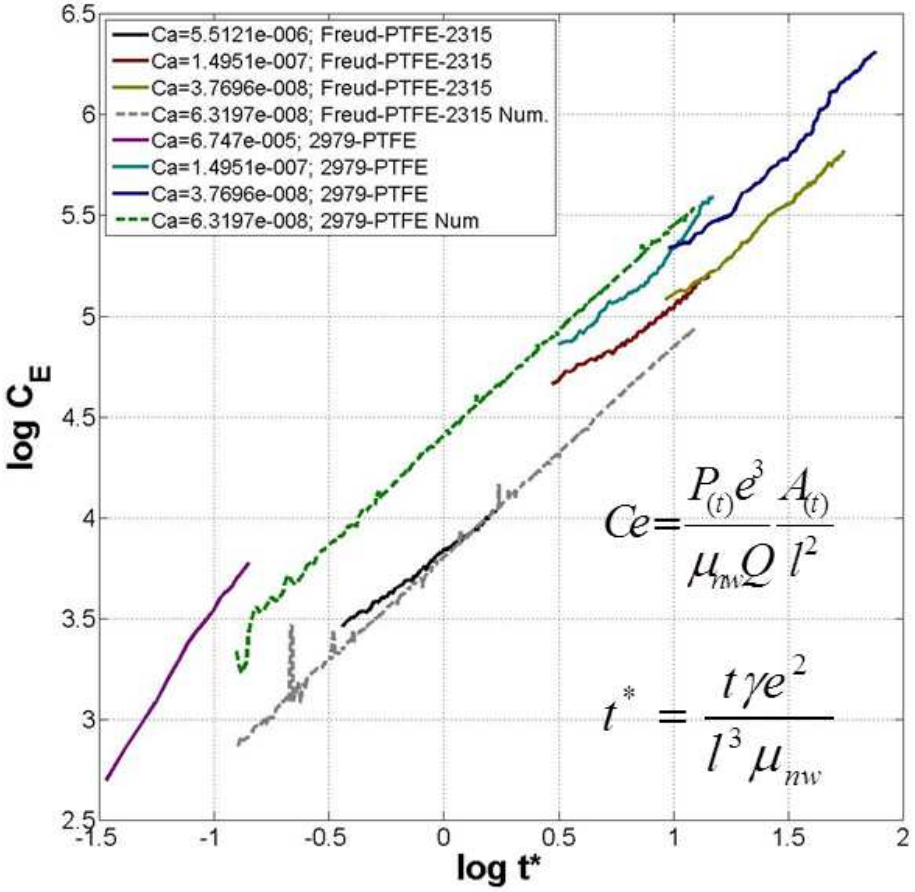

Figure 77.Ce-t* for the experimental measurements (solid lines) and numerical simulations (dashed lines) for a different injection flow rates as represented by the capillary number at the injection point for two different GDL materials.

Model Development – GDL Compression Effects

Experimentally, compression of the anode GDL can have a significant impact on low temperature performance. As compression is increased, the low temperature performance can be quenched, and this depended on GDL type. Two effects are immediately considered—the change in backing permeability under the lands and increased thermal conductivity, both potentially influential on low temperature performance.

In order to capture the effects of compression on the thermal properties of the porous transport layer (PTL), the thermal resistance for a solid-cylinder in the pore-network is modeled as function of material thermal conductivity and the contact resistance. The material thermal conductivity is kept constant and the effects of compression are captured by varying contact resistance as function of compression. The node-to-node thermal resistance of solid-cylinders is modeled as:

$$R_{solid-cyl} = \frac{l_s}{k_s A_s}(1-\chi)^2\left[1+(1-\chi)^m \frac{k_s}{k_c}\right]$$

where l_s, A_s, k_s, k_c, χ and $R_{solid\text{-}cyl}$ represent the length, cross-sectional area, material thermal conductivity, contact resistance, strain and thermal resistance for individual solid cylinder in the network model respectively. '*m*' is a tuning parameter that allows to match the thermal conductivity and values of k_s and k_c are obtained from iterations.

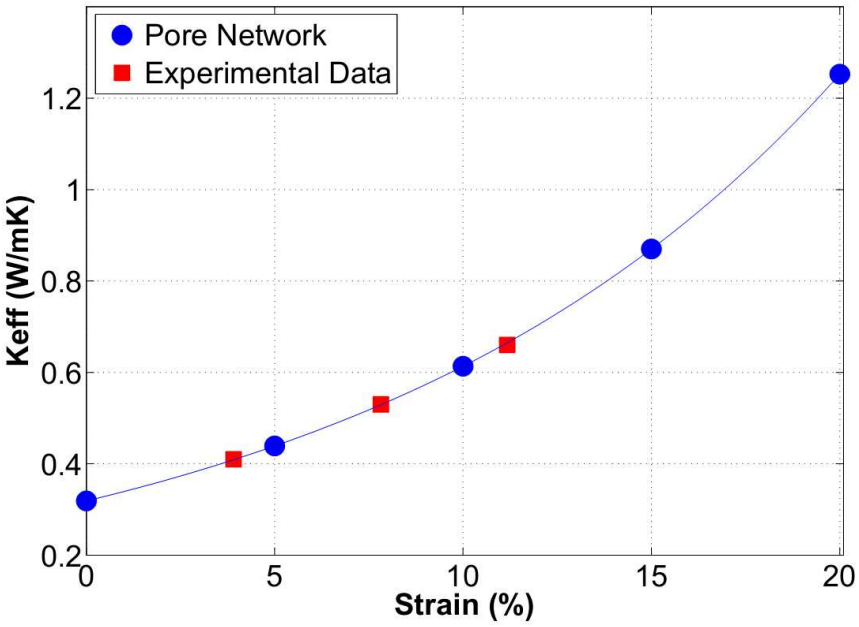

Figure 78. Comparison of Effective Thermal Conductivity of PTL from Pore-Network simulations and experimental data [1] for dry case under different compression.

For the present study, experimentally obtained thermal conductivity under different compressions of Toray-060 reported by Burheim et al. was selected. Pore network simulations were run under dry operating conditions and with varying compressions. A comparison of the effective thermal conductivity from the simulations and the experimental data is shown in Figure

78. The temperature profile inside the PTL under uniform compression is shown in Figure 79 (a-c). These simulations were run under dry operating conditions (i.e. no water) with top surface at 50°C and heat flux corresponding to 1.5A/cm^2 and 50% heat passing through cathode.

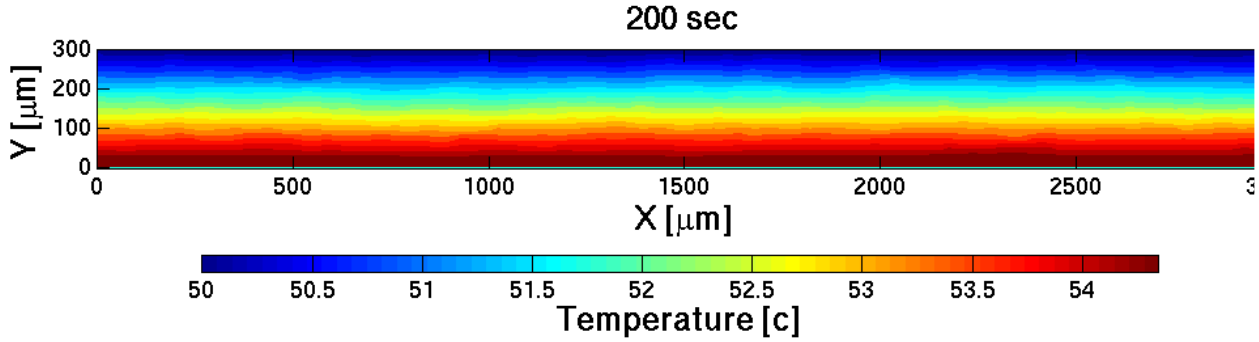

(a)

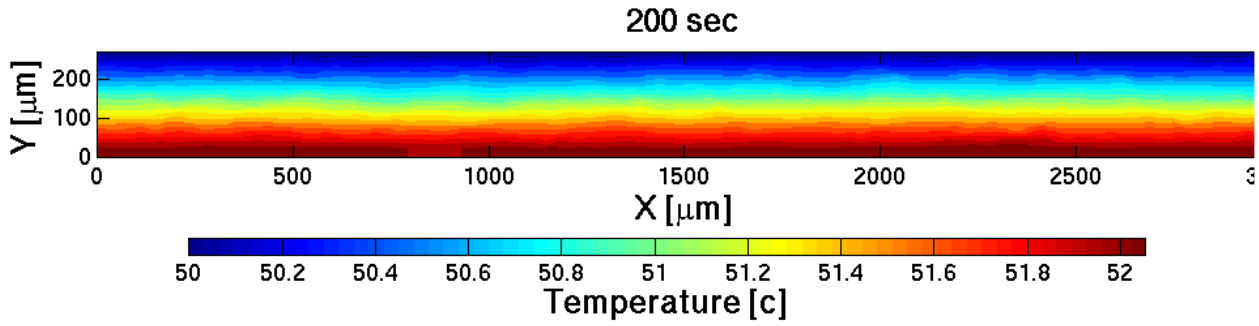

(b)

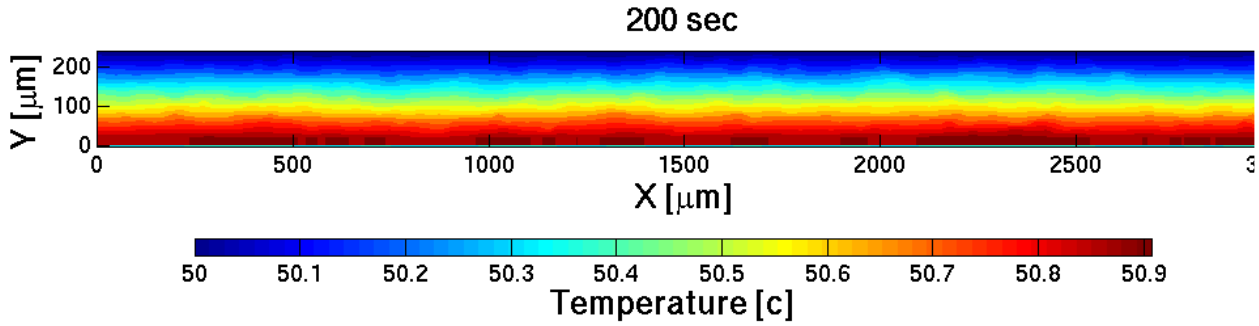

(c)

Figure 79. Temperature profile in PTL under uniform compression. (a) No Compression. (b) 10% Compression. (c) 20% Compression

Figure 80 represents the temperature profile in the PTL under a land-channel configuration with compression under the lands alone. For these simulations, the top boundary of PTL was kept constant at 50°C, heat flux corresponding to 1.5A/cm^2, and 50% heat passing through cathode. A gas-channel is present above the PTL, centered with width of 1.5mm, and lands (0.75mm wide) are present on either side of the channel. Compression was applied under the lands only. A larger

gradient in the temperature profile is visible under the gas-channel where no compression was applied.

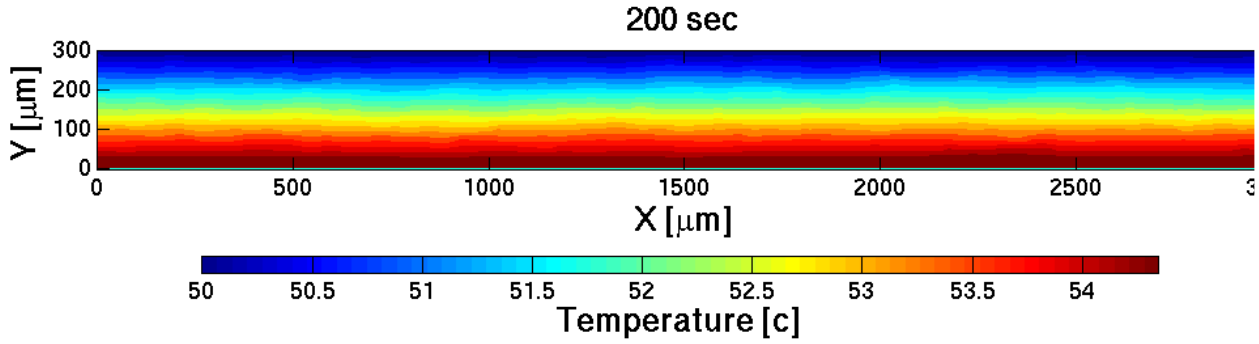

(a)

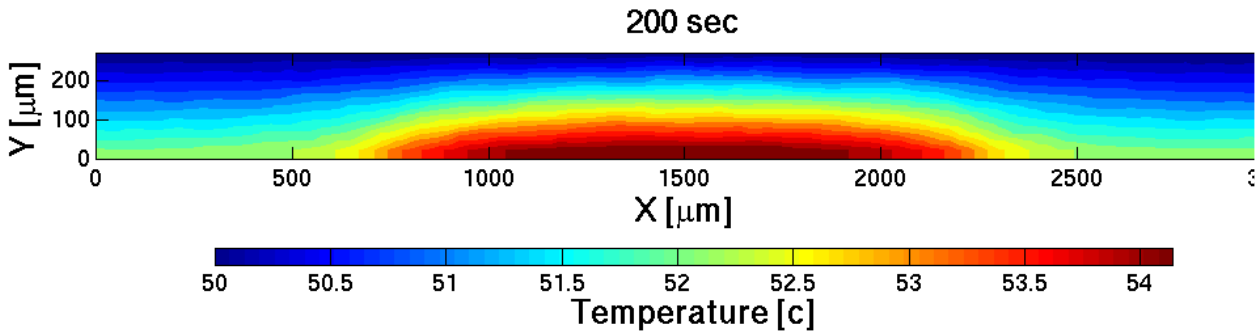

(b)

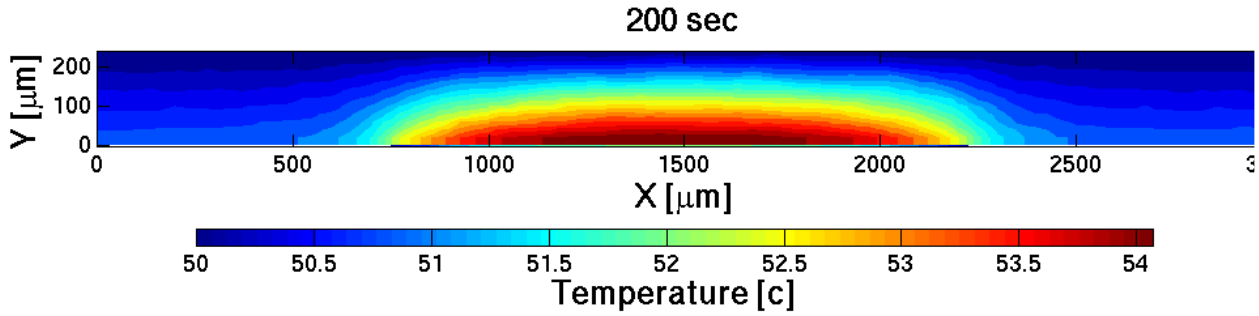

(c)

Figure 80. Temperature profile in PTLs with compression under lands only. (a) No Compression. (b) 10% Compression. (c) 20% Compression

Model Development – Density Modulated Backings

One key insight from Subtask 3.1 was the observed correlation between low temperature performance of the baseline project backings and the observed modulation in backing density. It was postulated that the low density regions may provide a low resistance pathway for liquid water permeation, or may decrease the bulk thermal conductivity of the backing solid phase. MTU conducted limited studies to evaluate how this density modulation may effect mass and heat transfer. A subset of the work is presented below.

For the density modulated GDLs, 3 configurations were selected: (i) Dense-sparse, (ii) Sparse-dense and (iii) Middle. Dense-sparse region corresponds to the dense region (smaller pores and more fibers) of the GDL lying under the land while the sparse region (bigger pores and few fibers) of the GDL lying under the channel. The width of the sparse region is set equal to the width of the channel. For the Sparse-dense region, the high density region lies beneath the channel and the sparse region under the lands. Finally, for the Middle case, one half of the domain is filled with dense region, and the other half with sparse region with the interface between the two regions being at the center of the channel. These configurations along with the distribution of water at the end of simulations are shown in Figure 81.

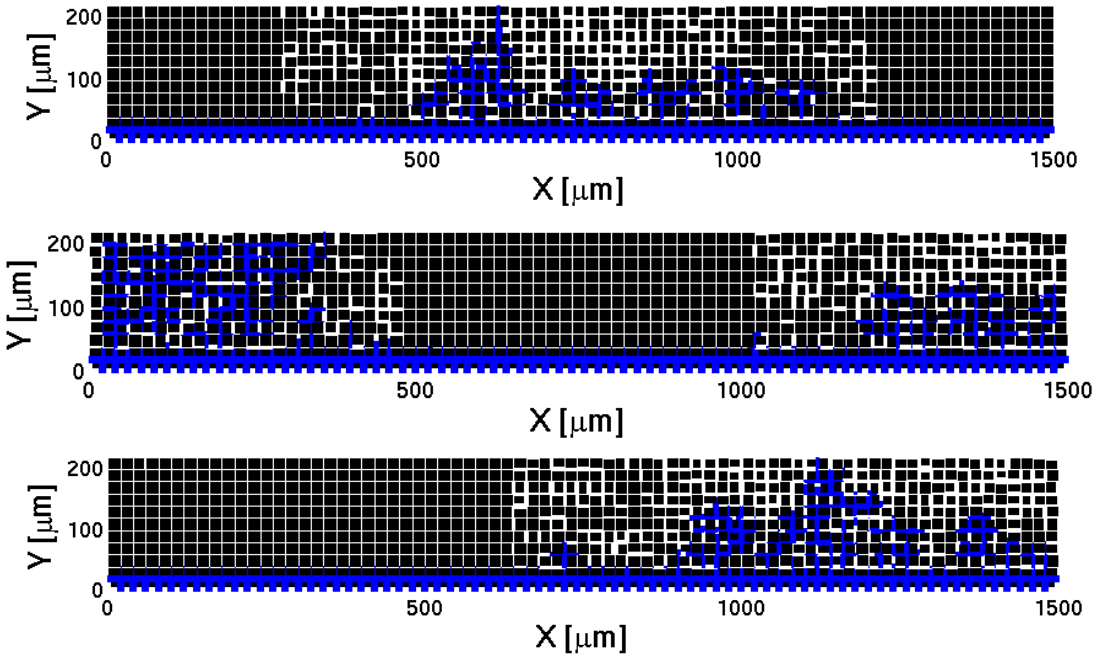

Figure 81. Distribution of water in GDLs at the end of simulations for 3 configurations of Density modulated GDL. (Top) Dense Sparse, (Center) Sparse Dense and (Bottom) Middle Configuration. Operating Conditions: 30°C, 60%RH, 1.5A/cm^2.

Anode GDL Permeability Modeling

The primary hypothesis entering the project was that the anode GDL was influencing net liquid water transport in the MEA, decreasing cathode flooding and thereby increasing performance. The key property of the anode GDLs, which enabled higher low temperature performance, was its propensity for drawing product water from the cathode electrode out to the anode flow field.
It was hypothesized that the anode GDL could also influence MEA performance in a more direct manner; if the anode GDL became significantly water saturated, H_2 transport to the anode electrode could limit overall performance.

Using water distribution realizations calculated from the PNM, a 2nd model was developed to calculate relative gas permeability as a function of operating conditions and model run time. The top of Figure 82 shows a typical liquid water distribution within a PTL. These liquid saturated regions were considered essentially impermeable to air.

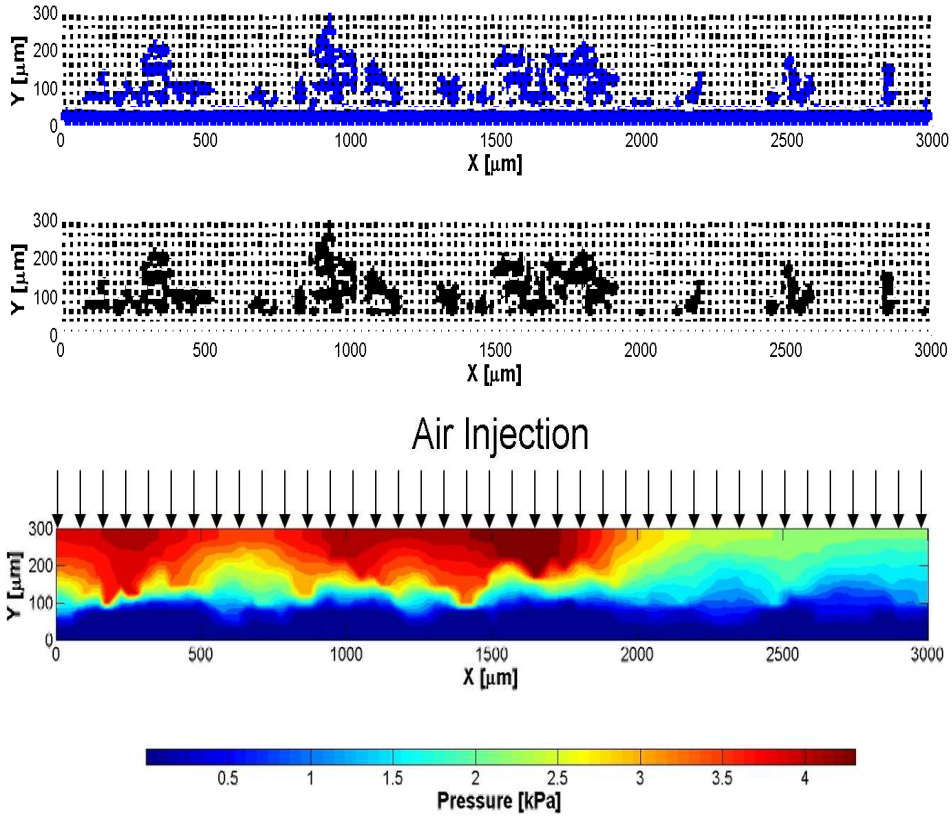

Figure 82. Gas permeation model development

Figure 83 shows the resultant permeabilities for three project anode GDLs. The gas permeability increased as the anode GDL was changed from MRC U105 to H2315 to a "dense-sparse" realization meant to simulate MRC MS3BE-040US. This permeability trended monotonically with low temperature performance (not shown).

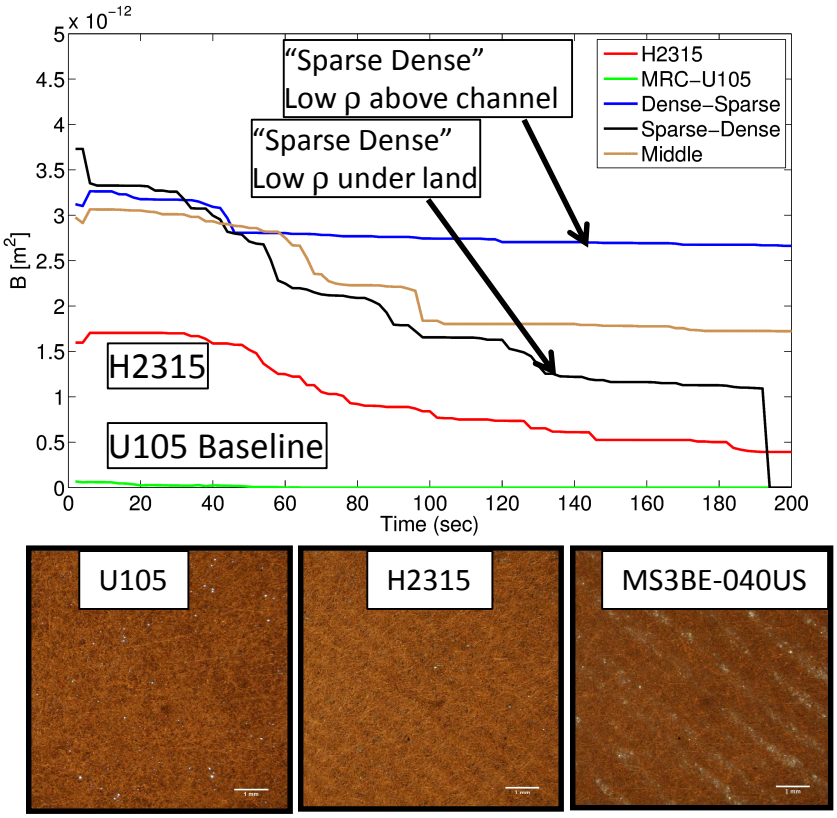

Figure 83. Modeled permeability of three anode backings, including those with density modulation.

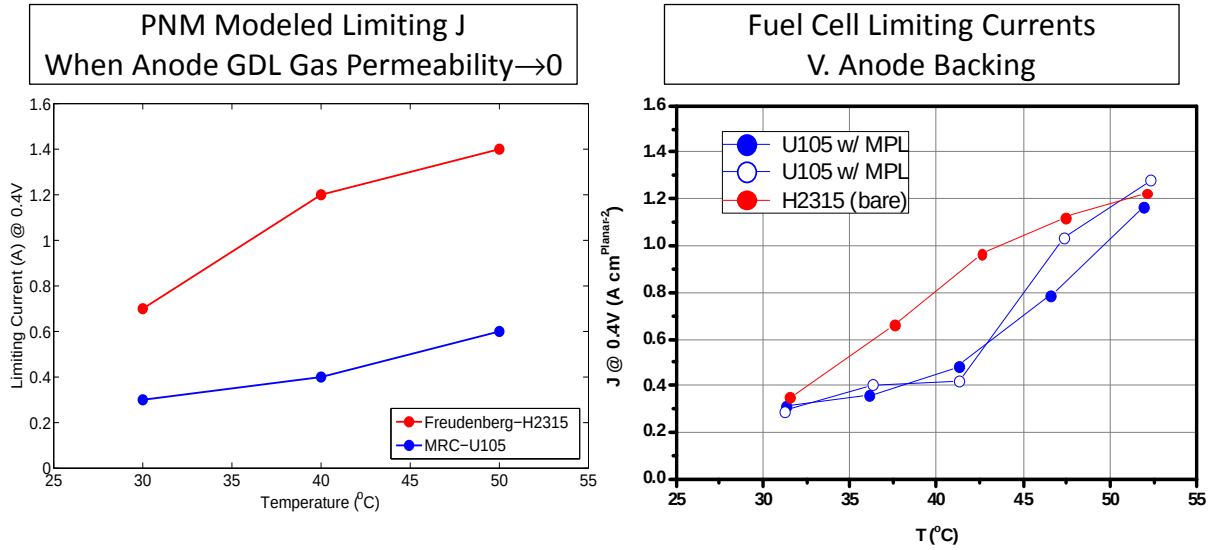

Figure 84. Simulated (left) and experimental (right) limiting current densities vs. anode GDL type.

Using the gas permeability model, MTU analyzed the maximum current density achievable at a given cell temperature where the anode backing gas permeability remained above 0. The model does not incorporate *cathode electrode* flooding, where transport loss occurs. Results were consistent *in trend* with measured fuel cell (FC) response and higher measured limiting anode water removal rates.

Subtask Conclusions

The pore network modeling approach was effective at capturing the mass and thermal transport within the anode GDL. Model development included incorporation of density modulated backing and the impact of GDL compression by flow field lands. Three project anode GDLs were modeled, and effective properties for reactant permeability and thermal conductivity were generated.

Future Directions

MTU has expressed interest in porting the PNM model to open-source modeling systems such as OpenFOAM for improved portability and ability for dissemination.

Subtask 3.3 MEA Modeling for Cold Start (LBNL)

Subtask Overview

Subtask 3.3's objective is incorporation of MEA material properties into the existing LBNL PEMFC model. This is for the express goal of determining the primary causal factors responsible for the wide variation in cold start response with differing anode GDLs from an overall MEA perspective, including thermal and water transport. It is expected that LBNL will incorporate 3-5 MEA component sets into the model.

Subtask High Level Work Summary

Limited MEA modeling trials were conducted with baseline NSTF MEAs.

Subtask Key Results

Coincident with this project, work was being conducted under LBNL's "Fuel Cell Fundamentals at Low and Subzero Temperatures" project. Results from that project indicated that the existing LBNL model captured several already observed trends with NSTF MEAs with baseline anode and cathode GDLs.

Figure 85 (left) compares LBNL model predictions for temperature sensitivity to experimental results with baseline NSTF MEAs. The model agreed quantitatively with experiment. Figure 85 (right) shows model predictions for H_2/air polarization curves and cathode saturation at either 24 or 40°C cell temperature. The model predicts that the limiting current is reached when the cathode saturation reaches approximately 80%.

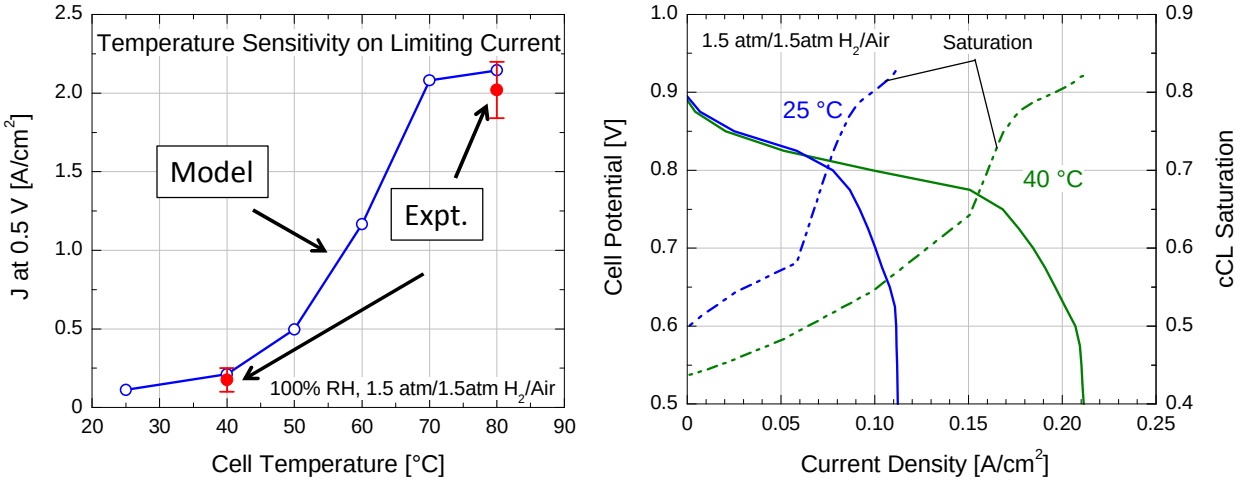

Figure 85. (Left): Comparison of modeled vs. experimental limiting current densities. (Right): Modeled polarization curves at cathode saturation levels at 25 and 40°C cell temperature.

Figure 86 shows modeled H_2/Air polarization curves, where the impacts of anode pressure and the presence of an anode microporous layer (MPL) were explored. Models were conducted with the cell temperature at 40°C and the cathode pressure was 1.5atmA. Figure 86 (left) shows that with 1.0 atmA anode pressure, presence of MPL greatly reduces the limiting current from in excess of 2A/cm^2 to less than 1A/cm^2. Figure 86 (right) shows that as the limiting current density decreases from 2.0 to less than 0.2A/cm^2, the anode pressure is increased from 1.5 to 1.6atmA just above the cathode pressure. The model captured the experimental observations in trend.

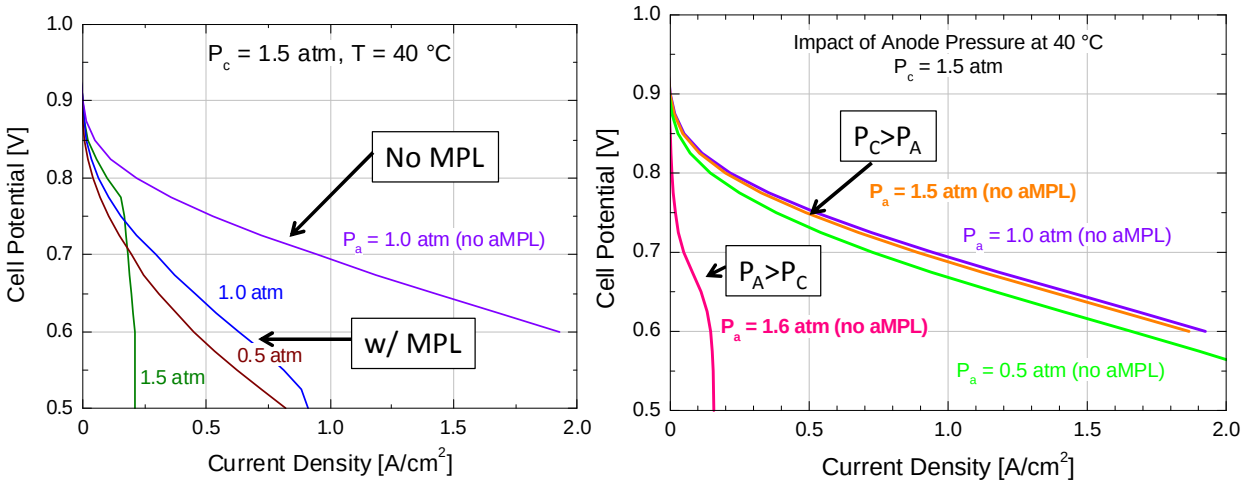

Figure 86. Modeled impacts of anode pressure on H_2/Air polarization curves at 40°C cell temperature.

Due to the reasonable predictive capability of the existing LBNL MEA model, further work was largely postponed until specific project anode GDL properties were available from Subtask 3.2. Project resources were directed towards characterization of project anode GDLs in Subtask 3.1.

Subtask Conclusions

The LBNL model was found to be reasonably predictive of experimental baseline NSTF MEA temperature sensitivity and the impact of anode reactant pressure and anode microporous layers.

Future Directions

The LBNL model was integrated with the MTU pore network model in Subtask 3.4.

Subtask 3.4 GDL, MEA Model Integration (LBNL, MTU)

Subtask Overview

Due to the computational demands of the MTU pore network model and the LBNL continuum models, they cannot be directly integrated within the same computational cluster, and as such, some work is needed to integrate results between the GDL and MEA level models; subtask 3.4 involves iterated runs of the respective models with results from one fed into the other until the models are well integrated for each component set.

Subtask High Level Work Summary

A method was developed for model integration.

Subtask Key Results

Early in the project, the largest perceived Task 3 challenge was coupling of the LBNL continuum model to the MTU pore network model. For water transport in the continuum model, the anode and cathode GDLs are assumed to have effective liquid water permeabilities and effective vapor diffusion coefficients. In the pore network model, liquid flow is modeled via the Poiseuille equation and vapor transport by concentration dispersion. Additionally, significant variation in transport properties within the plane of the GDLs is predicted with the PNM due to the modeling of liquid water percolation, as indicated in Figure 87. The initial plan was for MTU to modify the PNM to generate spatially and temporally variant effective liquid water permeability and vapor diffusion coefficients, provided as lookup tables. LBNL would modify the continuum model to utilize the PNM-predicted effective properties.

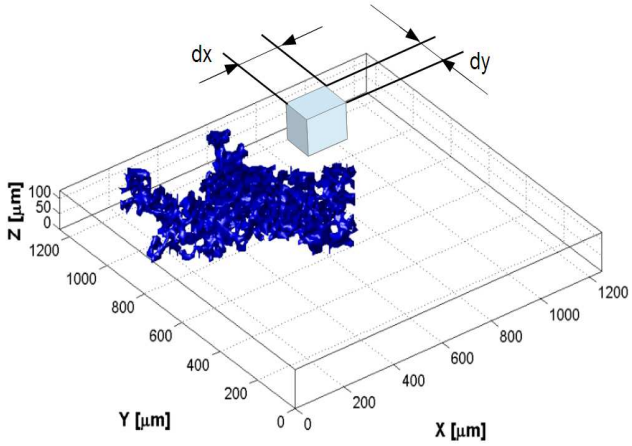

Figure 87. PNM modeled domain.

As the project progressed, three different coupling mechanisms were evaluated. One was downselected and is shown in the Figure 88 (left), and the coupling algorithm is shown in Figure 88 (right). An initial set of cell operating conditions and material properties are input to the continuum and pore network models. The continuum model generates an initial set of heat and mass fluxes based on the conditions, which are fed to the pore network model. The pore network model simulates the water distribution within the anode and cathode backings, from which spatially dependent effective parameters are determined. The parameters are the reactant species diffusivity and concentration, the backing thermal conductivity, and the liquid permeability.

These updated effective parameters are then fed back to the continuum model, and the process iterates until convergence is reached.

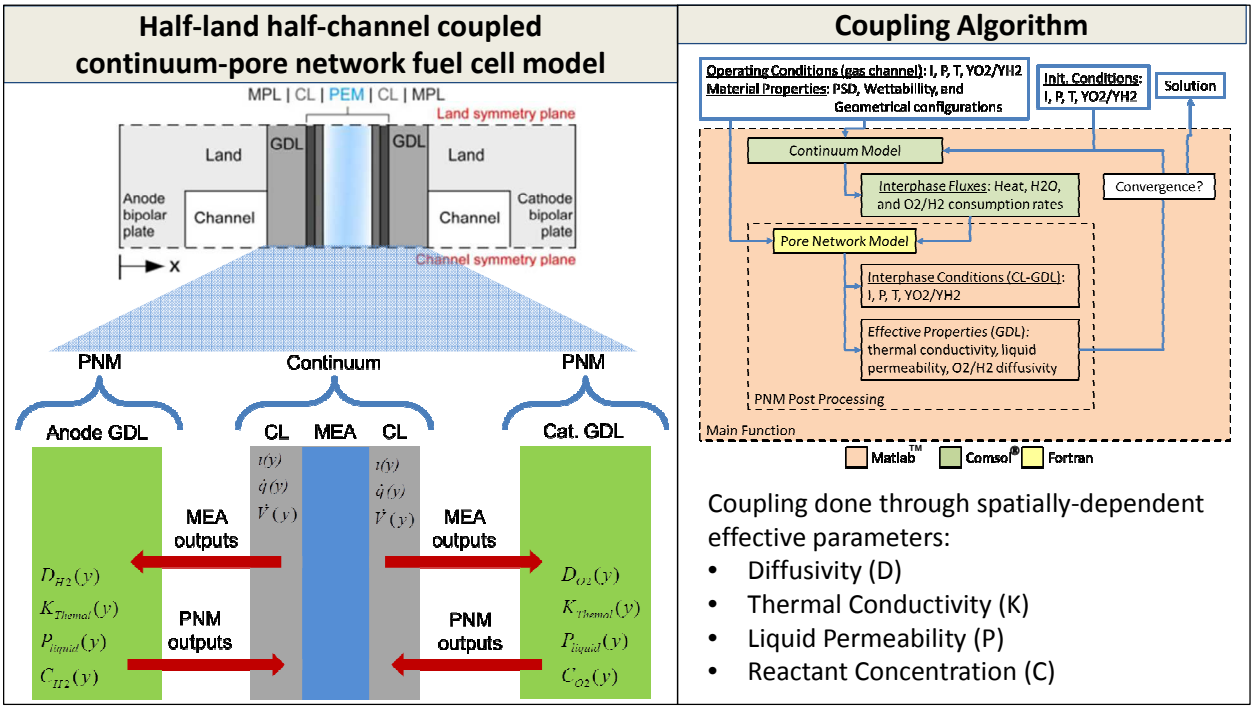

Figure 88. Downselected model coupling method

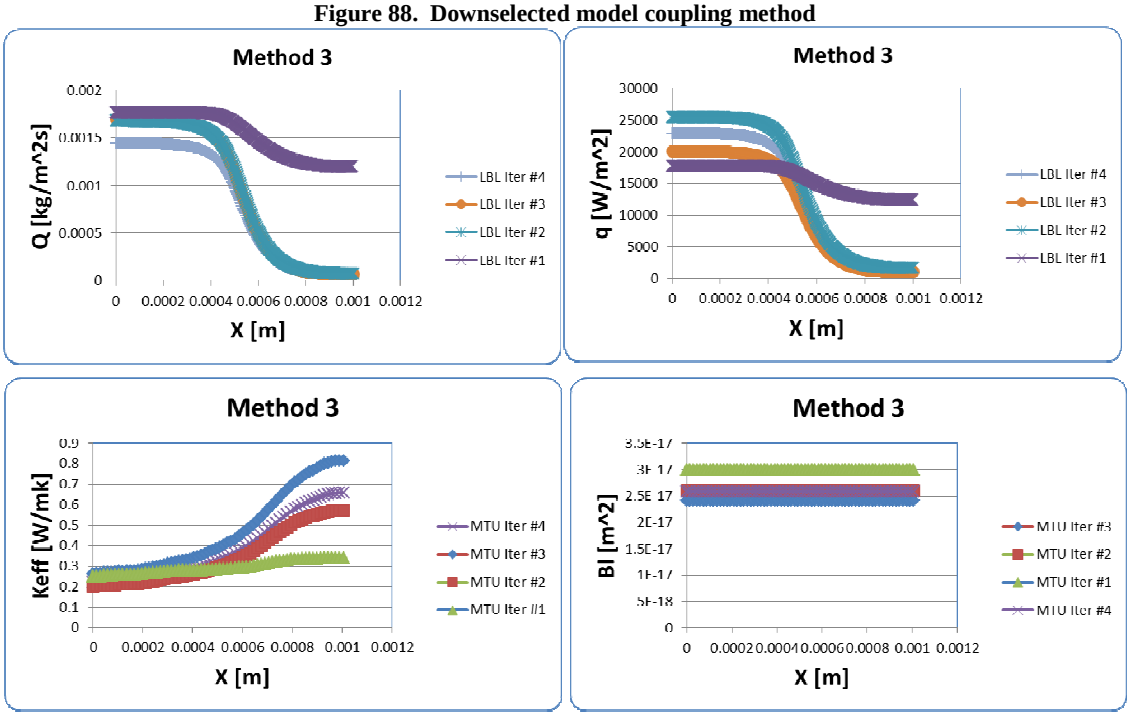

Figure 89. Model convergence method development. (Upper left): Convergence of mass flux. (Upper right): Convergence of heat flux. (Bottom left): Convergence of effective heat conductivity. (Bottom right): Convergence of gas permeability.

In initial model integration, the iterations between the continuum and PNL models were done manually, as shown in Figure 89. Once the approach was found satisfactory, code was generated to automatically iterate until overall model convergence was reached.

An in-depth analysis of the model integration activity is published by Zenyuk et al. in "Coupling continuum and pore-network models for polymer-electrolyte fuel cells", *Int. J. Hydrogen Energy* **40** (2015) 16831-16845.

Subtask Conclusions

A method was developed for coupling the MTU pore network model of gas diffusion layers to the LBNL MEA continuum model. The preferred method was through the use of effective thermal conductivities and diffusion coefficients, generated by the PNM model, which were then integrated into the continuum model via lookup tables.

Future Directions

None anticipated at this time.

Subtask 3.5 Model Validation

Subtask Overview

Subtask 3.5 consists of periodic fuel cell evaluations to validate model predictions and provide feedback for further model optimization.

Subtask High Level Work Summary

The integration PNM and continuum model evaluated H_2/Air performance sensitivity of NSTF MEAs with two anode GDLs, and results were compared with experiment. The model was considered validated.

Subtask Key Results

The primary activity of Subtask 3.5 was running the combined MTU-LBNL models for H_2/Air performance sensitivity to temperature with two of the project baseline materials, 3M 2979 and GDLs comprising Freudenberg H2315.

Figure 90 shows currents as a function of temperature for 2979 and H2315 as predicted by experiment (closed symbols) and model (open symbols). The model shows good agreement with experimental data. The model predicts higher currents for H2315 compared to 2979 due to less flooding in GDLs.

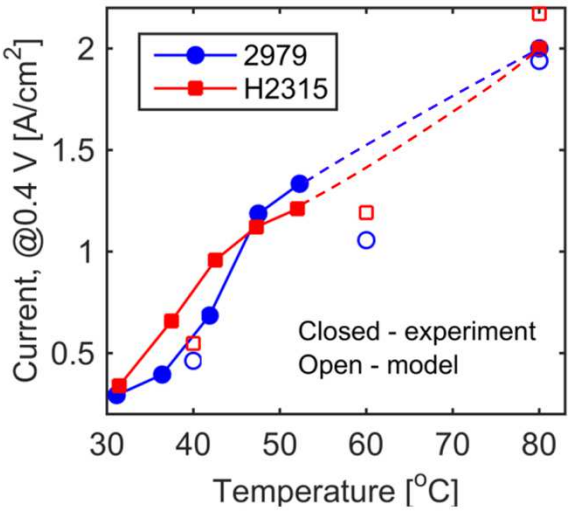

Figure 90. Current generated at V = 0.4 V, for RH =100/100 P = 150 kPa/100 kPa as a function of temperature for anode 2979 and H2315. The filled symbols show experimental data, whereas the open symbols show model predictions.

Figure 91a shows polarization curves for temperatures 40, 60 and 80°C for 2979 and H2315. H2315 shows higher currents for most of the testing conditions. To further understand the severe temperature dependence observed by both modeling and experimental results the liquid-water profiles generated by PNM were plotted as seen by Figure 91b. Liquid water front forms at CL|GDL interface and is advanced to about 50% of GDL thickness at 40°C, to 30% of its thickness at 60°C, and the front is limited to about 10% of thickness at 80°C. With increase in temperature, evaporation becomes the major transport mechanism for water removal from the CL.

PNM also predicts effective transport properties for the temperatures studied. Figure 92a shows increase in oxygen diffusivity with temperature and current; this is mainly due to decrease in liquid-water saturation. Liquid permeability increases on the cathode side for higher temperatures because in the way PNM computes it—it is inversely proportional to the width of the liquid-water front as shown by Figure 92b. Thermal conductivity on anode shows more complex behavior due to phenomena of phase-change induced flow and shows a decreasing trend with increasing temperature as Figure 92c shows.

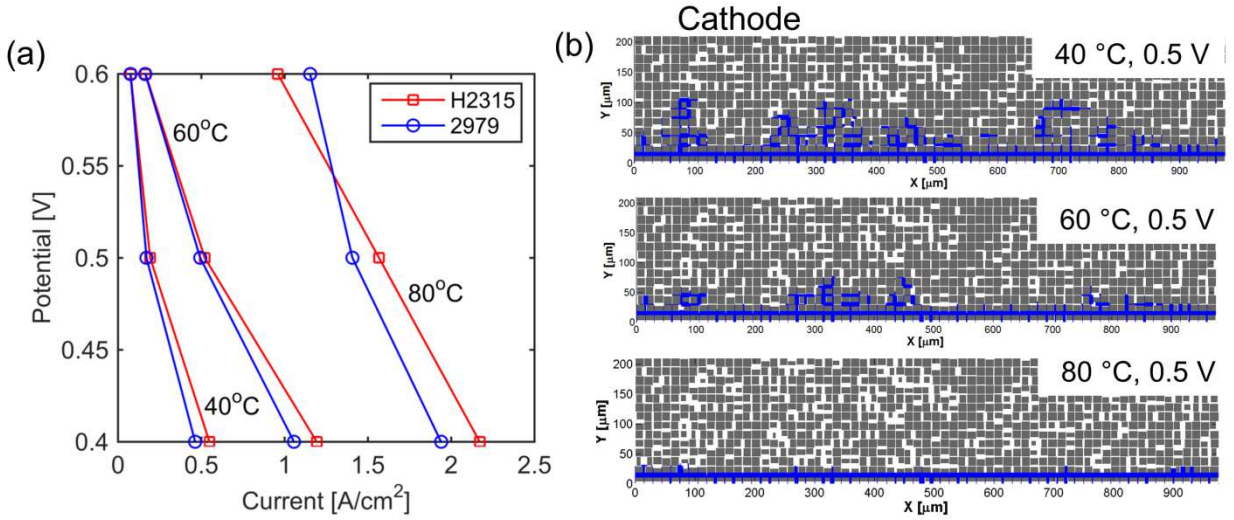

Figure 91 a) Polarization curves for 2979 and H2315 at temperatures 40, 60 and 80C. b) Corresponding water distribution in cathode gas-diffusion layer at V = 0.5 V and temperatures 40, 60 and 80C.

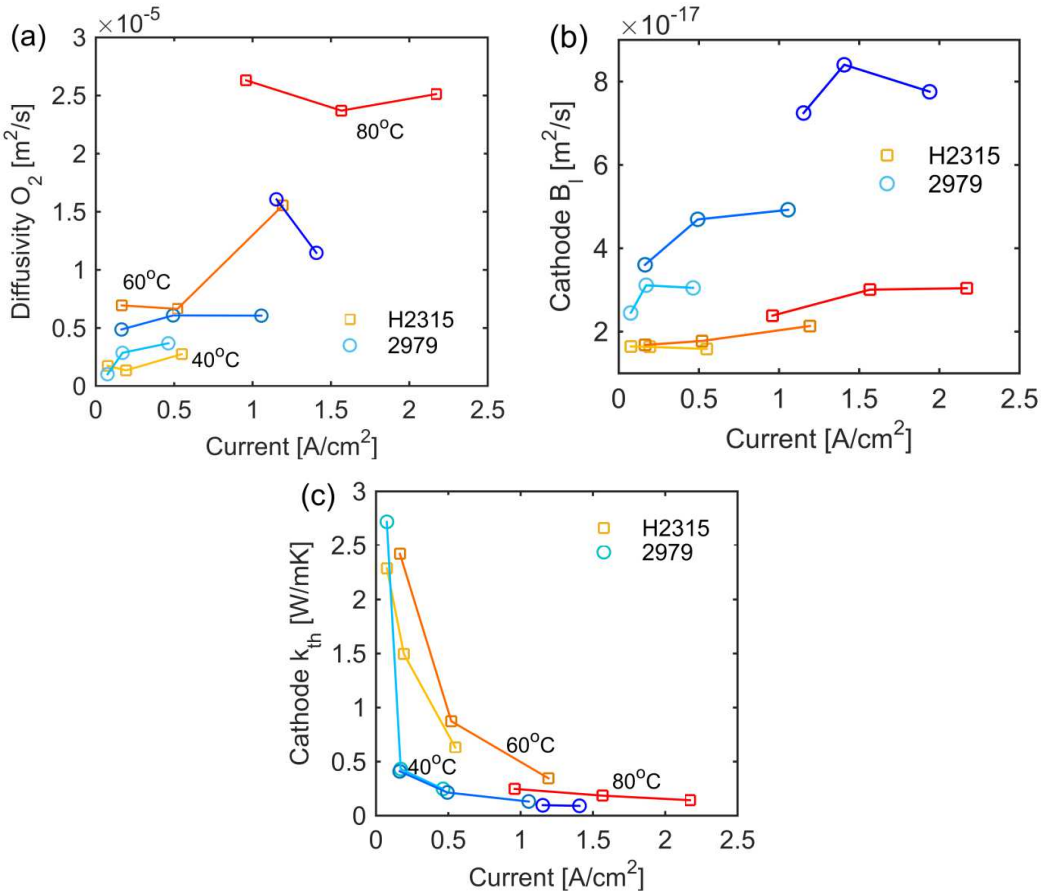

Figure 92. a) Oxygen diffusivity b) cathode liquid permeability and c) cathode thermal conductivity as functions of current for 2979 and H2315 for temperatures 40, 60, and 80C.

Figure 93 (left) shows modeled H_2/Air pol curves at 40 or 60°C cell temperature for MEAs with two different anode GDLs. As expected, performance increases with the temperature increase, and the modeled Freudenberg H2315 anode GDL, shown in red, has higher performance than 2979. Figure 93 compares modeled data at 40 and 60°C to experimental MEA temperature sensitivity measurements. At this point, the model current density predictions are within about 10 percent of experiment. Figure 94 shows the model determined anode hydrogen diffusivity and the cathode thermal conductivity. The higher-performing H2315 anode GDL has significantly higher H_2 diffusivity, due to lower water content, caused by the spatial variation in backing density.

With these results, the integrated model was considered validated.

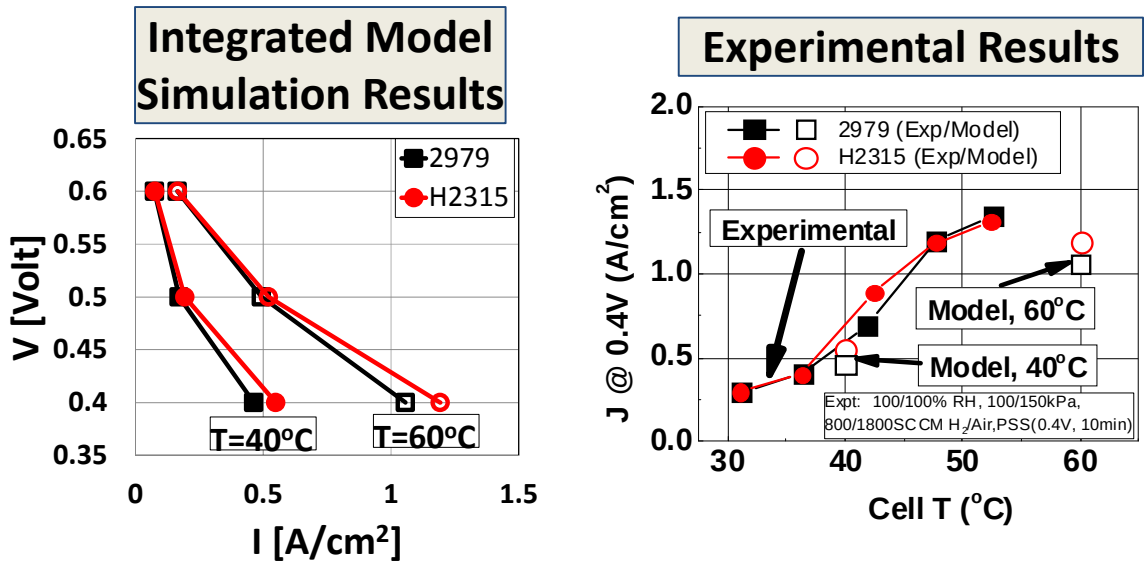

Figure 93. Model and experimental temperature sensitivity of NSTF MEAs with either 2979 or H2315 GDLs.

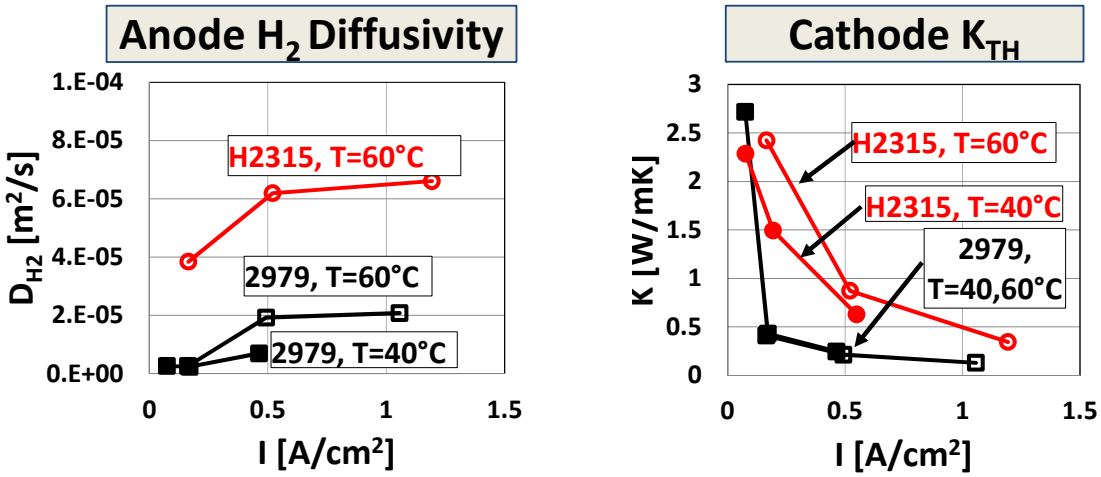

Figure 94. Model predicted anode H_2 diffusivity and cathode thermal conductivity.

Subtask Conclusions

The integrated PNM GDL and continuum MEA models yielded predictions of the H_2/Air performance variation of NSTF MEAs with one of two anode GDL types which were consistent with experiment. The GDL with density modulation yielded improved performance over the homogenous GDL, due to its ability to maintain higher cathode GDL oxygen permeability and anode GDL H_2 permeability, due in part to decreased liquid water resistance.

Future Directions

The validated integrated model should be used to evaluate the project downselect GDL, "X3" shown to be improved over the baseline GDLs identified at the beginning of the project. This work was not conducted within the project timeframe due to the lengthy characterization needed for percolation studies and pore size distribution analysis and the priority on refining the MTU model to establish predictive capability with two-phase flow.

Additionally, trials should be run with controlled variations in anode GDL properties, believed to be implementable physically, which would yield further improved low temperature performance. This would also provide further validation to the model.

Task 4. Best of Class MEA Integration Activities

- *Subtask 4.1 Best of Class Component Integration*
- *Subtask 4.2 Component Interaction Diagnostic Studies*

The overall objective of Task 4 is development of an overall Best of Class MEA, utilizing top component candidates identified in subtasks 1.1-1.5, 2.1, 2.2, 5.1, and 5.5, and to develop improved mechanistic understanding of component interactions which cause performance change.

Subtask 4.1 Best of Class Component Integration

Subtask Overview

In subtask 4.1, components will be integrated into a series of experiments to identify synergistically beneficial interactions, if any, between particular component sets, leading to identification of a few top performing MEA candidates with improved performance, durability, and cold start capabilities; evaluation will consist primarily of 50cm^2 single cell tests.

Subtask High Level Work Summary

The performance of several project interim and the final project best of class (BOC) MEA was evaluated. Operational robustness, break-in conditioning, and durability was assessed with the final project BOC MEA.

Subtask Key Results

On an annual or semi-annual basis, best status components for activity, durability, operational robustness, and pilot-scale manufacturability from Tasks 1, 2 and 5 were integrated into MEAs and evaluated. Upon evaluation, best of class MEAs representing current project and technology status were selected. Table 13 summarizes the evolution of components integrated into the seven project BOC MEAs. PGM contents were determined by calibrated X-ray Fluorescence. All components for the final project BOC MEA, 2015(Sept.), were fabricated on laboratory or pilot-scale continuous roll-to-roll equipment.

Table 13. **Project Best of Class MEAs. Primary evolutionary changes denoted in BOLD.**							
MEA	**Anode Electrode**	**Cathode Electrode**	**Anode GDL**	**Cathode GDL**	**PEM**	**Total PGM (mg/cm^2)**	**Flow Field**
2012 (Mar.) BOC Pre-Project	Pt/NSTF, $0.03mg_{PGM}/cm^2$	Pt_3Ni_7/NSTF, 3MDealloy+SET, $0.121mg_{PGM}/cm^2$	3M 2979	3M 2979	3M 825EW 24µ	**0.151**	QS
2012 (Sept.) BOC	Pt/NSTF, $0.03mg_{PGM}/cm^2$	**Pt_3Ni_7/NSTF, 3MDealloy+SET, $0.117mg_{PGM}/cm^2$**	3M 2979	3M 2979	3M 825EW 24µ	0.147	FF2
2013(March) BOC	**PtCoMn/NSTF, $0.02mg_{PGM}/cm^2$**	Pt_3Ni_7/NSTF, 3MDealloy+SET, $0.117mg_{PGM}/cm^2$	3M 2979	3M 2979	3M 825EW 24µ	0.137	FF2
2013(Dec.) BOC	PtCoMn/NSTF, $0.02mg_{PGM}/cm^2$	**Pt_3Ni_7/NSTF, 3MDealloy+SET, $0.109mg_{PGM}/cm^2$**	3M 2979	3M 2979	**3M 825EW 20µ**	0.129	FF2
2014(Mar.) BOC	PtCoMn/NSTF, $0.019mg_{PGM}/cm^2$	**Pt_3Ni_7/NSTF, JHUDealloy, $0.110mg_{PGM}/cm^2$**	3M 2979	3M 2979	3M 825EW 20µ	0.129	FF2
2015(Jan.) BOC	**PtCoMn/NSTF, $0.015mg_{PGM}/cm^2$**	**Pt_3Ni_7/NSTF, JHUDealloy, $0.103mg_{PGM}/cm^2$**	3M 2979	3M 2979	**3M-S 725EW 14µ**	0.118	FF2
2015(March) BOC	PtCoMn/NSTF, $0.015mg_{PGM}/cm^2$	Pt_3Ni_7/NSTF, JHUDealloy, $0.103mg_{PGM}/cm^2$	**3M X2**	**3M 2979 + Interlayer ($15µg/cm^2$, A)**	3M-S 725EW 14µ	0.133	FF2
2015(Sept.) BOC	**PtCoMn/NSTF, $0.019mg_{PGM}/cm^2$**	**Pt_3Ni_7/NSTF, JHUDealloy, $0.096mg_{PGM}/cm^2$**	**3M X3**	**3M 2979 + Interlayer ($16µg/cm^2$, B)**	3M-S 725EW 14µ	0.131	FF2

Comparison of Performance and Operational Robustness of Pre-Project Baseline MEA and Final Project BOC MEA

Over the course of the project, significant gains in absolute performance, specific power, reduced loading, and operational robustness were achieved. Figure 95 (left) and Table 14 summarize pre-project 2012 BOC MEA performance to that obtained with the final project BOC MEA. The test was conducted at 90°C cell temperature with 1.5atmA H_2/Air in $50cm^2$ format. The final project BOC MEA yielded $0.89W/cm^2$ and 6.8kW/g at 0.692V, the voltage required to achieve the MEA heat rejection target ($Q/\Delta T$=1.45kW/°C), as compared to 4.4kW/g for the pre-project MEA and the 8kW/g target. The performance at 0.80V also improved and slightly exceeded the DOE 2020 target of $0.30A/cm^2$. Loading was reduced from 0.151 to $0.131mg_{PGM}/cm^2$, as compared to the $0.125mg_{PGM}/cm^2$ target.

The final project BOC MEA also had markedly improved operational robustness, shown in Figure 95 (right). The baseline MEA was able to successfully execute load transients from 0.02 to $1.0A/cm^2$ between 70-80°C only; as the cell temperature decreased, the cell voltage was negative, indicative of the cathode reducing protons (i.e. HER) rather than oxygen (ORR). The final project BOC MEA, shown in blue, enabled a much wider operating temperature window, as low as 40°C. The ultimate Fuel Cell Tech Team (FCTT) target of successful transients at 30°C cell temperature was approached but not achieved.

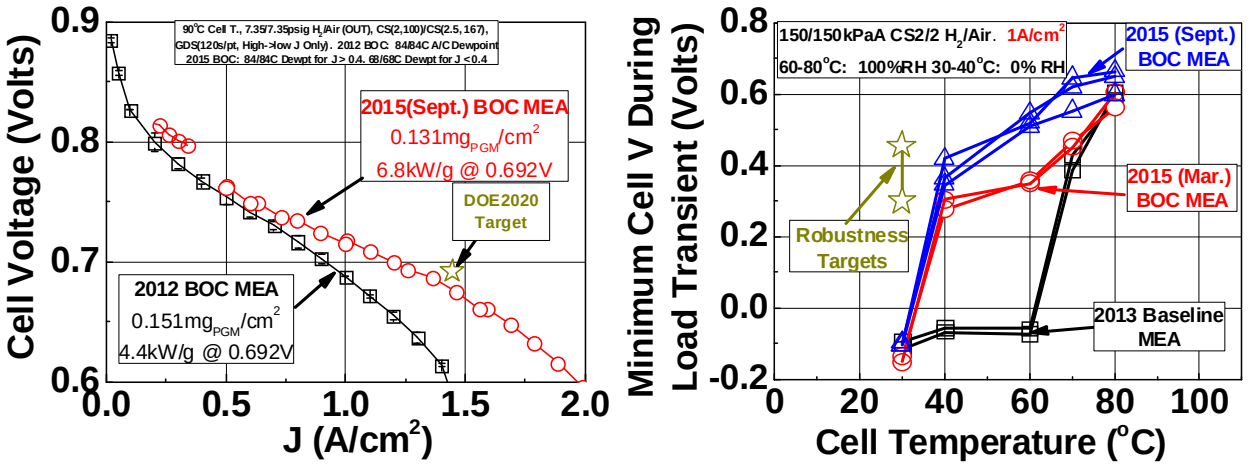

Figure 95. Comparison of Rated Power Performance and Operational Robustness.

Table 14. Performance and PGM loading status of pre-project and final project BOC MEAs.

Characteristic	Units	2020 Targets	3M Pre-Project Status ('12)	3M Final Project Status ('16)
Q/ΔT	kW / °C	1.45	1.45	1.45
Performance @ 0.8V	mA/cm^2	300	194	310
Performance @ rated power	mW/cm^2	1000	664	891
Platinum group metal total content (both electrodes)	g / kW (rated)	0.125	0.227	0.147
Platinum group metal (pgm) total loading	mg PGM / cm^2 electrode area	0.125	0.151	0.131
90°C, 150kPa H_2/Air, 84°C or 68°C Dewpoints, 2.0/2.5 H_2/Air Stoichiometry. Performance @ rated power, Q/ΔT characteristics calculated at 0.692V.				

Figure 96 summarizes the evolution of loading, rated power, and specific power over the project for the specific BOC MEAs. Steady progression in PGM reduction and rated power were achieved. Of note is that the PGM loading increased slightly with inclusion of the cathode interlayer in the 2015(March) BOC MEA, and specific power decreased commensurately. The final project BOC MEA, generated on continuous laboratory and pilot-scale equipment, yielded slightly higher performance than the nearly analogous laboratory made 2015(March) BOC CCM.

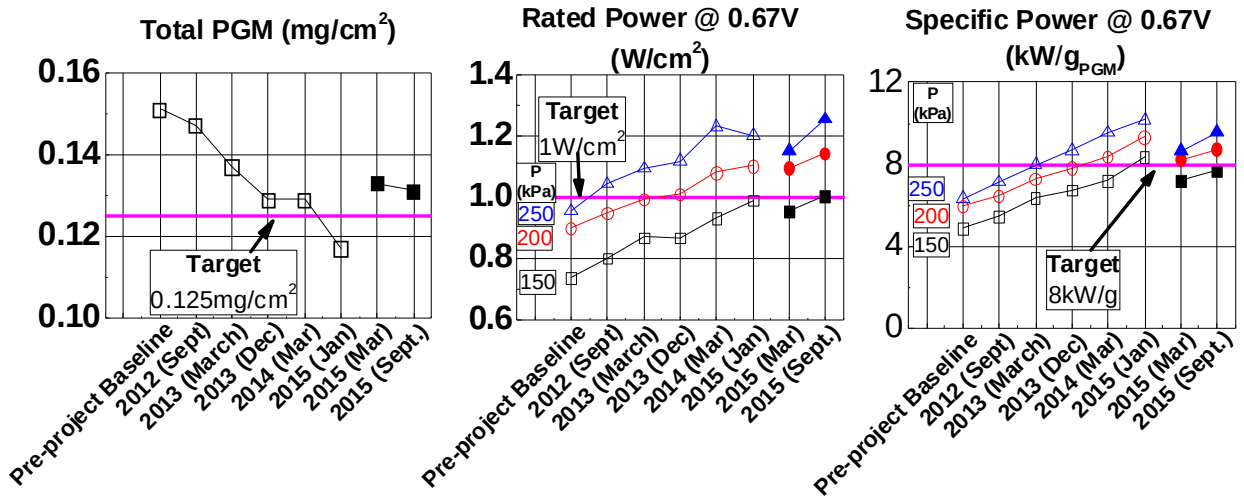

Figure 96. Evolution of loading, rated power, and specific power for project BOC MEAs. Results average of two or more BOC MEAs. Hollow: BOC MEAs without cathode interlayer. Solid: BOC MEAs with cathode interlayer (15-16µg/cm^2).

Performance of Final Project BOC MEA

After conditioning, BOC MEAs were evaluated for performance as a function of anode and cathode reactant pressure. Figure 97 summarizes polarization performance at 1.5, 2.0, and 2.5atm absolute (outlet) with 90°C cell temperature, and 1.5atm absolute (outlet) with 92°C cell temperature. Performance at a given condition was reasonably reproducible for the two MEAs evaluated. For all test conditions, limiting current densities exceeded 1.8A/cm^2 at 0.60V.

Of note are that MEA resistances were typically 0.05-0.07ohm-cm^2 near 1.5A/cm^2, higher than would be expected (~0.04ohm-cm^2) for state-of-the-art, high performance MEAs. One likely source of this resistance is due to increased PEM resistance caused by leaching of Ni from the cathode.

Figure 98 summarizes the absolute and specific power densities as a function of cell voltage. At 0.692V, which meets Q/ΔT=1.45kW/°C, specific power densities ranged from 6.8 to 8.5kW/g as operating pressure increased, and absolute power densities ranged from 0.89 to 1.11 W/cm^2.

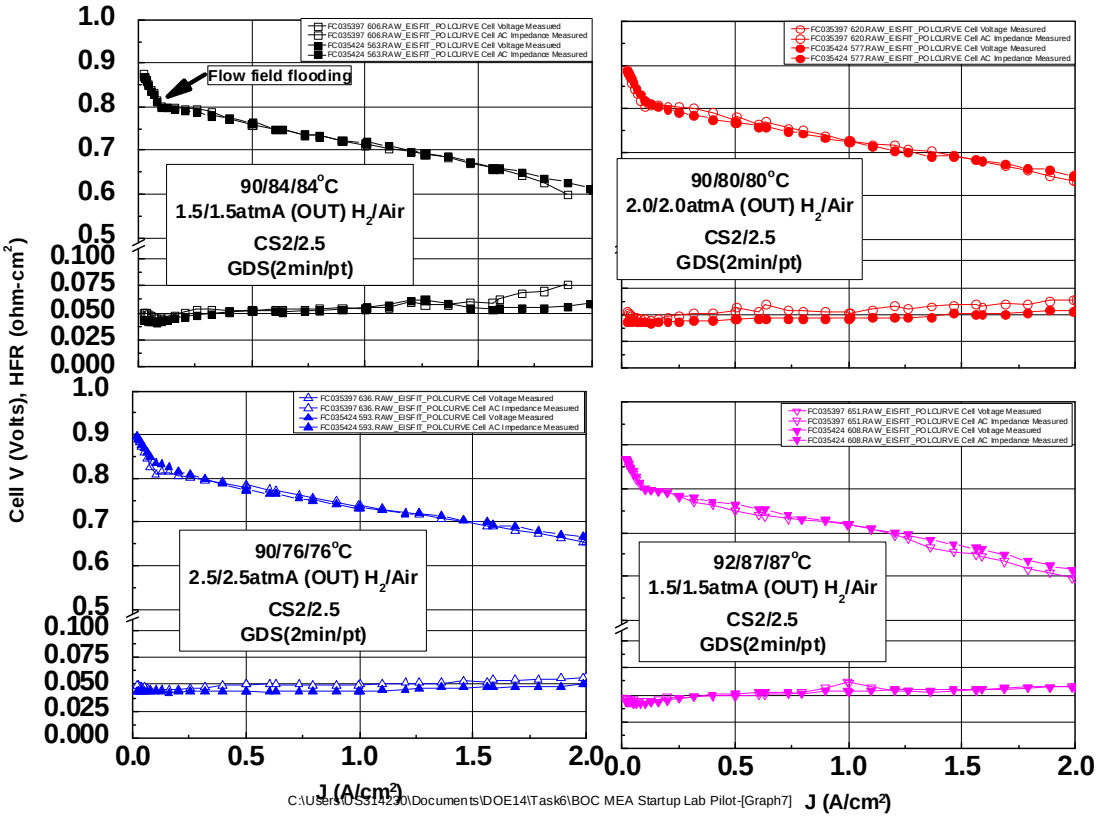

Figure 97. H_2/Air performance and HFR vs. stated operating conditions of 2015(Sept.) Best of Class MEAs.

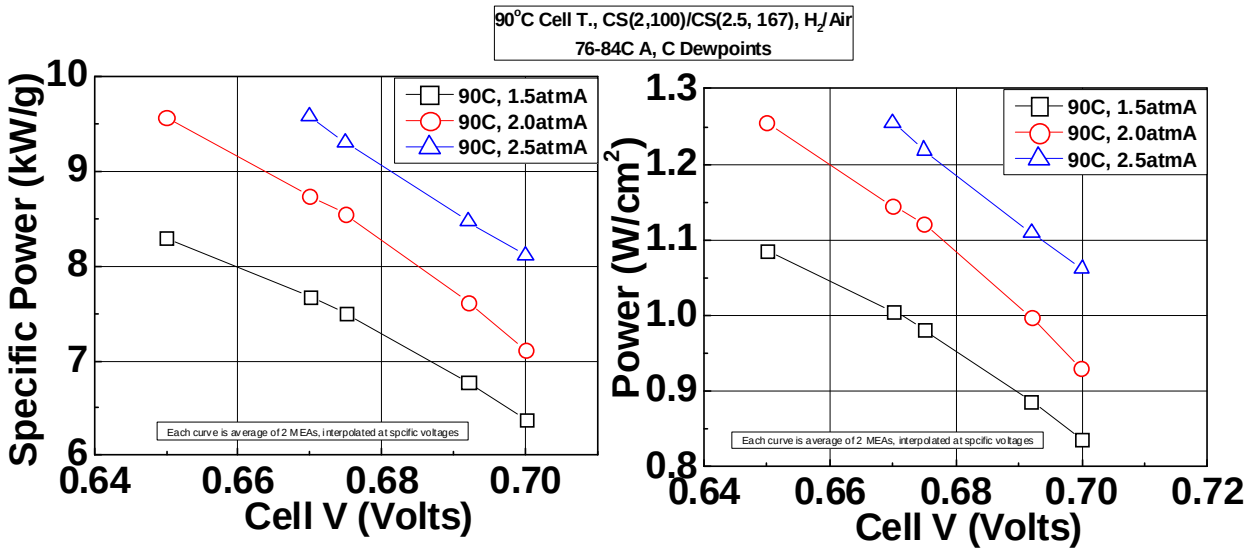

Figure 98. Specific and absolute power vs. cell voltage for 2015(Sept.) Best of Class MEAs.

At the test conditions used for high rated power performance above, the performance at lower current densities is suppressed. Analysis conducted in 2015 determined that the FF2 flow field used for BOC MEAs suffers from flooding at low current densities (low absolute flow rates), and significantly improved performance is obtained when the RH is reduced. Figure 99 (left) shows the sensitivity of performance to RH, plotted vs. the MEA HFR; as the RH was reduced, the cell voltage at 0.31A/cm^2 increased over 20mV. Figure 99 (right) shows that this FF flooding

resulted in a nearly 66% loss in performance as compared to optimal RH. At the optimal RH, the 2015 (Sept.) BOC MEA current density at 0.80V exceeds 0.30A/cm^2.

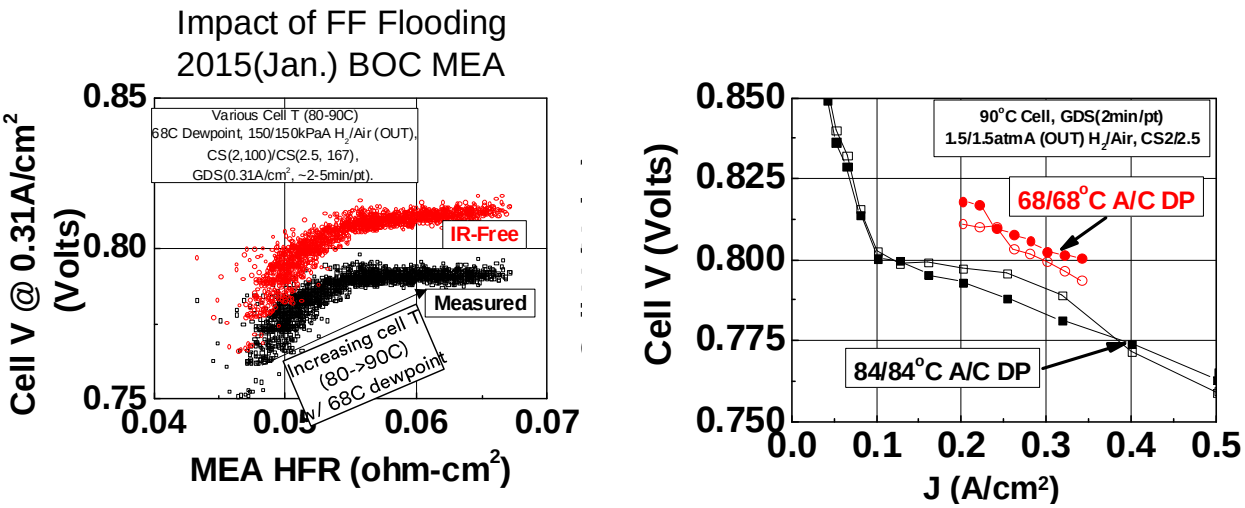

Figure 99. Sensitivity of BOC MEA apparent kinetic performance to RH due to FF flooding. (Left): Impact of increasing cell temperature (reducing RH) on performance at 0.31A/cm^2. (Right): Polarization performance of 2015(Sept.) BOC MEA at high and low RH.

Lower-load Cathode BOC MEA Candidates

Outside this project, additional cathode candidates with high activity and reduced cathode loading were identified, incorporated into the 2015(Mar.) BOC MEA format, and evaluated for performance. In these MEAs, the cathode loading was reduced from 0.103 to 0.097 and 0.075 mg$_{PGM}$/cm^2, yielding MEA total loadings as low as 0.105mg/cm^2. Figure 100 shows that high performance was achieved with the ultra-low cathode loadings. As total loading was reduced, the curves shifted downward, consistent with the absolute cathode activity losses. Specific power remained constant at ca. 0.155g/kW. The results suggest that achievement of the DOE 2020 target of 0.125g/kW will require increased cathode mass activity.

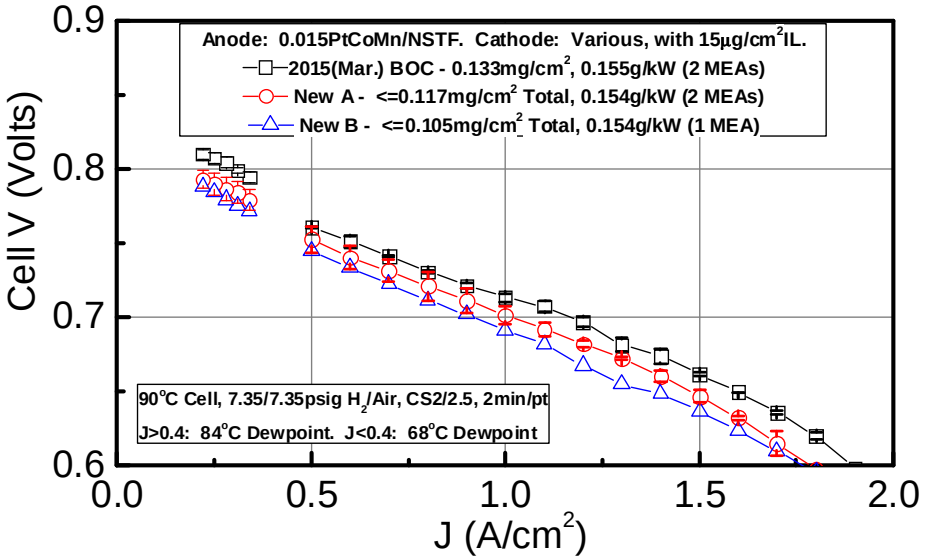

Figure 100. BOC candidate MEAs with total MEA PGM loadings ranging from 0.133 to 0.105mg$_{PGM}$/cm^2.

Operational Robustness of Final Project BOC MEAs

Incorporation of the improved "X3" anode GDL and the downselected type "B" interlayer from Task 2 resulted in large improvements in operational robustness over pre-project status. Figure 101 shows that under steady state temperature sensitivity testing, the final project BOC MEA yielded better than 2x the limiting current density between 31-33°C over the pre-project baseline MEA without baseline diffusion media and no interlayer.

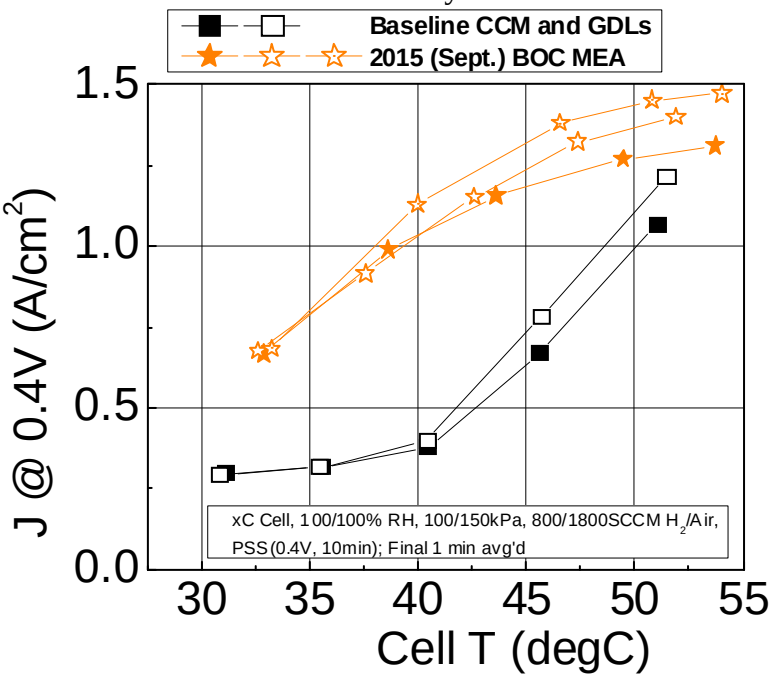

Figure 101. Performance sensitivity to temperature for 2015 (Sept.) Best of Class MEAs.

Figure 102 compares performances obtained under load transient testing for a baseline MEA w/o interlayer, baseline MEAs with interlayer, and the BOC MEA. At a majority of test conditions ranging from 30 to 60°C cell temperature, the BOC MEA was generally able to pass the load transient tests, i.e. maintain a positive cell voltage during a transition from 0.02 to 1.0A/cm^2 and during a subsequent 30 second hold. The only consistent point of failure was at 30°C, where after 30s, the BOC MEA cell voltage went negative.

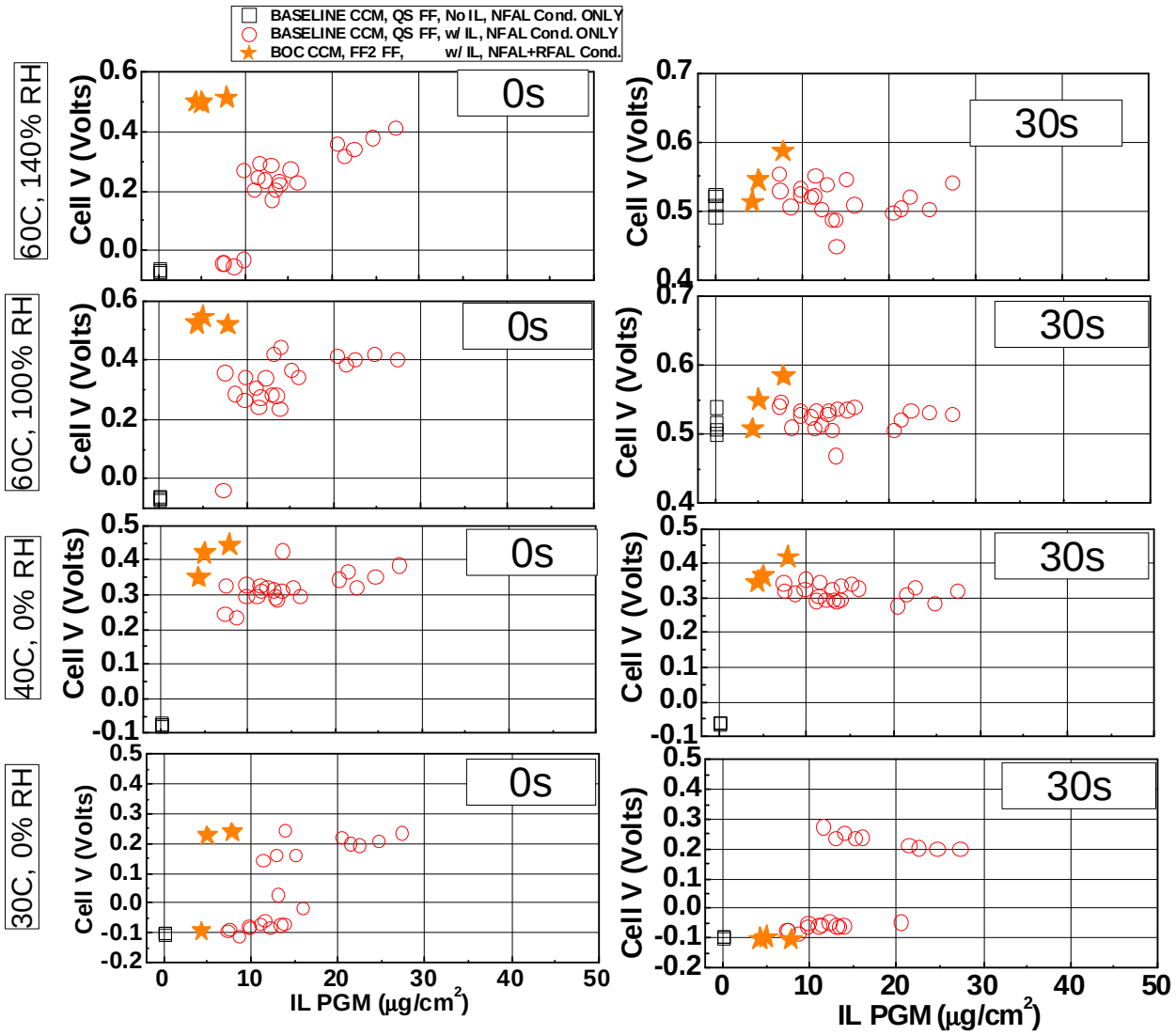

Figure 102. Load transient performance of 2015(Sept.) Best of Class MEAs.

The final project BOC MEA was not evaluated for robustness under the FCTT protocol, but the 2015 (March) MEA was evaluated. Figure 103 shows that the '15 March BOC MEA was not able to achieve transient or steady state operation at 1A/cm^2, 30°C, 100% RH conditions, consistent with the 3M protocol data in Figure 101 and Figure 102. Figure 104 shows that the BOC MEA was able to pass the FCTT Hot test.

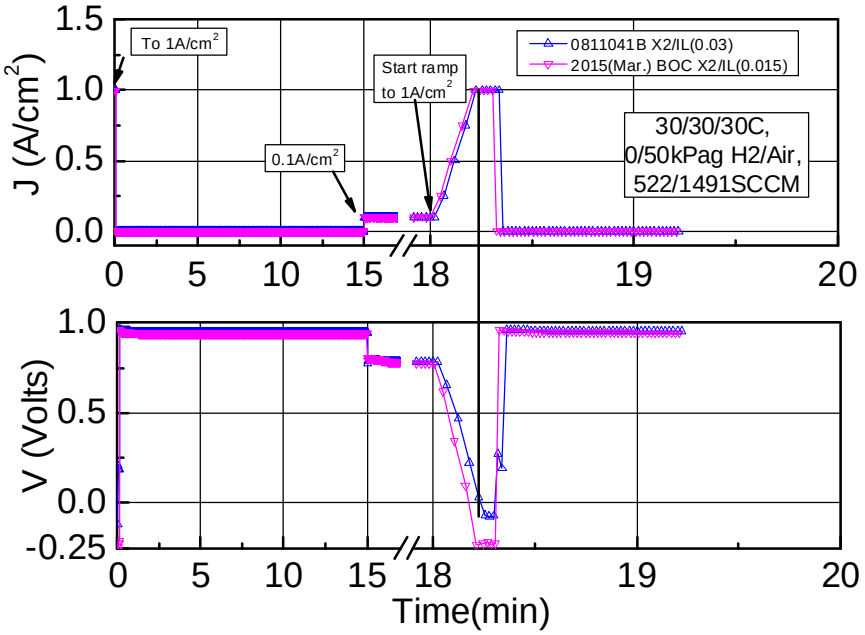

Figure 103. Performance of 2015(March). BOC MEA under FC Tech Team Cold and Cold Transient Test.

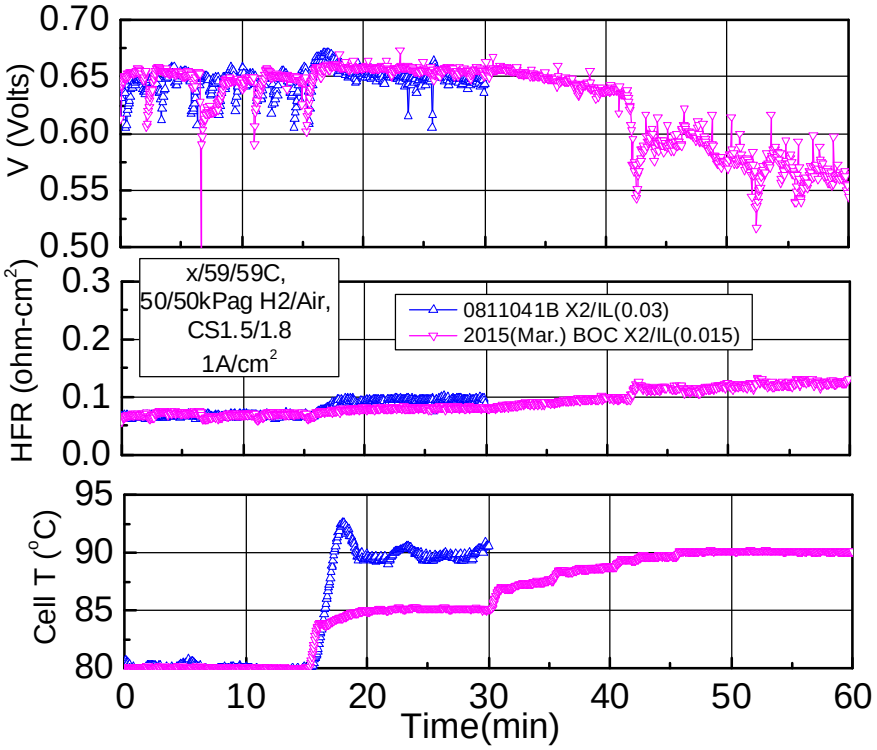

Figure 104. Performance of 2015(March) BOC MEA under FC Tech Team Hot Test.

Conditioning of Final Project BOC MEA

Final project BOC MEAs were conditioned using the standard "thermal cycle" 3M protocol used with NSTF MEAs. The thermal cycle protocol consists of repeated temperature and potential cycles conducted over several hours. Historically, this procedure results in marked performance improvement over the first 10-20 hours, after which incremental improvements are observed, as shown in Figure 105. Entitlement H_2/Air performance and operational robustness of BOC MEAs requires anode activation, otherwise severe suppression results (Figure 106).

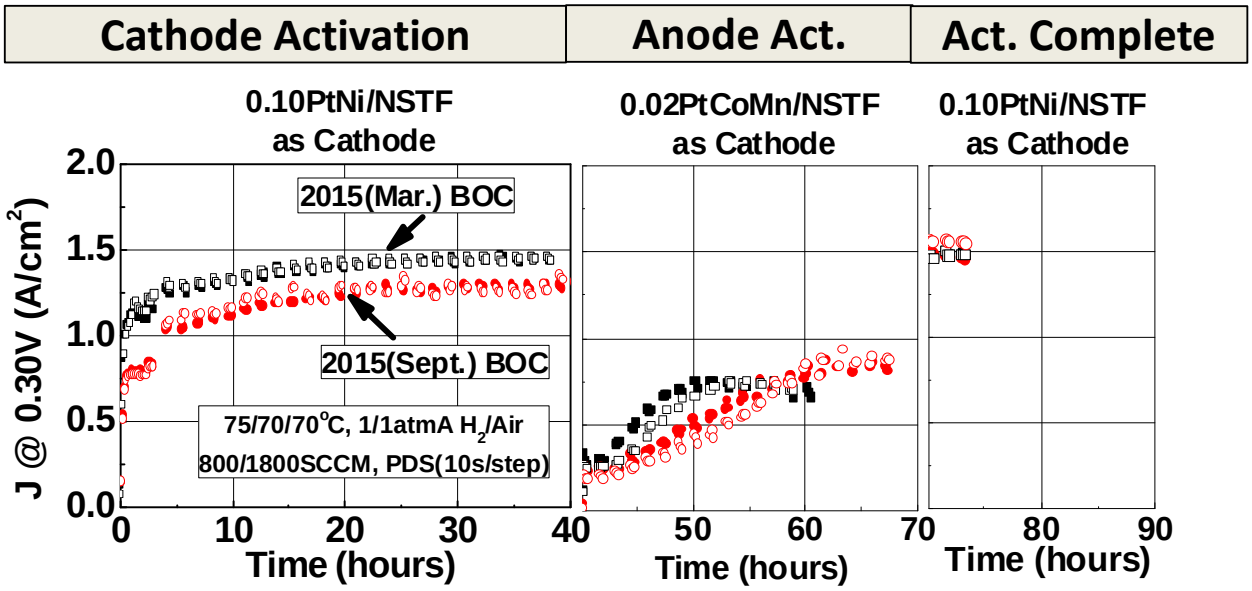

Figure 105. BOC MEA conditioning protocol.

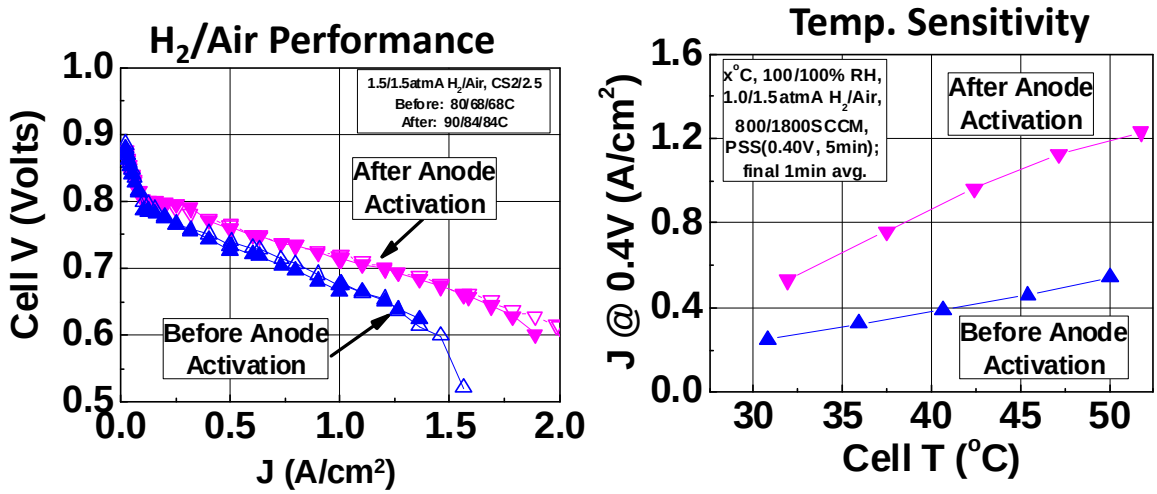

Figure 106. Impact of anode conditioning on H_2/Air performance (left) and temperature sensitivity (right).

This conditioning process is too long for practical end-use applications. Previous development work has indicated that this process can be highly accelerated, and is discussed further in the Task 4.2 section. Ultimately, material-based solutions will be needed.

Durability of 2015 (March) and (Sept.) BOC MEAs

Durability of individual components was assessed where possible, and are summarized in Section 5. In general, the key component-level durability concern identified in that work was the relative instability of the dealloyed PtNi/NSTF cathode against Electrocatalyst AST cycling, where mass activity losses typically ranged from 60-80% due to coarsening of nanoporosity and nickel dissolution.

2015 (March) BOC MEAs were evaluated for durability under the MEA chemical durability test. Figure 107 shows that these BOC MEAs readily achieved the 500 hour DOE target, but failed within about 700 hours. By comparison, 2011 baseline MEAs (PtCoMn/NSTF, unsupported PEM w/ additive) exceeded 1000 hours, after which one started to fail. While the DOE target was achieved, room for improvement is possible, perhaps by increasing the additive level.

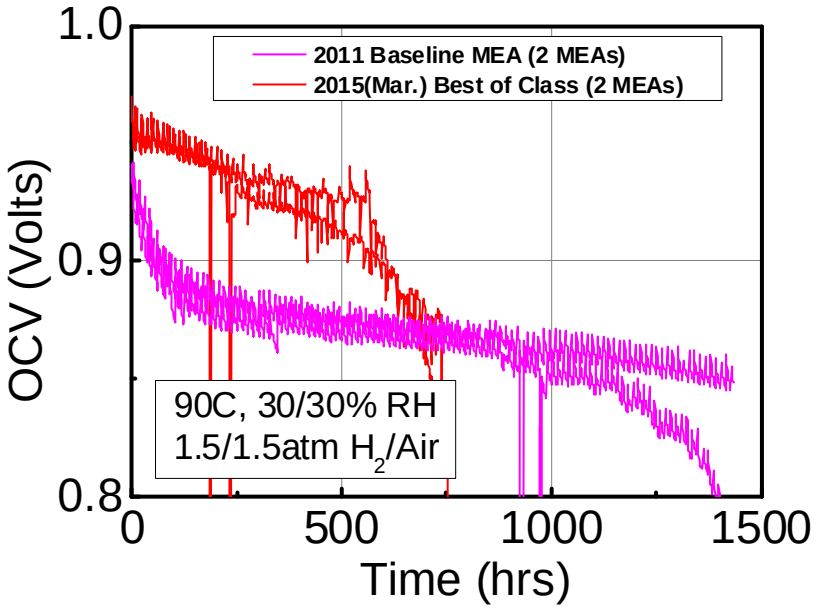

Figure 107. MEA Chemical Durability of 2015 (March) BOC MEA.

Load Cycle Durability of Final Project BOC MEAs

In this testing, the cells are operated continuously under the load cycle (80°C cell, subsaturated RH), other than for unintended shutdowns due to station issues or facility shutdowns. During this testing, OCV has remained largely steady, but performance losses have been observed. Note that under this test, both reversible and irreversible losses are expected to occur with BOC MEAs. Under the test protocol above, reversible losses continue to accumulate and are not recovered until the cell is reconditioned.

Three BOC MEAs initiated under 3M load/RH cycle testing. Two failed in < 1000 hours, likely due to numerous uncontrolled test shutdowns due to facility issues. One remaining MEA was evaluated for > 3000 hours, shown in Figure 108. The OCV remained healthy over entire test. The cathode F^- release rate was a relatively low 7.3±1.8 ng/cm^2/hr between 1300-2800 hours and was steady.

Table 15 summarizes the estimated performance loss rates. To achieve the 10% V loss target (ca. 70mV) in 5000 hours, the voltage loss rate would need to average 14µV/hr. This was largely achieved at low current densities. At OCV and 0.2A/cm^2, the performance loss rates were 10-15µV/hr. However, at 0.8A/cm^2 the loss rate was appreciably higher than the allowable rate. Over the first 656 hours, the loss rate at 0.8A/cm^2 was ca. 81µV/hr, and over the first 1864 hours the loss rate was 47µV/hr, on average. An acceleration in loss rate may have occurred after 600 hours, consistent with an uncontrolled shutdown. Based on these limited results, the estimated lifetime to 10% voltage loss (at 0.8A/cm^2) is between 656-1864 hours.

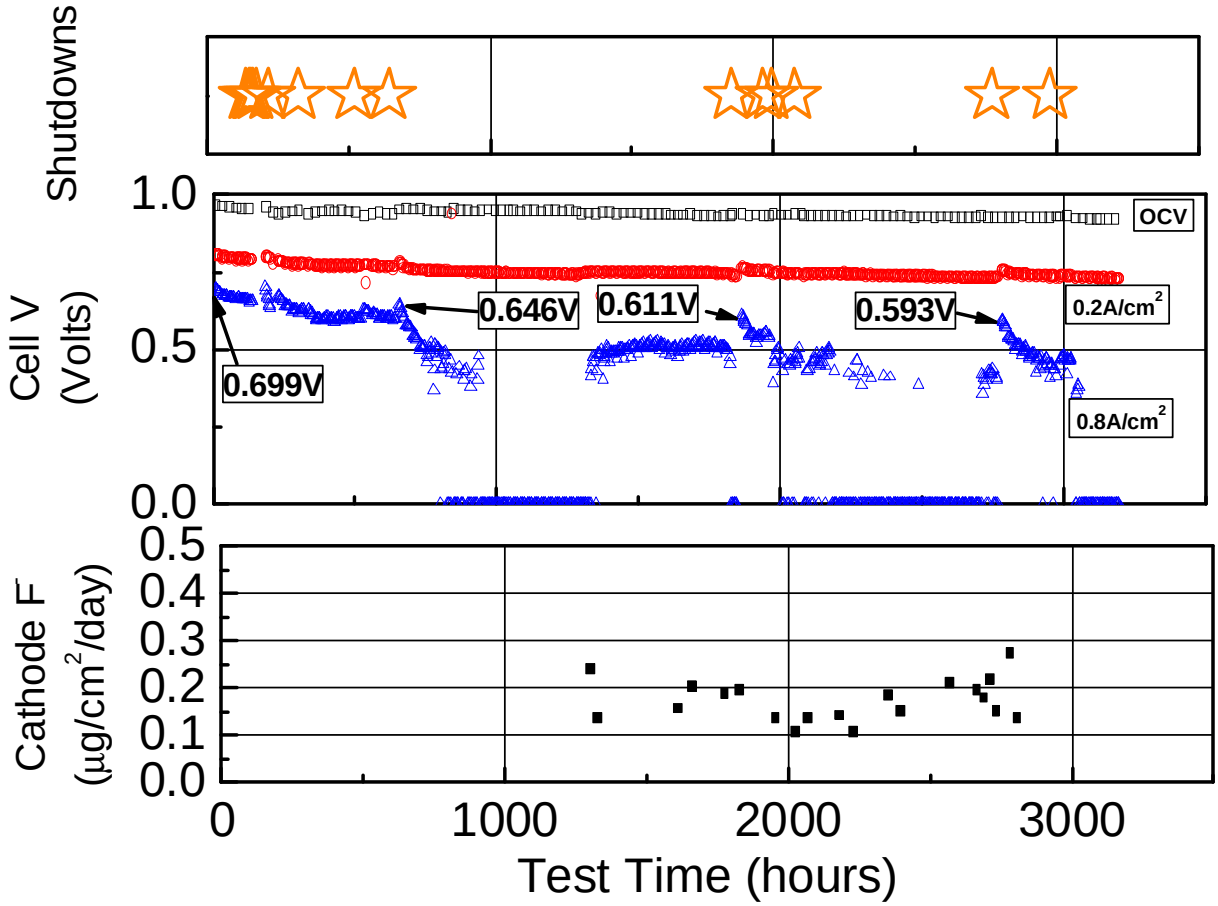

Figure 108. Performance over time during Shiva load cycling of 2015 (Sept.) BOC MEA.

Table 15. Estimated performance loss rates during 3M Shiva load cycling

Current density	Decay rate	Time period	Estimate type
OCV	-9.7 ± 0.4µV/hr	0-3200	regression
0.2A/cm^2	-15.2 ± 0.4µV/hr	0-3200	regression
0.8A/cm^2	-81µV/hr	0-656	average
0.8A/cm^2	-47µV/hr	0-1864 (hours)	average

There are two known factors influencing rated power loss of NSTF MEAs, both of which are related to loss of ORR absolute activity from the cathode. One factor is based on work conducted in collaboration with ANL and discussed in the Task 5 section, which is that PFSA decomposition induces ORR activity loss in NSTF MEAs, likely due to accumulation of

irreversibly adsorbed contaminants, possibly long-chain perfluorocarboxylic acids. Based on that work, which correlated rated power loss to cumulative F^- emission, suggests that at the F^- emission rates here, 10% voltage loss would occur within a few hundred hours. A second factor is the intrinsic instability of the PtNi/NSTF cathode, shown to lose 60-70% mass activity after the DOE Electrocatalyst AST.

Subtask Conclusions

Over the course of the project, significant gains in absolute performance, specific power, and reduced loading were achieved. At 90°C cell temperature and 1.5atmA reactant pressures, performance at 0.80V increased 60% and performance at rated power (0.692V) increased 34% while the total loading decreased 13%, resulting in an improvement in specific power of 54% (kW/g). The Q/ΔT target of 1.45kW/°C was achieved.

Evaluation of BOC MEA candidates with further reduced PGM loading, as low as $0.105mg_{PGM}/cm^2$ total, were suggestive that DOE performance and total loading targets are feasible if increased activity cathodes were incorporated.
Operational robustness was also improved substantially. The operating temperature window under which successful load transients (0.02 to $1.0A/cm^2$) could be achieved was increased from 70-80 to 40-80°C, nearly achieving the recommended target by the USCAR FC Tech Team of load transients down to 30°C.

The final project BOC NSTF MEAs require a specific and lengthy conditioning protocol to achieve entitlement performance and operational robustness. Both anode and cathode electrodes need to be conditioned.

The durability of the final project BOC MEAs was assessed by the DOE MEA chemical durability test and a 3M 80°C load/RH cycle test. The BOC MEAs appear to be chemically stable, evidenced by low F- emission rates and steady OCVs > 500 hours for the OCV hold and > than 3000 hours in the load/RH cycle. Voltage degradation rates under load cycling were modest at low current densities but were 3-5x higher than acceptable at $0.8A/cm^2$. Loss factors, identified in other work and discussed in the Task 5 section, are known and believed mitigatable.

Future Directions

The break-in conditioning rate of NSTF MEAs must be improved to enable market acceptability, to less than a few hours and ideally without any onerous method requirements. More rapid methods have been demonstrated, discussed in the Task 4.2 section. Contaminants remain a primary concern, and detailed studies to evaluate the types and sources would help provide guidance on material pathways to eliminate them.

Development of high performance MEAs at PGM loadings below the DOE 2020 target have been demonstrated. Achievement of the specific power, rated power, and PGM loading targets simultaneously will require a higher activity cathode. Such development work is currently in progress.

The load cycle durability of NSTF MEAs must also be improved. Root causes are believed to be understood, and namely caused by two sources of ORR activity loss, caused by intrinsic

degradation of the nanoporous PtNi/NSTF cathode and PFSA decomposition. Incorporation of more durable cathodes, ideally with even higher BOL mass activity, would help mitigate the first cause. The second cause, PFSA decomposition, is a more difficult concern. NSTF MEA PFSA degradation rates are already very low. Some improvements are likely to be found via optimization of mitigation additive levels. Ultimately, resolution may require new ionomer chemistries to mitigate formation of relevant contaminants. Such work in both paths is currently in progress at 3M.

Subtask 4.2 Component Interaction Diagnostic Studies (3M)

Subtask Overview

Subtask 4.2 involves experimental work aimed at developing mechanistic understanding of component interactions leading to particular performance response, particularly water management and cathode reactant utilization; experimental work will include segmented cell studies, AC impedance spectroscopy, no-gradient cell testing, and product water distribution measurements.

Subtask High Level Work Summary

The influence of anode GDLs on NSTF water balance was assessed on several MEAs. Limited segmented cell studies evaluated the influence of operating conditions on current density distribution across the active area.

Extensive work was conducted on establishing the impact of break-in conditioning on BOC MEA performance and operational robustness, diagnostic studies to break-down between anode and cathode conditioning impacts, and determining accelerated break-in methods.
A new-to-3M testing method (differential cell) was established and validated, useful for generating data for performance and cost modeling.

Subtask Key Results

Impact of Anode GDL on NSTF MEA Water Balance

As noted in the Subtask 2.1 section, the anode GDL backing has a very strong effect on the temperature sensitivity of NSTF MEAs. In this work, diagnostic experiments were conducted to develop mechanistic understanding of the anode GDL influence. NSTF MEAs (0.05/0.15PtCoMn, 3M 825EW 20u, 3M 2979 GDL) were evaluated with varying anode GDLs comprised of differing backings, all treated with similar PTFE treatment and with 3M MPL.
Product water collections were made with a custom-built, automated water collection system. The cell effluent streams were passed through individual tube-in-tube heat exchangers to substantially condense out water vapor, then liquid product water was collected in chilled, insulated separatory funnels, and the gas phase effluent streams were vented. The heat exchangers and separatory funnels were chilled to 5°C. After sufficient operating time (t = J / (30 minutes per A/cm^2); 30 minute minimum), computer-controlled solenoid valves were periodically opened to allow the collected liquid water to drain to computer-interfaced balances, where the initial and final masses were recorded. Three measurements were made in succession at each operating condition. Anode and cathode liquid effluent water flow rates were corrected for the assumed residual 5°C dewpoint vapor in the vented effluent streams and the collection efficiency (typically > 90%), and the fraction of the total corrected water flow rate which exited the cell via the anode effluent stream was calculated.

Figure 109 provides an overview of the typical results and analysis, with results from either a baseline or improved anode GDL. The top left set of figures are polarization curves at temperatures between 30 and 60°C. For both GDLs, performance decreased with decreasing temperature, but the improved anode GDL had modestly higher performance. The bottom set of figures is the fraction of product water exiting out the MEA anode. With either GDL, the fraction exiting the anode at 60°C was very low, between 10 and 30% with a dependence on current density. As the temperature decreased, the fraction exiting the anode increased. For the baseline GDL, the maximum anode water removal rate was ca. 40% of product water, whereas for the improved anode GDL the maximum apparent fraction was much higher, closer to 60%.

As the temperature decreased to 30°C, the maximum current density evaluated was 0.25A/cm^2. Figure 109 (right) shows how the cell voltage at 0.25A/cm^2 may depend on the *limiting* anode water removal rate for the 30-60°C data. At high temperature, the performance is high and the water removal rate is low. As T decreases towards 30°C, performance decreases and water removal rates out the anode increase. The figure is suggestive that the performance loss occurs when the water removal out the anode becomes limited.

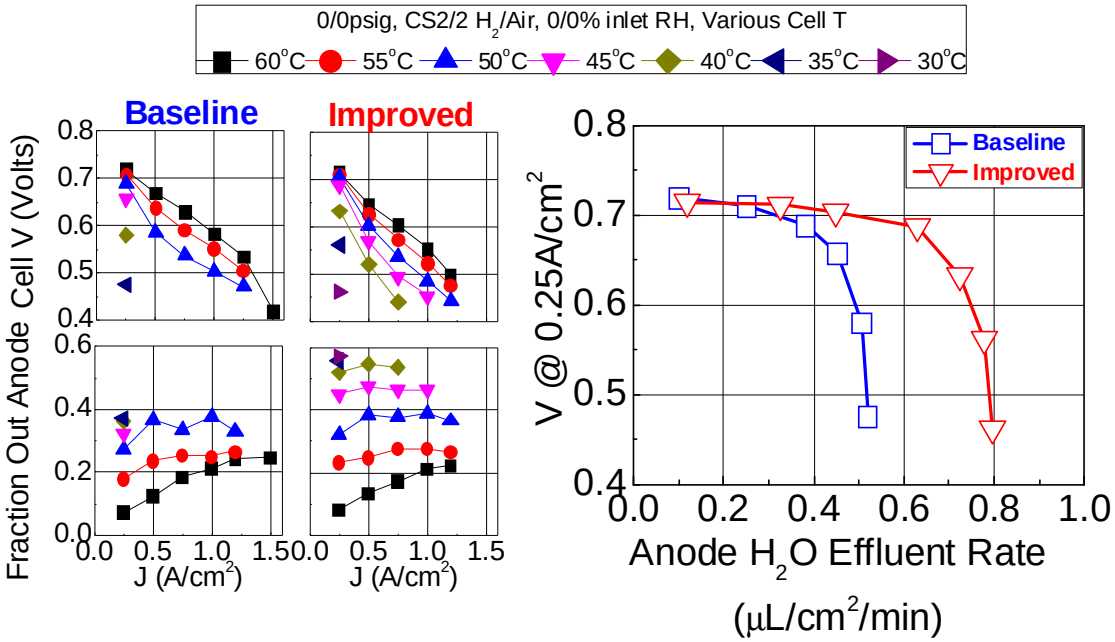

Figure 109. Water balance analysis of NSTF MEAs with either baseline or improved anode GDLs. (Left): H2/Air pol curves and fraction of water removed out anode vs. operating temperature. (Right): Apparent limiting water removal rates vs. performance.

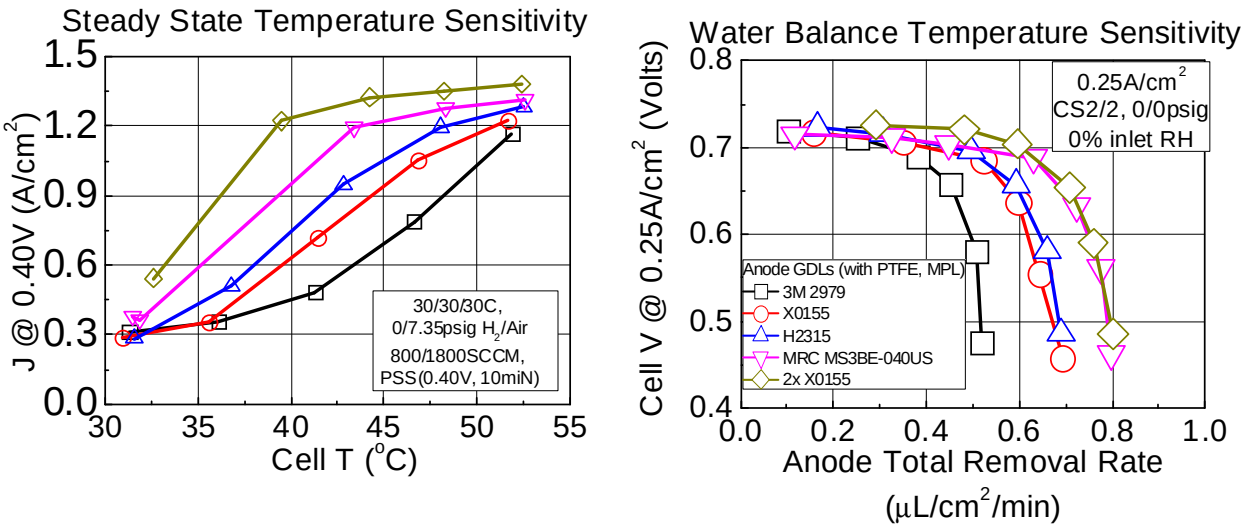

Figure 110. Temperature sensitivity and water balance with several anode GDLs.

Additional experiments were conducted with several relevant anode GDLs, including the base X0155 used as the project downselect. As noted in the subtask 2.1 and shown in Figure 110 (left), the performance at low temperature depends strongly on anode backing type. The right plot shows that the water balance observation noted above also holds for the other GDLs; GDLs which enable improved low temperature performance have generally higher limiting anode water removal rates.

The nature of the apparent limiting water removal was explored further, and summarized in Figure 111. As noted above, as the temperature decreases, performance at 0.25A/cm^2 decreases and the anode water removal rate increases, but at a decelerating rate. Figure 111 shows that for the 5 GDL types evaluated, the NSTF MEA low temperature performance decreases when the anode GDL's capability for water removal decreases.

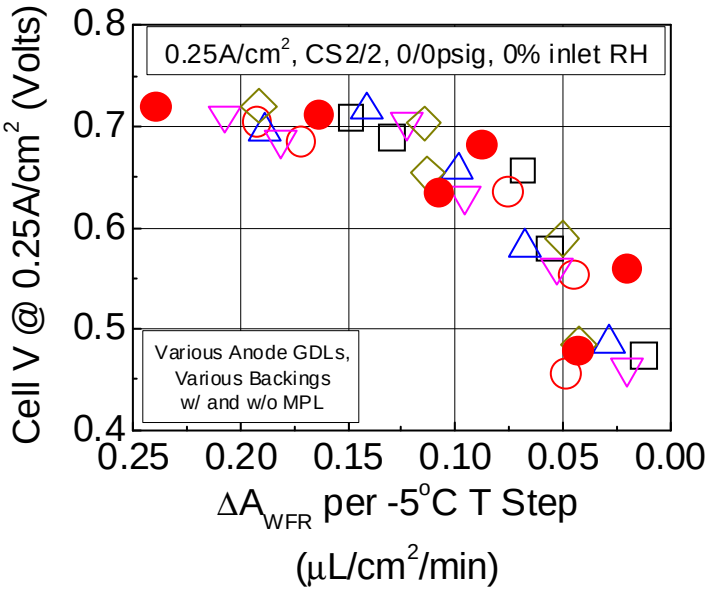

Figure 111. Limiting water removal analysis for various GDLs

These results provide clear insight into how the anode GDL influences water management in NSTF MEAs. This diagnostic data and insight was provided to LBNL and MTU for the Task 3 characterization and modeling effort.

Segmented Cell Studies of NSTF MEA Water Management

Limited experiments were conducted to evaluate the current density distribution for baseline NSTF MEAs operated under steady state and transient conditions. The objective was to understand if large current density areal inhomogeneity is a contributing factor to the poor operational robustness of baseline NSTF MEAs.

Experiments were conducted with use of a segmented current collector (S++), which was installed in a standard 50cm^2 test cell in place of the typical homogenous current collector. The only modification needed was to use a relatively thin flow field adjacent to the current collector. Segmentation of the flow field or MEA was not needed. Figure 112 provides details of the segmentation. Tests were conducted with a baseline MEA (0.05/0.15PtCoMn/NSTF, 3M 825EW 20u PEM, 3M 2979 anode and cathode GDLs).

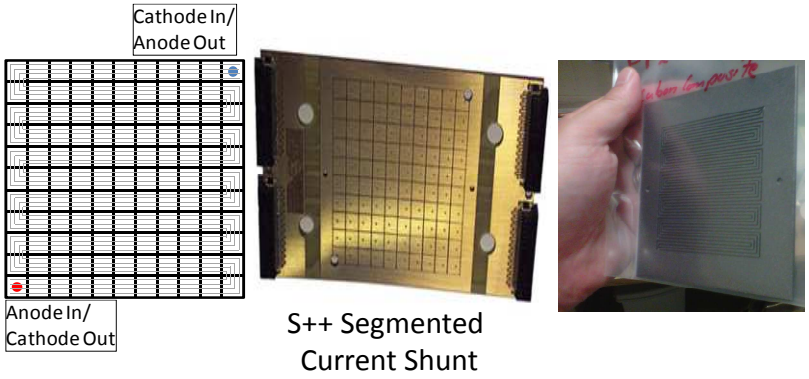

Figure 112. 3M 121 segment fuel cell. (Left): Segment/flow field layout. (Middle): S++ segmented current shunt. (Right): Specialized thin, homogenous flow field.

Figure 113 summarizes the areal current density distribution during a steady state temperature sensitivity measurement. The top left plot shows how the mean segment current density varied with temperature, increasing from 0.2 to 0.9A/cm^2 as T increased from 30 to 80°C. The top right plot shows that the segment current density standard deviation is relatively low at 30°C, increases as T increases to 50°C, then decreases at 60°C. Increased standard deviation indicates relatively larger degrees of current density inhomogeneity.

The bottom set of plots in Figure 113 summarize the current density distribution. At 30°C cell temperature, the current density is low and uniformly distributed. As the temperature increased to 50°C, the current density distribution evolved, where the edges corresponding to the cell anode and cathode inlet channels had much higher current density than the middle region of the cell. At 80°C, a constant gradient in current density was observed, where current density was highest at the cathode inlet and lowest at the cathode outlet, consistent with oxygen depletion.

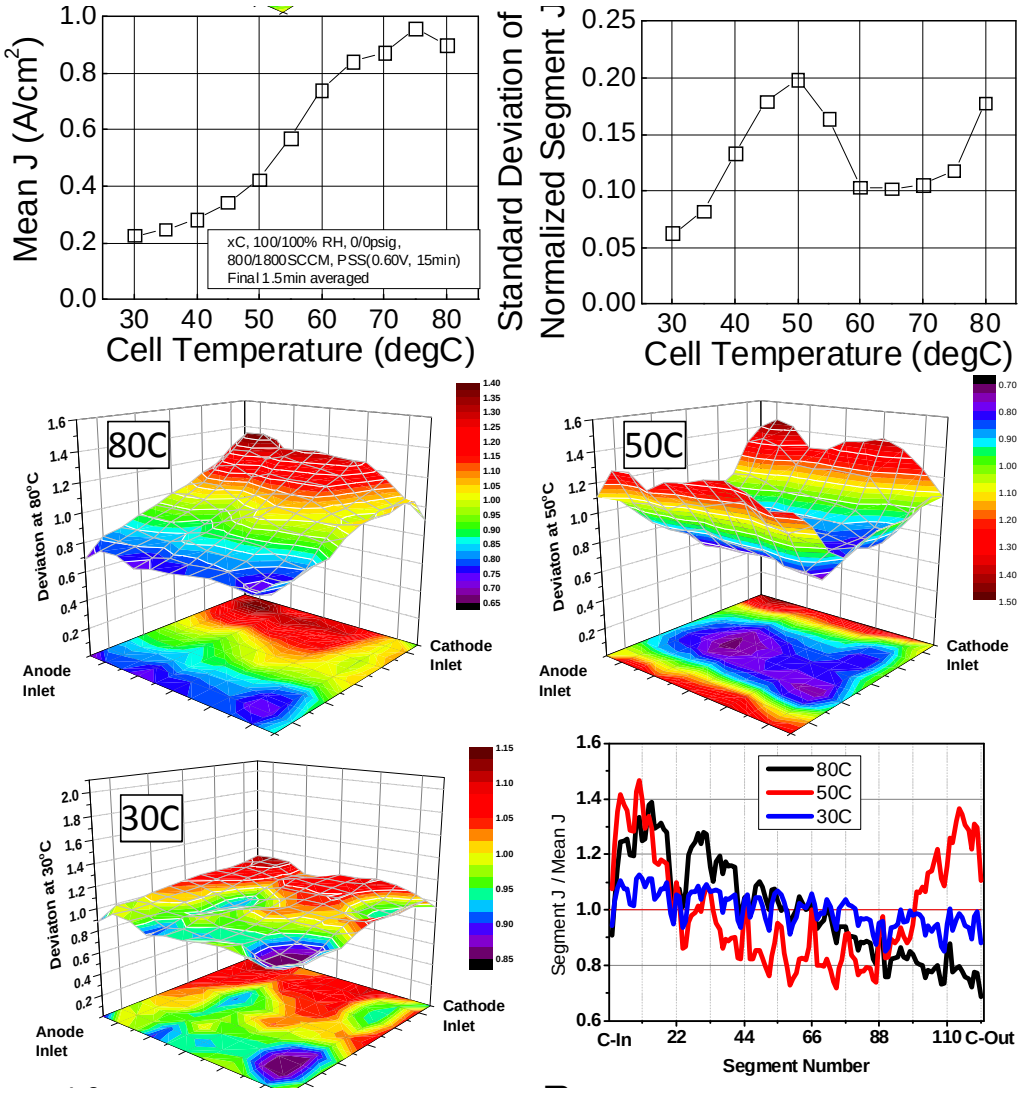

Figure 113. Areal current density distribution during steady state operation at low, moderate, and high cell temperatures.

The current density uniformity distribution was also analyzed for load transients taken at 60-80°C cell temperature. Figure 114 provides a high level overview. The left plot shows how the cell voltage varied during the transition from 0.02 to 1.0A/cm^2 and a subsequent 30s hold. At 80°C, cell voltage remained positive throughout the transition. At 70°C, the cell voltage initially went negative (meaning the cathode is oxygen reactant starved and is evolving hydrogen rather than reducing oxygen), but recovered spontaneously after ca. 18seconds due to electrode deflooding. At 60°C, the cell voltage remained negative throughout the entire test. The middle plot shows the standard deviation of the current density distribution and the right plot shows the median segment current density, where a median value below 1.0 indicates that a majority of the 1A/cm^2 mean current density is provided by a relatively small fraction of segments.

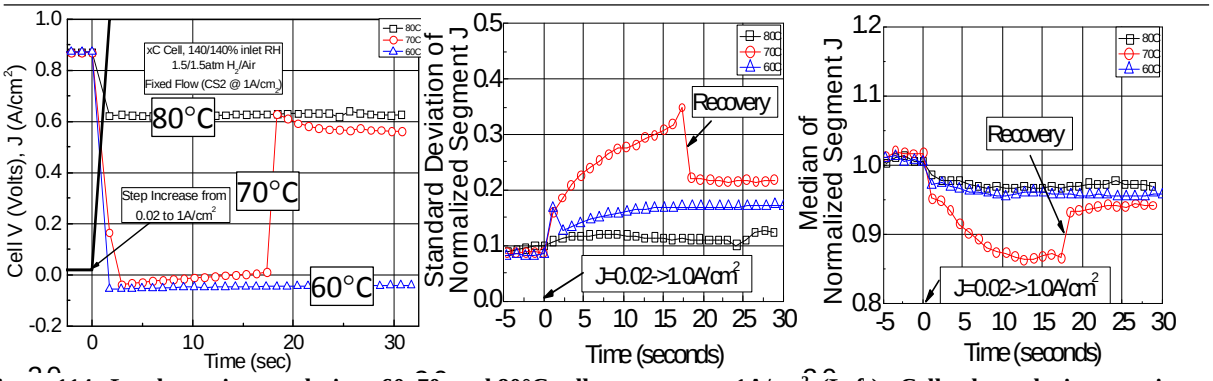

Figure 114. Load transient analysis at 60, 70, and 80°C cell temperature, 1A/cm^2. (Left): Cell voltage during transients. (Middle): Standard deviation of segment current densities. (Right): Median segment current density at 1A/cm^2

Figure 115 (top row) shows how the segment current densities varied during the load transient. At 80°C, where the cell operated well, relatively little change was observed during and after the transient. At 70°C, the distribution changed markedly at the transient point (negative cell voltage), with a high degree of inhomogeneity; some segments had current densities 1.8x the mean. When the cell voltage recovered at 18s, the distribution suddenly tightened. At 60°C, where the cell voltage remained negative during the entire transient, the distribution increased similarly as at 70°C, but with lower magnitude.

The bottom row of Figure 115 shows the spatial distribution of segment current densities for the 70°C case where the cell spontaneously transitioned from HER to ORR on the cathode. In both cases, the current density was highest near the cathode inlet, but the magnitude of variation was larger for the HER operation than for ORR.

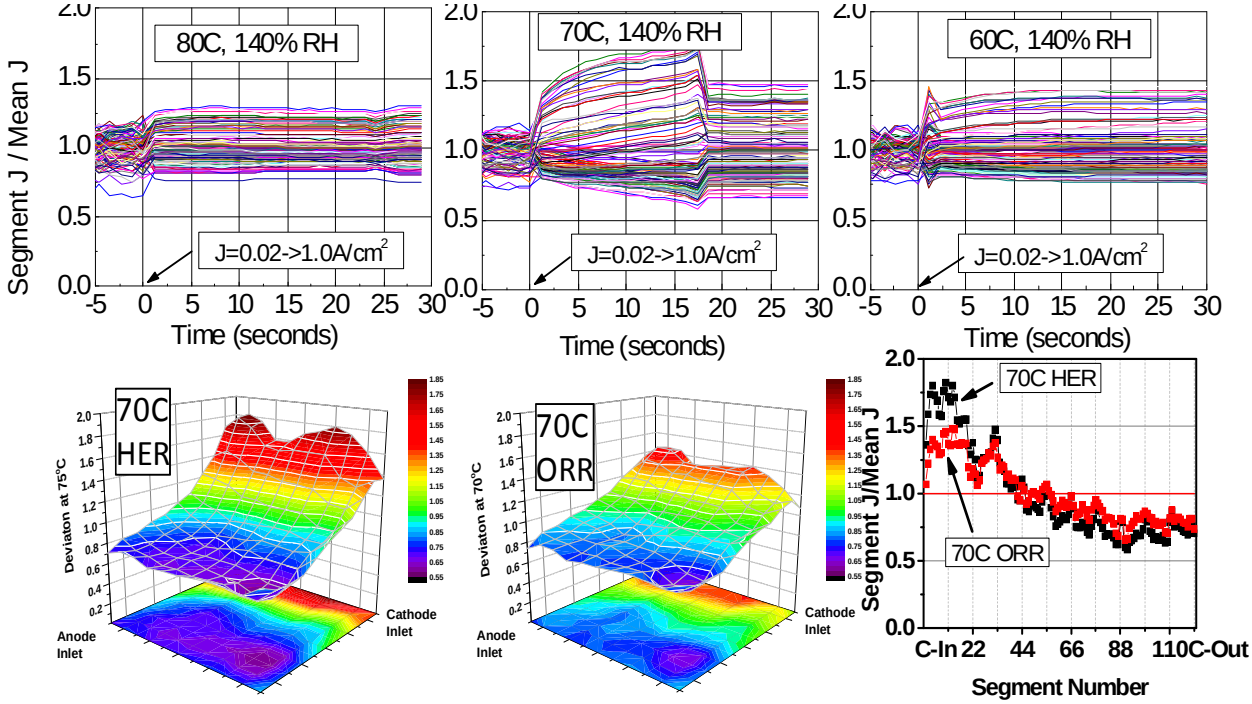

Figure 115. Segment current density distributions during load transients at 60, 70, and 80°C cell temperature.

NSTF MEA Break-in Conditioning Studies

Final project BOC MEAs were conditioned using the standard thermal cycle 3M protocol used with NSTF MEAs. The thermal cycle protocol consists of repeated temperature and potential cycles, conducted over several hours. Historically, this procedure results in large performance improvement over the first 10-20 hours, after which incremental improvements are observed. This conditioning process is too long for practical end-use applications.

Some work towards development of understanding have been conducted, and summarized at a high level below. While the primary mechanism of thermal cycling is not confirmed, it is believed that thermal cycling effectively removes contaminants from the NSTF electrocatalyst surface, increasing the active surface area and absolute activity, directly improving overall performance. Other effects are also possible, but none were immediately detected in this work.

Baseline Conditioning Method – Thermal Cycling

Figure 116 shows how the cell current density at 0.30V, 75°C cell temperature evolved with time during the entire thermal cycle break-in process, and Figure 117 shows representative polarization curves. For the first ca. 50 hours, the cell was operated with the 96µg/cm^2 PtNi/NSTF electrode as cathode ("NFAL"). Notable performance gains occurred over the first 5 hours, followed by moderate gains through cs. 20 hours, after which performance gains were modest. After this initial 50 hour process, the 20µg/cm^2 PtCoMn/NSTF electrode was operated as the MEA cathode ("RFAL"). Over 15 hours, the performance improved nearly 3x. After the 15 hours of RFAL conditioning, the PtNi/NSTF electrode was again operated as the fuel cell cathode ("NFAL"). Immediately, performance was substantially improved relative to the initial NFAL.

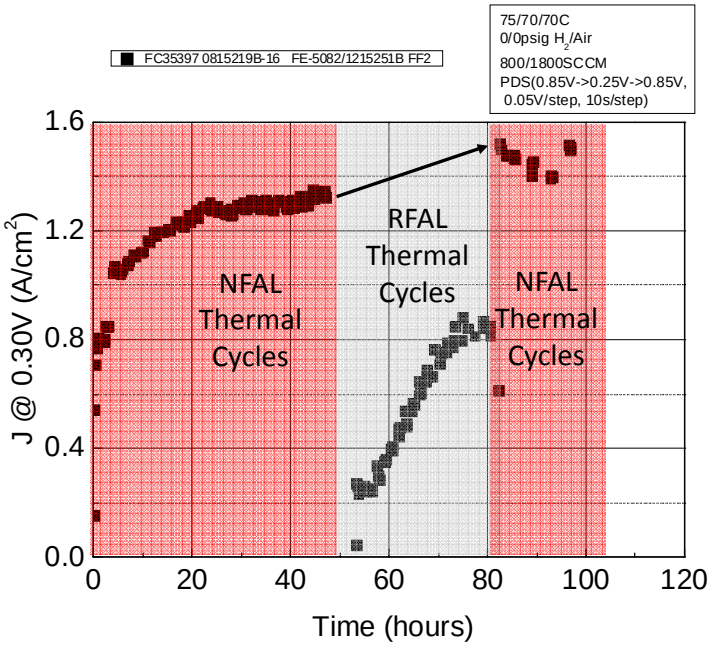

Figure 116. H_2/Air performance evolution for 2015 (Sept.) BOC MEA during break-in conditioning.

Figure 117 compares ambient pressure, 75°C cell temperature H_2/Air performance changes during the break-in conditioning. The left figure shows the performance evolution with the PtNi

electrode as cathode with 0 -29 NFAL thermal cycles, and then after the 0.02PtCoMn anode was conditioned (RFAL). With 0 thermal cycles, the MEA performance suffers from apparent kinetic loses, higher slope, and reduced limiting current. After one thermal cycle, the apparent kinetics improved dramatically, the slope was reduced, and limiting current density was improved modestly. 29 thermal cycles appears to improve the apparent slope and limiting current density further. After conditioning of the NSTF anode (RFAL), the slope and limited current density are further improved. The right figure shows how the 0.02PtCoMn electrode improves during RFAL conditioning (operated as cathode). The limiting current density improves over 3x with 19 RFAL cycles.

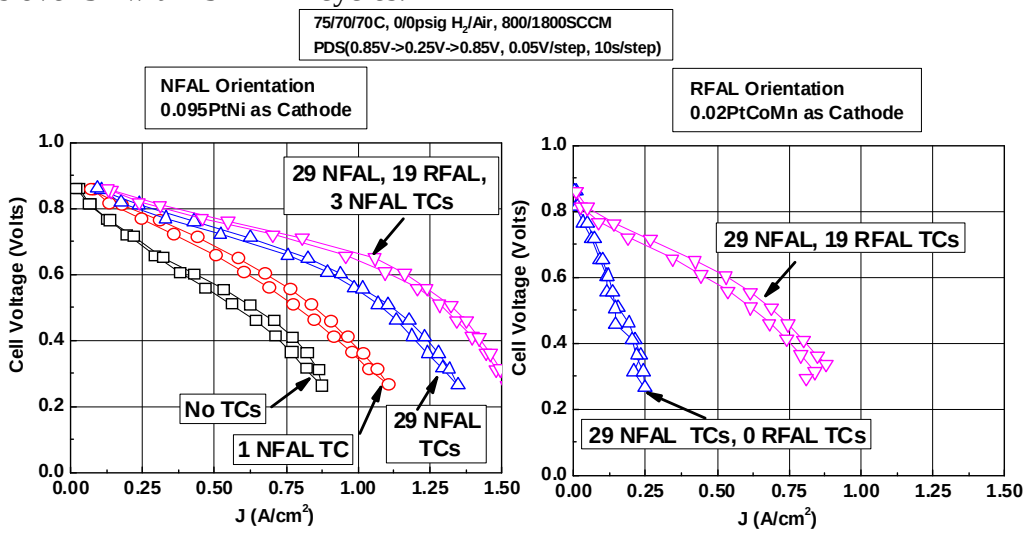

Figure 117. "PDS" H2/Air performance vs. conditioning state and MEA orientation (NFAL vs. RFAL).

Impact of Conditioning on BOC MEA Performance and Operational Robustness

Figure 118 summarizes the impact of anode conditioning on rated power performance (80°C) and steady state temperature sensitivity between 30 and 50°C. The left figure shows similar gains in H_2/air performance as indicated in Figure 117. HFR is relatively unchanged. The right figure shows that performance between 30-50°C is more than doubled after anode conditioning.

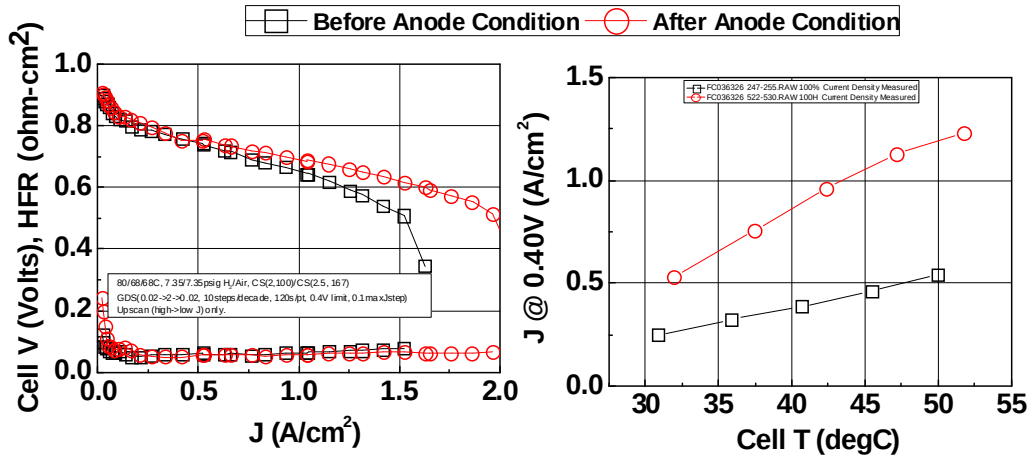

Figure 118. Impact of anode conditioning on 80°C H_2/Air performance (left) and steady state temperature sensitivity (right).

Mechanism Studies of Anode Break-in Conditioning

As noted in the Subtask 1.2 section, low-loaded, low surface area NSTF anode electrodes can suffer from substantial HOR kinetic losses, especially when not conditioned. ANL model predictions were that for the BOC MEA anode (0.02PtCoMn/NSTF with ca. 2.5cm^2/cm^2 SEF), the expected HOR kinetic loss at 80°C, 1atm$_{H2}$ would be about 15-20mV when unconditioned and < 5 mV when fully conditioned (Figure 119).

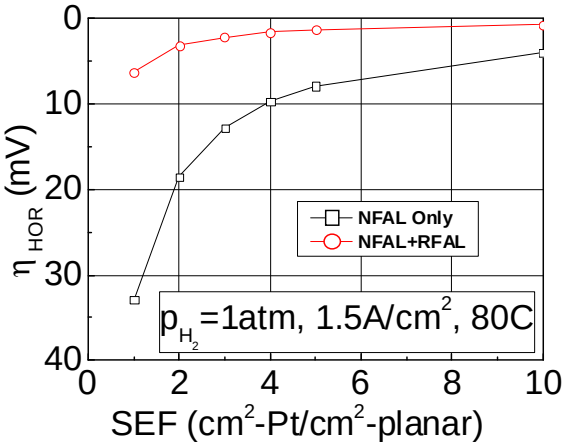

Figure 119. Modeled. HOR vs. anode conditioning state

Experimentally, the unconditioned HOR overpotential with the BOC MEA anode was closer to 60mV and conditioned was about 20mV (Figure 120). The cause for this larger-than expected unconditioned vs. conditioned HOR overpotential was not determined.

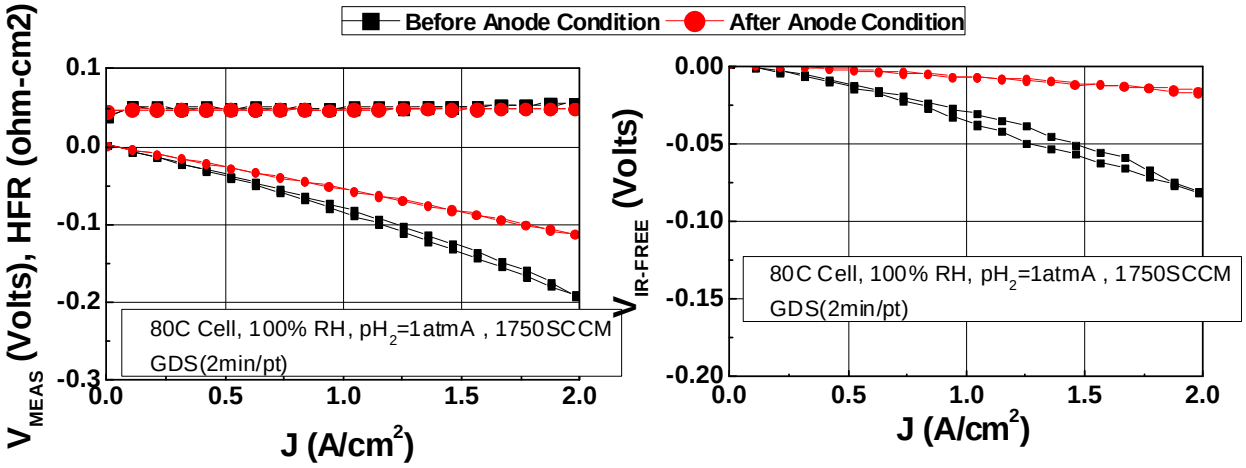

Figure 120. Impact of anode conditioning on 80°C H_2 pump polarization losses. (Left): Measured cell voltage and HFR. (Right): IR-Free cell V.

HOR losses were found to be the likely predominant reason for the large 80°C performance improvement after RFAL conditioning. Figure 121 (left) shows that BOC MEA performance depended strongly on anode conditioning state. HFR was relatively similar for all polarization curves, indicating resistance was not responsible for the performance differences. H_2 pump polarization curves (not shown) were used to correct the measured H_2/Air curves for ohmic and HOR losses, and the resultant curves are shown in Figure 121 (right), where the curves overlap over much of the polarization curve. This result strongly suggests that anode HOR losses were responsible.

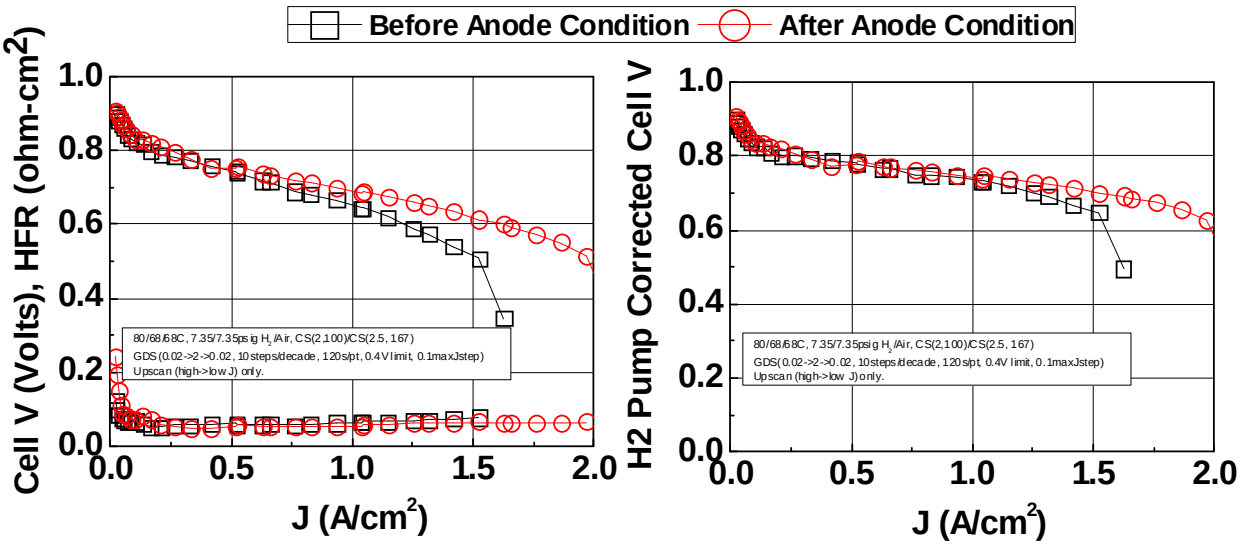

Figure 121. Evaluation of HOR losses as performance determining factor for BOC MEAs in either quad serpentine or FF2 flow fields, as a function of anode conditioning state.

Additional experiments were conducted to evaluate the state of the anode electrode vs. conditioning state via cyclic voltammetry. Figure 122 (left) shows that with only minimal anode conditioning (one thermal cycle), the hydrogen evolution kinetics (HER) are highly suppressed. After full anode conditioning (right), HER kinetics are improved. Surface areas by H_{UPD} are modestly similar between the two states.

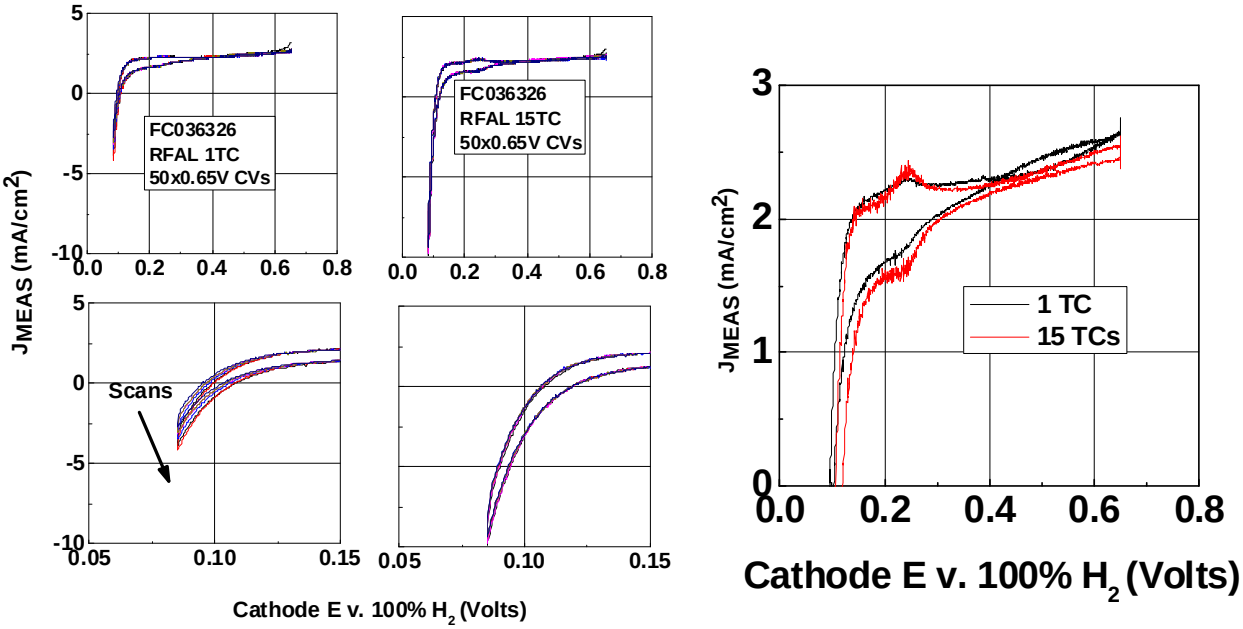

Figure 122. CVs of BOC MEA anode before anode conditioning (left) and after (right).

The anode conditioning also influenced the operational robustness of the BOC MEAs. ANL model predictions indicate that with a fully activated $2cm^2_{Pt}/cm^2_{planar}$ NSTF PtCoMn anode, the HOR overpotential at 80°C, 1atm H_2 is about 25mV, whereas at 20°C the overpotential is nearly 90mV. If the NSTF anode is flooded with water, leading to reduction in H_2 concentration at the

electrocatalyst surface, additional losses would be expected; reducing p_{H2} from 1.0 to 0.1atm will lead to a predicted 1.5A/cm^2 HOR overpotential of 90mV.

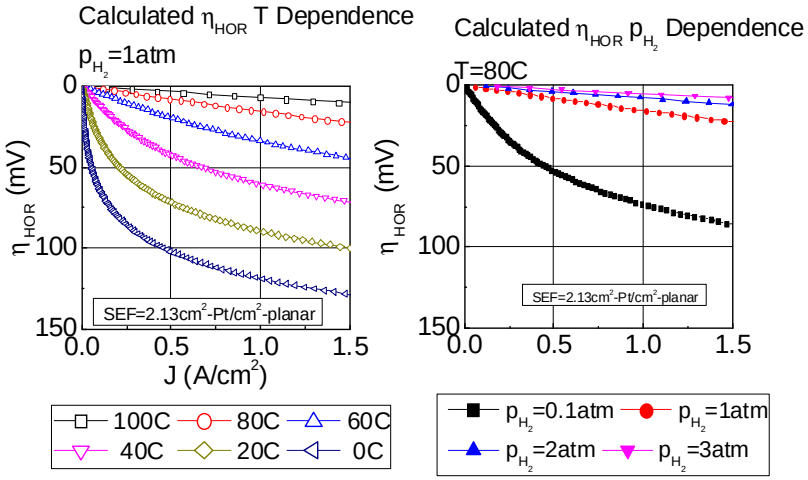

Figure 123. Modeled HOR overpotentials vs. T and p_{H2}. (Left): Impact of T at p_{H2}=1atm. (Right): Impact of p_{H2} at 80C.

The model predictions of the impact of poor HOR kinetics on low T performance were assessed via H_2 pump, taken at 45°C. Figure 124 (right) shows that prior to anode conditioning, the H_2 pump prior to anode conditioning showed extraordinarily poor H_2 pump performance, ca. 220mV at 0.1A/cm^2. After anode conditioning, the voltage at 0.1A/cm^2 was reduced to 9mV. A 200mV anode overpotential is qualitatively consistent with the 2x loss in 0.40V (cell) current density under H_2/Air, shown in Figure 124 (left).

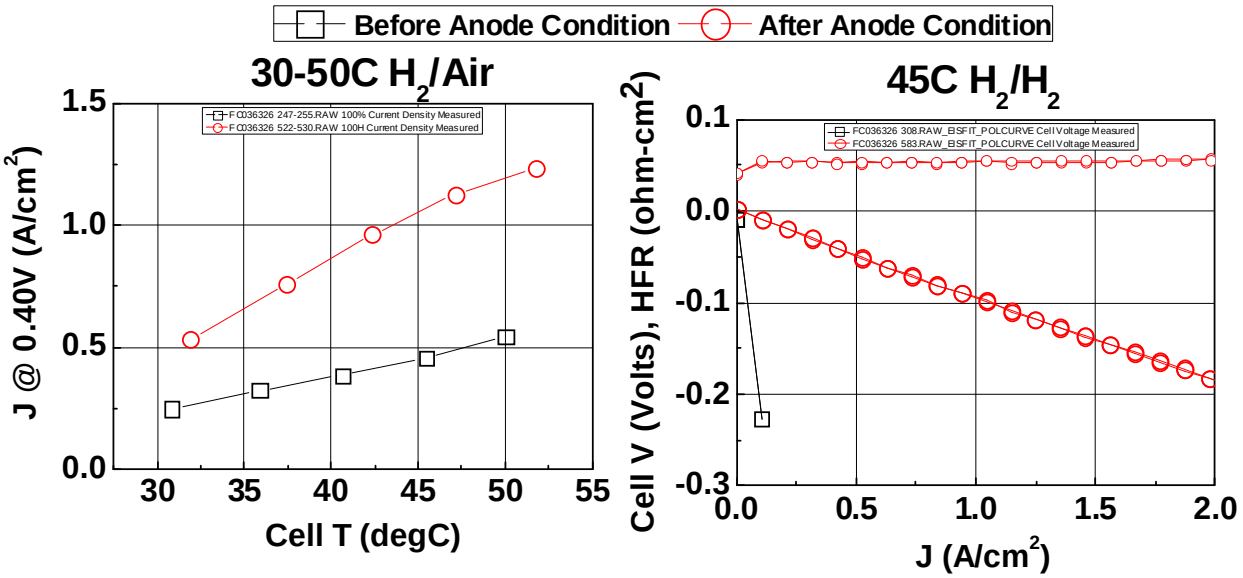

Figure 124. Impact of anode conditioning on temperature sensitivity (left) and 45°C H_2 pump.

In summary, anode conditioning has a very strong influence on rated power and low temperature performance with the BOC MEA. The loss is likely due to very poor HOR kinetics prior to conditioning. The root cause with the BOC MEA is not clear.

One possibility is the use of supported PEMs with the BOC MEA. As discussed in the Subtask 1.3 section, supported PEMs can have strong influence on ORR kinetics, depending upon the support type and PEM processing conditions. The subtask 1.3 work focused on the impact on ORR kinetics, but did not evaluate the influence on ultra-low PGM HOR anodes.

One check of this hypothesis is a comparison of break-in conditioning for BOC vs. baseline NSTF MEAs. Figure 125 compares the break-in process for BOC MEAs (left) and baseline NSTF MEAs (right), and Figure 126 summarizes polarization curves at various conditioning states. The baseline MEA contained 0.05PtCoMn/NSTF anode, 0.15PtCoMn/NSTF cathode, and a 3M 825EW 20u unsupported PEM. At the start of the RFAL anode conditioning phase, the baseline MEA anode had significantly higher H_2/Air performance than the BOC (comparison of red polarization curves). RFAL break-in rate of the baseline MEA was appreciably faster than the baseline (perhaps ~ 5 hours vs. 20hrs). Final performance at the end of RFAL conditioning was improved for both MEAs. Of key point is that for the baseline MEA, conditioning of the CCM anode did not improve the performance with the CCM cathode as the fuel cell cathode, whereas with the BOC MEA the performance was improved substantially.

This result is consistent with the hypothesis that the impact of the unconditioned BOC MEA anode, with BOC MEA supported PEM is the root cause for the need for extensive conditioning with BOC MEAs for entitlement performance and robustness. The experiments here are consistent, but have several confounding variables (cathode type, GDL types, and cathode interlayer).

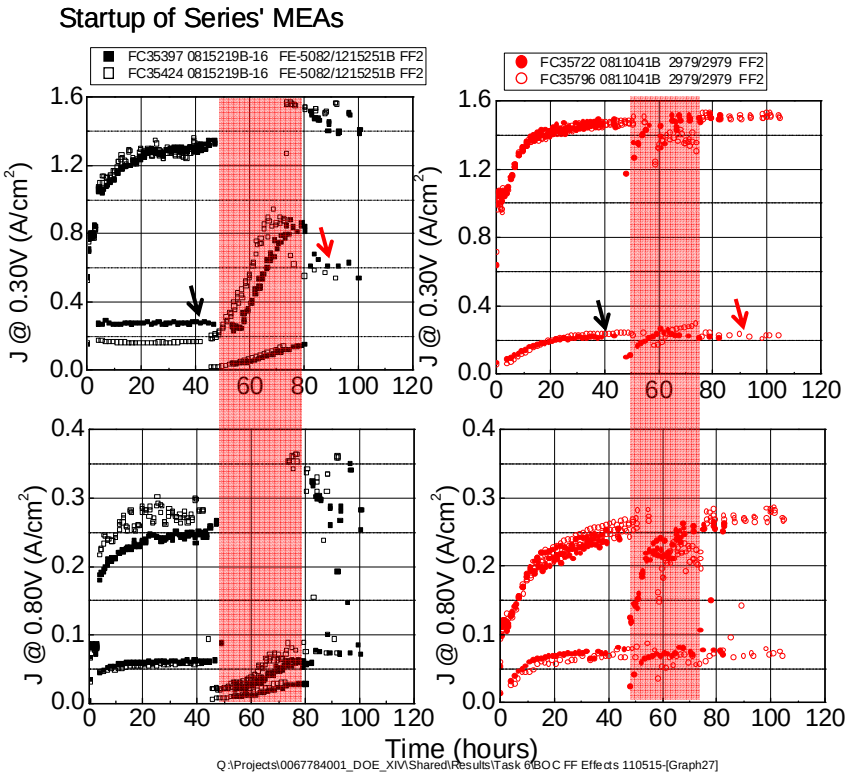

Figure 125. Comparison of break-in conditioning rates vs. MEA type. (Left): 2015(Sept.) BOC MEA. (Right): Baseline PtCoMn/NSTF MEAs. (Top): 0.30V current density. (Bottom): 0.80V current density. Red shaded region is RFAL conditioning.

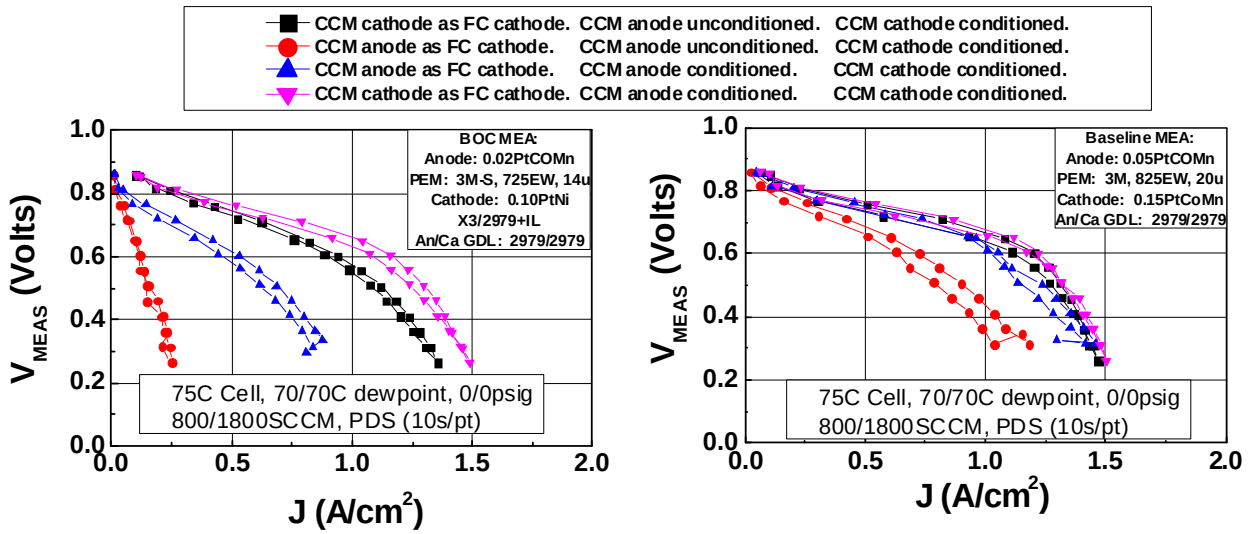

Figure 126. H_2/Air polarization curves vs. conditioning state. (Left): BOC MEA. (Right): Baseline MEA.

Limited experiments were also conducted to evaluate if the some factor with the pilot-scale fabrication caused an issue, such as differences in CCM fabrication process conditions or the input lots used. Figure 127 compares the break-in rate for BOC MEAs with either laboratory vs. pilot fabricated CCMs during initial cathode conditioning; input lots may not have been identical. Within a few hours, the laboratory CCM yielded demonstrably higher performance than the pilot-scale CCM, both near 75°C cell temperature and near 40°C cell temperature. As such, improved performance with relatively less break-in with BOC MEA components is feasible. Future work will include optimization of components and processes for more rapid anode conditioning and to lessen the anode conditioning requirement.

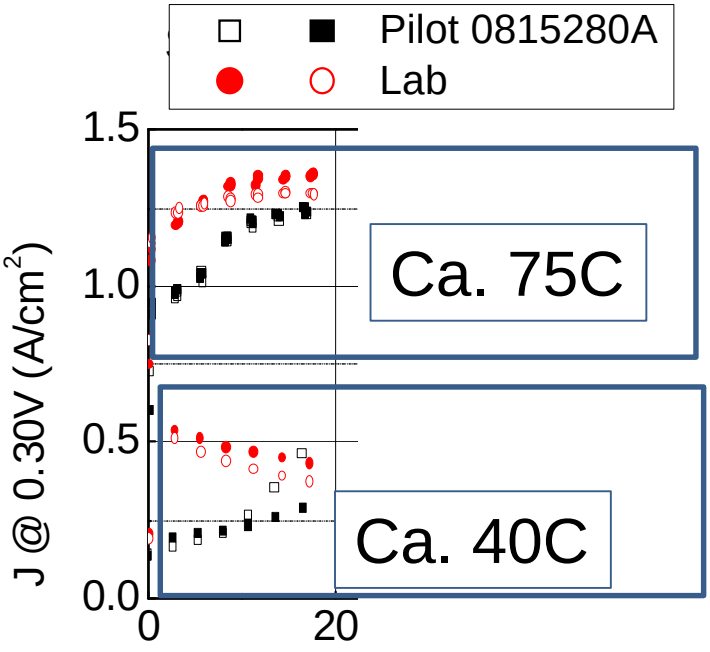

Figure 127. Comparison of initial break-in rates lab vs. pilot scale BOC CCMs

Mechanism Studies of Cathode Break-in Conditioning

In a first set of diagnostic experiments, the impact of cathode thermal cycles on mass activity under H_2/O_2 was evaluated. Project BOC MEAs were installed in cell, and H_2/O_2 and H_2/Air pol curves were taken as a function of the number of thermal cycles. Figure 128 (left) compares the H_2/O_2 pol curves as a function of thermal cycles, ranging from 0 up to 8. Each thermal cycle takes 1.5 hours. A small improvement was noted after 1 thermal cycle, with no changes thereafter. By comparison, large performance improvements were observed under H_2/Air (Figure 128 [right]), both in the kinetic regime and transport regime, consistent with previous results. HFR is essentially unchanged with thermal cycling.

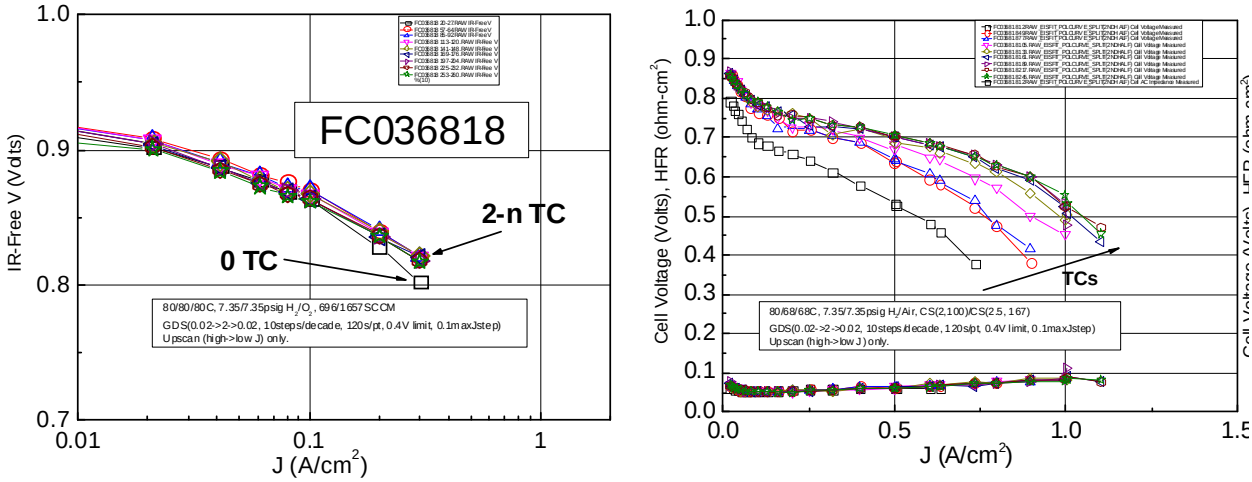

Figure 128. $H_2/O2$ (left) and H_2/Air polarization curves (right) with 0-n cathode thermal cycles

Figure 129 (left) summarizes the $0.900V_{IR\text{-}FREE}$ mass activity, extracted from the H_2/O_2 pol curves. Note these values are different than what is typically reported by 3M, possibly due to the differences in protocol (typically we measure using 20min holds at 0.90V). Mass activity was found to be completely established after a single thermal cycle, and decayed with each subsequent cycle, perhaps due to sample crossover failure noted at the end of the test. Figure 129 (right) compares IR-Free cell voltage at $0.02A/cm^2$, extracted from the H_2/O_2 and H_2/Air pol curves. Under H_2/O_2, the $0.02A/cm^2$ cell voltage is largely established without any thermal cycles. However, under H_2/Air, performance increases over 60mV with 1 thermal cycle, and is then steady. To reiterate, H_2/O_2 activity is established with the BOC cathode after 1 thermal cycle. The results in total are suggestive that with the BOC MEA, the key effect of cathode thermal cycles is a measurable reduction in transport restrictions of the cathode.

Additional experiments were conducted to evaluate the ORR activity break-in rate of PtNi/NSTF catalyst in RDE. Break-in seemed to occur in less than 100 cyclic voltammograms (CVs) and less than 2 hours. P1 Pt_3Ni_7 ($0.115mgPt/cm^2$ on substrate) was deposited on a glass carbon disk ($50ug/cm^2$) and cycled to various upper potential limits at 50mV/s, with periodic measurements of surface area and ORR activity. The experiments are summarized in Figure 130. Specific activity was found to increase over the first 8 to 30 scans (as high as $8mA/cm^2_{Pt}$ @ 0.900V), after which it decayed steadily. Specific area developed more slowly than specific activity, and typically reached a peak value within about 50 scans, and was modestly stable afterwards. The mass activity, dependent upon both specific activity and specific area, tended to peak between 20

– 100 scans. Each CV scan required on the order of 46 seconds, suggestive of the possibility of rapid activity and surface area development.

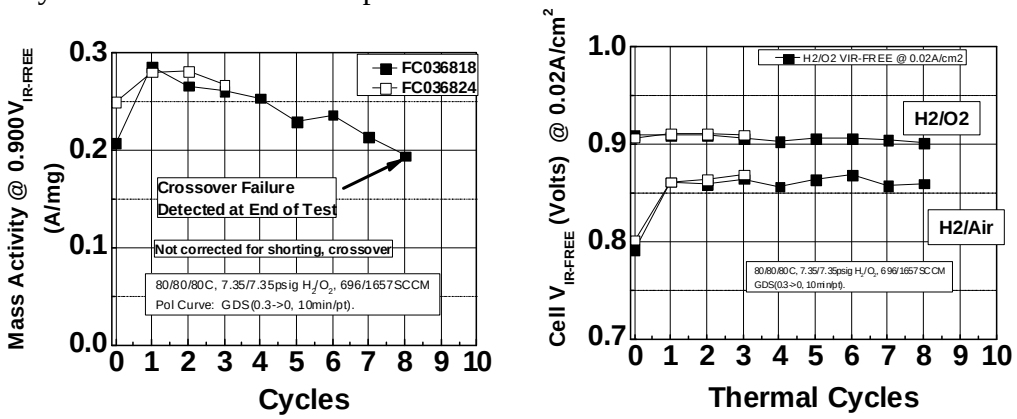

Figure 129. Mass Activity Evolution during Thermal Cycles, (from H_2/O_2 pol curves)

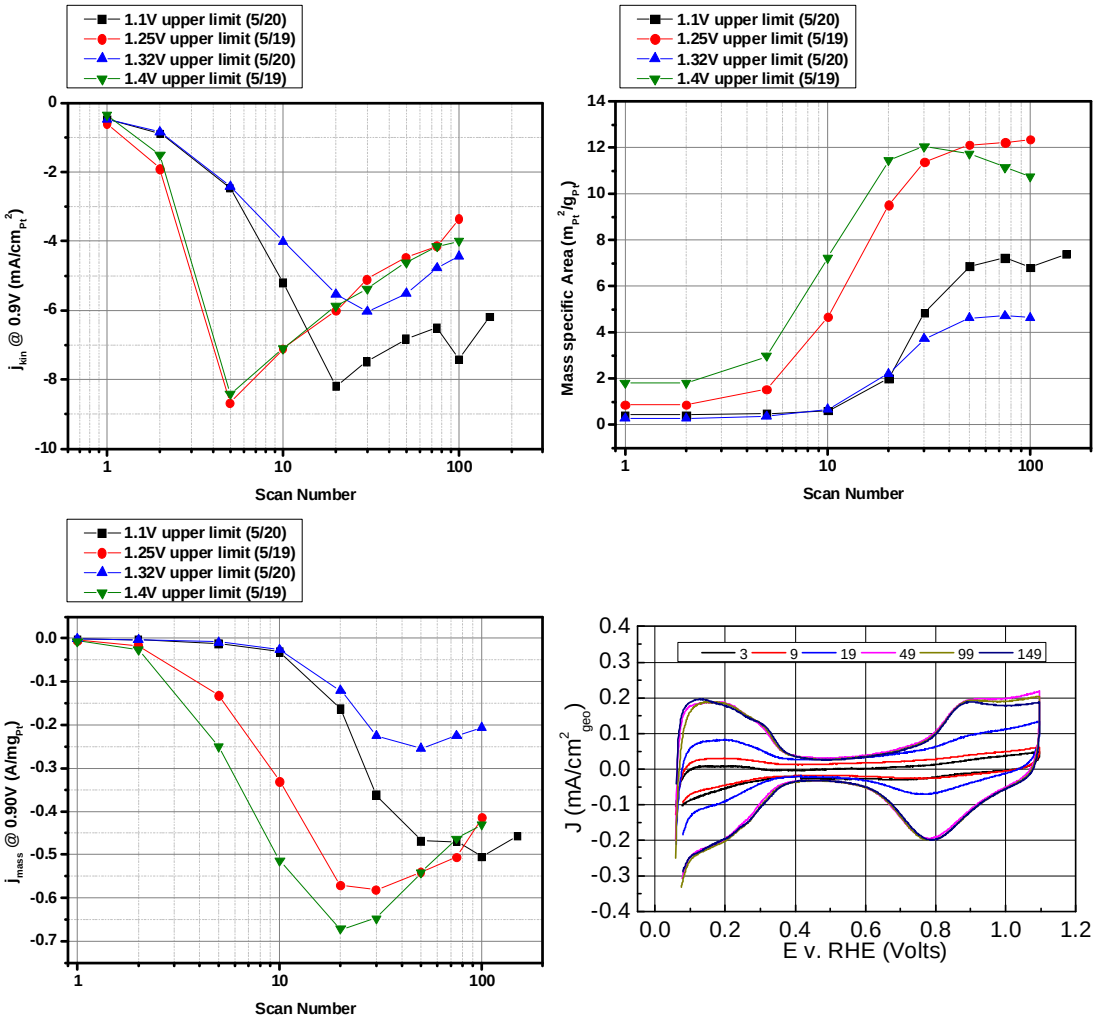

Figure 130. RDE assessment of P1 Pt_3Ni_7 activity and area evolution with cycles to different upper potential limits ($0.115 mgPt/cm^2$ on NSTF substrate, $50 ug/cm^2$ on GC disk). (Top left): Specific activity at 0.90V. (Top right): Specific area. (Bottom left): Mass activity. (Bottom right): CVs during RDE break-in.

The experiments in composite are consistent with the conclusion that the longer-than-desirable break-in rates of NSTF MEAs are not likely due to development of cathode activity. In the MEA

environment, peak mass activity occurs within one thermal cycle. These results are consistent with the observed improvement in H_2/Air kinetic performance shown in Figure 117 after a single thermal cycle. As such, we can discount the probability that the long break-in rate is due to contaminants which specifically adsorb to the cathode catalyst surface, such as Cl-, generic hydrocarbons, CO, and sulfur species.

Rapid Anode Break-in Method Development

In the anode break-in mechanism discussion above, thermal cycling was found to be effective at improving the HOR kinetics, resulting in dramatically improved H_2/Air performance and operational robustness. In 3M's experience, thermal cycling yields consistent results against a wide variety of contaminants (hydrocarbons, anions, sulfur) and is effective at reversibly reducing highly oxidized Pt electrocatalysts.

3M has previously explored methods to rapidly condition NSTF anodes, which typically involves repeated brief exposures of the anode to high potential, e.g. between 1.0 and 1.5V, where certain catalyst contaminants can be oxidized and removed.

As discussed in the anode mechanism section, one symptom of suppressed HOR kinetics with BOC anodes is a severe suppression of HER kinetics, measurable by CV. Figure 131 shows that good HER kinetics can be achieved with either 15 anode conditioning thermal cycles (2nd column) or with 100x CVs to 1.2V.

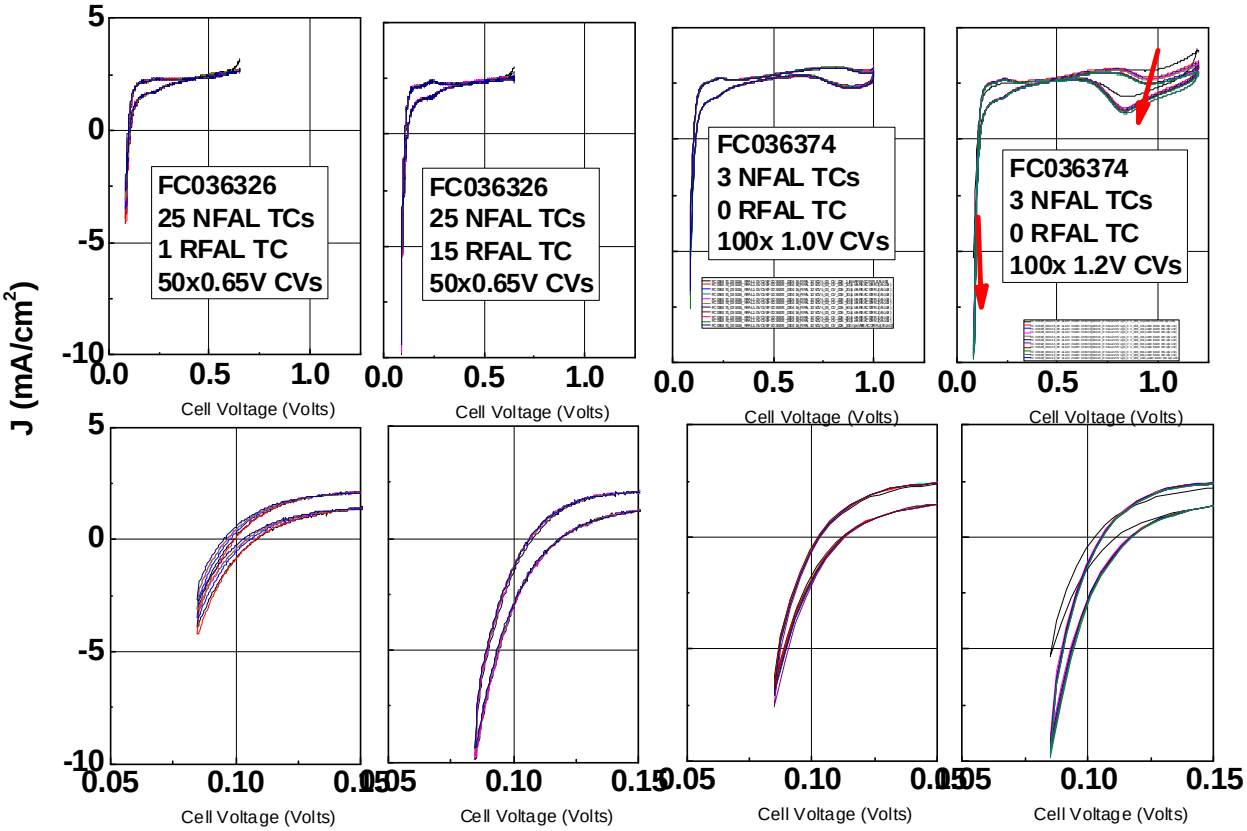

Figure 131. Impact of conditioning method on BOC anode HER kinetics. (Leftmost column): BOC MEA with full cathode conditioning and minimal anode conditioning. (2nd column): BOC MEA with full cathode and anode conditioning by thermal cycles. (3rd column): BOC MEA with partial cathode conditioning and attempted anode conditioning by 1.0V CVs. (Rightmost column): BOC MEA with partial cathode conditioning and attempted anode conditioning by 1.2V CVs.

Figure 132 shows that the anode HOR kinetics can also be improved by the anode CVs and to comparable performance as that obtained with thermal cycling.

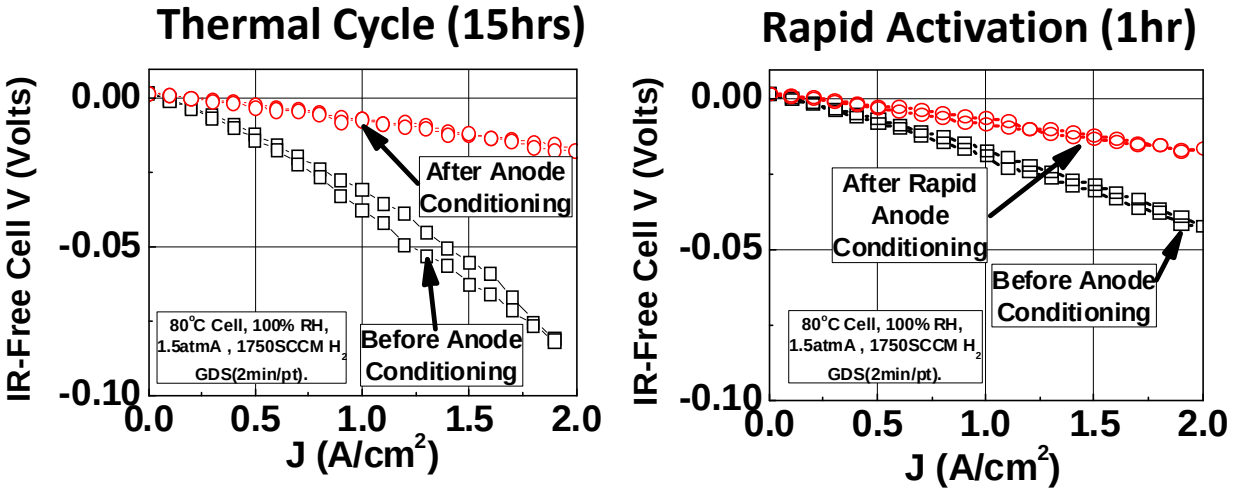

Figure 132. Impact of thermal cycling or anode CVs on HOR kinetics.

Figure 133 summarizes a sensitivity study to upper potential limit during anode conditioning with CVs. As the upper potential limit was increased from 0.60 to 0.80V, surface enhancement factor (SEF, or roughness factor) increased from 1.2 to 2.3cm^2/cm^2, and increased to 3.5cm^2/cm^2 at 1.1V (bottom left). The HER kinetics (bottom right) increased with scans to 1.0 or 1.2V.

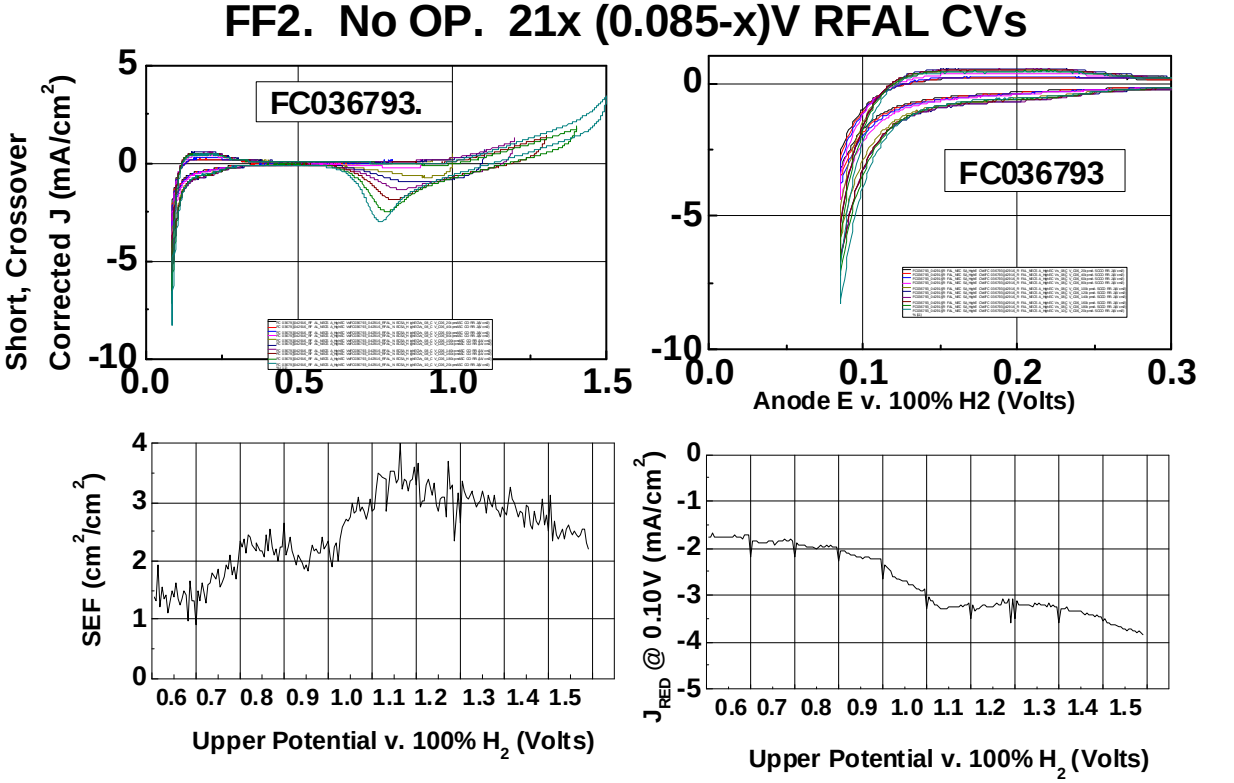

Figure 133. Evolution of anode CVs (top row), surface area (bottom left), and HER kinetic current density vs. CV upper potential limit ranging from 0.6 to 1.5V. 21 scans per upper potential limit.

While CVs were effective at activating the anode, it is not a practical solution to do in end-use stacks, as every cell would likely need to be individually cycled. Our understanding is that the important aspect of this anode conditioning approach is repeated exposure to high potentials.
One method believed to be more practical is operating the cell in the absence of hydrogen fuel, putting the anode into oxygen evolution mode with potential greater than 1.2V. Work was conducted to evaluate this as a possibility.

Numerous experimental variations on this approach were evaluated, including the fuel starvation current density, hold duration, and frequency of application. Figure 134 summarizes the performance during break-in for BOC MEAs, either with the standard cathode, then anode activation with thermal cycles, or by a cathode thermal cycle activation protocol which also incorporates frequent fuel starvation cycles. When fuel starvation cycles were incorporated, the H_2/Air performance at 0.30V (sensitive to HOR kinetics) increased much more rapidly and to a larger extent than without the fuel starvation cycles. Cathode H_2/Air kinetic performance (0.80V, right) appeared to be largely unaffected by the repeated fuel starvation cycles.

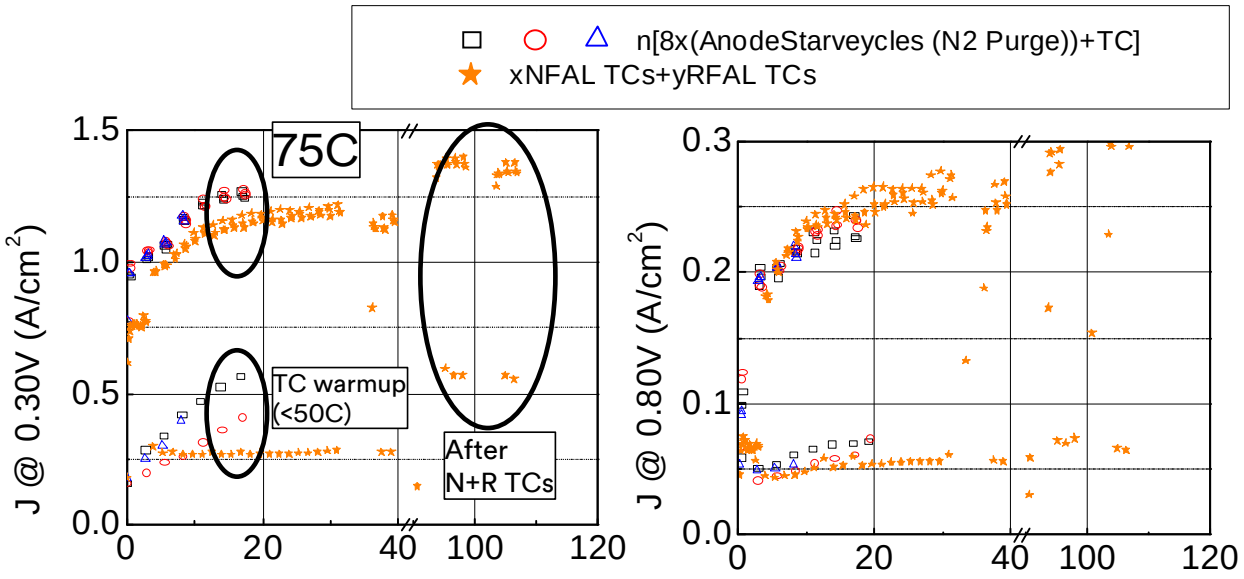

Figure 134. Cathode thermal cycle break-in conditioning with and without anode fuel starvation cycles. Orange stars are baseline method (cathode activation, then anode activation by CVs). Black, red and blue are combined cathode activation by thermal cycles and anode activation by fuel starvation.

The combined cathode thermal cycle with anode fuel starvation was ultimately effective at achieving entitlement performance, but very long conditioning times were needed. Figure 135 shows that performance under the 3M "High-Current Test" (HCT) (1.5atmA, 80°C) continued to improve over the course of 190 hours with the repeated cathode thermal cycles and fuel starvation, ultimately achieving the performance obtained with cathode, then anode thermal cycles alone.

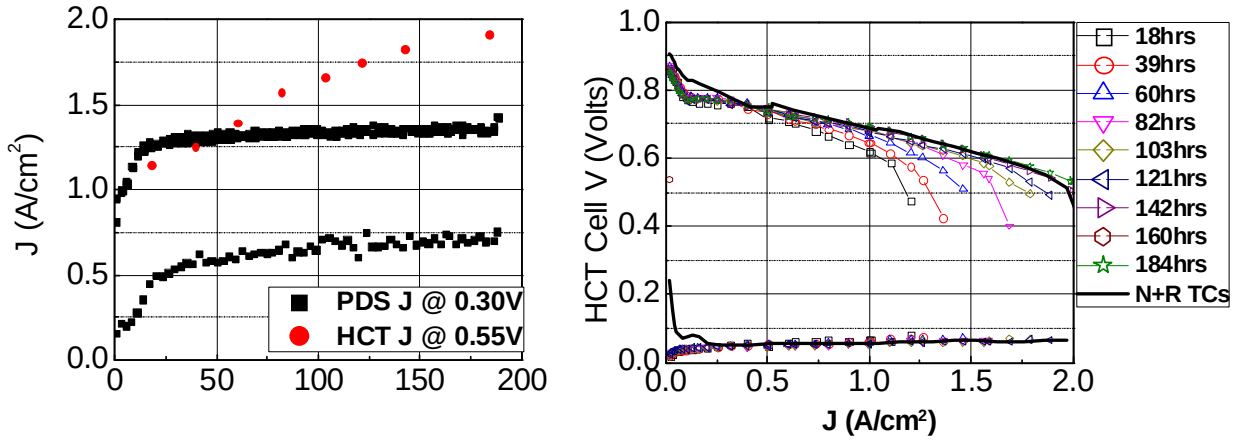

Figure 135. H_2/Air performance evolution with extended cathode thermal cycle and anode fuel starve conditioning. (Left): H_2/Air performance under ambient pressure PDS and 1.5atmA H_2/Air "HCT" performance. (Right): HCT H_2/Air performance.

Expected operational robustness was also achieved with extended anode starvation conditioning, as shown in Figure 136.

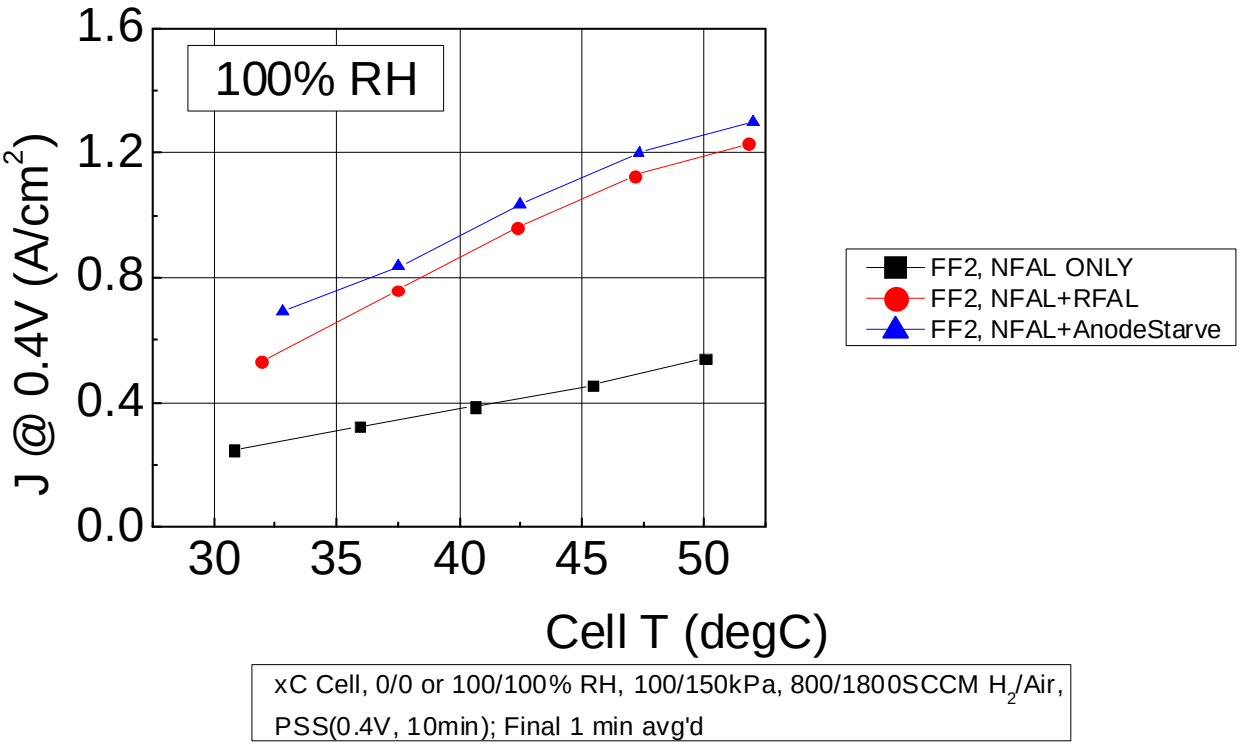

Figure 136. Temperature sensitivity for unconditioned anode (black) and anodes conditioned with either thermal cycles (red) or with anode starvation cycles (blue).

While effective, the time required made it impractical for use in the Task 6 stack testing at GM. An anode CV protocol was ultimately recommended and implemented.

Rapid Cathode Break-in Method Development

3M had previously developed a "fast" cathode conditioning protocol which consists of relatively rapid temperature and potential cycles. This protocol does not consist of the liquid water injection step used in the traditional 3M "thermal cycle" protocol. This protocol had previously

been found to be beneficial for dealloyed PtNi/NSTF cathodes, nearly achieving entitlement performance in ca. 4 hours (Figure 137).

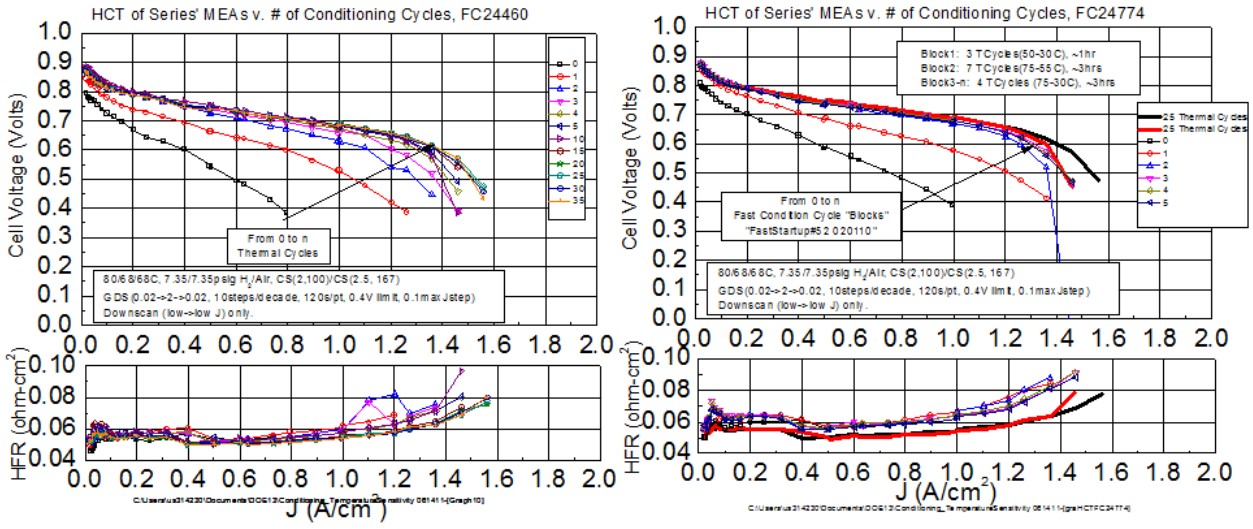

Figure 137. Comparison of Performance Evolution v. Conditioning Method. Dealloyed PtNi/NSTF cathode (not BOC, previous work). Left: Thermal Cycle. Right: Rapid Cycle.

Figure 138 compares the performance evolution obtained with BOC MEAs with either thermal cycling or with the fast conditioning protocol used in the previous work above. During the first 3 hours, the cell is operated with potential cycling only (no temperature cycling), after which either thermal cycling or fast conditioning commenced. With the BOC MEA, conditioning with the "fast" protocol did not occur any more quickly than for thermal cycling, and ultimate performance was below that obtained with thermal cycling.

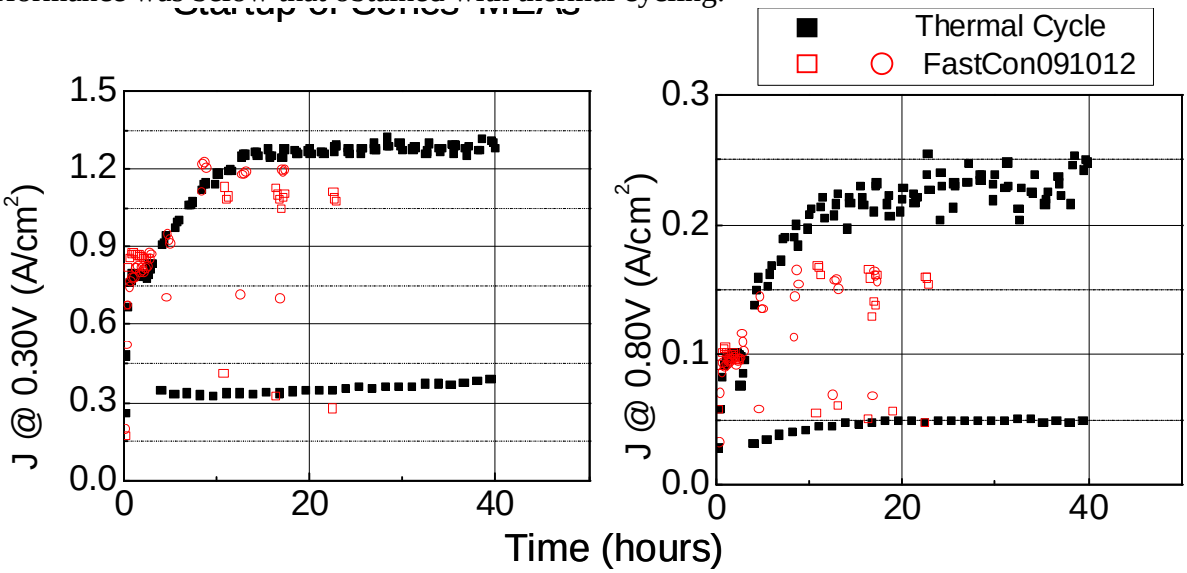

Figure 138. Comparison of Fast Conditioning to Thermal Cycle H_2/Air Performance evolution with BOC MEA.

One complexity with the BOC MEA is that the anode also requires substantial conditioning, and it is unclear if the fast protocol is activating the anode in a similar manner. To test this possibility, a second set of experiments were conducted where the BOC MEA anode was pre-activated by using anode CVs to high potential. Figure 139 shows that anode pre-activation by CVs was very effective at improving the initial performance at 0.30 and 0.80V. At 0.30V,

performance immediately reached 1.1A/cm^2 vs. ca. 0.80A/cm^2 without anode CVs. At 0.80V, performance achieved 0.18A/cm^2 vs. 0.10A/cm^2 without anode CVs.

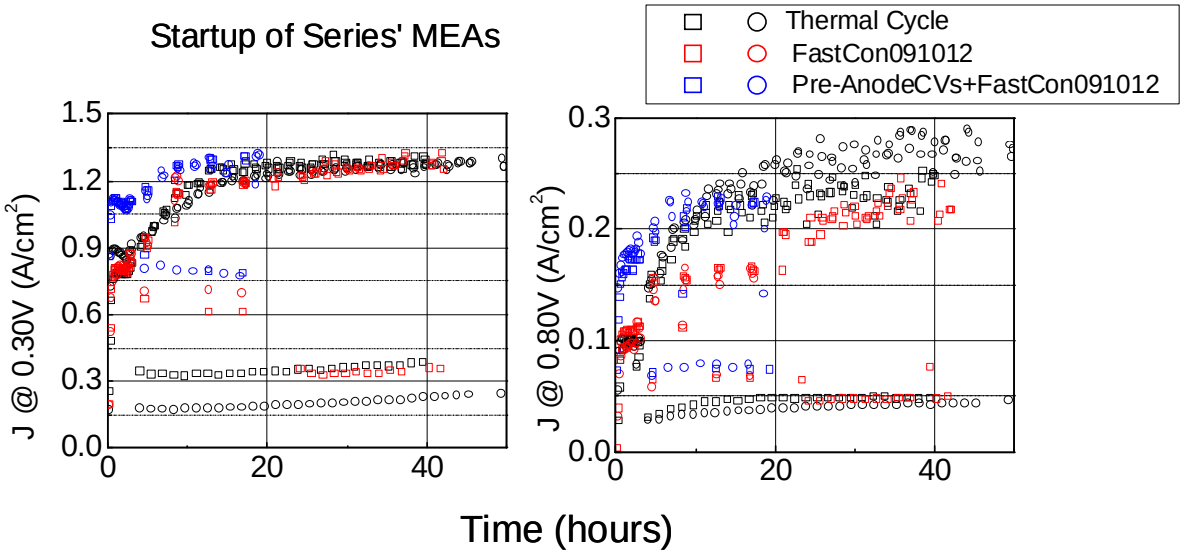

Figure 139. Comparison of Thermal Cycling to Fast Cathode Conditioning with or without Anode Pre-Activation by CVs.

Project BOC MEA Differential Cell Method Development

Per a request from Argonne, March and Sept. (2015) BOC MEAs were evaluated in differential cell to establish a performance model, ultimately used to generate a cost model.
Differential cell evaluation had not been conducted before at 3M with NSTF MEAs. Significant development was required to enable accurate, repeatable differential cell testing methodologies.
Tests were conducted in a differential cell to minimize data inaccuracy due to down-the-channel effects. A 50cm^2 active area MEA was installed in a 50cm^2 test cell with FF2 cathode, and a 1 mil polyimide sheet with 5cm^2 aperture was placed between the CCM cathode and cathode GDL to define a 5cm^2 active area. This was ultimately determined to be a problematic method, leading to abnormally high electronic shorting and hydrogen crossover, suppressing the OCV. This will be discussed in more detail later.

During method development, several significant issues were identified and resolved. One key general challenge was that performance in the segmented cell was lower than that obtained in 50cm^2 format, with identical materials, unless substantial conditioning was conducted. A second key issue was that the segmented cell MEAs suffered from higher rates of reversible performance loss than for 50cm^2 format MEAs.

One example of the challenge is shown in Figure 140, which compares the performance evolution during initial cathode conditioning with project BOC MEAs in either 50cm^2 or 5cm^2 differential format. Performance in 5cm^2 differential format was highly suppressed relative to the 50cm^2 MEAs at all cell voltages. The only difference between the two test types was the inclusion of the 1 mil polyimide layer in the differential cell (it is not believed that the polyimide was the cause, based on several other experiments not discussed here).

Based on our work towards understanding the break-in conditioning requirements for project BOC MEAs, it was suspected that conditioning of the NSTF MEA anode would be required to achieve entitlement performance. Figure 141 compares the performance evolution during break-in conditioning of identical project BOC MEAs in 50cm^2 non-differential and 5cm^2 differential cells. The plot summarizes performance at both 0.30V and 0.80V, and includes both cathode conditioning ("NFAL", red regions) and anode conditioning ("RFAL", gray regions). Both cell's cathodes were initially conditioned over the first 50 hours after which steady performance was apparently achieved. The performance in the 5cm^2 cell was substantially below that with the 50cm^2 cell. Next the MEA anodes were conditioned for ca. 24 hours. With both cell configurations, performance improved during anode conditioning, suggesting that prior to this conditioning the anode HOR was highly suppressed. Conditioning of the MEA cathode was then resumed. NFAL performance for both MEA types improved as compared to the NFAL performance prior to anode conditioning.

With the differential cell, additional testing was conducted between 60 and 150 hours, and the performance degraded, even with frequent cathode reconditions. The MEA anode was then again conditioned, after which the NFAL performance was recovered. This result suggests that the degradation between 60 and 150 hours was due to anode deactivation. This process was repeated several additional times, and performance at 0.30V continued to improve.

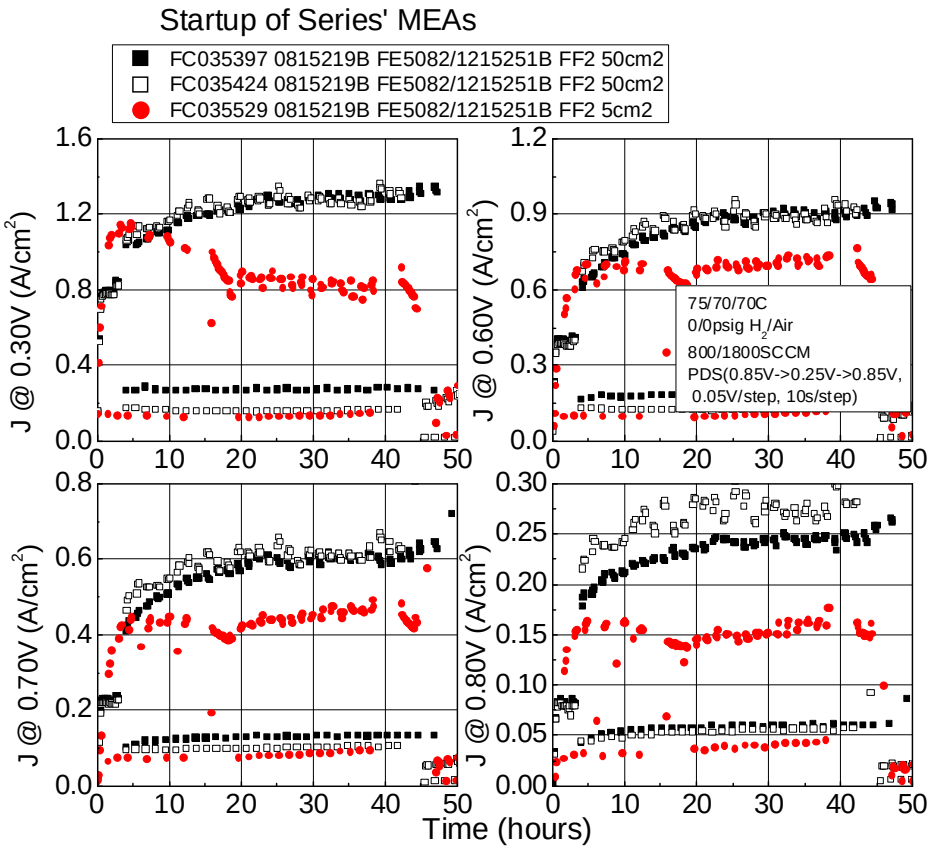

Figure 140. Break-in Conditioning of BOC MEAs in FF2 (non-differential v. differential).

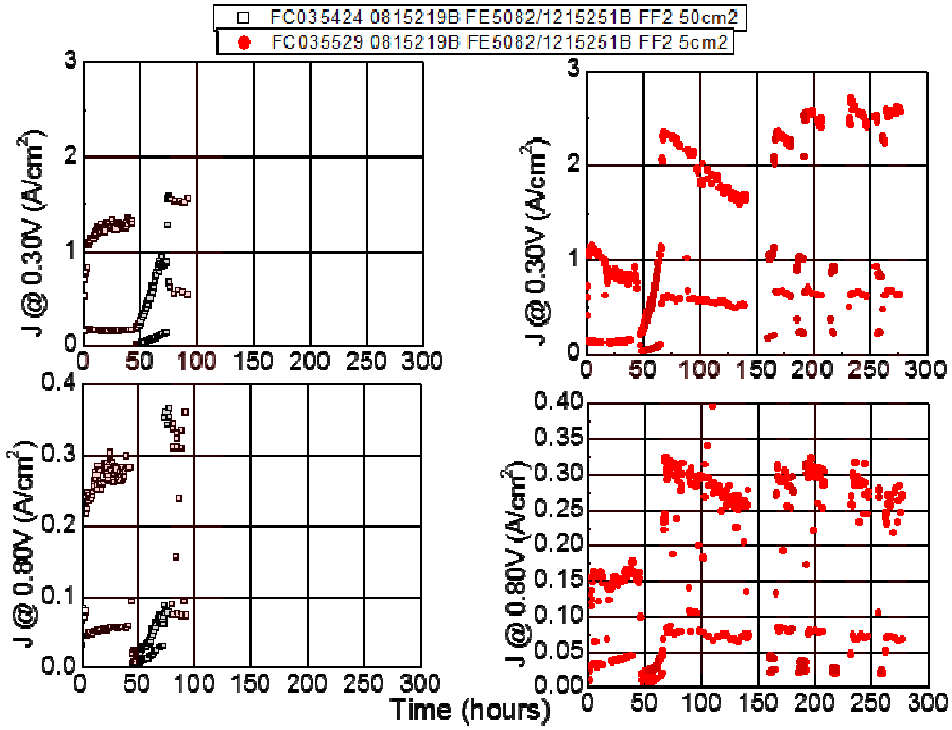

Figure 141. Conditioning Time Traces of BOC MEA in either 50cm² non-differential (left) or 5cm² differential cell (right). Red shaded region refer to NFAL operation, grey-shaded regions correspond to RFAL operation. 75/70/70°C cell, 800/1800SCCM H_2/Air, 0/0psig.

Figure 142 summarizes how the differential cell performance and HFR evolved over time at a baseline test condition (80°C, 100% RH, 1.5atmA). The conditioning protocol predominately impacted the high current density performance, with only modest changes in HFR. The results are consistent with the performance improvement being due to improving HOR kinetics with conditioning.

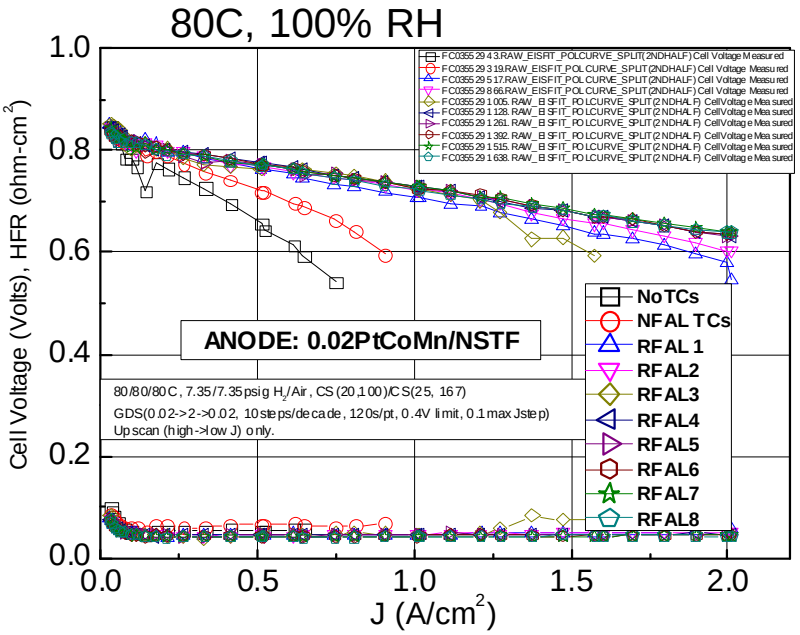

Figure 142. Differential Cell H_2/Air Performance Evolution w/ Repeated NFAL+RFAL Condition.

The unstable performance in differential cell, noted earlier in this section, was determined to be at least in part due to a test station issue. In essence, the station was forcing a small current (2mA/cm^2) when the station not supposed to apply any current, forcing the anode into OER mode. This lead to suppressed and erratic performance, summarized in Figure 143 ("before station repair"). The performance suppression was due to the high degree of extended oxidation leading to suppressed HOR, requiring anode-specific conditioning to reverse. The erratic, non-repeatable performance before station repair was likely due to different amounts of time spent in reversal, leading to varying extents of Pt oxidation and HOR suppression. Once the station issue was identified and resolved, significantly improved, repeatable performance was obtained.

With testing issues resolved, performance and mass activity in differential cell was found to be largely similar to that obtained in 50cm^2, non-differential mode. Figure 144 shows excellent agreement between differential and non-differential cells between 0 – 2 A/cm^2. Table 16 shows that the mass activity between non-differential and differential cells was essentially identical, but the specific area in differential cell was larger than non-differential, perhaps due to the high crossover and shorting induced by the differential cell build method.

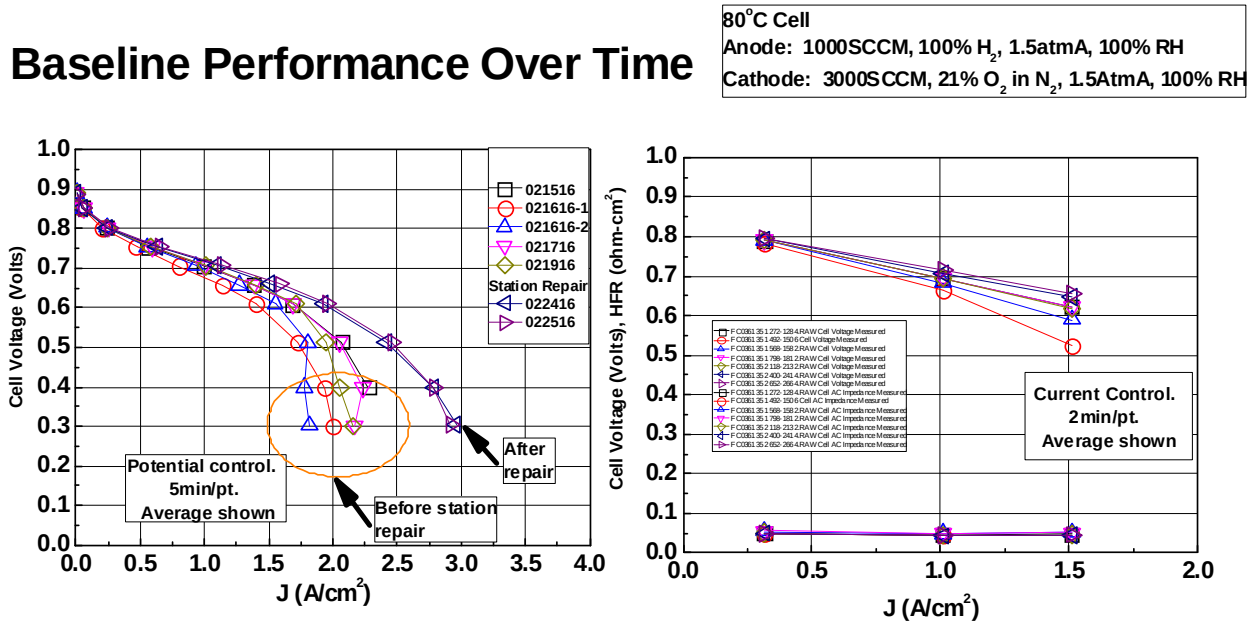

Figure 143. Baseline Performance, Before and After Station Repair.

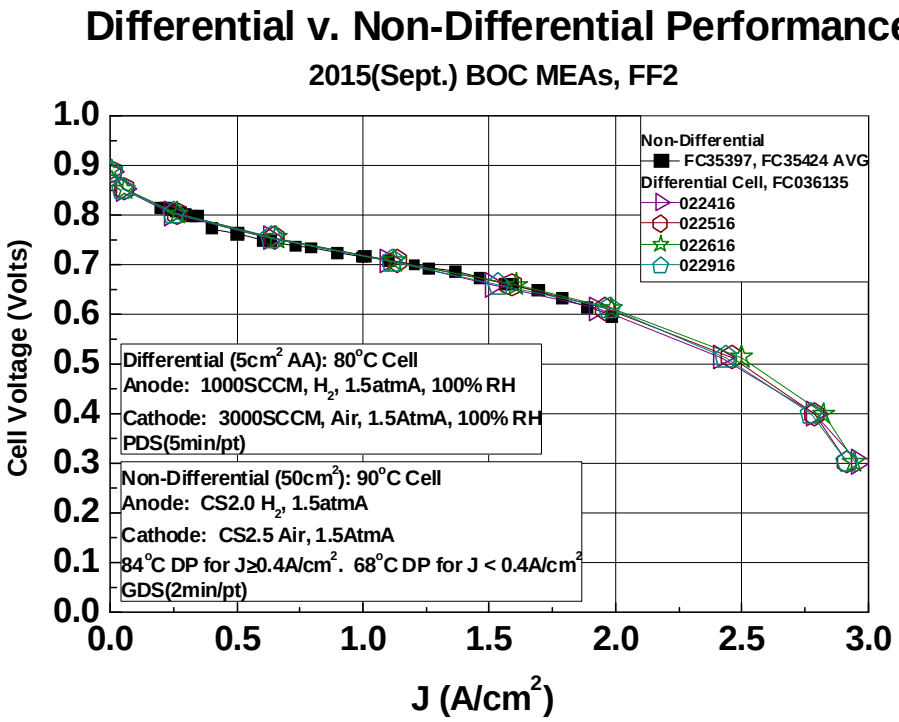

Figure 144. Comparison of project downselect BOC MEAs' 1.5atmA H_2/Air performance for differential and non-differential cells

Table 16. Specific Area, Mass Activity of Several Differential and non-Differential BOC and BOC-like MEAs			
	# of MEAs	Specific Area (m^2/g)	Mass Activity (A/mg)
$5cm^2$ differential	10	22±2.6	0.38±0.064
$50cm^2$ non-differential	4	18±2.5	0.38±0.058

One consistent observation with the differential cell testing has been low OCV, and high electronic shorting conductivity and H_2 crossover. An analysis summarized in Table 17 shows that on average, the $5cm^2$ differential cells had shorting conductivity nearly 40x higher than the non-differential $50cm^2$ cells, and the H_2 crossover was nearly 2x higher. Assuming 70mV/decade kinetics, the increased shorting and crossover of the differential cells would cause ca. 60mV of loss in OCV, qualitatively consistent with the observed OCV gap between differential and non-differential cells.

Table 17. Shorting and Crossover of Several Differential and non-Differential BOC and BOC-like MEAs			
	n MEAs	e- Short Cond (mS/cm^2)	H_2 Crossover (mA/cm^2)
$5cm^2$ differential, edge protected	10	19 ± 8	8±2
$50cm^2$ non-differential, edge protected	2	0.5 ± 0.3	3.5 ± 0.25

It was ultimately determined that the likely cause of the higher shorting conductivity and crossover was a physical artifact due to the method used to assemble the differential cells; it does not reflect intrinsically higher shorting and crossover in the $5cm^2$ active area. The differential cells used standard $50cm^2$ components (4x4" CCM, $50cm^2$ anode and cathode gaskets, $50cm^2$ anode GDL, $50cm^2$ cathode GDL w/ IL), where the $5cm^2$ active area was determined by placing

a 1mil polyimide layer between the NSTF cathode (on CCM) and the cathode interlayer (on GDL). The polyimide layer had a die-cut 5cm^2 aperture in the center of the flow field area, and was located at the cathode only. Under typical operation, it was expected that the limited lateral oxygen transport through the thin NSTF cathode electrode (< 1micron) and the relatively low ionic conductivity of the cathode interlayer would be sufficiently low to effectively limit all reaction within the 5cm^2 active area in each respective layer. The good agreement in mass activity and H_2/Air performance between differential cell and non-differential cell supports this expectation, as discussed above.

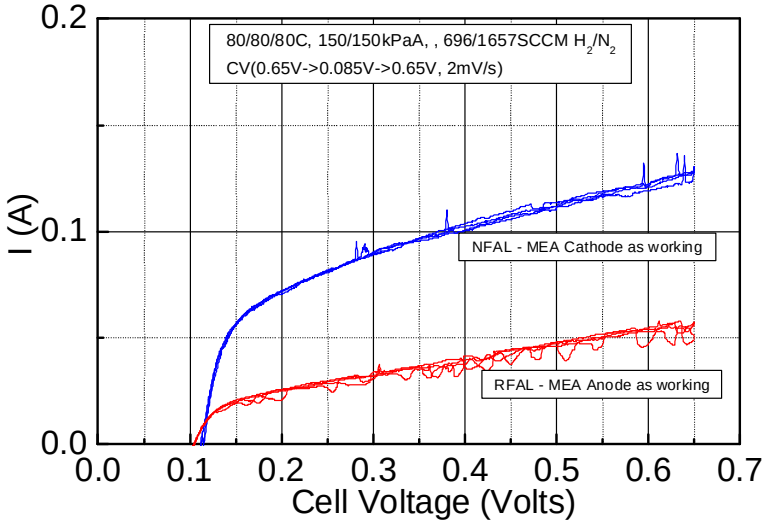

Figure 145. Shorting and Crossover Measurements v. Working Electrode.

However, what was not appreciated initially is that this mode of area limitation creates an artifact for electronic shorting and crossover measurements. In our laboratory, these are typically estimated by operating the cell with H_2/N_2 (N_2 to working) and taking slow (2mV/s) CVs. The slope and intercept of the CVs is estimated (between 0.4-0.6V) to determine the shorting conductivity and crossover, respectively (see Figure 145). With the physical differential cell setup, we were likely measuring shorting and crossover of the entire 50cm^2 area of the CCM. For crossover, we feed 100% H_2 to the MEA anode; H_2 crosses over through the entirety of the exposed PEM (50cm^2) to the NSTF cathode (50cm^2), where it is electrochemically oxidized and the total current is measured. For electronic shorting, a similar situation arises. To test this hypothesis, shorting and crossover measurements were made with the MEA in both normal and reversed orientations (either MEA cathode or MEA anode as working). As expected, the crossover was reduced when the MEA cathode was used as the 100% H_2 counter/reference, as the crossover area is limited to 5cm^2. Shorting was relatively unchanged, as expected.

Subtask Conclusions

Experiments were conducted to understand how the anode GDL backing, demonstrated to substantially impact low temperature steady state performance, influences MEA water balance. Anode GDLs which enable higher performance have higher apparent limiting water removal rates than low performing anode GDLs. All GDLs evaluated appear to follow a trend that low temperature steady state performance of NSTF MEAs decreases as the limiting anode GDL water removal rate is approached.

Significant work was conducted evaluating the impact and mechanism of the required break-in conditioning of BOC MEAs, and methods were evaluated towards accelerating the break-in. Studies confirmed that both the NSTF anode and cathode need to be conditioned to enable entitlement performance and operational robustness. The cathode mass activity was found to be obtained very rapidly with standard 3M conditioning protocols, in a few hours or less. The anode conditioning appears to dramatically improve the HOR kinetics. Model predictions indicate that HOR overpotential losses of low loaded, low area anode electrodes can be strongly impacted by operating temperature, blocked surface area, and dilution, qualitatively consistent with the observed experimental effects. BOC MEA performance and operational robustness were demonstrably improved with specific anode conditioning.

Work was conducted to develop more rapid, stack friendly conditioning methods. For anode conditioning, use of high potential excursions were effective, either through use of anode CVs or fuel starvation protocols. For cathode conditioning, a previously-determined method found to be effective for PtNi/NSTF cathodes was not effective for the BOC cathode.

Lastly, work was conducted to establish reliable, reproducible differential cell testing with BOC MEAs at 3M. Challenges related to required break-in conditioning of the NSTF anode, as well as a test station issue, were identified and overcome, resulting in expected and relatively stable performance. The resultant method was used to generate data to be used for performance and cost modeling at ANL and SA, respectively.

Future Directions

Break-in conditioning remains a key commercialization gap for this technology. Additional work is needed to determine specific component interactions with BOC MEA components which influence break-in, with a key initial focus on evaluating BOC anode interactions with supported PEMs.

Task 5. Durability Evaluation and Performance Degradation Mitigation

- *Subtask 5.1 Candidate Component Evaluation and Ex-situ Characterization Subtask 5.2 Baseline MEA Evaluation and Ex-situ Characterization*
- *Subtask 5.3 Interim Best of Class MEA Evaluation and Ex-situ Characterization*
- *Subtask 5.4 Best of Class MEA Evaluation and Ex-situ Characterization*
- *Subtask 5.5 Mitigation of Irreversible and Reversible Rated Power Performance Degradation*

A first overall objective of Task 5 is evaluation of components and integrated MEAs towards achieving the MEA durability targets, evaluated via 50cm^2 single cell accelerated stress tests. The primary objectives of sub-tasks 5.1-5.4 are fuel cell evaluation under specified accelerated stress tests (1-4, 6, U.S. DRIVE Partnership Fuel Cell Technical Team "Cell Component Accelerated Stress Test and Polarization Curve Protocols for Polymer Electrolyte Membrane Fuel Cells, Rev. Dec. 16, 2010) with periodic in-situ diagnostics to evaluate performance as the MEA ages and ex-situ diagnostics to determine the root-cause component material changes responsible for performance loss.
A second objective of Task 5, addressed in subtask 5.5, is mitigation of reversible and irreversible modes of rated power loss. As background, reduction in rated power output is known to occur in the literature via several well-documented modes, including cathode catalyst mass activity degradation, membrane conductivity degradation, and gas diffusion layer reactant transport degradation; the mechanisms by which these component degradations result in rated power loss are relatively well-understood. However, at least one additional rated power loss mode has been observed to occur in both conventional supported nanoparticle and extended-surface area catalyst systems, such as 3M NSTF, which appears to be caused by an entirely new and not-fully-understood mechanism. The loss is manifested as a reduction in peak current density and is correlated to cathode catalyst Pt surface area per unit MEA area (cm^2_{Pt}/cm^2_{planar}) below a critical level, SA_{CRIT}, which depends upon the cathode catalyst support, loading, and composition. SA_{CRIT} for 3M NSTF Pt alloy cathodes occurs at loadings near or below the cathode PGM loadings necessary to achieve the 2017 targets (~0.075-10mg_{PGM}/cm^2_{planar}); based on literature reports, the loading at which this issue occurs with conventional supported Pt nanoparticle cathodes can be significantly higher (onset at ~0.3mg_{Pt}/cm^2).

This SA_{CRIT}-related rated power loss mode has both irreversible and reversible components, both related due to decrease of active cathode surface area. *Irreversible* rated power loss, due to this mode, is caused by irreversible decrease of the cathode Pt surface area below SA_{CRIT}, such as induced by well-documented catalyst degradation modes such as Pt dissolution and agglomeration. *Reversible* rated power losses are believed to occur by reversibly adsorbed catalytic contaminants (such as Cl^- ions), and the rated power loss is recovered by removing the adsorbed contaminants. The mechanism(s) by which the above physical causes induce the rated power loss is not known with certainty, but hypotheses exist which provide direction for initial study.

The work under subtask 5.5 will begin with internal and external literature review to gather data to support or refute our existing hypotheses and if warranted, generation of new hypotheses. The team will then design specific 50cm^2 fuel cell experiments, coupled with in-situ and ex-situ

diagnostics, to further refine mechanistic understanding and narrow in on a few specific likely root causes. If identified, these root causes will provide experimental direction towards specific material modifications to reduce rated power loss.

Subtasks 5.1-5.4 - Component/MEA Durability Evaluation (ASTs)

Subtask Overview

Evaluation of components and integrated MEAs towards achieving the MEA durability targets, evaluated via 50cm^2 single cell accelerated stress tests. The primary objectives of sub-tasks 5.1-5.4 are fuel cell evaluation under specified accelerated stress tests (1-4, 6, U.S. DRIVE Partnership Fuel Cell Technical Team "Cell Component Accelerated Stress Test and Polarization Curve Protocols for Polymer Electrolyte Membrane Fuel Cells, Rev. Dec. 16, 2010) with periodic in-situ diagnostics to evaluate performance as the MEA ages and ex-situ diagnostics to determine the root-cause component material changes responsible for performance loss.

Subtask High Level Work Summary

Several Best of Class MEA candidate components were evaluated for durability under the DOE MEA chemical, cathode support, and cathode electrocatalyst ASTs.

Subtask Key Results

MEA Chemical Durability

Several BOC MEA candidate components were evaluated for their impact on the MEA chemical durability, including several ultra-low PGM anode catalysts, two cathode catalysts, and the PEMs with and without additive.

Initial experiments evaluated the impact of NSTF cathode catalyst composition. At the time of the experiment, the anticipated downselected cathode catalyst was a dealloyed PtNi/NSTF catalyst. A key concern was the expected relatively larger amount of Ni transition metal leaching from the cathode to the PEM, possibly leading to accelerated chemical degradation. Figure 146 compares NSTF MEAs with either the baseline 0.15PtCoMn/NSTF cathode or a dealloyed 0.125PtNi/NSTF cathode. Tests were conducted with unsupported 20u PEMs with additive. The baseline MEAs exceeded 1000 hours, surpassing the DOE 500 hour target. OCV decreased rapidly over the first 100 hours but then stabilized. The rapid deactivation is due largely to reversible deactivation of ORR kinetics on the cathode. With PtNi/NSTF cathode, the MEAs exceeded 500 hours with relatively stable OCV, after which the test was halted. F^- emission rates remained stable and low, and electronic shorting and crossover were unchanged. The OCV remained appreciably higher with the PtNi cathode than the PtCoMn, likely due to the intrinsically higher ORR activity. It was concluded that PtNi did not appear to induce additional degradation over PtCoMn.

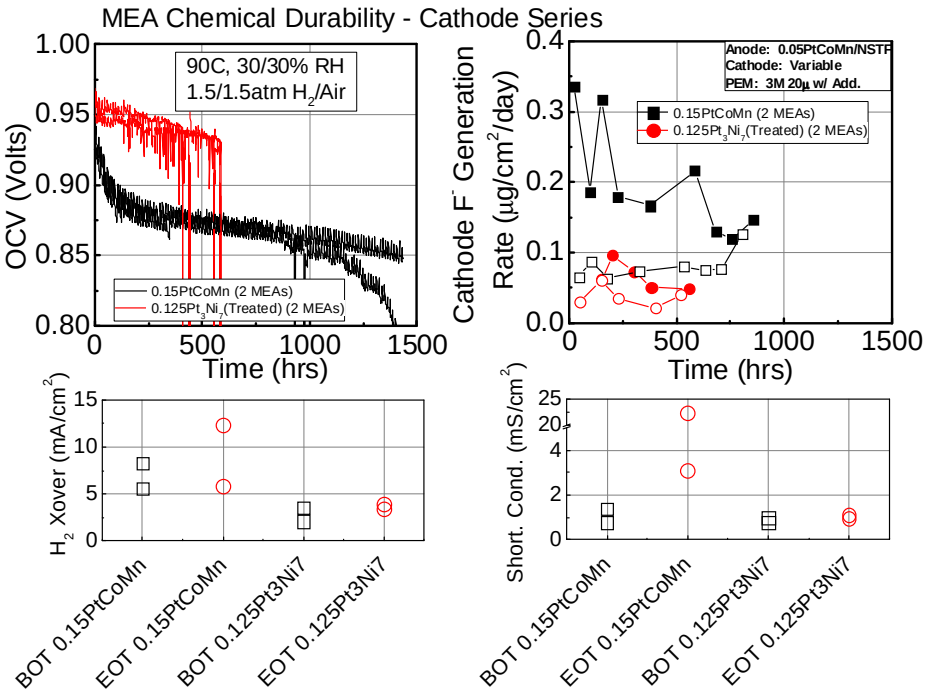

Figure 146. OCV hold durability vs. cathode type

Next, the impact of anode catalyst type was evaluated. Regarding the anode, the primary programmatic direction was to decrease the anode PGM content to as low as possible. One key concern for reduced anode loading was that it may accelerate ionomer decomposition due to crossover oxygen from the cathode to anode, where peroxide can be formed at the low anode electrode potential. Figure 147 summarizes the MEA chemical durability evaluation of 4 NSTF anodes, comprised of the baseline 0.05PtCoMn and BOC MEA component candidates of 0.02PtCoMn, 0.02 Pt_3Ni_7, and 0.018Pt_3Ni_7M which contained a reversal tolerant additive. All MEAs appeared to pass the test, and yielded relatively consistent and low post-test H_2 crossover. OER containing catalysts maintained higher OCV. It was concluded that the anode candidates evaluated here did not appreciably impact the MEA chemical durability.

Finally, the impact of PEM chemical stabilizing additive was evaluated. Figure 148 confirms that with the 0.02PtCoMn/NSTF anode and 0.125PtNi/NSTF cathode, additive was necessary to pass the OCV hold test, as the post-test H_2 crossover was severely increased when no additive was present. Work to determine optimal additive content was not conducted.

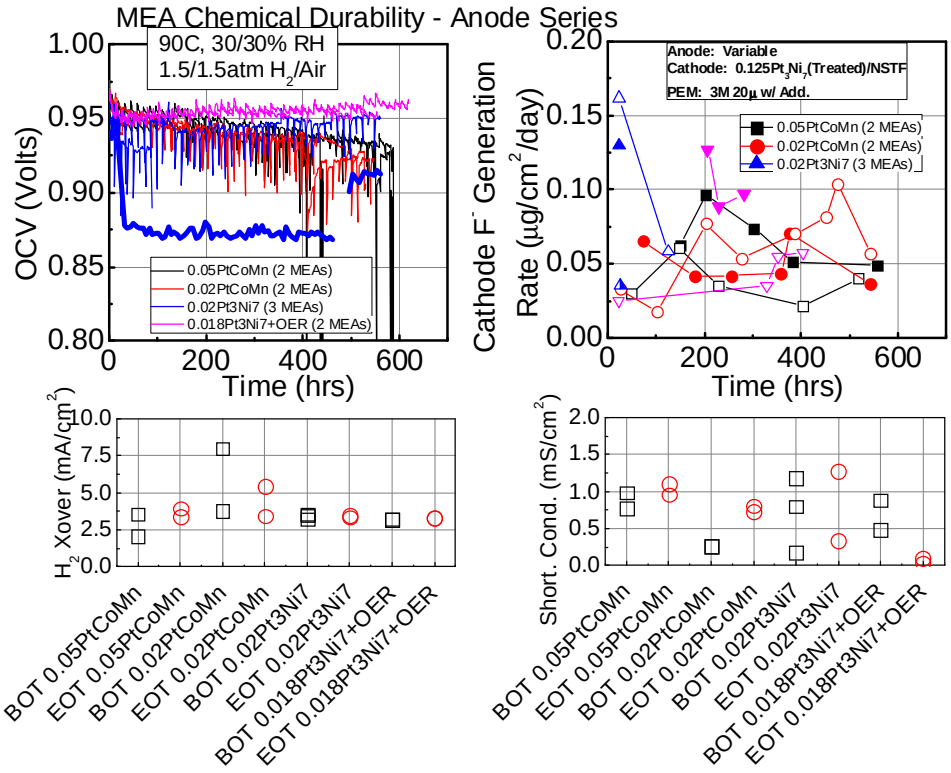

Figure 147. OCV durability vs. anode catalyst type.

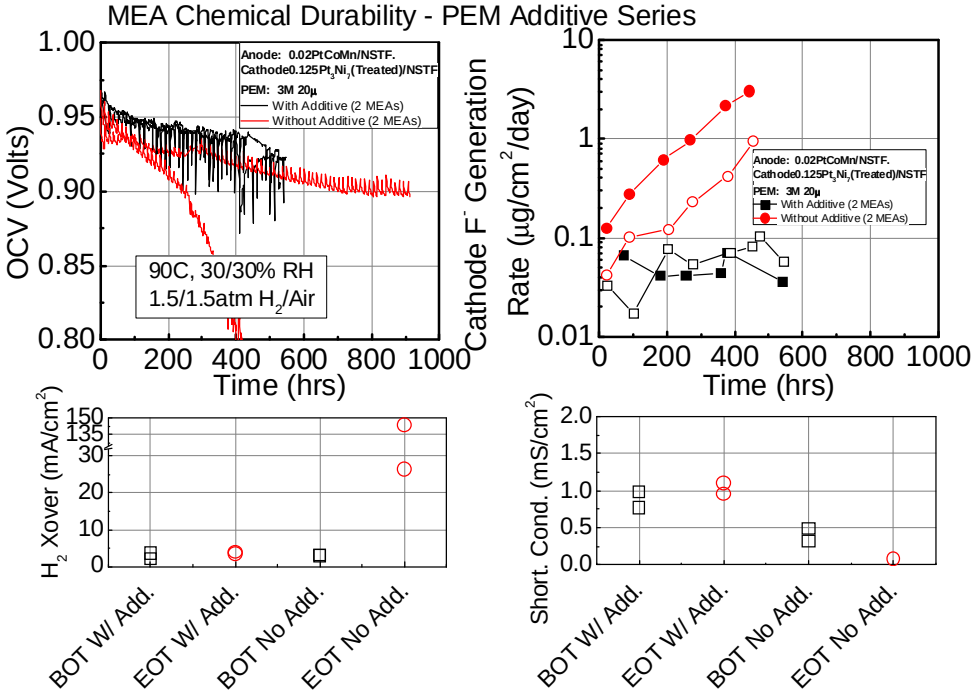

Figure 148. OCV durability for PEMs with and without additive.

Support Cycle Durability

The primary BOC cathode candidate, dealloyed PtNi, was evaluated for support durability under the DOE 1.2V hold durability test. Figure 149 shows that after 400 hours at 1.2V, the cathode passed the DOE targets. H_2/Air performance loss was less than 30mV and specific area loss was ~25%. Mass activity loss was 40%, just meeting the DOE target.

Due to this result and previous history of NSTF cathodes passing this test, no additional support cycle testing was performed with candidate cathodes. Some work was performed evaluating NSTF MEAs with cathode interlayers, detailed in the Subtask 2.2 section.

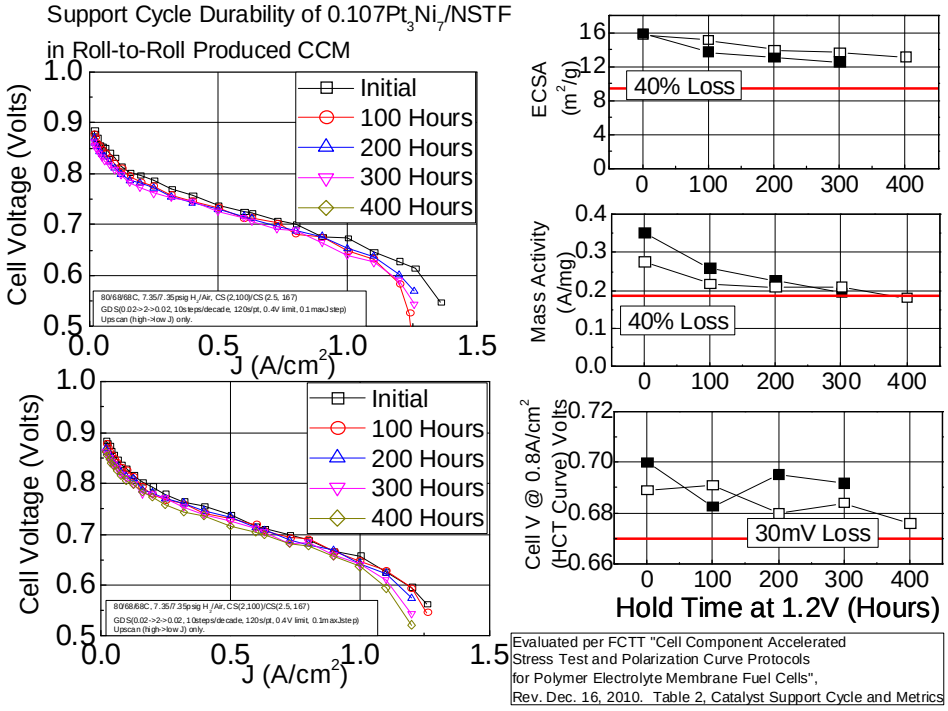

Figure 149. Support cycle durability of dealloyed PtNi/NSTF

Electrocatalyst Cycle AST

The primary BOC cathode catalyst candidate was evaluated under the DOE Electrocatalyst cycle (30k cycles between 0.6-1.0V). Figure 150 summarizes results from 3 MEAs. While H_2/Air performance and specific area losses were relatively low, the mass activity losses exceeded the target of 40%, due to large specific activity loss. Samples of analogous PtNi/NSTF cathodes were provided to ORNL for analysis (Figure 151). Electrocatalyst cycling resulted in modest coarsening of the nanoporous structure, consistent with the modest area loss, but more importantly significant loss of Ni, likely contributing to the dominating specific activity loss.

Several new annealed cathode PtNi/NSTF catalysts from Subtask 1.1 were also evaluated for durability, summarized in Figure 152. The objective was to determine if annealing, which increases grain size and mass activity, would also help with stabilization. While the annealing resulted in substantially improved mass activity (due to increased specific activity), the post-test mass and specific activities were relatively similar, decreasing from as high as 0.45A/mg to about 0.15A/mg.

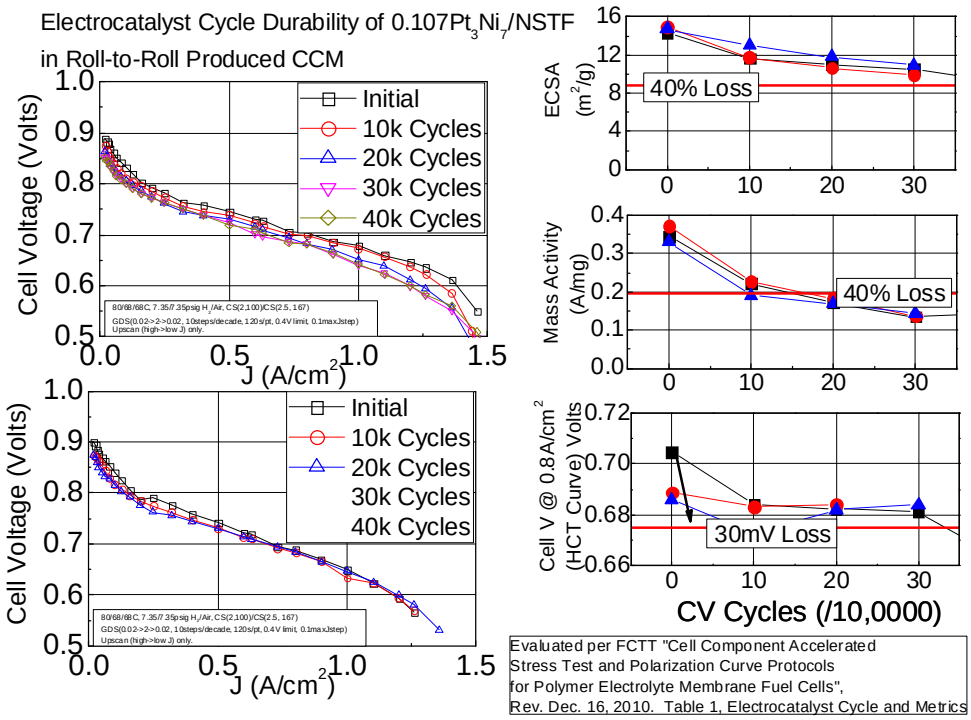

Figure 150. Electrocatalyst cycle durability of dealloyed PtNi/NSTF.

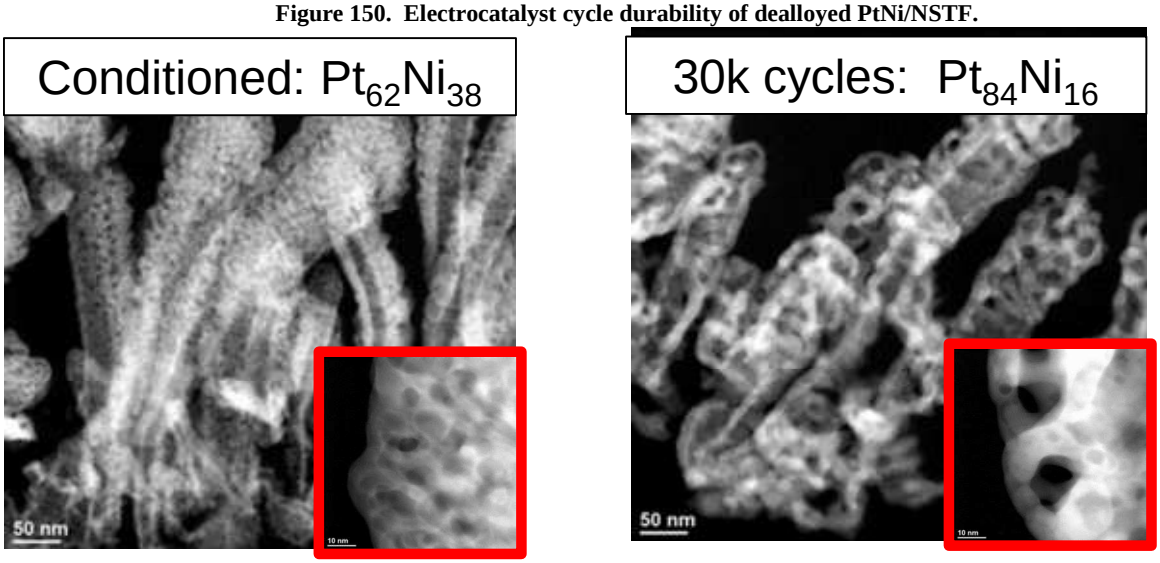

Figure 151. TEM and EDS analysis of PtNi/NSTF before (left) and after (right) the electrocatalyst AST.

The electrocatalyst durability of PtNi was recognized as a key durability concern for the MEA concept. In 3M-funded work outside the project, concurrent work was in progress to develop a nanoporous PtNi with improved durability. Considerable additional work with other PtNi variations (different compositions, fabrication methods) also indicated poor durability. However, it was determined that an additive, "M", improved PtNi stability allowing it to pass the DOE 2020 durability target. However, work to optimize the additive for performance and continuous manufacturability (via dealloying) was not able to be completed within the timeframe of the current project. Subsequent work (2016) lead to an improved PtNiM catalyst which enabled good H_2/Air performance and durability which achieved the DOE 2020 target.

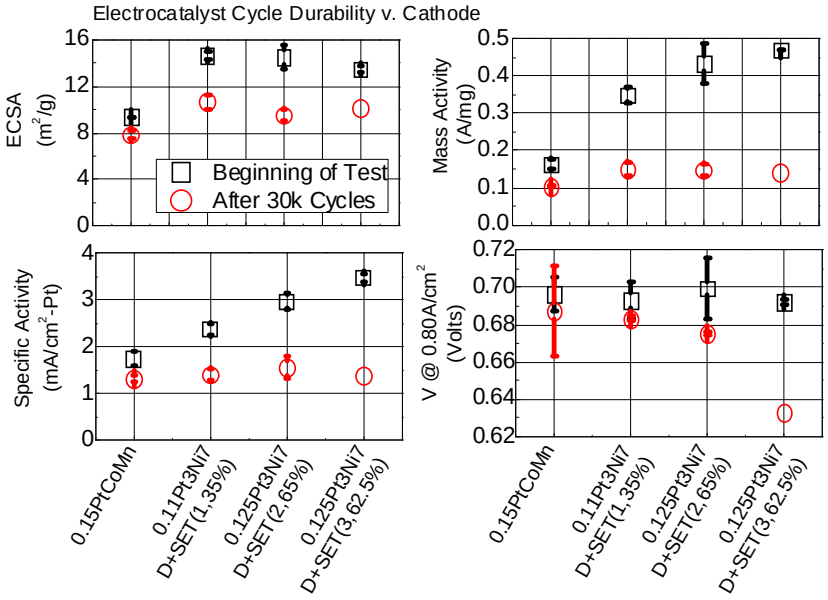

Figure 152. Electrocatalyst AST of several dealloyed+annealed PtNi/NSTF candidates.

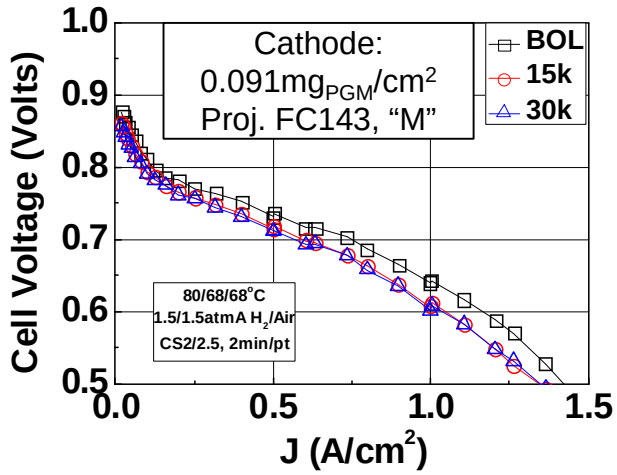

Metric	Change/DOE Tgt
Mass Activity (A/mg)	-40±0.8 / -40%
V @ 0.8A/cm²	-28±1.4 /-30mV
Surf. Area (m²/g)	-14±0.15 / NA %

Figure 153. Performance and durability of PtNiM.

Load Cycle Durability

Extensive load cycle durability evaluations were conducted with several BOC MEA candidate components – see the Subtask 5.5 section. The durability of the project BOC MEA is discussed in the Subtask 4.1 section.

Subtask Conclusions

BOC MEA candidate components were evaluated for durability under the DOE chemical durability test, support cycle, and electrocatalyst cycle ASTs. The BOC candidates indicated generally good durability, with most target metrics met or exceeded. The key challenge (under

ASTs) was the electrocatalyst cycle stability of dealloyed PtNi, which routinely lost in excess of 65% mass activity with cycling, primarily due to specific activity loss which correlated to additional Ni leaching from the PtNi cathodes. A PtNi stabilization approach was developed outside of the project, but was not able to be implemented with high performance and manufacturability, necessary for the project short stack deliverable.

Future Directions

Stabilization of nanoporous electrocatalysts remains a key area of activity at 3M, currently occurring within a DOE-funded effort. Such work is leading to high performance, high activity PtNiM catalysts.

Subtask 5.5 Mitigation of Irreversible and Reversible Rated Power Performance Degradation

Subtask Overview

A second objective of Task 5, addressed in subtask 5.5, is mitigation of reversible and irreversible modes of rated power loss. The loss is manifested as a reduction in peak current density, is correlated to cathode catalyst Pt surface area per unit MEA area (cm^2_{Pt}/cm^2_{planar}) below a critical level, SA_{CRIT}, which depends upon the cathode catalyst support, loading, and composition.

Subtask High Level Work Summary

The durability of rated power performance was assessed in several studies which evaluated both material and operational factors, several of which were influential. New experimental PEMs were generated with improved durability properties. A mechanism study was conducted which determined a likely key correlation between rated power loss and PFSA decomposition. An NSTF MEA durability model was developed.

Subtask Key Results

Background

In pre-project work, a key durability issue of NSTF MEAs was identified. While the individual components were generally sufficiently stable to pass most DOE component durability tests, significant irreversible performance loss was observed to occur with extended load cycling of NSTF MEAs. The performance loss manifested as increased apparent slope in H_2/Air polarization curves and reduced limiting current density. Figure 154 provides one key example, showing H_2/Air performance of an NSTF MEA with PtCoMn/NSTF electrodes ($0.20mg_{Pt}/cm^2$) on anode and cathode and 3M 825EW PEM evaluated for over 8000 hours under a load cycle. After 3800 hours of load cycling, the apparent slope increased and limiting current decreased, which was further exacerbated after 8550 hours. Cathode surface area losses and MEA HFR increases were modest. The solid black line shows the predicted loss after 8550 hours, using the typical expressions for correcting for cathode activity loss (-70mV/decade of activity loss) and HFR increase (ohm's law). The actual performance after 3800 and 8550 hours was substantially larger than the model prediction.

Development work was driven by two hypotheses of how high current density ("rated power") performance of NSTF MEAs degrades with use. In pre-project work conducted at General Motors, rated power loss was suggested to be due to coverage of the NSTF with ionomer, perhaps induced by ionomer creep over the electrocatalyst. This ionomer coverage lead to higher oxygen transport losses. This work is summarized in Kongkanand et al., "Degradation of PEMFC Observed on NSTF Electrodes", *J. Electrochem. Soc.* 161(6) F744 (2014). Additionally, 3M had historically observed a correlation between rated power performance and cathode surface area, where the loss of performance occurred when the cathode roughness factor decreased below ca. $10cm^2_{Pt}/cm^2_{planar}$ (Figure 155). The correlation appeared valid whether the surface area variation was due to accelerated stress tests of numerous types (load cycle, electrocatalyst AST, start/stop) or due to decreased cathode loading at beginning of life. These two hypotheses were used as guiding principles for the experimental plan.

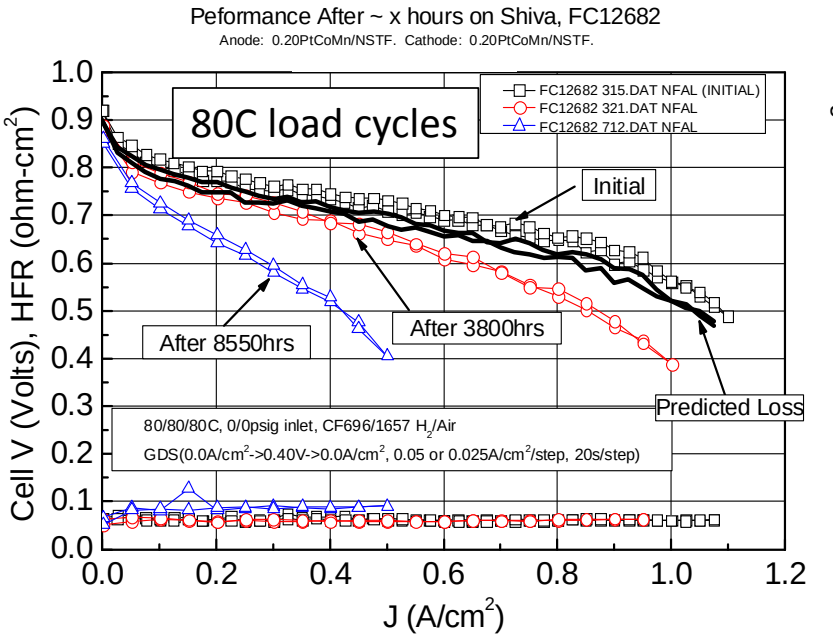

Figure 154. H_2/Air performance of NSTF MEA during 8550 hours of load cycling.

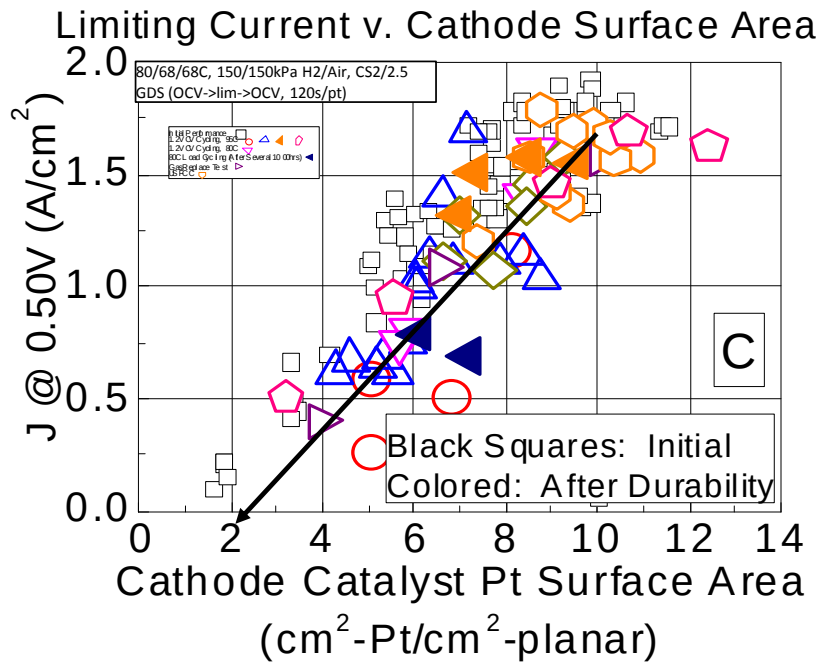

Figure 155. Correlation of H_2/Air limiting current density with NSTF cathode surface area.

Experimental Overview

Several material and operational factors were identified as being strong candidates for being influential towards rated power loss, summarized in Table 18. Materials factors included cathode catalyst type and loading, anode catalyst type and loading, PEM variables including EW, support, and additive. Operational factors included cell temperature, operating potential, and the reconditioning method used to recover reversible performance losses. The baseline material set and operating conditions are highlighted in orange; most new experiments consisted of variation of one factor from the baseline set. As the final project best of class MEA components were

being downselected, a set of MEAs with that construction were also evaluated, outlined in the final row of the table.

Table 18. Material and Operational Factors Evaluated

Material Factors				Operational Factors		
Cathode	**Anode**	**PEM**	**PEM Additive**	**Cell Temp. (°C)**	**Load Cycle**	**Recovery Method**
0.15PtCoMn/ NSTF	0.05PtCoMn/ NSTF	20u 825, uns.	N	90	0.85-0.60V (cycles)	1 Thermal Cycle
0.125Pt_3Ni_7 (Dealloy+SET) / NSTF	0.05Pt/C	20u 734, uns.	Y	80	0.90V (hold)	High E scans
0.10PtCoMn/ NSTF		20u 1000, uns.		100	0.60V (hold)	
0.20PtCoMn/ NSTF		Mitigated#1, uns.			0.30V (hold)	
0.20Pt/NSTF						
0.10Pt_3Ni_7 (JHUDealloy)/ NSTF	0.02PtCoMn/ NSTF	14u 725EW supported	Y	80	0.85-0.60V (cycles)	1 Thermal Cycle

The baseline test method is outlined below. The MEA would be load cycled for 10 hours and then reconditioned with a single thermal cycle. This 10 hours of load cycling plus recondition would be done for typically 2-3 days. The MEA would then be more fully reconditioned (3 thermal cycles), after which cathode activity and surface area and MEA H_2/Air performance were measured. This overall process was typically repeated several times until typically several hundred hours of load cycling was completed.

```
WHILE_TIME < 400 HOURS
        WHILE_TIME_< 3 DAYS
                WHILE_TIME_< 10 HOURS
                        LOAD CYCLE
                END_WHILE_TIME
                RECONDITION (1)
        END_WHILE_TIME
        RECONDTION (3)
        ACTIVITY, ECSA, H2/AIR POL. CURVE
END_WHILE_TIME
```

The typical baseline load cycle protocol is outlined below for a 50cm^2 MEA. Both load and RH were cycled. Tests were typically done at 90°C cell temperature and 1.5atmA reactants. The procedure consisted of 5 minutes of load cycling between 0.85 and 0.60V with 93°C dewpoints (oversaturated), followed by a 2 minute transition at 0.70V, followed by another 5 minutes of load cycling between 0.85 and 0.80V with highly undersaturated gases (61°C dewpoint).

SET_CELL_TEMPERATURE (090C)
SET_ANODE_FLOW (CF0835)
SET_CATHODE_FLOW (CF1789)
SET_ANODE_PRESSURE (07.35PSIG)
SET_CATHODE_PRESSURE (07.35PSIG)
SET_CATHODE_HUMIDIFICATION (CD093C)
SET_ANODE_HUMIDIFICATION (CD093C)
WHILE_COUNT < 5
    SET_X-SS (PSS(0.85V,0.5MIN))
    SET_X-SS (PSS(0.60V,0.5MIN))
END_WHILE_COUNT
SET_ANODE_HUMIDIFICATION (CD079C)
SET_CATHODE_HUMIDIFICATION (CD079C)
SET_ANODE_FLOW (CF0521)
SET_CATHODE_FLOW (CF0994)
SET_X-SS (PSS(0.70V,2.0MIN))
SET_ANODE_HUMIDIFICATION (CD061C)
SET_CATHODE_HUMIDIFICATION (CD061C)
SET_ANODE_FLOW (CF0217)
SET_CATHODE_FLOW (CF0414)
WHILE_COUNT < 5
    SET_X-SS (PSS(0.80V, 30s))
    SET_X-SS (PSS(0.85V, 30s))
END_WHILE_COUNT

Experiments consisted of operating 50cm^2 NSTF MEAs under a 3M load cycle protocol, typically consisting of load cycles between 0.60 and 0.85V with fixed operating conditions during the course of the experiment. Periodically, testing was interrupted, the cell was reconditioned, and cathode surface area, mass activity, and MEA H_2/Air performance were evaluated. The total time under the load cycle was typically several hundred hours.
Experiments were conducted at three test sites, 3M St. Paul, 3M Menomonie, and Los Alamos National Laboratories. There was some initial difficulty in getting reasonable site-site agreement in terms of beginning of life H_2/Air performance, but they were largely ultimately resolved. Some difficulty remained in getting good agreement in decay rates; after some effort at identifying and attempting to resolve the site-site discrepancy, it was decided to move forward by generating site-specific baselines and comparing the impact of new materials and/or operational factors against the baselines.

Impact of Operating Temperature

One key initial experimental series was the evaluation of load cycle temperature. Baseline MEAs were cycled with the baseline test method, but the cell temperature was held at either 80, 90 or 100°C. Figure 156 summarizes the impact of cell temperature on the H_2/Air performance, mass activity, and specific surface area. In general, two consistent differences were observed. Cell voltage at 1A/cm^2 was a strong function of cell temperature, increasing monotonically as cell temperature increased from 80 to 100°C. Additionally, mass activity was retained better at 80°C than at 90 or 100°C.

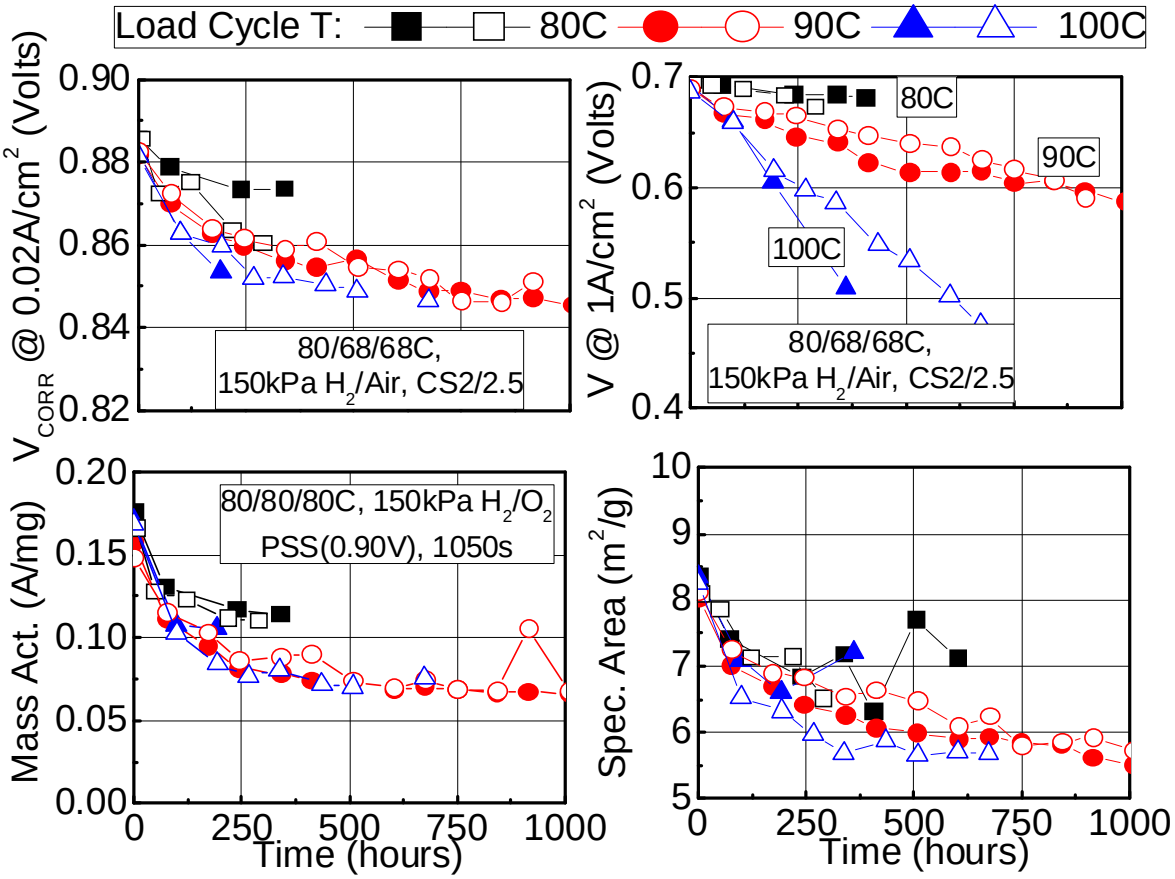

Figure 156. Impact of cell temperature on H_2/Air performance (top), mass activity (bottom left), and specific area (bottom right).

Impact of PFSA PEM Equivalent Weight

A second key initial study evaluated the impact of the PFSA PEM equivalent weight. Figure 157 shows that H_2/Air performance retention at 0.02 and 1.0A/cm^2 and mass activity retention improved with increasing equivalent weight, but specific area retention was independent of PEM EW.

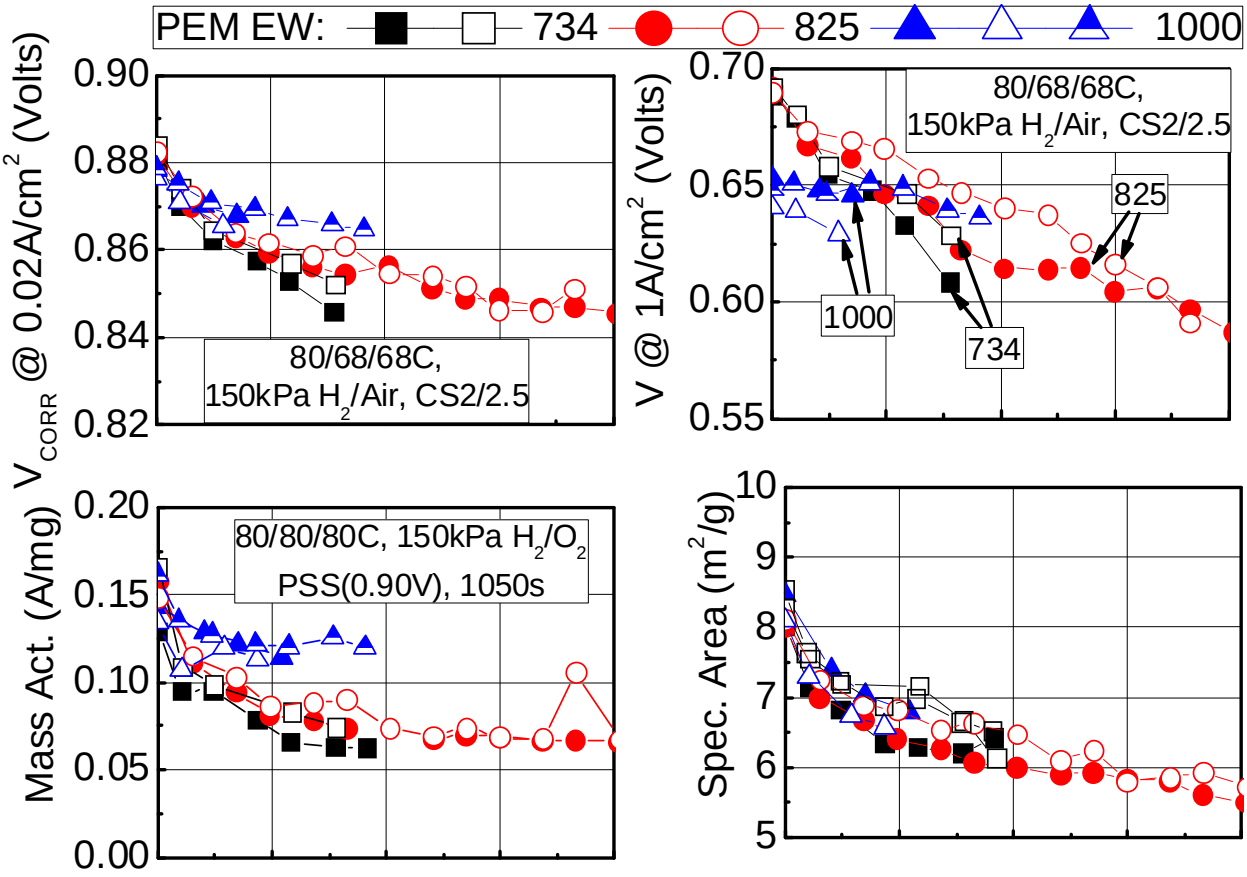

Figure 157. Impact of PEM equivalent weight on H_2/Air performance (top), mass activity (bottom left), and specific area (bottom right).

The improved durability obtained with the 1000EW was intriguing, but ultimately was not a solution to the issue, as the beginning of life H_2/air performance at high current density was suppressed, as shown in Figure 158.

Due to the strong material-based impact of EW, NSTF CCMs were further evaluated by SEM to determine if there were any notable changes in electrode morphology. Figure 159 and Figure 160 summarize the SEM analysis of the fast-decaying CCM with 734EW PEM after 100 hours and 400 hours). At the available magnification, little obvious change was noted vs. testing time. After 400 hours, the only consistent observation was a modest qualitative increase in the density of cracks in the surface of the electrode.

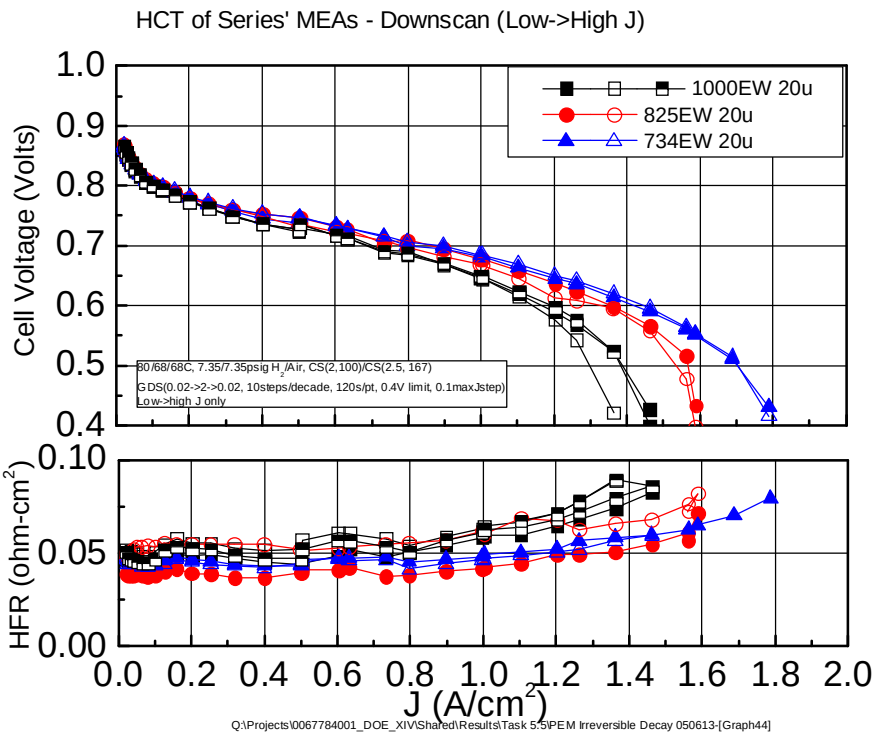

Figure 158. BOL H_2/Air performance vs. PEM EW

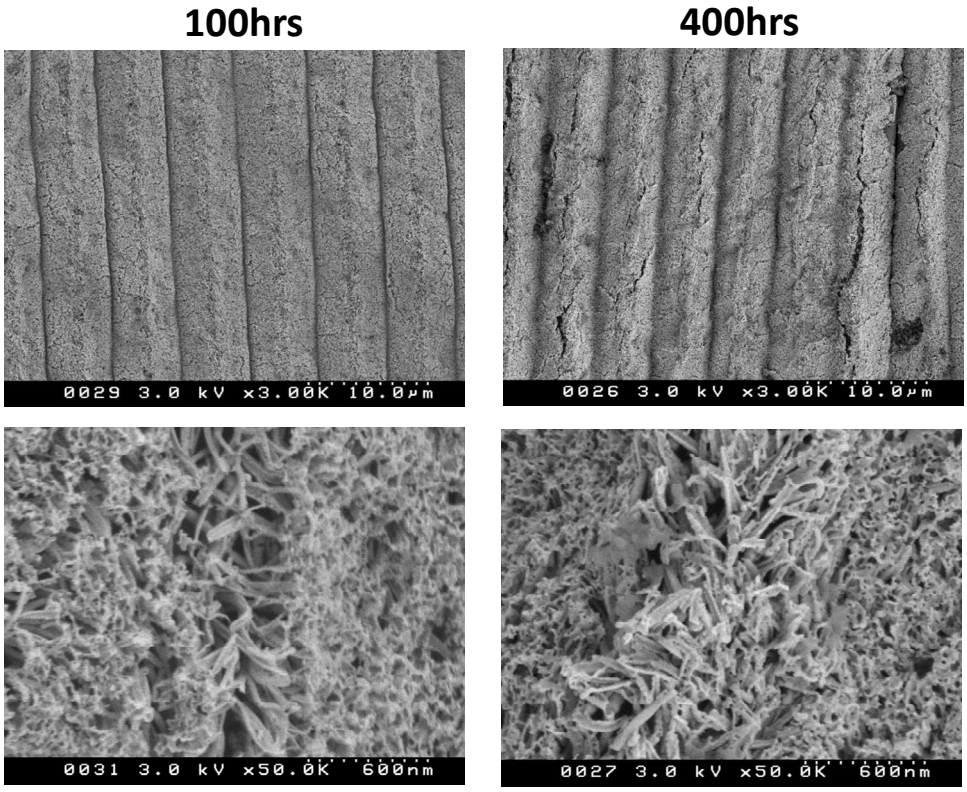

Figure 159. SEM of cathode electrode for NSTF MEA with 734EW PEM after either 100 hours of load cycle test time (left) or after 400 hours (right).

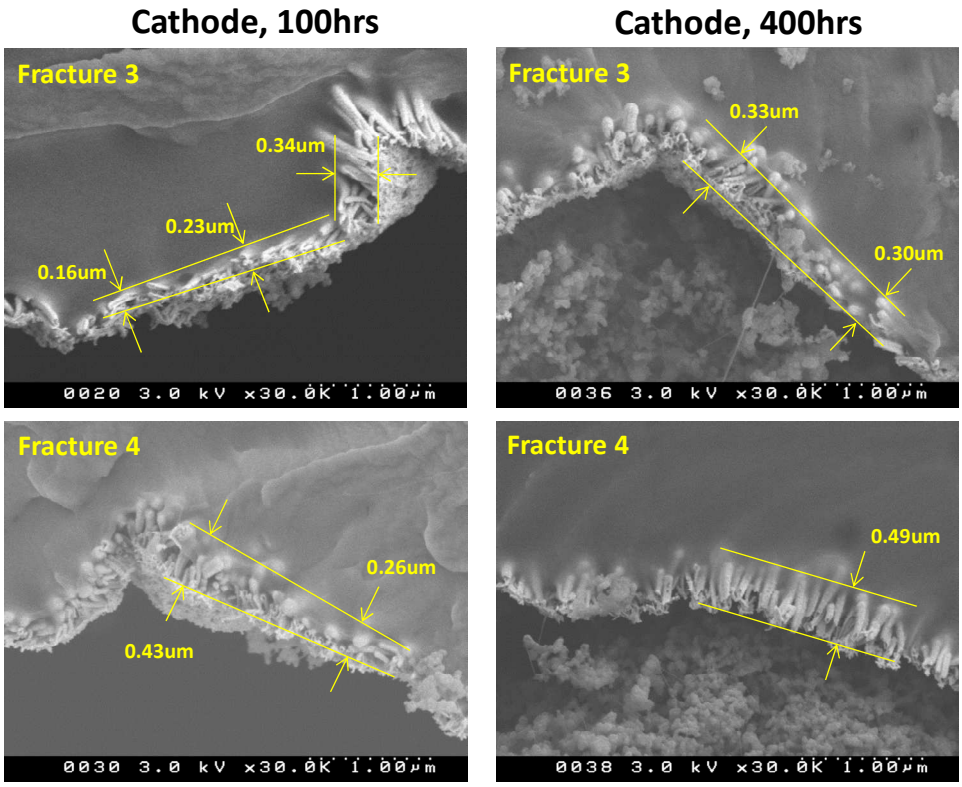

Figure 160. SEM of cathode electrode (cross section) after 100 hours (left) or 400 hours (right).

Impact of PFSA PEM Decomposition Mitigating Additive.

The influence of PEM decomposition mitigating additive was evaluated. In these experiments, the baseline PtCoMn/NSTF anode and cathode electrocatalysts were replaced with pure Pt, as Mn is a known PFSA decomposition mitigator. Figure 161 compares H_2/Air polarization curves taken at BOL and after about 100 hours of testing for 725EW PEMs without additive (left) and with level 700, 2100, and 2800 additive. Without additive, extraordinarily rapid and severe performance loss was observed. With additive, losses were dramatically reduced.

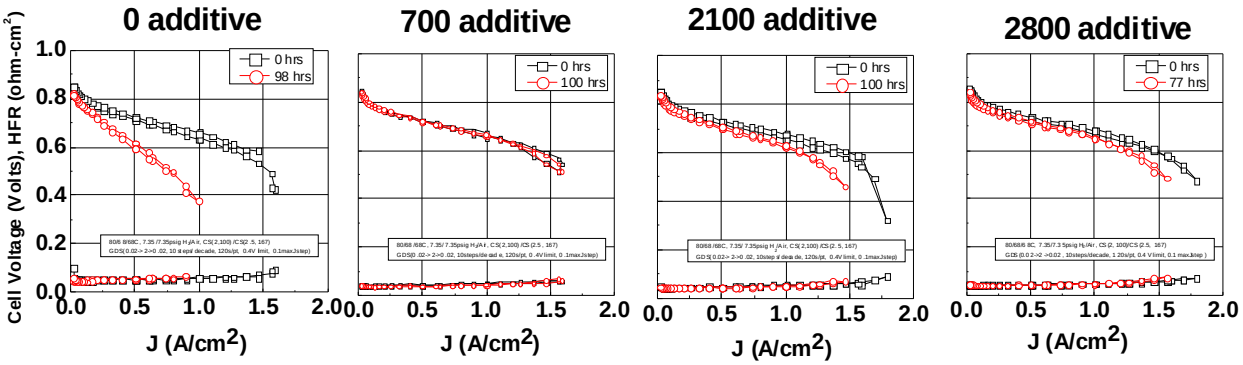

Figure 161. Impact of additive on performance before and after 100 hours of testing.

Correlation of high current density H_2/Air performance to cathode oxygen activity

During the PEM equivalent weight, temperature, and additive series, it was observed that MEAs which tended to have higher performance loss at high current density also had higher oxygen

activity losses. Figure 162 summarizes this relationship for the EW, temperature, and additive series MEAs at beginning of life and during the load cycle testing. Additional BOL data is provided from two other MEA series with comparable constructions ("Contam." and "Ca. Ldg.). The data from all MEAs appears to largely track on a single trend line. A fit of the data indicates that the curve follows a 122 ± 2 mv loss per decade of current density decrease. This result is significant, as it indicates that performance loss during load cycling is due to loss of cathode oxygen activity alone, and that at 1A/cm^2 performance losses are rather modest until the oxygen absolute activity decreases below about 10-15mA/cm^2. Barring additional loss mechanisms (e.g. TM dissolution), rated power loss of NSTF MEAs over time can be managed if the cathode absolute activity is kept above 15mA/cm^2. In addition to the mitigating the underlying source of ORR activity loss (PFSA decomposition, discussed below), this result suggests that higher absolute activity, durable cathode electrocatalysts will also mitigate the high current density loss.

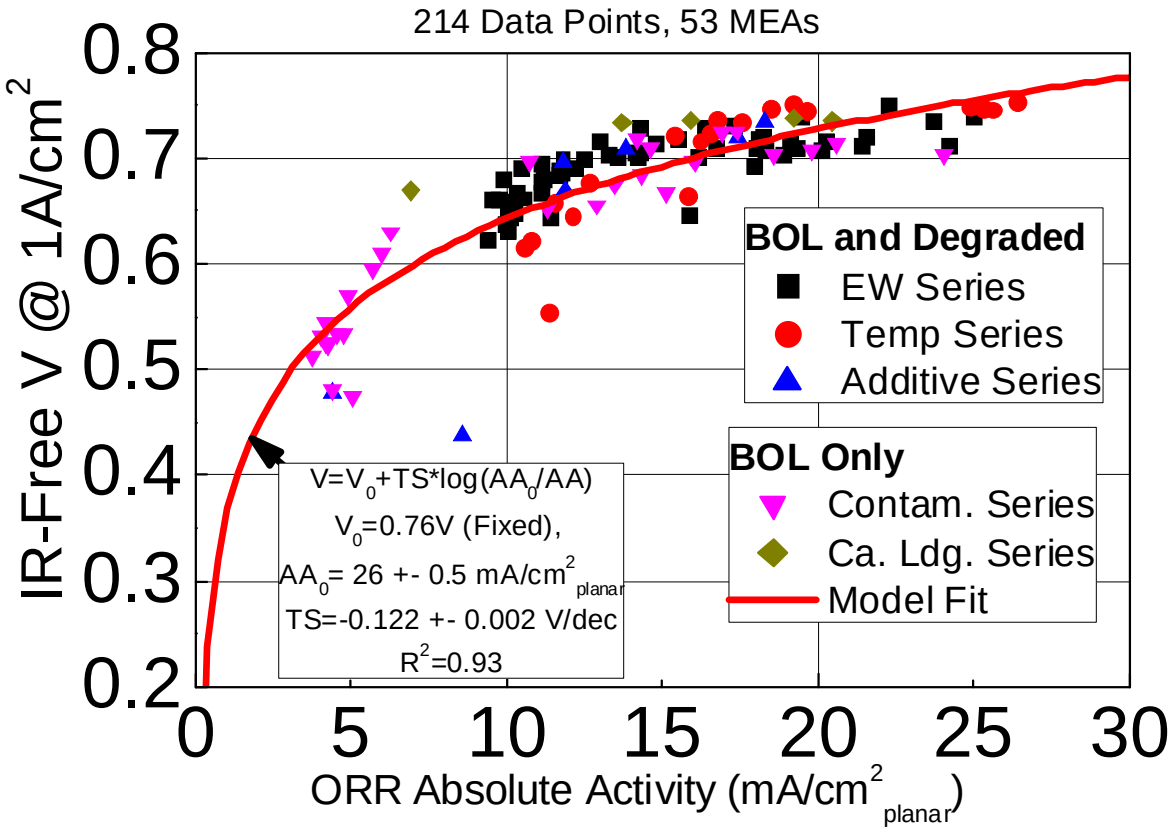

Figure 162. IR-free cell voltage vs. measured ORR absolute activity for BOL and degraded MEAs

Impact of PFSA PEM Ionomer Type

A majority of work was conducted with 3M PFSA ionomers. Due to the strong influence of PFSA PEM additive and equivalent weight, it was posited that the decay was related to PFSA type. An experiment was conducted to assess if an alternative PFSA ionomer would be influential. Figure 163 compares the activity and H_2/Air performance for MEAs with either 3M 825EW ionomer or an alternative 800EW PFSA ionomer. Decay rates were qualitatively similar for the two ionomer types.

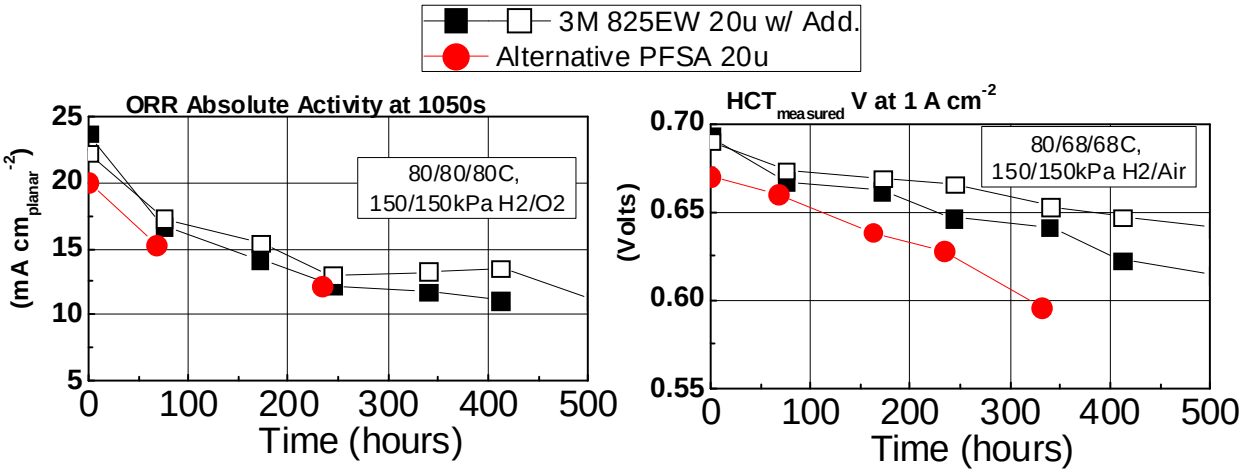

Figure 163. Impact of ionomer type on oxygen activity loss (left) and H_2/Air performance at 1A/cm^2 (right).

Impact of Anode Catalyst Type

Limited experiments were conducted to determine if the NSTF anode catalyst was contributing to the rated power loss rate. Baseline MEAs were evaluated with either the baseline 0.05PtCoMn/NSTF or a 0.05Pt/C anode catalyst, with ca. 5x higher specific surface area. Figure 164 shows that the anode catalyst type had little effect, suggesting anode absolute surface area is not a influential mechanistic factor.

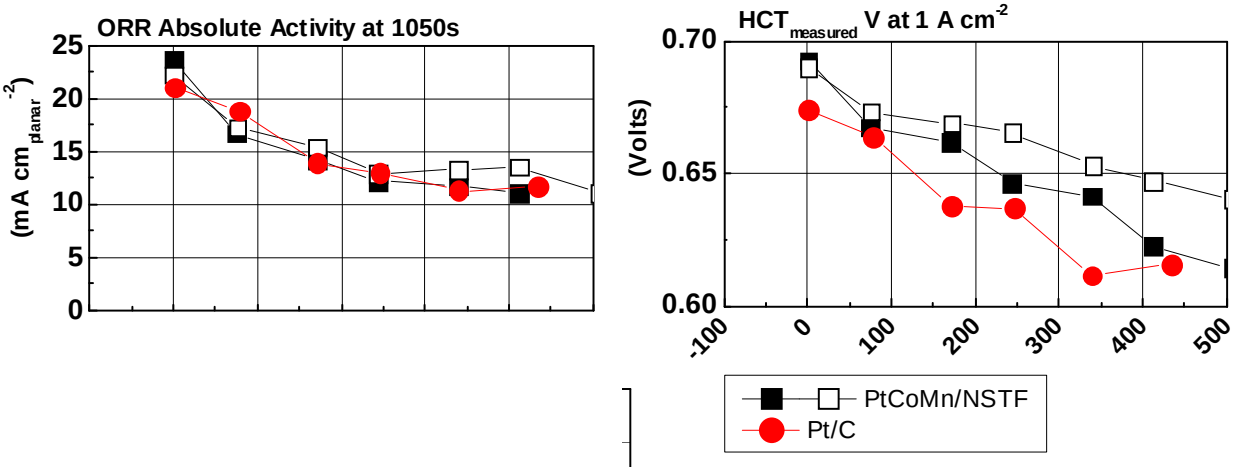

Figure 164. Impact of anode catalyst type (0.05PtCoMn/NSTF or 0.05Pt/C) on ORR activity and H_2/Air performance loss rates.

Impact of Cathode Catalyst Loading

Limited experiments at LANL evaluated the impact of cathode loading. Baseline NSTF MEAs with PtCoMn/NSTF cathodes with either 0.15 or 0.10mgPt/cm^2 were evaluated, compared in Figure 165. As the cathode loading was reduced from 0.15 to 0.10, the rate of performance

decay increased, even after considering that the lower loaded MEA developed an electronic short which accentuated the loss.

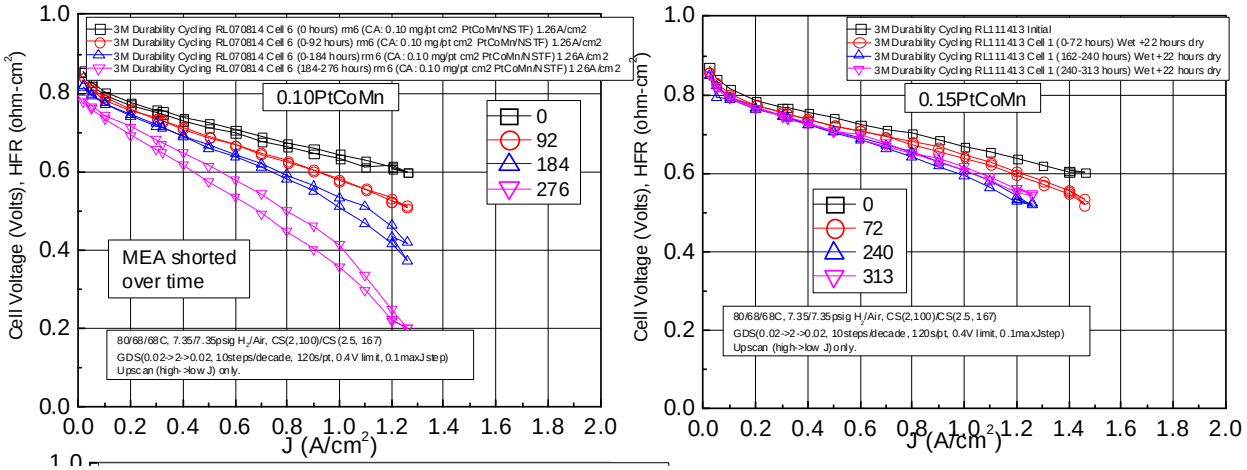

Figure 165. Impact of PtCoMn/NSTF cathode loading on decay rate.

Mechanism study of rated power loss

In collaboration with ANL, a study was designed to directly test the hypothesis that rated power loss with NSTF MEAs is caused by PFSA ionomer decomposition.

Two series of tests were conducted, involving control of cell voltage (cathode potential) and cell temperature. In the first series, degradation rate was controlled by controlling the cathode potential at fixed 90°C cell temperature; it was posited that lower potential would lead to higher H_2O_2 generation rates. In the second series, different operating temperatures were explored between 60 and 90°C with fixed potential of 0.60V, to obtain activation energy information on PFSA decomposition in NSTF MEAs. In both series, product water was collected and analyzed to determine F^- emission rates. Tests were conducted with baseline NSTF MEAs (0.05PtCoMn/NSTF anode, 0.15PtCoMn/NSTF cathode, 3M 825EW 20u PEM w/o additive, 3M 2979/2979 GDLs) in 50cm^2 quad serpentine flow fields.

Figure 169 summarizes the H_2/Air performance curves measured periodically during the experiment after full reconditioning, and the bottom right plot summarizes the H_2/Air cell voltage at 0.8A/cm^2. As the cell voltage decreased, the apparent rate of performance loss increased, most notably at higher current densities. Note that for the 0.300V decay rate, the test was halted after 210 hours due to severe performance loss, whereas tests at 0.90 and 0.60V were conducted for approximately 560 hours.

Figure 167 summarizes cathode CVs at BOL and after ca. 210-240 hours of testing. After 210-240 hours, all cathodes showed modest degradation in apparent H_{UPD} area. The cathode surface area loss (SEF) appeared to be a function of test time and not cathode potential.

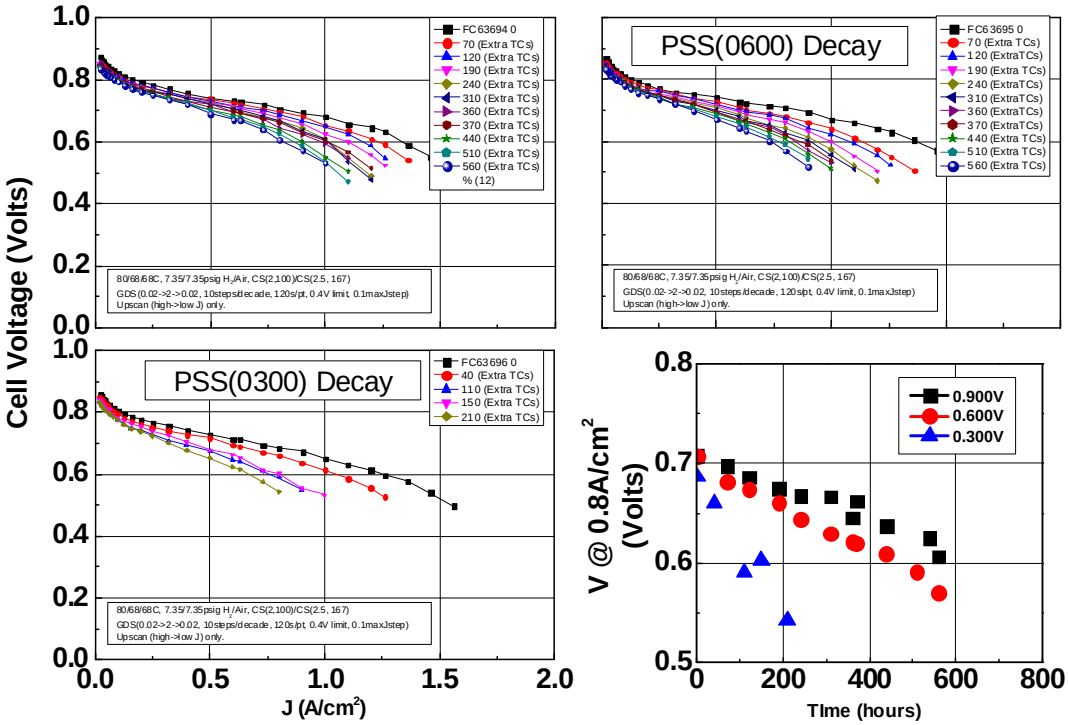

Figure 166. H_2/Air polarization curves during potentiostatic tests. Bottom right is H_2/Air performance at 0.8A/cm^2 during the test.

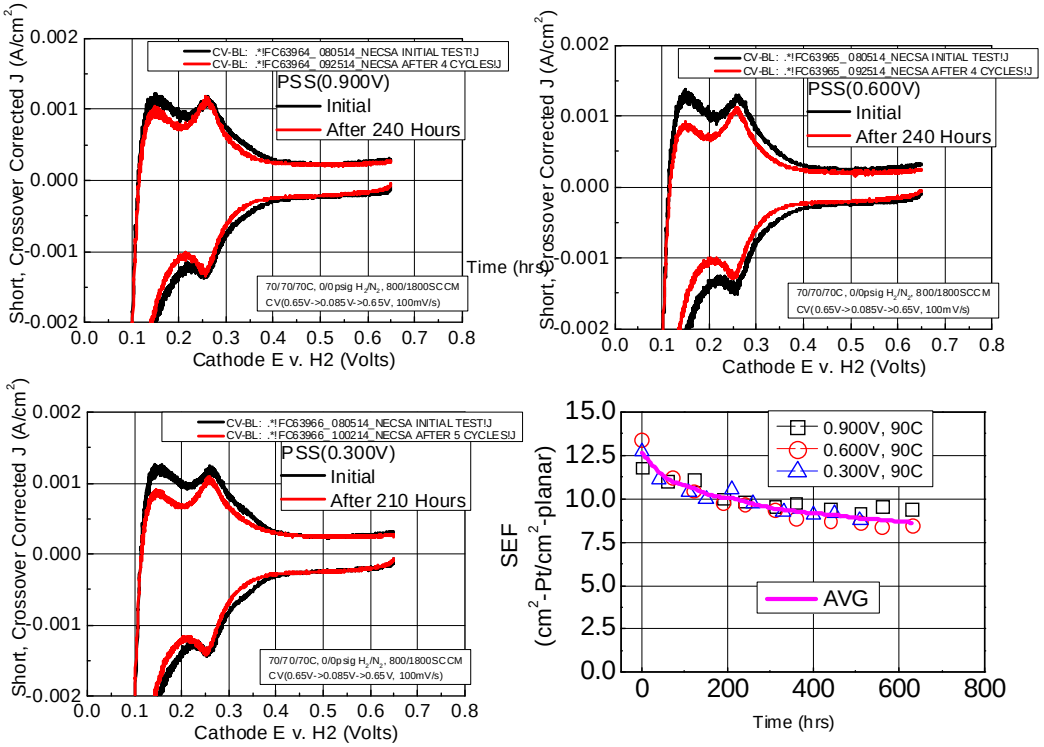

Figure 167. Cathode CVs at beginning and midpoint of potentiostatic tests. Calculated cathode SEFs in bottom right.

After testing, CCMs from the 0.90V and 0.60V tested MEAs were provided to ORNL for TEM analysis of the cathode catalyst to determine if any observations of electrocatalyst degradation would explain the differences in loss rate. The catalysts appeared morphologically similar and

compositionally identical. One caveat is that the 0.90V sample was tested over two times longer than the 0.30V sample.

Figure 169 left summarizes the key findings from the potentiostatic study. The left set of figures shows the measured H_2/Air cell voltage at 0.8A/cm^2, ORR absolute activity, and total cumulative F- emission as a function of test time. As cell voltage (cathode potential) decreased, the H_2/Air performance and ORR activity decreased and the total F- generation increased.

The top right set of figures shows that the H_2/Air performance at 0.02 and 0.8A/cm^2 appear related to ORR activity, consistent with the correlation shown in Figure 162, above. There are two primary factors influencing ORR absolute activity, the cathode roughness factor and the specific activity. The bottom right set of plots shows that the cathode surface area variation is largely independent of potential, but the specific activity does have a potential dependence.

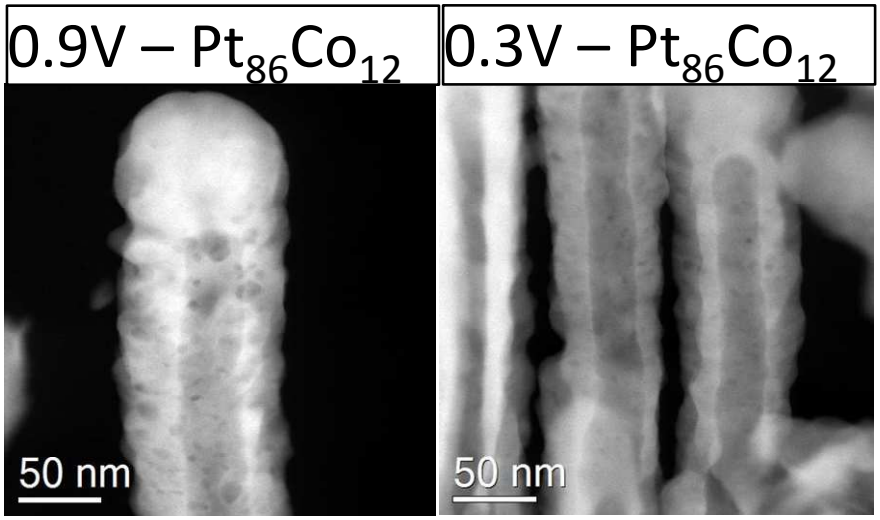

Figure 168. TEM and composition analysis of 0.90 and 0.30V degraded cathodes.

Figure 170 reveals key correlations between the cathode activity, H_2/Air performance, and PFSA decomposition. The left figure shows that the exchange current density appears to be reasonably correlated to the cumulative cathode F- emission, a measure of PFSA decomposition. The right figure shows that the limiting H_2/Air current density also is also correlated to cumulative cathode F- emission.

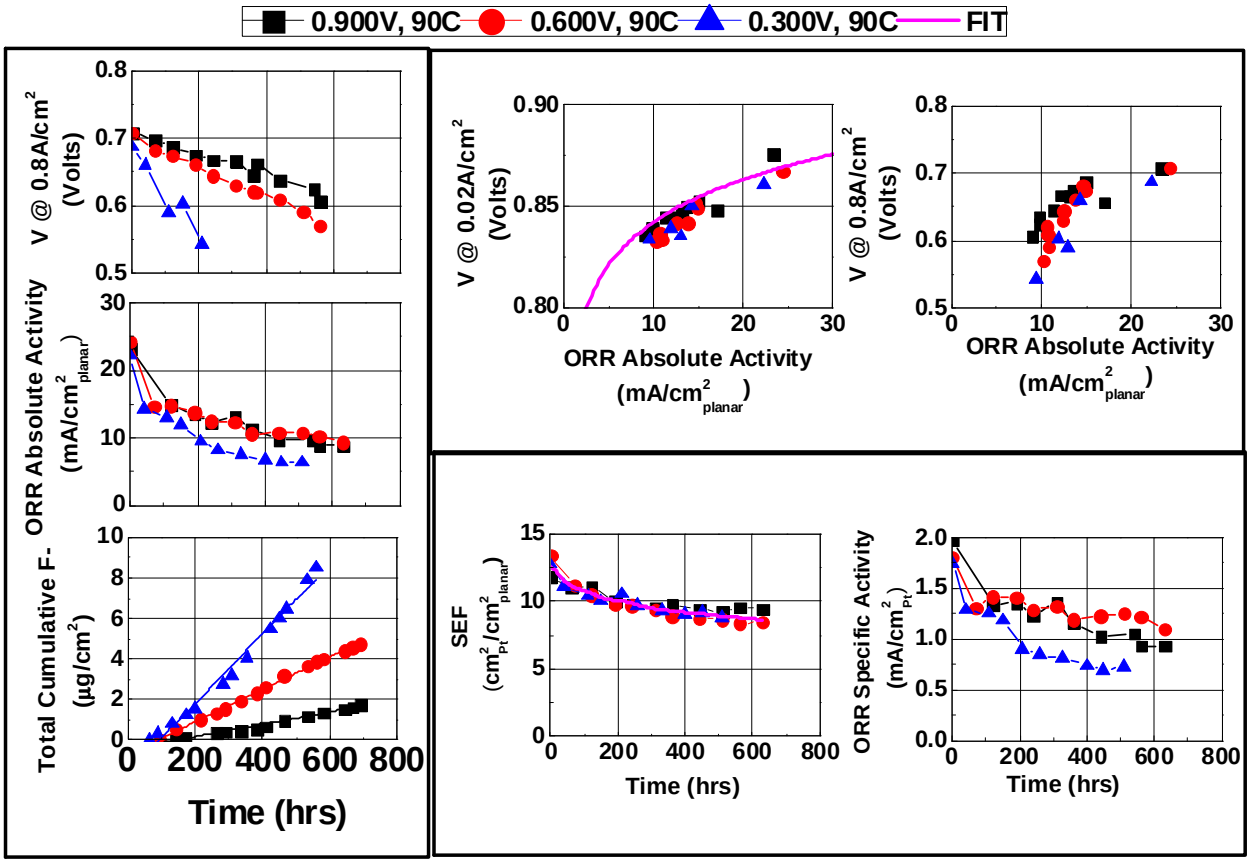

Figure 169. Summary of cell potential control study.

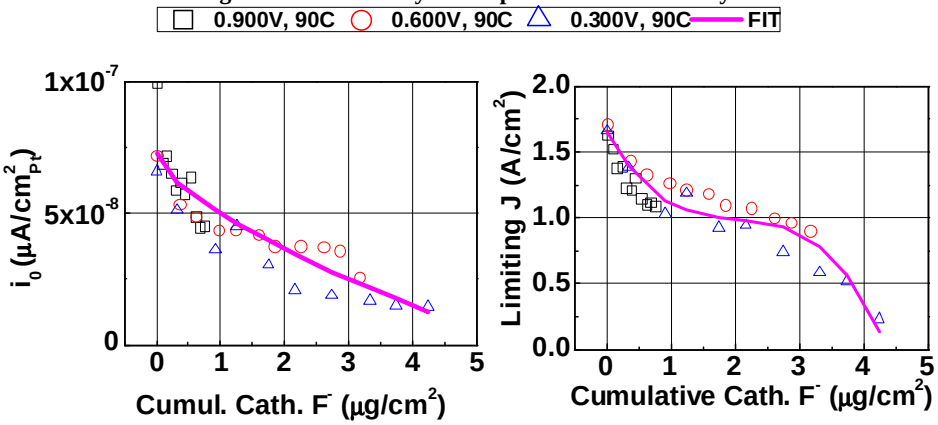

Figure 170. Correlation of cumulative cathode F- generation to specific activity and H_2/Air limiting current density.

In the second part of the study, experiments were conducted where the cell temperature was varied and the cell voltage was fixed at 0.60V. Figure 171 compares ORR activity, cathode SEF, and total (anode and cathode) cumulative F- emission for the potential and temperature control series. For the temperature series, ORR activity loss extent, SEF loss, and F- emission rates were similar between 60 and 75C, but increased substantially at 90°C. The right set of plots shows relatively good agreement between the two series at 0.60V, 90°C cell temperature.

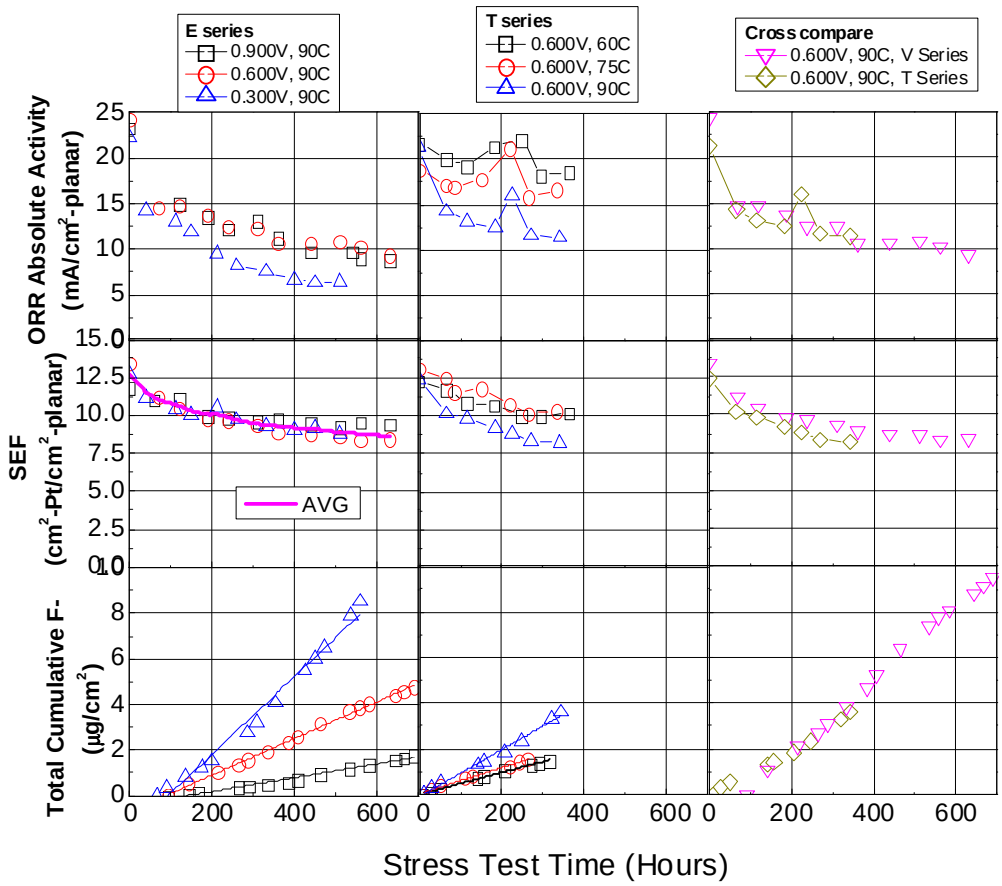

Figure 171. Comparison of potential control series (left), temperature control series (middle), and a cross comparison at identical conditions (right).

The datasets were provided to Argonne National Laboratory (R. Ahluwalia) for analysis and NSTF MEA durability model development. The overall assessment are shown in Figure 172 and Figure 173 from ANL's 2016 annual merit review presentation. The model predictions are that projected lifetime under a high durability drive cycle (minimized high temperature excursions), the time to 10% voltage loss is ca. 800 hours, due to increased ORR overpotentials and apparent mass transport losses due to F- emission. ANL's assessment differs from 3M's, in that ANL separately estimates the ORR activity and cathode mass transport overpotentials' dependences on cathode F- emission, whereas 3M's assessment is that the ORR activity loss alone determines the mass transport loss.

Irreversible Increase in Mass Transfer Overpotentials

Limiting current density (i_L) defined for convenience as the reference current density at which the mass transfer overpotential (η_m) equals 300 mV

- i_L can be correlated with CFR without any explicit dependence on hold potential or exposure temperature
- **2 µg.cm^{-2} suggested as the absolute upper limit of CFR for NSTF MEA**: Value at which i_L becomes <1 A/cm^2 at 3M standard conditions

Mass transfer overpotential (η_m) correlated with i/i_L and the cumulative fluoride release at cathode (CFR)

- **CFR has to be restricted to <0.5 µg.cm^{-2}** to limit increase in η_m at EOL to 35 mV at 1 A/cm^2 (half of target 10% degradation at EOL)

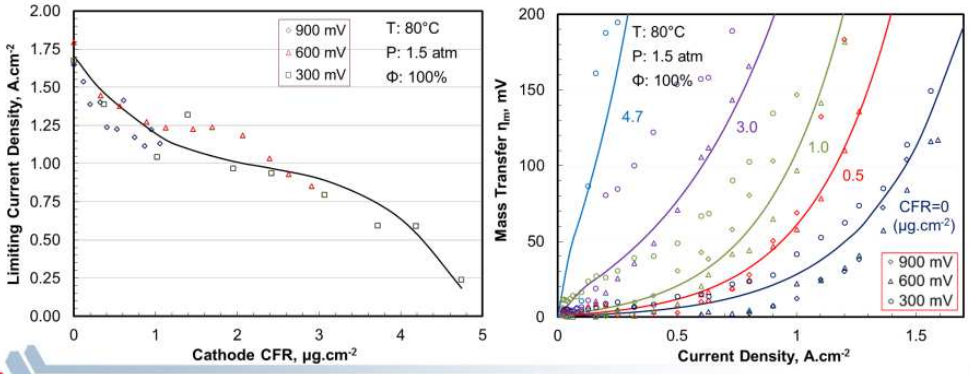

10

Figure 172. ANL analysis of NSTF MEA limiting current density and mass transfer overpotentials dependences on cumulative cathode F- emission.

Projected Durability of Stacks with NSTF MEA

Projected durability over lifetime represented as repeated FUDS and FHDS schedules

- Stack Design Point: 2.5 atm stack inlet pressure; 95°C coolant exit (stack) T; SR_c = 1.5; 40°C ambient T; 1.45 kW/°C Q/ΔT constraint
- High Performance: Coolant exit T (88°C at full power) and SR_c (1.7 at full power) determined for maximum performance; 25°C ambient T
- High Durability: Coolant exit T (80°C at full power) and SR_c for 1% lower than maximum efficiency; 25°C ambient temperature
- **Increased ORR kinetic losses contribute 30% and mass transfer losses contribute 70% of the projected 10% performance degradation at 800 h**
- **Need to limit CFR to 0.7 µg.cm^{-2} over 5,000 h**
- **Mitigation strategies: Improve catalyst and support to reduce ECSA loss by 50% (not as critical); More stable membrane to reduce FER by ~80% (critical)**

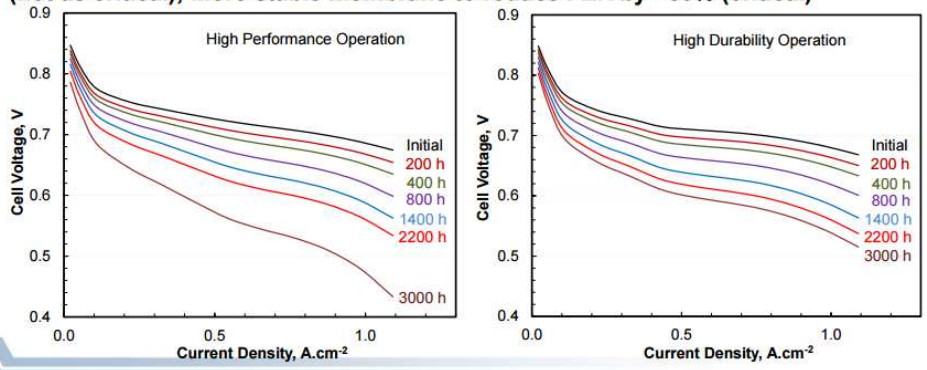

11

Figure 173. ANL analysis of NSTF MEA lifetime

Subtask Conclusions

In extensive studies, rated power durability of baseline NSTF MEAs was found to depend upon several material and operational variables. Performance degradation was accelerated by incorporation of low EW PEMs, lack of PEM decomposition mitigating additive, lower cathode loading, increased operating temperature, and decreased operating potential.

A key correlation was identified between H_2/Air performance at 1A/cm^2 and cathode absolute activity from over 53 MEAs and over 200 individual data points. A numerical fit of the correlation indicates an ~ 120mV/decade dependence at 1A/cm^2. The correlation suggests that cathode activity loss alone may be responsible for rated power loss in NSTF MEAs, and that maintenance of activity above ca. 15mA/cm$^2_{planar}$ may be sufficient to mitigate the effect. The mechanism for why ORR activity influences H_2/Air performance in this manner is not known.
A material based approach to improving rated power durability was identified, but performance was insufficient to allow downselection for project BOC MEAs.

Mechanism studies confirmed the hypothesis that rated power loss of NSTF MEAs is due to ORR absolute activity loss, induced by two means, cathode surface area loss and specific activity loss. A correlation was identified between specific activity loss and cumulative cathode F- emission, a measure of PFSA decomposition.

The correlations between H_2/Air performance, ORR activity, and F- emission were used to generate a durability model of NSTF MEAs. The model indicates that with baseline NSTF MEAs, the expected time to 10% voltage loss is approximately 800 hours. To attain the 5000 hour durability target, cathode FER must be reduced by ca. 80% by incorporation of more stable membranes.

The specific root cause mechanism for the ORR specific activity loss with PFSA decomposition is not yet known with certainty, but the hypothesis consistent with all of the experimental results is that PFSA decomposition could conceivably produce water insoluble ionomer fragments which are catalyst poisons, such as long-chain perfluorocarboxylic acids, which adsorb to the cathode catalyst thereby decreasing the activity. Based on the performance decay rates, it is estimated that the generation rate of such contaminants is at least two orders of magnitude less than the F- emission rates.

Future Directions

The work above has set the path for two primary approaches to implement a materials-based solution to rated power loss of NSTF MEAs.

A first high-level pathway is to incorporate durable NSTF cathode catalysts with improved specific area. Based on the current mechanistic understanding, improved specific area catalysts will maintain the cathode absolute activity above the ca. 15mA/cm^2 threshold for severe rated power loss for longer periods of time, assuming constant contaminant delivery rates. This work is on-going at 3M.

A second high-level pathway is incorporation of PEMs which are more chemically stable and/or produce a smaller proportion of the irreversibly adsorbed contaminants per unit PFSA decomposition. This work would be accelerated if the specific proposed contaminant species

could be detected via analytical technique. The challenge is two-fold; the generation rates are likely orders of magnitude smaller than the F- emission rate (already low), and the proposed contaminants are not believed to exit the cell in the effluent water (irreversibly adsorbed).

Task 6. Short Stack Beginning of Life Performance, Power Transient, and Cold Start Evaluation

- *Subtask 6.1 Baseline MEA Evaluation*
- *Subtask 6.2 Interim Best of Class MEA Evaluation*
- *Subtask 6.3 Best of Class MEA Evaluation*

The work under Task 6 consists of evaluation of 1 stack with the interim best of class MEAs determined from subtask 4.1 (subtask 6.2), and in the final year, 1 stack containing Best of Class Integrated MEA candidates from subtask 4.1 (subtask 6.3). Short stack evaluation is a necessary benchmark to validate improvements observed in the single cell MEA development work done under other tasks, especially improvements towards cold start and power transient, as well as to demonstrate freeze start. The results of subtask 6.3, combined with the durability testing results from subtask 5.4, will be used to determine the final Best of Class Integrated MEA to be incorporated into the final short stack deliverable.

Short stack evaluation in Subtask 6.2 and 6.3 is to occur at General Motors, contingent upon passage of three MEA robustness criteria in 50cm^2 MEA testing at 3M (Table 3). Delivery of the final project short stack is also contingent upon passage of the criteria.

Subtask 6.1 Baseline MEA Evaluation

Subtask Overview

Short stack evaluation is a necessary benchmark to validate improvements observed in the single cell MEA development work done under other tasks, especially improvements towards cold start and power transient, as well as to demonstrate freeze start. The results of subtask 6.3, combined with the durability testing results from subtask 5.4, will be used to determine the final Best of Class Integrated MEA to be incorporated into the final short stack deliverable.

Subtask High Level Work Summary

Baseline MEA materials for stack testing were procured and validated. New terms to enable stack testing at a project subcontractor, GM, were negotiated and accepted by 3M, GM and DOE. The new terms disallowed stack testing to occur with project baseline materials.

Subtask Key Results

Baseline Stack Material Validation

Two baseline material sets were identified, with a 0.05PtCoMn/NSTF anode, 3M 24µm 825EW PEM, 3M 2979 anode and cathode GDLs, and a cathode electrode consisting of Pt_3Ni_7(Dealloy+SET)/NSTF at either 0.10 or 0.125mg$_{PGM}$/cm^2. Outside of this project, roll-good catalyst coated membranes (CCMs) were generated on 3M production equipment and 2979 GDL was procured from existing stock, in sufficient quantities to support short stack evaluation.

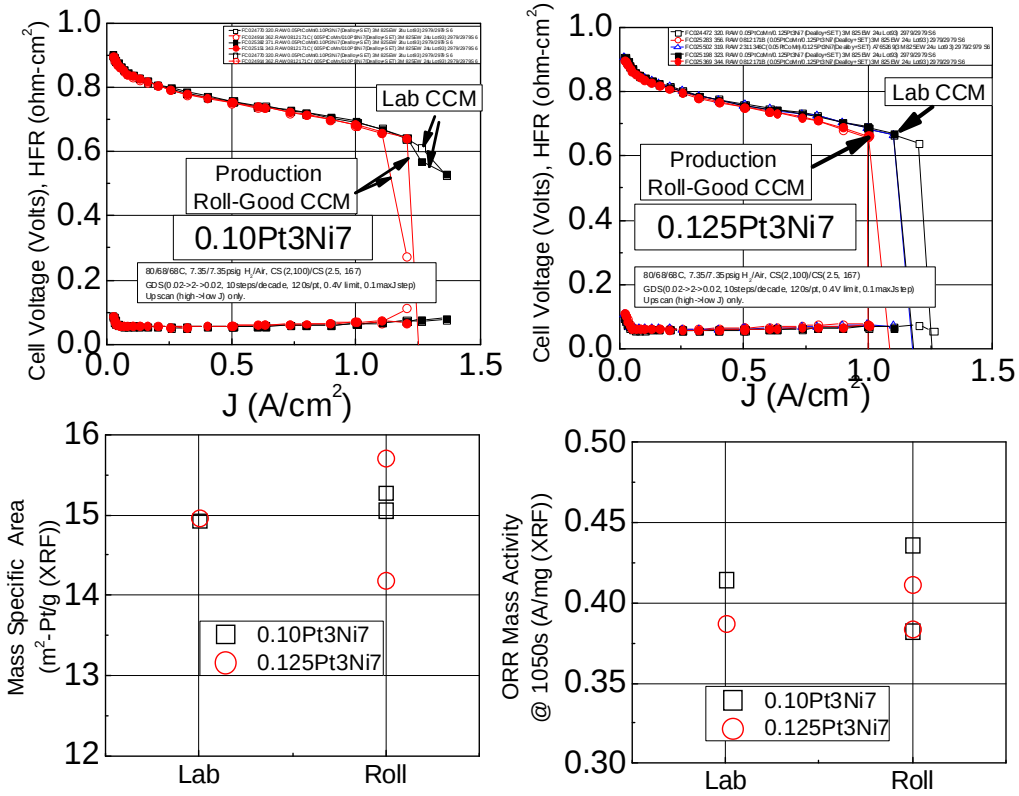

Figure 174. H_2/Air Performance, Specific Area, and Mass Activities of Roll-Good CCMs to be Used for Stack Testing, as Compared to Lab-Made.

Figure 174 compares the fuel cell H_2/Air performance, ORR mass activity, and catalyst surface area for the production roll-good CCMs to lab made CCMs, using similar or same input materials. Under H_2/Air, the roll-good CCMs yielded similar kinetic response as the lab made CCMs, but the limiting current densities were slightly lower. The mass specific area and ORR mass activities were similar between lab and production CCMs.

Stack Testing Resource Challenge and Plan Adjustment

On Oct. 5th, 2012, General Motors publicly announced that it will be closing its Honeoye Falls, NY fuel cell research facility. The work GM was to conduct under this project, including stack testing, was to primarily have occurred at the Honeoye Falls facility.

In January, 2013, GM informed 3M that stack testing could occur at GM only upon passage of three robustness criteria. This was unacceptable to 3M, as the terms of 3M's SOPO indicated stack testing was a key deliverable.

Negotiations continued. During a May, 2013 phone conference between 3M (E. Funkenbusch, A. Steinbach), GM (M. Matthias) and DOE (K. Epping-Martin, G. Kleen), a resolution was identified. It was agreed by all that GM would evaluate 3M MEAs in stacks under this project, contingent upon demonstration of substantial progress on three robustness criteria, two related to low temperature operation and one to operation under high temperature operation with reduced RH. It was also agreed that 3M will not be contractually responsible to conduct stack testing if the criteria are not met. Table 19 lists the agreed-upon criteria.

Table 19. Robustness criteria to enable stack testing at General Motors		
Demonstration of the three robustness criteria to occur in subscale (e.g. 50cm^2) hardware with stack candidate materials. Evaluation to occur at 3M.		
Criteria name	Description	Value
Cold Operation	Stack voltage at 30°C as a fraction of the stack voltage at 80°C operation at 1.0 A/cm^2, measured using the protocol for a polarization curve found in Table 3. A 25°C dew point is used only for 30°C operation.	>0.3
Hot Operation	Stack voltage at 90°C as a fraction of the stack voltage at 80°C operation at 1.0 A/cm^2, measured using the protocol for a polarization curve found in Table 3. A 59°C dew point is used for both 90°C and 80°C operations.	>0.3
Cold Transient	Stack voltage at 30°C transient as a fraction of the stack voltage at 80°C steady-state operation at 1.0 A/cm^2, measured using the protocol for a polarization curve found in Table 3. A 25°C dew point is used only for 30°C operation. 30°C transient operation is at 1 A/cm^2 for at least 15 minutes then lowered to 0.1 A/cm^2 for 3 minutes without changing operating conditions. After 3 minutes, the current density is returned to 1 A/cm^2. The voltage is measured 5 seconds after returning to 1 A/cm^2.	>0.3

Based on existing data, the baseline material set was assessed to have a very low probability of achieving the Table 19 metrics, so baseline stack testing did not occur.

Subtask Conclusions

Baseline MEA stack testing did not occur.

Future Directions

N/A

Subtask 6.2 Interim Best of Class MEA Evaluation

Subtask Overview

Short stack evaluation is a necessary benchmark to validate improvements observed in the single cell MEA development work done under other tasks, especially improvements towards cold start and power transient, as well as to demonstrate freeze start. The results of subtask 6.3, combined with the durability testing results from subtask 5.4, will be used to determine the final Best of Class Integrated MEA to be incorporated into the final short stack deliverable.

Subtask High Level Work Summary

Interim Best of Class MEAs were evaluated in single cells and did not achieve the required robustness metrics outlined in Table 19. No stack testing was conducted.

Subtask Key Results

In CY14Q01, experiments were conducted to evaluate status against the three robustness criteria needed to allow stack testing. The MEA was the baseline CCM used in the interlayer testing (0.05/0.15PtCoMn, 3M 825EW 20u), the interim Best of Class Anode GDL ("X2"), and the interim Best of Class cathode interlayer with ca. 0.03mg_{PGM}/cm^2. Table 20 summarizes the results from this testing. The MEA passed the hot operation test, but did not pass the cold operation or cold transient tests under specific conditions. A modest modification of test conditions, decreasing the anode pressure from 150 to 100kPa, resulted in near passage for both the Cold Operation and Cold Transient tests.

Table 20. Robustness Criteria Needed for Stack Testing at GM

Demonstration of the three robustness criteria to occur in subscale (e.g. 50cm^2) hardware with stack candidate materials. Evaluation to occur at 3M.

Criteria name	Description	Target Value	Status
Cold Operation	Stack voltage at 30°C as a fraction of the stack voltage at 80°C operation at 1.0 A/cm^2, measured using the protocol for a polarization curve found in Table 3. A 25°C dew point is used only for 30°C operation.	> 0.3	~ 0 (w/ 150kPa anode) *0.29 w/ 100kPa*
Hot Operation	Stack voltage at 90°C as a fraction of the stack voltage at 80°C operation at 1.0 A/cm^2, measured using the protocol for a polarization curve found in Table 3. A 59°C dew point is used for both 90°C and 80°C operations.	> 0.3	1.0 (*performance increased)*
Cold Transient	Stack voltage at 30°C transient as a fraction of the stack voltage at 80°C steady-state operation at 1.0 A/cm^2, measured using the protocol for a polarization curve found in Table 3. A 25°C dew point is used only for 30°C operation. 30°C transient operation is at 1 A/cm^2 for at least 15 minutes then lowered to 0.1 A/cm^2 for 3 minutes without changing operating conditions. After 3 minutes, the current density is returned to 1 A/cm^2. The voltage is measured 5 seconds after returning to 1 A/cm^2.	> 0.3	~0 w/ 150kPa anode "almost" achieved @ 100kPa anode

Figure 175 (top) summarizes results from the cold operation and cold transient tests. The test protocol calls for 150/150kPa reactant pressures during the test, but based on our experience we believed that improved performance could be achieved by decreasing the anode reactant pressure lower than the cathode, which increases anode water removal and generally increases low T performance. For the Cold Operation Test (upper left), steady state performance at 30°C, 1A/cm^2 is evaluated. The MEA performance was relatively unstable with 125 or 150kPa anode pressure, oscillating between H_2 evolution (negative V) and oxygen reduction (positive V) at the cathode. At 100kPa, positive cell voltage (ORR) was maintained, but the voltage was too low and the test station software automatically reset the cell load to OCV. It is possible the MEA would have passed at 100kPa if the software low V safety setting was modified. On the upper right, the Cold Transient performance showed a similar result as for the Cold Operation test, in that negative voltages were obtained at 125 and 150kPa anode pressure, but at 100kPa the cell was showing signs of recovering.

Figure 175 (bottom) shows that under the Hot Operation test, the MEA performance increased slightly with 90°C operation, easily passing the test. We suspect that the cathode interlayer is providing some benefit under this test in maintaining the PEM hydration state.

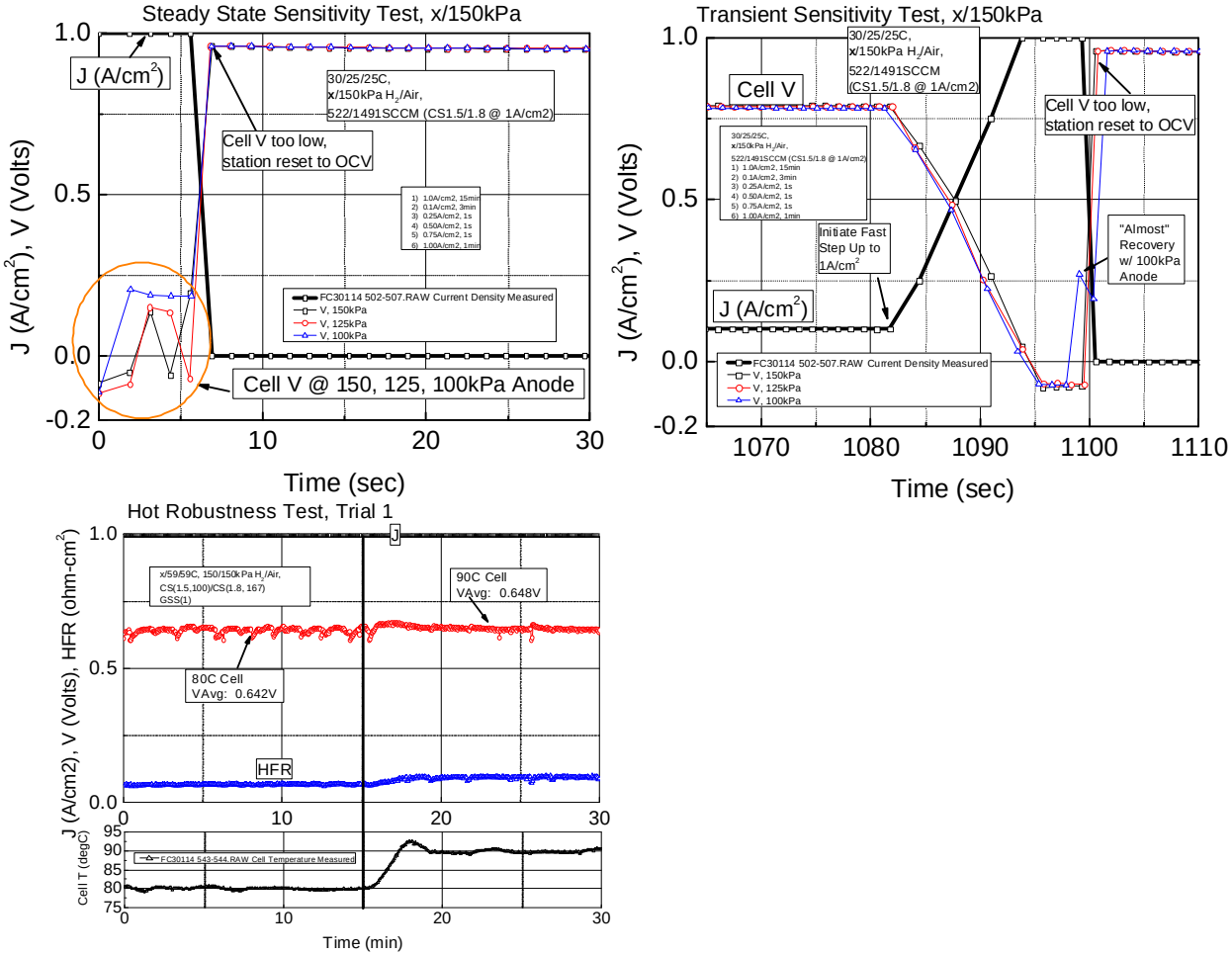

Figure 175. Evaluation of NSTF MEA w/ Interim Downselect Anode GDL and Cathode Interlayer Against Robustness Tests.

Due to the "almost" passing of the Cold Operation and Cold Transient tests at 100kPa, it is suspected that a modest additional improvement in interlayer performance would result in passage of these tests. Currently, at BOL, the interim downselect IL provides about a 20°C improvement in operating temperature range over no IL in our screening testing, so we estimate that if the IL generated a 25-30°C improvement it would pass these tests.

Subtask Conclusions

A baseline CCM with interim downselect anode GDL and cathode interlayer achieved one of three robustness metrics. Reduction of anode reactant pressure from 150 to 100kPaA resulted in the MEAs nearly passing the Cold Operation and Cold Transient tests.

Due to not passing the robustness metrics, stack testing did not occur.

Future Directions

N/A

Subtask 6.3 Best of Class MEA Evaluation

Subtask Overview

Short stack evaluation is a necessary benchmark to validate improvements observed in the single cell MEA development work done under other tasks, especially improvements towards cold start and power transient, as well as to demonstrate freeze start. The results of subtask 6.3, combined with the durability testing results from subtask 5.4, will be used to determine the final Best of Class Integrated MEA to be incorporated into the final short stack deliverable.

Subtask High Level Work Summary

Subtask Key Results

Best of Class MEA Operational Robustness

Project 2015 Best of Class MEAs (March and Sept.) were evaluated for operational robustness using 3M protocols. Figure 176 compares load transient performance of these BOC MEAs to the pre-project baseline. Both BOC MEAs allowed both stable and transient operation to as low as 40°C cell temperature, as compared to 70°C with the baseline MEA. The BOC MEAs were not able to achieve operation at 30°C, suggesting challenges against the Table 19 robustness Cold Operation and Cold Transient metrics. In fact, the March BOC MEA had *lower* 30°C performance than the baseline. Our assessment was that this operational challenge was likely due to significant contamination of the PFSA PEM by Ni cations from the cathode.

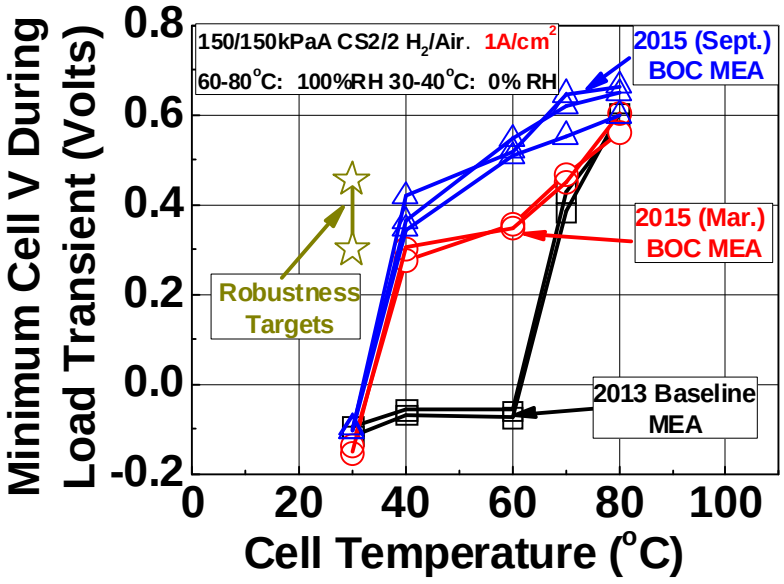

Figure 176. Evaluation of project baseline and 2015 (March) and (Sept.) BOC MEAs in 3M load transient testing.

Figure 177 compares baseline 0811041B or 2015(March) BOC) on the response under the Tech Team Robustness Cold Operation and Cold Transient test. In this figure, the anode pressure was reduced from the protocol spec'd 50kpa to 0kPag. Both MEAs contained the interim X2 anode GDL and the interim downselect cathode IL. Both MEAs failed the transient test, although the baseline 0811041B MEA "almost" recovered after the step change. The 2015BOC CCM performance at 1A/cm^2 was significantly worse than the 0811041B. This is a similar response as was observed in the 3M load transient test at 30°C (Figure 176).

Figure 178 compares these MEAs under the Tech Team Hot Operation test. Both MEAs passed, but the 2015BOC MEA showed a larger loss than the baseline 0811041B CCM, again likely due to the PEM contamination by Ni^{2+}.

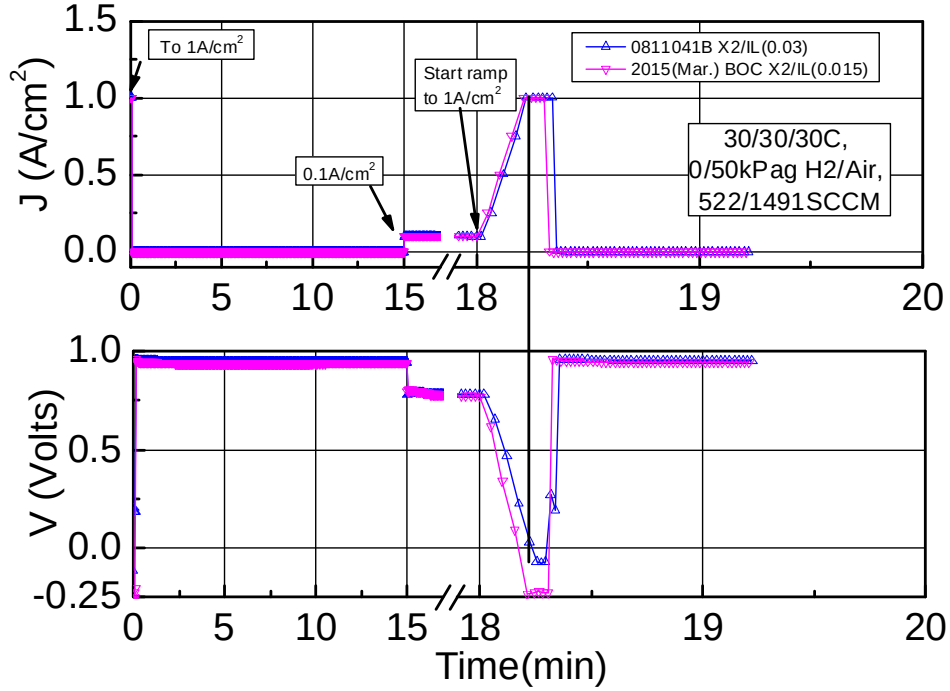

Figure 177. Tech Team Cold Operation, Cold Transient (Modified, 0kPag anode)

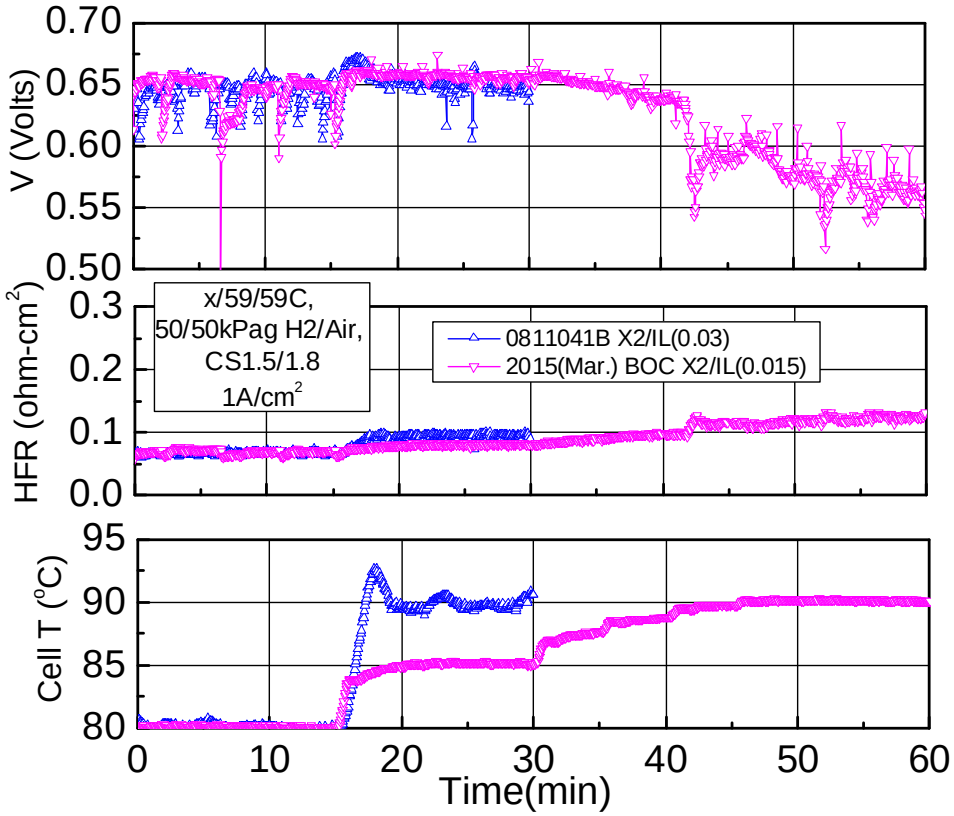

Figure 178. Tech Team Hot Operation

In June 2015, 3M (A. Steinbach) and GM (B. Lakshmanan) met at the Annual Merit Review and GM agreed to conduct stack testing under the project. The plan was for 3M to provide validated materials sufficient for a short stack test by early September.

MEA Production and Validation for Stack Testing

Two pilot scale CCM production runs were conducted and resultant CCMs were evaluated. In the first process trial (0815219B), the objective was to tune the continuous lamination process for this new anode/cathode/PEM component combination. ~43 lineal feet were produced, using a first dealloyed catalyst lot "A". A second process trial, 0815280A, produced ~ 90 lineal feet of CCM with optimized transfer conditions using cathode catalyst lots "C" and "D". Due to the experimental nature of the input materials, optimized CCM fabrication conditions had not been established, so some preliminary process optimization was conducted during production. As such, the CCMs were sectioned and each section was analyzed for visual quality and catalyst transfer extent. XRF analysis was conducted on the input anode and cathode catalyst before and after CCM transfer for the first CCM lot, 0815219B. The average total CCM PGM content was $0.105 mg/cm^2$.

Representative acceptable CCM sections were conditioned, then evaluated for BOL fuel cell performance and mass activity. Figure 179 compares break-in conditioning rates for laboratory vs. pilot scale CCMs (both lots). Note that the MEAs were tested in standard "quad serpentine" flow field test cells with baseline diffusion media, and that only the MEA cathode was conditioned. Break-in rate and extent were generally comparable and within expectation. The only observed difference was that during the first 3 hours of conditioning, the pilot scale CCMs had lower performance at 0.30V, but afterwards the two CCM types were similar. This small difference was not considered to be of concern.

After cathode conditioning, Figure 180 shows that the pilot scale CCMs (both lots) slightly outperformed laboratory CCMs using the same input lots with qualitatively good reproducibility. Table 21 shows that the pilot scale CCM had modestly higher mass activity and specific area than the laboratory CCMs. Pilot scale CCM mass activity was comparable to expectation for the continuous dealloyed catalyst discussed in the Subtask 1.1 section.

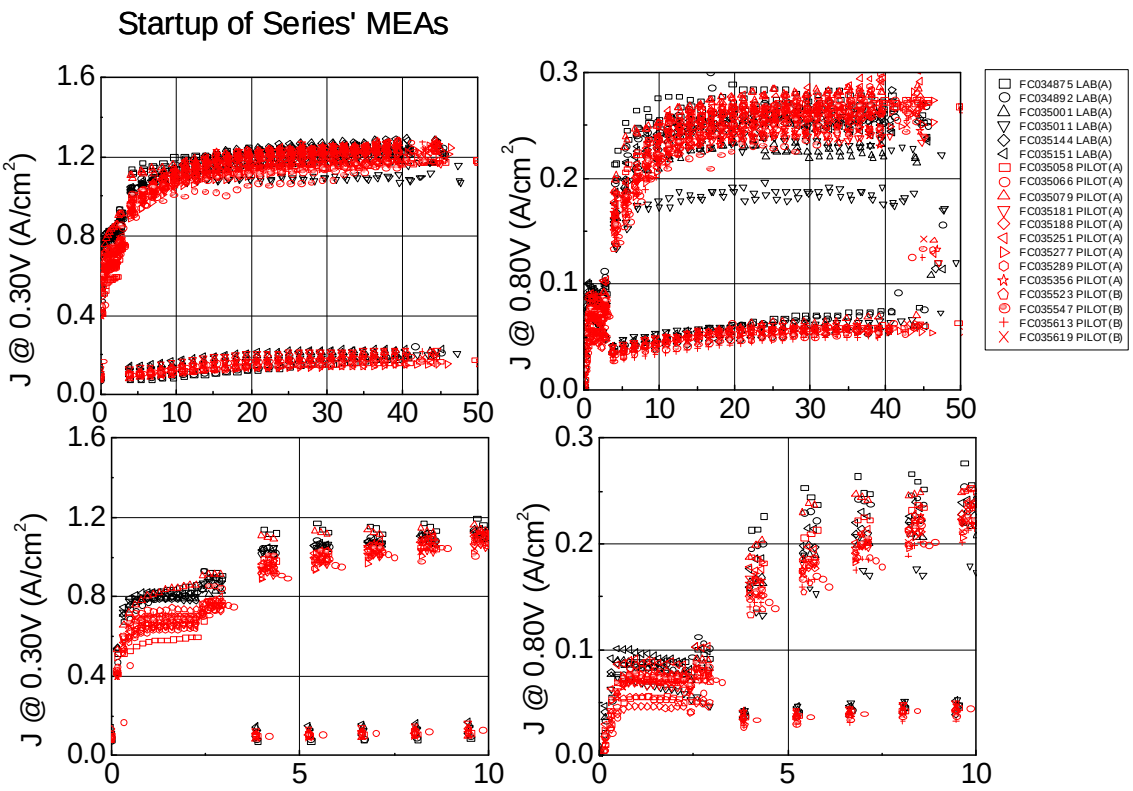

Figure 179. Cathode break-in conditioning of BOC MEAs. (Black): Lab CCM. (Red): Pilot CCM.

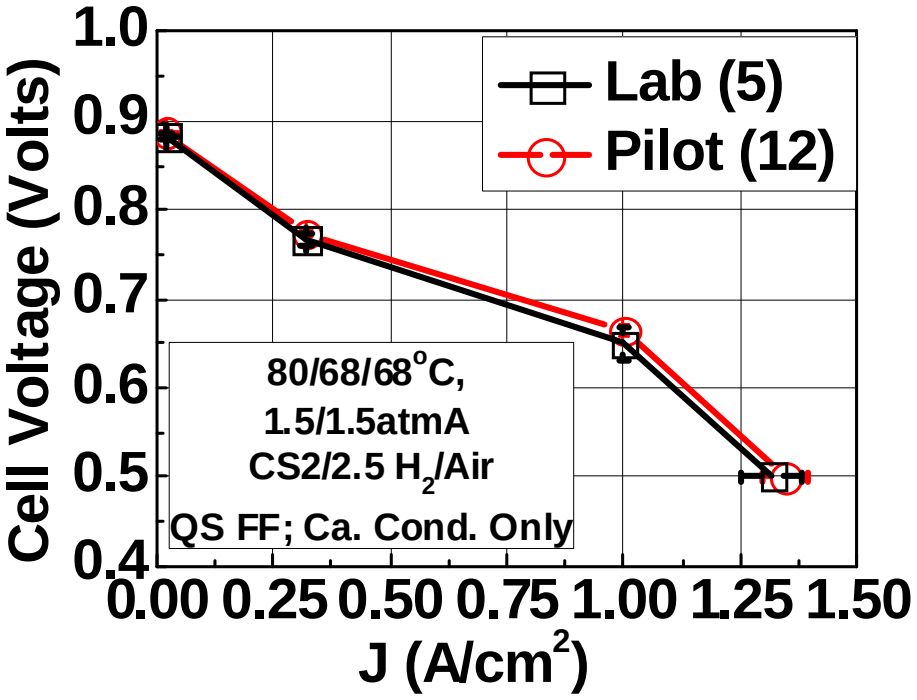

Figure 180. H_2/Air performance of 2015 (Sept.) BOC CCMs (not BOC MEAs).

Table 21. Mass activity and specific areas		
	Lab (5)	**Pilot (12)**
Mass Activity (A/mg_{PGM})	0.28 ± 0.03	0.33 ± 0.03
Specific Area (m^2/g_{PGM})	11.8 ± 1.4	14.5 ± 0.7

BOC MEAs were assembled using the 0815219B lot of CCM and project downselect anode GDL and cathode GDL with interlayer from Task 2 and FF2 flow field. MEA anodes and cathodes were conditioned per usual procedure. Figure 181 shows that the Sept. BOC MEA with pilot-scale CCM outperformed the March BOC MEA (laboratory scale CCM) for both H_2/Air performance and operational robustness.

Based on the results above, the Sept. BOC MEA was assessed as validated and suitable for stack evaluation, based on the generally comparable or improved break-in conditioning rates, H_2/Air performance, mass activity, specific area, and operational robustness over the comparative materials evaluated.

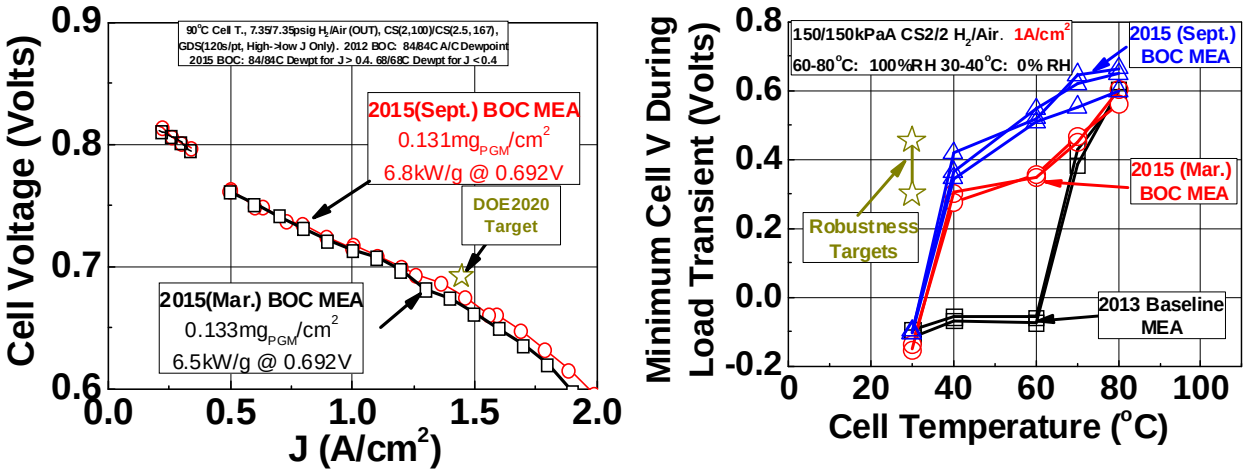

Figure 181. Comparison of H_2/Air performance and operational robustness of 2015 (March) and (Oct.) BOC MEAs.

While break-in conditioning between the pilot-scale Sept. BOC MEAs was similar to the laboratory MEAs made with the same material (Figure 179), it was slower than previous BOC MEAs, such as the 2015 (March) BOC MEA with very similar material sets (Figure 182). This aspect was not recognized at the time of the above assessment. As discussed in the Subtask 4.1 section, the lower performance during the Cathode Activation phase was a bellwether for an apparent severe anode deactivation with the Sept. BOC MEAs. This anode deactivation lead to reduced performance and operational robustness *if the anode was not fully activated*. While the necessary break-in procedure was readily conducted in single cells, it ultimately was difficult to implement in stack and resulted in relatively poor performance and operational robustness in stack testing.

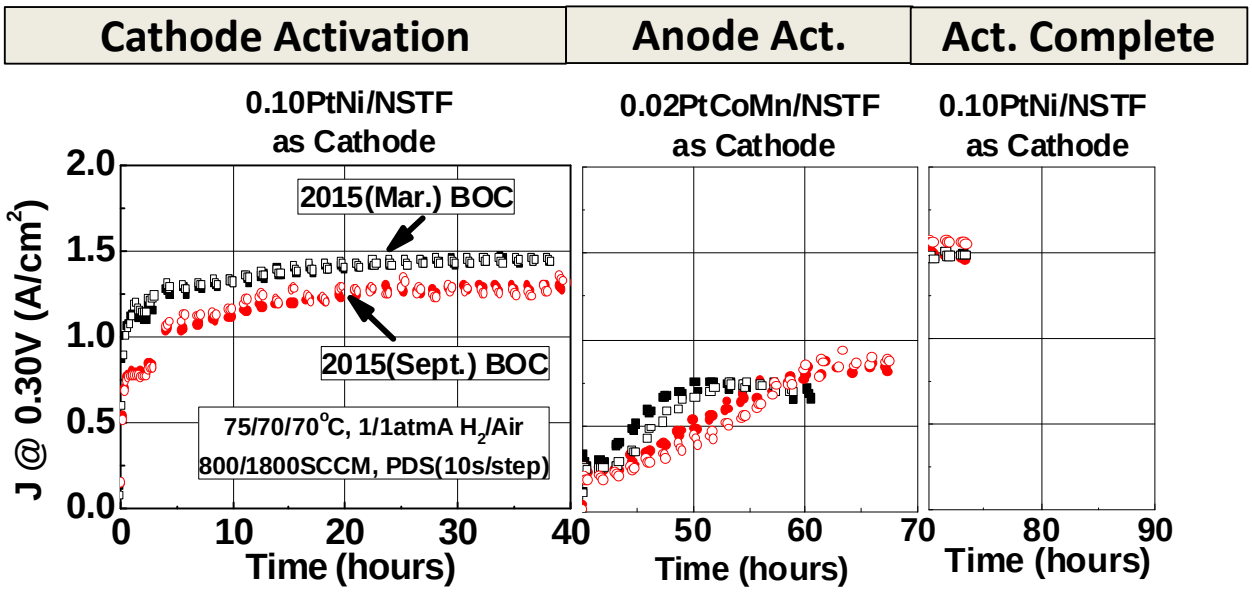

Figure 182. Comparison of Break-in Conditioning

Task 6 Work Overview at General Motors

The work initiated at GM in CY15Q3, and consisted of single cell and stack testing of 3M BOC MEAs.

The single cell work consisted of initial fit/function assessments. Some performance and operational robustness differences were observed between sites, and collaborative work between 3M and GM was conducted to resolve the site-site discrepancy. This included a site visit by a GM engineer to 3M to closely evaluate the 3M testing protocols and to enable a more direct assessment of possible testing differences. A summary of single cell work from GM will follow below, followed by a summary of 3M's support work.

Three stacks were built and evaluated at GM between ca. Nov. '15 and Aug. '16. The first was a 3-cell stack for initial fit/function assessment and protocol troubleshooting. The second stack was a 29-cell stack consisting of GM baseline MEAs, two types of 3M baseline MEAs, and 3M BOC MEAs. Evaluation of the second stack occurred in CY16Q1 into Q2. Some cells in the stack were damaged during testing. A third stack, also 29-cells, was built in CY16Q2 and evaluated periodically through the end of the project in Aug. '16. A summary of stack testing will follow below.

Single Cell Studies at GM

Initial work focused on establishment of methods for obtaining reliable data with NSTF MEAs at GM, which was reasonably consistent with 3M results. Work included evaluation of impacts of cell compression, conditioning method optimization, and test method implementation.

Figure 183 summarizes H_2/Air polarization curves measured at 3M and GM, for 3M BOC MEAs, 3M baseline MEAs, and GM baseline MEAs, described later in Figure 192. Under the GM test conditions (80°C, 1.5atmA, 32% RH), relatively similar performances were observed with modest differences in the kinetic and mass transport regimes (Figure 183 left). At low current density, the 3M BOC MEA yielded the highest performance, and at 1.5A/cm^2 the best

performance was obtained with the 3M baseline. Figure 183 (right) compares the 3M baseline and BOC MEAs, evaluated at 3M at 90°C cell temperature, 1.5atmA, and modest subsaturation (84°C dewpoints). 3M results indicated that the BOC MEA yielded performance which was substantially higher the baseline MEA. Close comparison of the 3M baseline data reveals reasonably comparable performances between sites. However, the 3M BOC MEA yielded appreciably lower performance at GM than at 3M, on the order of 50mV at 1.5A/cm^2.

Table 22. Configuration of various Membrane Electrode Assemblies (MEAs) that were used in the small scale experiments

MEA Type	Anode GDL[a]	Anode	Membrane	Cathode GDL[a]	Cathode
GM Baseline	GM GDL	Pt/GrV	GM Proprietary (18 µm)	GM GDL	Pt-alloy/C
3M Baseline	2979	0.05 PtCoMn NSTF	3M 825 EW PFSI (20 um)	2979	0.15PtCoMn NSTF
3M Best of Class	"X3" Low phobic treated	0.02 PtCoMn NSTF	3M-S 725 EW PSFI (14 µm)	2979 w/ IL (0.02 mg_{Pt}/cm^2)	0.10Pt_3Ni_7 NSTF

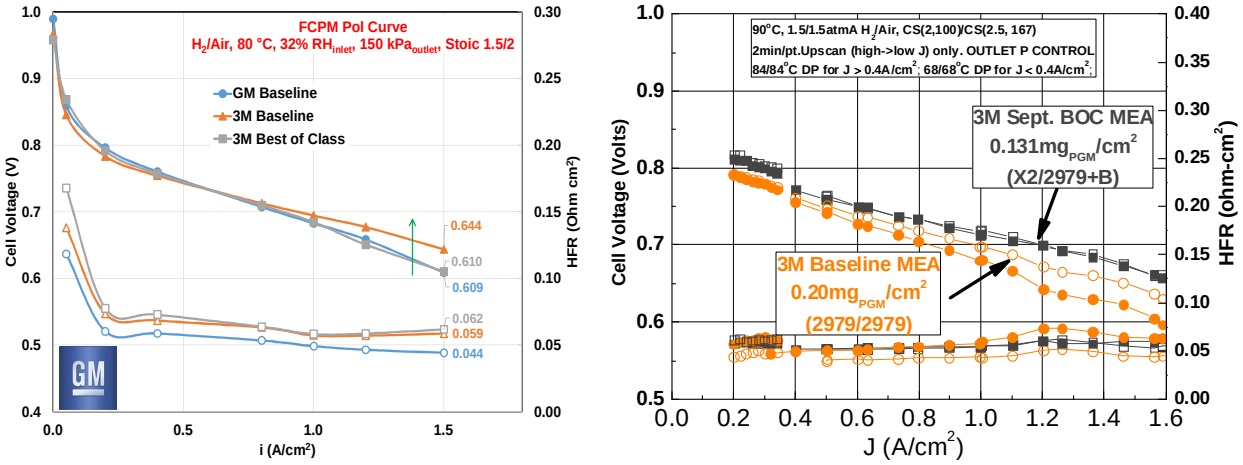

Figure 183. H_2/Air polarization curves of GM baseline, 3M baseline, and 3M Best of Class MEA. (Left): 80°C cell temperature, 32% RH, at GM. (Right): 90°C cell temperature, subsaturated RH at 3M.

Possible factors for the BOC MEA performance site-site discrepancy include differences in test conditions, different flow fields, and differences in break-in protocol. GM evaluated the impact of test conditions, specifically RH level. Figure 184 shows that at 60% and 100% RH, the NSTF MEA performances decreased compared to the GM baseline, essentially over the entire polarization curve. This is in sharp contrast to the comparable performances obtained between the MEA types at 32% RH in Figure 183 (left), above.

3M evaluated the impact of break-in protocol and flow field type. 3M implemented GM's protocol at 3M, and resultant performance with the GM protocol was qualitatively similar to the performance obtained at GM (Figure 185). It is possible that the relatively low performance of the 3M BOC MEA at GM was due to test protocol.

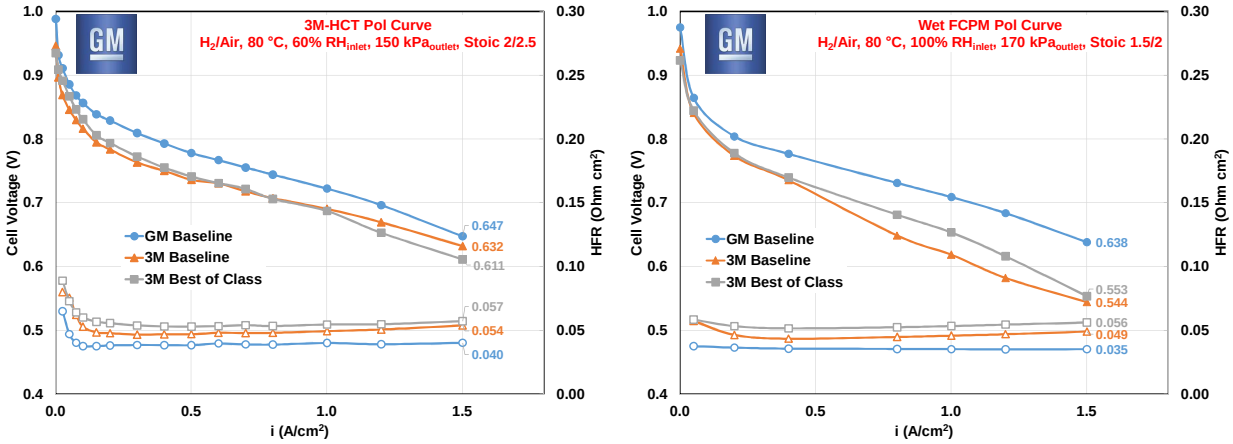

Figure 184. GM Evaluation of 80°C H_2/Air performance vs. inlet RH. (Left): 60% RH. (Right): 100% RH

Another possible reason for the relatively low BOC MEA performance at GM is if the anode was not sufficiently conditioned. Figure 186 shows that with minimal anode conditioning, the BOC MEA performance was essentially identical to that obtained with the 3M baseline MEA, and performances are essentially the same to that obtained at GM in Figure 183 (left).

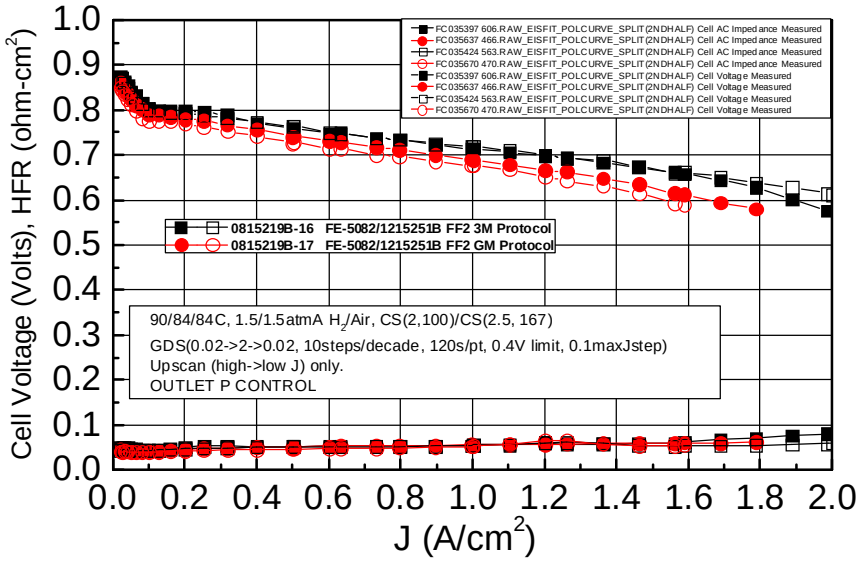

Figure 185. Comparison of BOC MEA performance after conditioning with 3M protocol (black) and GM protocol (red).

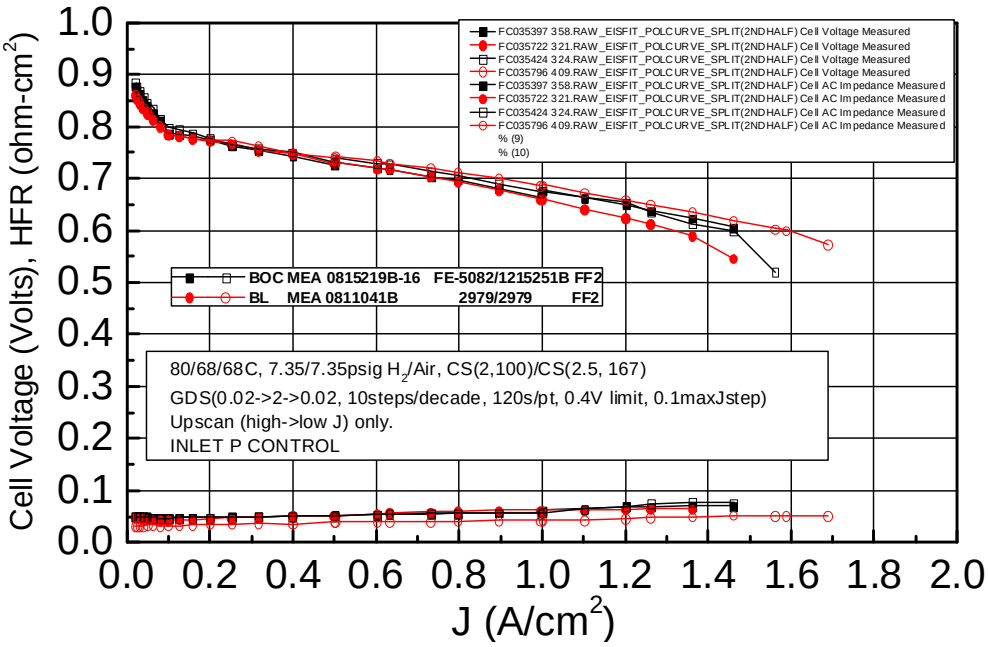

Figure 186. Comparison of 3M baseline MEA to BOC MEA with insufficient anode conditioning.

Flow field type was also determined to be a strong factor; use of a quad serpentine flow field from Fuel Cell Technologies resulted in dramatically reduced performance over most of the polarization curve (Figure 187). 3M and GM later inspected the GM flow field and the 3M FF2 and the differences identified were believed to be minor, and as such likely not responsible for the site-site performance difference.

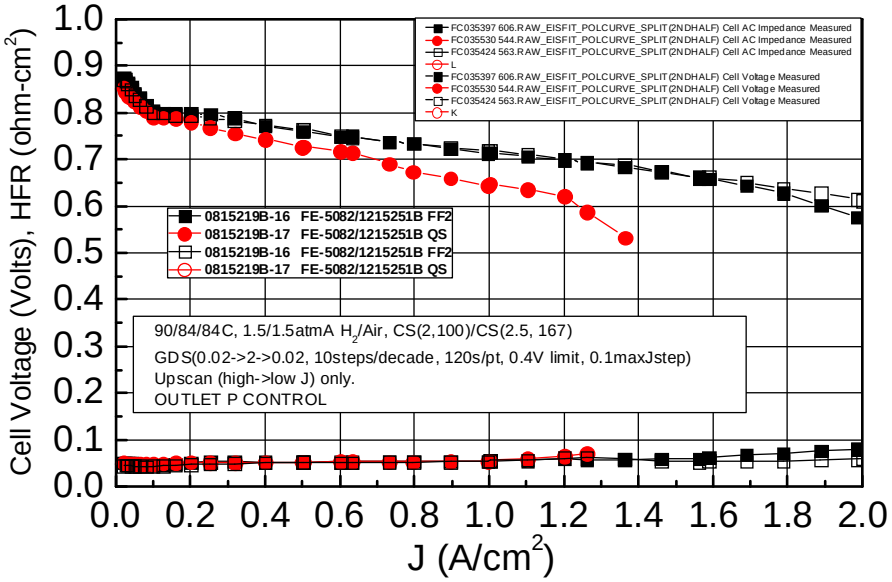

Figure 187. Comparison of BOC MEA performance in baseline quad serpentine flow field (red) or project downselect FF2 (black).

To aide in understanding performance discrepancies, GM evaluated the mass activity of the various MEAs. BOC MEA and baseline MEA mass activities were as expected and similar to 3M values.

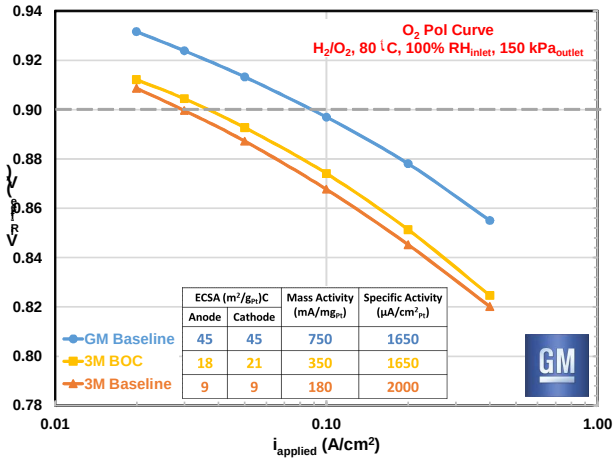

Figure 188. Kinetic analysis of GM baseline, 3M baseline, and 3M Best of Class MEAs.

Operational robustness measurements were also conducted at GM and compared to 3M values. Figure 189 compares steady state performances at low temperature. GM evaluated via 40°C H_2/Air polarization curves, which showed that the BOC MEA had improved limiting current density over the 3M baseline MEA which was comparable to the 3M data. However, at higher cell voltages where waste heat generation is lower, the BOC MEA had lower performance than the GM baseline data. The GM measurements of 3M baseline and BOC MEA limiting current densities at 40°C were close to those measured at 3M (right).

In addition, operational robustness towards load transients were also evaluated at GM. Initially, GM results with the 3M BOC MEA were substantially below 3M values, and were generally comparably (poor) to the 3M baseline MEA. After significant effort, including a visit by a GM engineer to 3M, it was determined that modest differences in test protocol were likely responsible, including changes in dwell time prior to the transient and placement of the cell thermocouple (end plate vs. in cathode flow field). After adjustments, reasonably good agreement *in trend* was observed between the two sites.

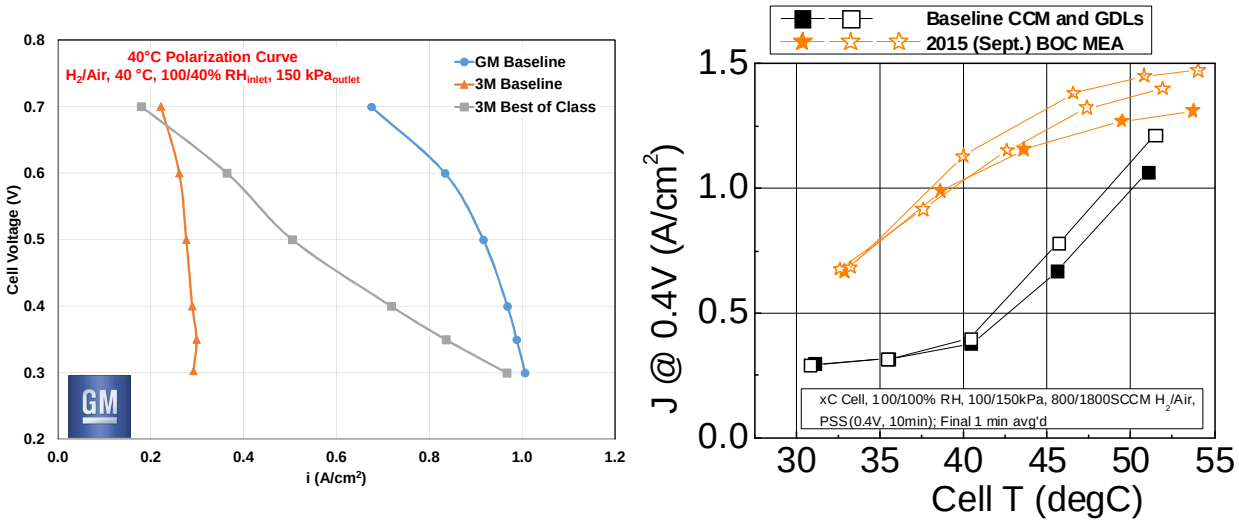

Figure 189. Comparison of steady state low temperature performance between test sites. (Left): 40°C H_2/Air polarization curves at GM. (Right): 0.40V temperature sensitivity measurements at 3M.

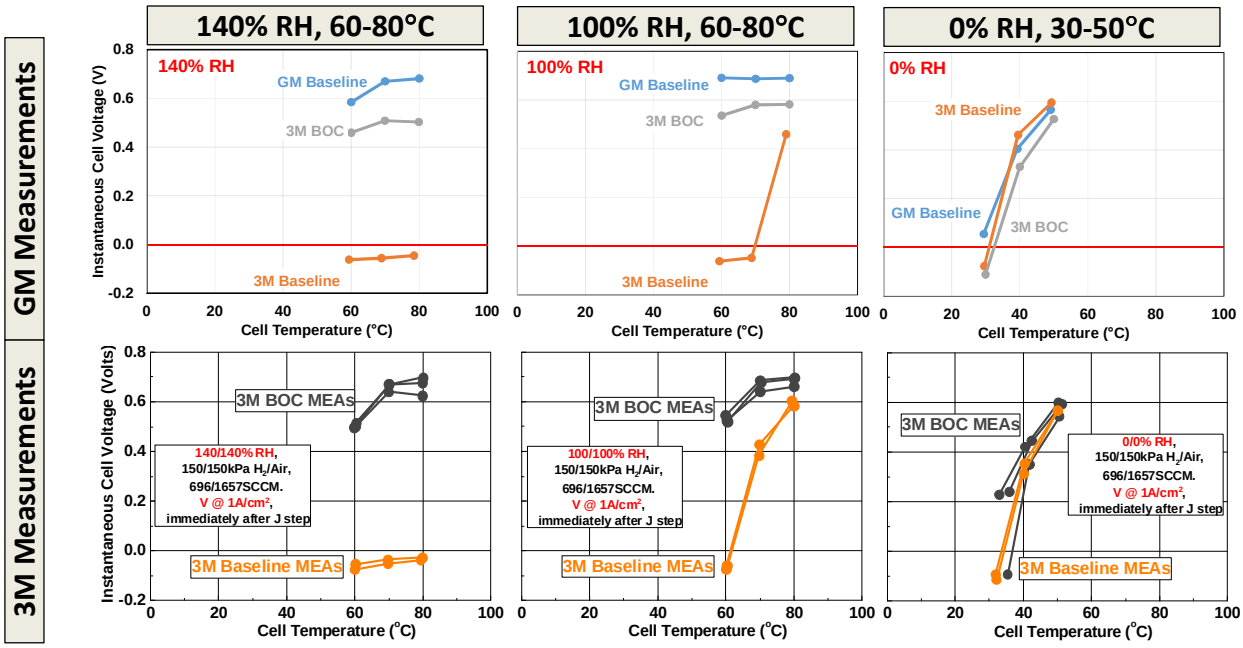

Figure 190. Load transient analysis of GM baseline, 3M baseline, and 3M Best of Class MEAs at several temperatures and relative humidities. (Top): Measurements at GM. (Bottom): Measurements at 3M.

In conclusion, at the single cell level, a majority of the performance, activity, and operational robustness characteristics reported at 3M were validated at GM. One primary area of remaining discrepancy is the relatively low rated power performance of the BOC MEA. Insufficient conditioning of the anode is a reasonable possible factor, but was not confirmed or refuted.

Short stack evaluations of BOC MEAs.

Initial 3-cell short stack evaluation

A 3 cell stack comprising BOC MEAs was built and conditioning was initiated. Conditioning used GM's best effort at implementing the 3M single cell protocol. Initial performance after 40 conditioning cycles was promising, achieving 1.4A/cm^2 at 0.40V, reasonably similar to single cell values. However, the measured HFR was ca. 4x higher than expectation. Based on this, the stack compression was increased and performance decreased. It was later determined that the high HFR was an artifact due to the use of too low of an AC impedance measurement frequency (1 kHz used vs. 7-10 kHz preferred for NSTF). Testing was halted due to the degraded performance.

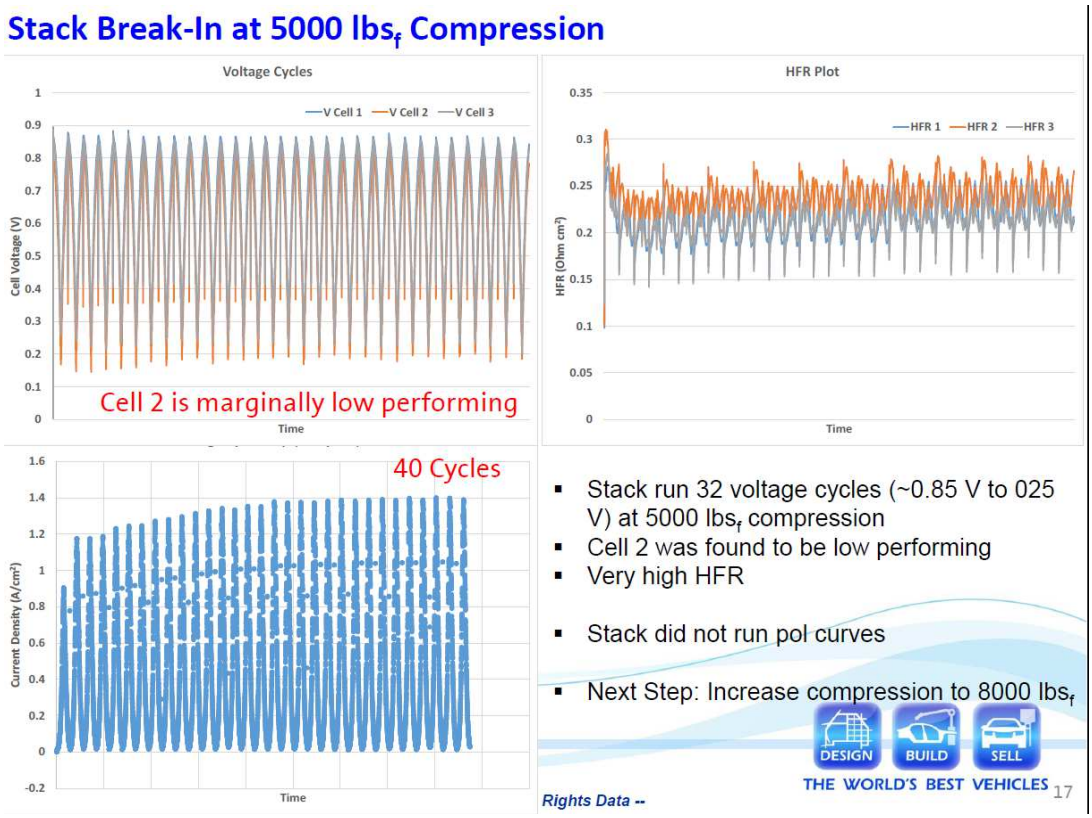

Figure 191 3-cell BOC MEA stack during break-in. (Top left): Cell voltage. (Top right): HFR. (Bottom left): Stack current density.

First 29-cell short stack

Based on the promising 3-cell stack results, a 29-cell short stack was built comprising GM baseline MEAs, two types of 3M baseline MEAs, and the 3M BOC MEA.

In this reporting period, a 29-cell rainbow short stack was built, conditioned, and evaluated for H_2/Air performance and load transient. The short-stack test stand was modified to incorporate liquid water flushing. Figure 192 summarizes the MEAs incorporated into the stack. 10 Sept. BOC MEAs were installed, as well as 10 GM baseline MEAs. Two 3M baseline CCMs were included, which contained 0.05/0.15PtCoMn/NSTF anode or cathode electrodes with either 825EW 20u supported PEM or the BOC PEM. All MEAs used 3M "X3" anode GDL and 2979 cathode GDL; the BOC MEAs also included the type "B" interlayer.

Short Stack Design

- Stack consisted of the following CCM MEAs

#	Type	Anode Description	Membrane	Cathode Description	No. of Cells
1	3M Baseline CCM	PtCoMn/NSTF 0.05 mg_{Pt}/cm^2	3M 825EW 20 µm	PtCoMn/NSTF 0.15 mg_{Pt}/cm^2	4
2	3M 'Baseline' CCM with 14 µm membrane	PtCoMn/NSTF 0.05 mg_{Pt}/cm^2	3M-S 725EW 14 µm w/ additive	PtCoMn/NSTF 0.15 mg_{Pt}/cm^2	4
3	3M March BOC CCM	PtCoMn/NSTF 0.02 mg_{Pt}/cm^2	3M-S 725EW 14 µm w/ additive	Dealloyed Pt_3Ni_7/NSTF 0.095 mg_{Pt}/cm^2 3M 2979 w/ "B" Interlayer IL Loading – 0.016 mg_{Pt}/cm^2	10
4	GM Baseline CCM	Dispersed Pt/C 800EW Ionomer	18 µm PFSA	Dispersed Pt-alloy/C 800EW Ionomer	10

- Following GDLs were used
  - Anode – 3M-X2 Low phobic GDL
  - Cathode – 3M 2979
- Short stack stands were equipped with DI Water Flush lines for thermal cycle break-in process

General Motors Company

-- Unlimited Rights Data --

Figure 192. First 29-Cell Stack Build Plan.

After assembly, the stack was installed on station and break-in conditioning was initiated (Figure 193). Approximately 170 conditioning cycles were conducted, including operation with Reversed MEA orientation to allow conditioning of the anode. The figure shows that MEA performances improved only marginally over time over the first 50 cycles. In single cell testing, performance improves considerably over the first 20 conditioning cycles. Under reversed MEA conditioning, performance was largely unchanged; in single cell testing, performance at the limiting current density increases at least 4x. When switched back to normal MEA orientation, performance improved modestly; the NSTF BOC MEA, increasing the performance from ca. 0.25V @ 1.1A/cm^2 to 0.41V. The BOC MEA performance was significantly below the NSTF baseline MEA, inconsistent with 3M and 3M single cell data. The GM baseline MEA outperformed the NSTF MEAs by ca. 100mV at 1.1-1.2A/cm^2.

Figure 194 summarizes the H_2/Air performance after conditioning. Performances were normalized to the GM baseline to protect GM confidential information. The BOC MEA performance was below the GM baseline and 3M baseline MEAs, attaining 70% of the absolute performance at 1.2A/cm^2. The BOC MEA did yield improved performance in the kinetic regime over the 3M baseline MEAs, as expected.

Figure 195 and Figure 196 summarize stack load transient performances at a variety of test conditions, noted in the figure captions. The BOC MEAs failed under all test conditions

evaluated, including 80°C cell temperature. The GM baseline MEAs largely passed the conditions tested.

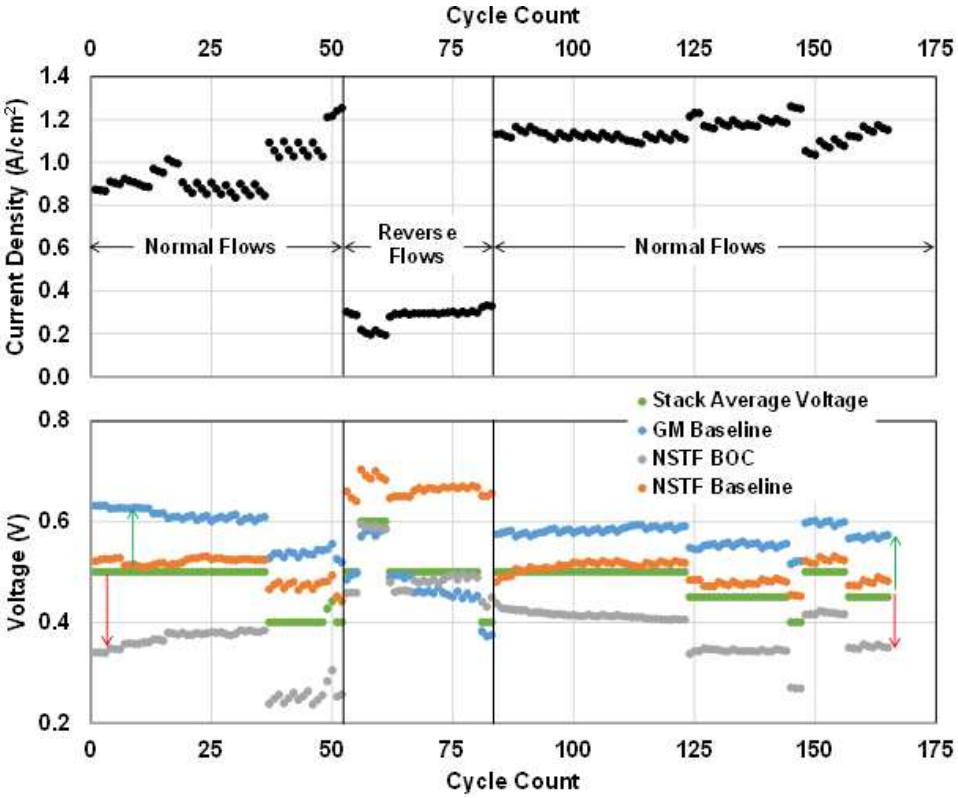

Figure 193. Performance Evolution During Stack Break-in Conditioning.

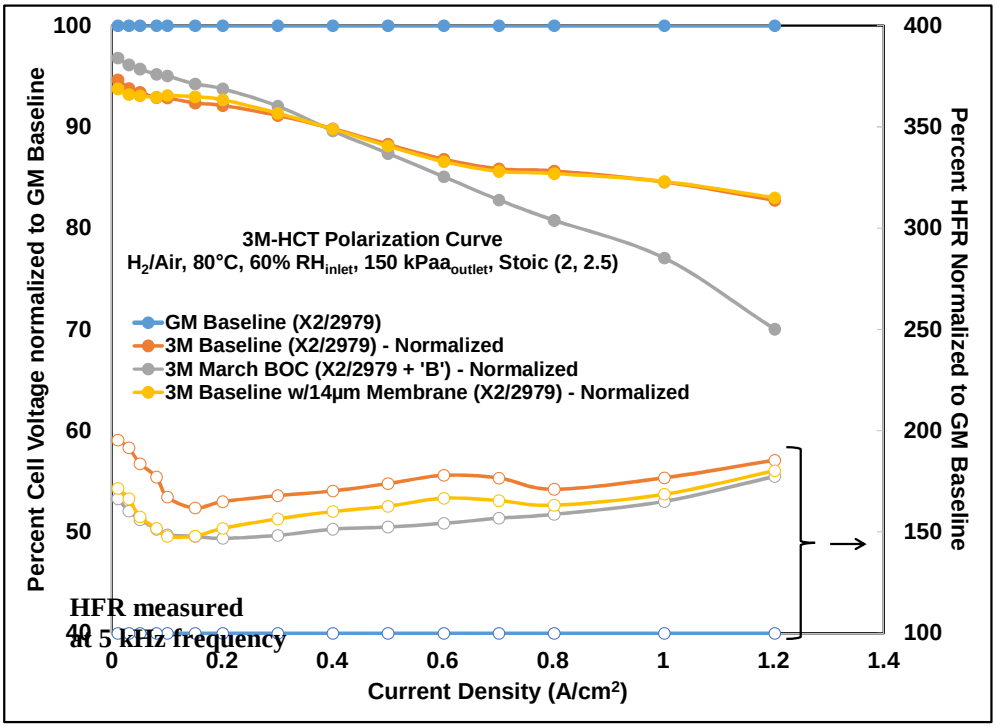

Figure 194. Normalized cell performance in stack.

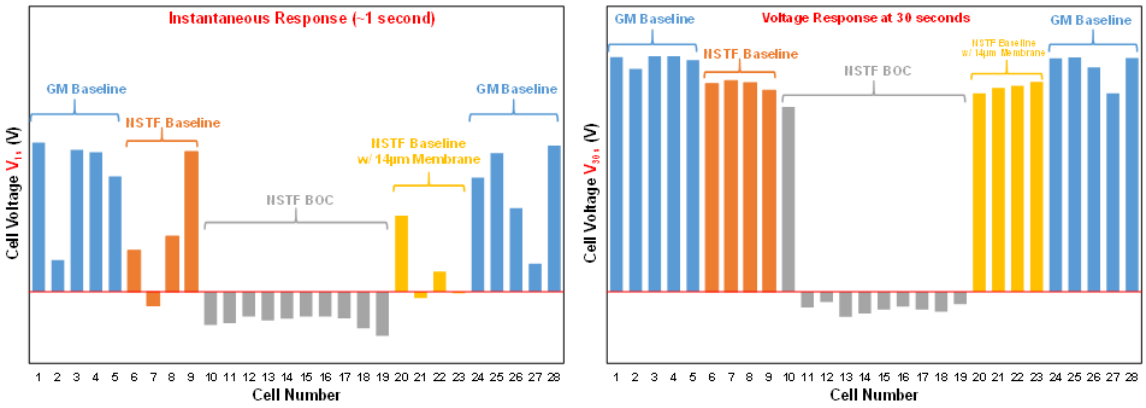

Figure 195. Stack load transient performance at 80C, 100% RH. Left: instantaneous response (0s after transient). Right: after 30s.

Figure 196. Stack Load Transients at 70C, 100% RH; 50C, 0% RH; and 40C, 0% RH (top to bottom). Left: Instantaneous. Right: After 30s.

The stack test results of the BOC MEAs are very significantly below expectation based on extensive single cell testing at 3M and at GM. In those tests, the BOC MEAs outperform the baseline MEAs under rated power testing, and also have dramatically improved load transient. One possibility to explain the BOC MEA underperformance, even when compared to the interlayer-free 3M baseline MEA, is insufficient anode conditioning in the stack format. As discussed in the Subtask 4.1 and 4.2 sections, an under-conditioned BOC anode can result in poor H_2/Air performance and very poor operational robustness due to low HOR kinetics.

Testing was halted due to the poorer than expected performance of the BOC MEAs and damage to a few cells which occurred during aggressive testing.

Second 29 cell stack test at GM

Late in CY16Q2, a second short stack was built with fresh MEA, outlined in Table 23. MEAs comprised three types of 3M baseline CCMs (20u or 14u PEM, w/ and w/o IL), the BOC MEA, and the GM baseline. The primary objective with this second stack was to determine if improved stack level performance and operational robustness with the BOC MEAs could be realized by using a recently-developed anode conditioning procedure, high potential CVs taken periodically. This approach was found to be reasonably successful in single cell work, discussed in the Subtask 4.2 section.

Table 23. Build of 2nd 29-cell short stack

#	Type	Anode Description	Membrane	Cathode Description	Cells
1	3M Baseline CCM w/ IL **(UEA0098G)**	PtCoMn/NSTF 0.05 mg_{Pt}/cm^2	3M 825EW 20 µm	PtCoMn/NSTF 0.15 mg_{Pt}/cm^2 3M 2979 w/ "B" Interlayer IL Loading – 0.016 mg_{Pt}/cm^2	**1 - 5**
2	3M Baseline CCM **(UEA0098B)**	PtCoMn/NSTF 0.05 mg_{Pt}/cm^2	3M 825EW 20 µm	PtCoMn/NSTF 0.15 mg_{Pt}/cm^2	**6 - 9**
3	3M BOC CCM **(UEA0098D)**	PtCoMn/NSTF 0.02 mg_{Pt}/cm^2	3M-S 725EW 14 µm w/ additive	Dealloyed Pt_3Ni_7/NSTF 0.095 mg_{Pt}/cm^2 3M 2979 w/ "B" Interlayer IL Loading – 0.016 mg_{Pt}/cm^2	**10 - 19**
4	3M - 14 µm Baseline CCM w/IL **(UEA0098F)**	PtCoMn/NSTF 0.05 mg_{Pt}/cm^2	3M-S 725EW 14 µm w/ additive	PtCoMn/NSTF 0.15 mg_{Pt}/cm^2 3M 2979 w/ "B" Interlayer IL Loading – 0.016 mg_{Pt}/cm^2	**20 - 23**
5	GM Baseline CCM **(UEA0098E)**	Dispersed Pt/C 800EW Ionomer	18 µm PFSA	Dispersed Pt-alloy/C 800EW Ionomer	**24 – 28**

Figure 197 summarizes the stack performance over time during break-in. During the first 80 voltage cycles (including 10 cathode thermal cycles), performance of the stack on average increased. At $0.50V_{AVG}$ control voltage, the current density increased from $0.5A/cm^2$ to ca. $0.95A/cm^2$. As the current density increased, the average voltage of the BOC MEAs decreased, whereas the average voltage of the 3M baseline w/ IL increased substantially. The performance of the other MEA types was relatively steady.

After ca. 80 cycles, specific anode conditioning was conducted via use of CVs to 1.2V ("Anode MHAD1"). Performance of the stack overall and individual MEA types was relatively unchanged immediately afterwards (scans 80-100).

Voltage cycling, cathode thermal cycling, and periodic anode CVs were conducted for an additional 40 hours. During this time, overall stack performance remained relatively steady for most MEA types. The BOC MEA improved on the order of 50mV. The 3M Baseline MEA w/ IL showed decreasing performance with time, predominantly stepwise coincident with the anode CVS (MHAD 2, 3, and 4). The low and declining performance of the 3M baseline w/ IL could have been due systematically-flipped CCMs (CCM anode operated as cathode), evidenced by ECSA data discussed below.

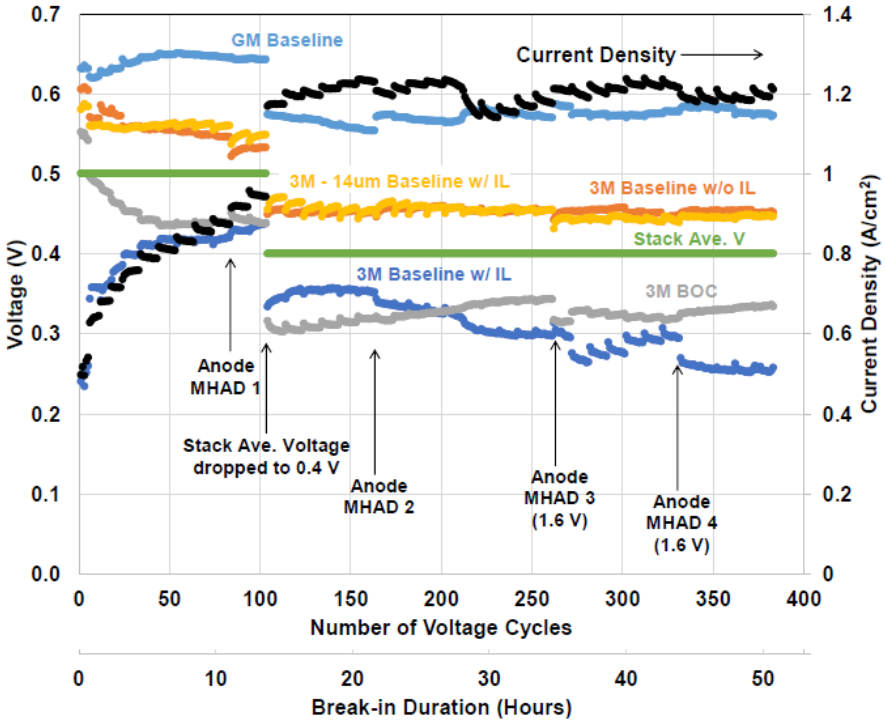

Figure 197. Break-in time trace with periodic anode condition cycles.

Figure 198 summarizes the ECSA evolution during MHAD 1. For the NSTF-based MEAs, ECSA increased with anode cycling. Most MEAs yielded expected ECSA values, except for 3M Baseline w/ IL, which had much higher ECSA values than all other MEA types, including the GM baseline with dispersed anode. This is wholly unexpected. The 3M Baseline w/ IL anode was 0.05mgPtCoMn/NSTF, the same as the other three 3M baseline MEAs. The reported ECSA value of ca. $32 m^2/g$ is reasonable if one assumes that the CCM was flipped, and the 0.15PtCoMn/NSTF cathode was installed as MEA anode. Converting for the loading difference results in ca. $11 m^2/g$, in line with expectation for 0.15PtCoMn/NSTF.

Due to the unexpectedly poor and decreasing H_2/air performance during conditioning and the unusual ECSA values with the 3M Baseline w/ IL, suggesting a possible CCM flip, we are excluding those results from consideration.

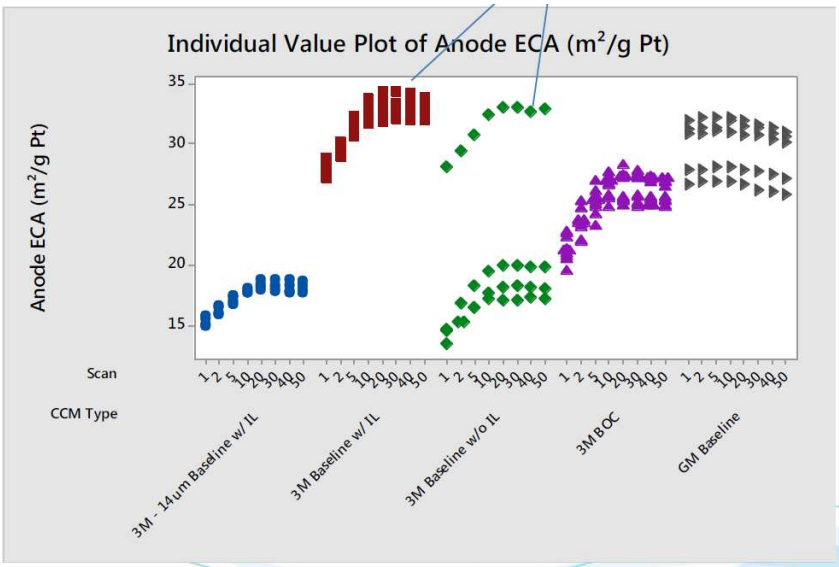

Figure 198. ECSA evolution during MHAD1 for different MEA types.

Figure 199 summarizes H_2/Air performance after 54 hours of conditioning, plotted relative to the GM baseline. Relative to the GM baseline MEA, the 3M MEAs all yielded lower performance across the entire polarization curve. Within the kinetic regime (0-0.2A/cm^2), the NSTF MEAs (with confirmed CCM orientation) yielded performance within about 5% of the GM baseline, with the 3M BOC yielding slightly higher performance than the 3M baselines. The performance difference increased considerably at higher current densities. At 1.2A/cm^2, the BOC MEA performance was lower than the 3M baselines. The BOC MEA performance at high current density appeared to be similar to the first stack (Figure 194).

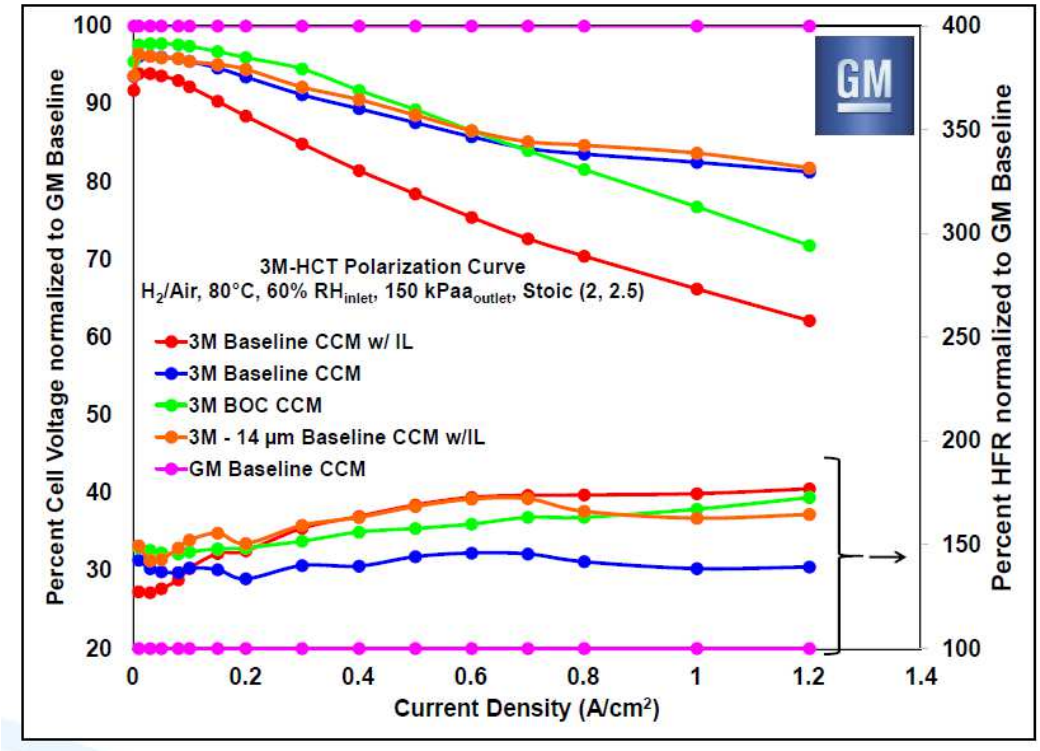

Figure 199. H_2/Air performance after 54 hours of conditioning.

Figure 200 shows the average BOC MEA performance during the course of the conditioning. The first curve was taken after the first 10 thermal cycles, anode CVs, and 8 additional thermal cycles. Additional cathode thermal cycle and anode CV conditioning resulted in a modest performance loss.

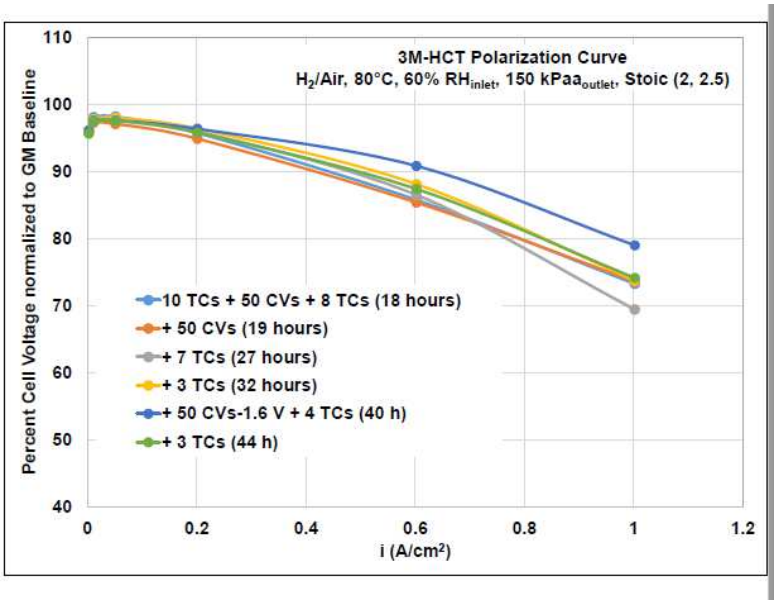

Figure 200. Example anode CVs to 1.6V for potential conditioning

Figure 201 summarizes the evolution of BOC MEA anode CVs during MHAD #1. The 1st CV exhibited an oxidation stripping peak near 0.70V, not present in subsequent scans. Further scans resulted in modest H_{UPD} growth, consistent with single cell work at 3M, but did not increase the apparent HER kinetics, inconsistent with numerous 3M single cell results. Confirmation of HOR kinetic improvement of the BOC anodes with CV cycling would have required conducting H_2 pump measurements, which were not done at GM.

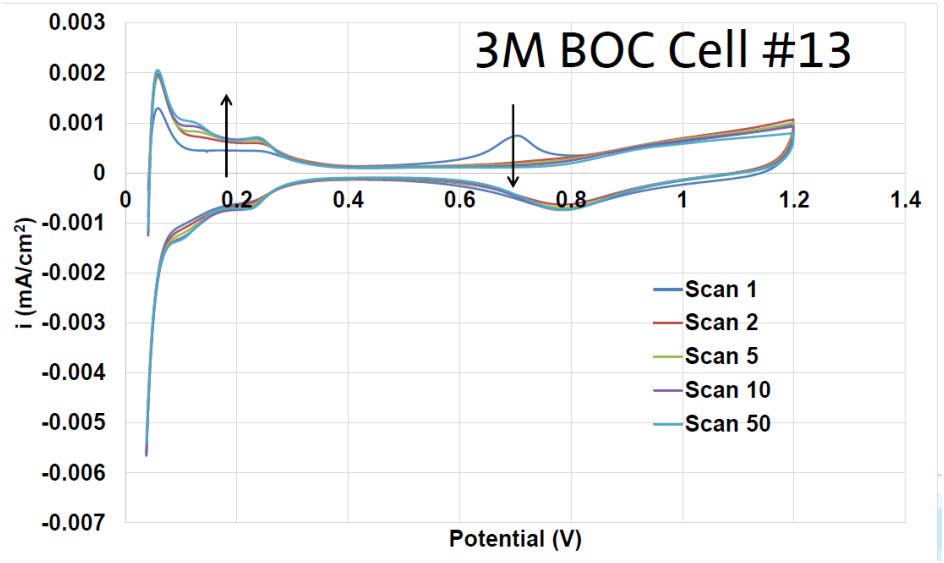

Figure 201. CVs of a BOC MEA anode during MHAD1.

After conditioining, the stack was evaluated for load transient capability at several conditions, summarized in Figure 202 and Figure 203. The BOC MEAs were able to achiving passing load

transients at 80°C, 100% RH and 50°C, 0% RH, but failed at 70°C 100% RH and 40°C, 0% RH. This was improved over the first stack, where the BOC MEAs had failing load transients for each of the stated conditions (Figure 195 and Figure 196). The robustness of the 3M 14um Baseline w/ IL also improved modestly in stack 2 as compared to the first stack.

One key, positive result was that the 3M Baseline MEAs with project downselected anode GDL passed all operational robustness tests evaluated, including transients down to 30°C stack temperature. The cathode interlayer yielded possible benefit at the lowest cell temperature evaluated. This provides strong validation to the anode GDL and cathode interlayer approaches developed in this project.

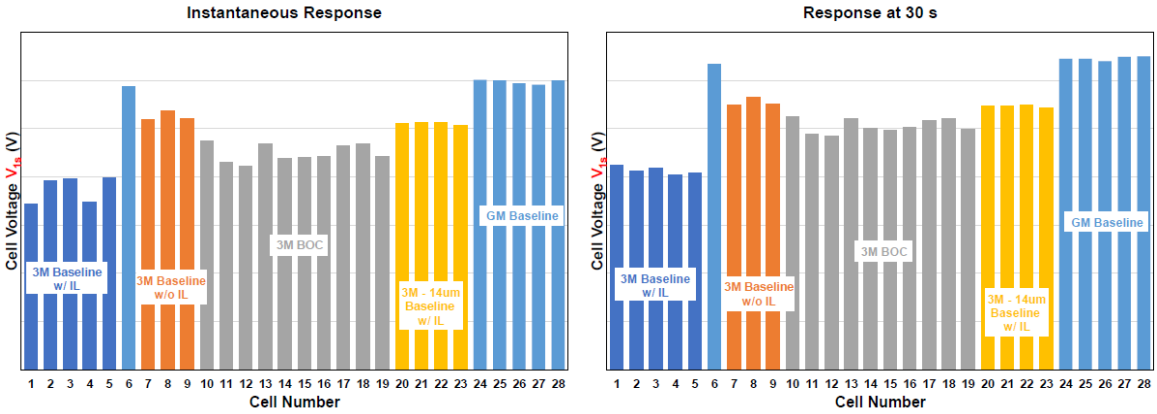

Figure 202. Stack load transient performance at 80C, 100% RH. Left: instantaneous response (0s after transient). Right: after 30s.

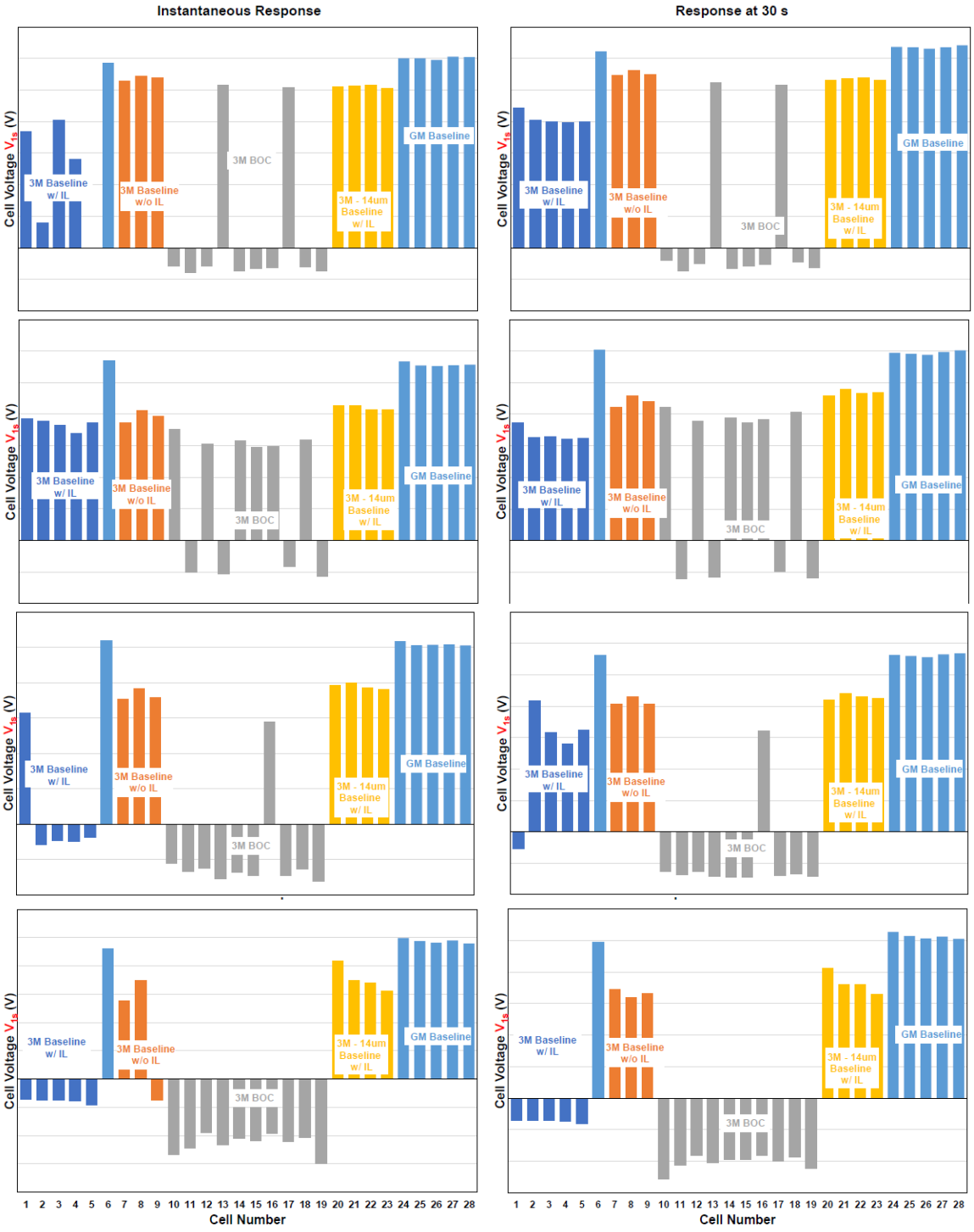

Figure 203. Stack 2 load transients at 70C, 100% RH; 50C, 0% RH; 40C, 0% RH ; and 30C, 0% RH (top to bottom). Left: Instantaneous. Right: After 30s.

Subtask Conclusions

All components for the final project 2015 (Sept.) Best of Class MEAs and stack testing were producible on continuous pilot scale equipment, including the experimental anode GDL, cathode GDL with interlayer, dealloyed cathode catalyst, ultra-low loaded anode catalyst, and the catalyst coated membrane. Resultant MEA rated power performance, specific power, and operational robustness were improved relative to the previous generation 2015 (March) BOC MEA, *when both the anode and cathode electrodes were fully conditioned.*

Single cell validation of 3M reported results at General Motors was partially successful. The rated power performance of baseline materials was comparable between sites, but the 3M BOC performance at GM was lower than at 3M. Possible factors included differences in test conditions and break-in protocols; the specific cause(s) was not specifically determined. With considerable effort and careful control of testing parameters, the operational robustness improvements of the BOC MEA over the baseline were validated at GM.

Stack evaluation of Best of Class MEAs at General Motors in a single 3 cell and two 29-cell short stacks yielded performance below expectation, based on both 3M and GM single cell testing. The BOC MEAs' average cell voltage at 1.2A/cm^2 was below the 3M baseline MEAs' average cell voltage, and only 70% of the GM baseline MEAs' average cell voltage. This contrasts sharply with the 3M results, which show that the BOC MEA yields improved performance over the baseline. GM single cell results were also in contrast to the short stack results, where the 3M Baseline and BOC MEAs yielded similar performances.

Several possible factors may be responsible for the low BOC MEA performance in GM stack testing, but none were experimentally confirmed. A first possible factor is that the test conditions used for the stack evaluation may not have been optimal for maximum BOC MEA performance. As shown in Figure 183 and Figure 184, the Baseline and BOC NSTF MEA performances at 80°C were found to be sensitive to inlet RH, and significant performance reductions were observed when the RH was increased. A second factor is the influence of flow field geometry in the GM stack. As shown in Figure 187, relatively wider lands and channels lead to lower performance than narrower channels. The flow field geometry of the GM stack was proprietary and not disclosed to 3M. A third possible factor is incomplete activation, especially of the low loaded BOC anode. Figure 186 shows that in single cell, incomplete anode conditioning substantially suppresses BOC MEA performance. It is possible that one or more of the above factors, or additional unsuspected factors, may have been ultimately responsible, but were not confirmed or refuted experimentally.

Operational robustness of BOC MEAs in stack were also below expectation, and was evaluated by use of load transient testing at a variety of stack temperatures. In the first 29-cell stack, the BOC MEAs were unable to pass load transients under any of the specific conditions evaluated. A modified MEA activation procedure was used in the second 29-cell stack, and BOC MEAs load transient performances were somewhat improved relative to the first stack, but still below expectation based on 3M and GM single cells.

A key result is that 3M Baseline MEAs with the project downselect anode GDL and cathode interlayer successfully passed all load transient conditions evaluated, including transients at 30°C

stack temperature. This result provides validation of the electrode-extrinsic water management approaches developed within the project in Task 2. The result also indicates that the stack-level operational robustness challenges with the BOC MEAs were likely due to factors specific to that type of MEA, including insufficient or incomplete anode conditioning.

Future Directions

A key future direction is development and implementation of materials-based improvements to allow rapid activation of NSTF electrodes with protocols similar to those used with traditional dispersed electrode MEAs. Based on the conclusions above, incomplete electrode activation were reasonable and likely contributors to the relatively poor Best of Class MEA performance and operational robustness in stacks. Challenges associated with translating protocols developed in single cell to stack also likely contributed. Detailed studies of the potential roles of contaminants, electrocatalyst/ionomer interface development, and other possible factors may be first needed to identify the key root cause(s) and to provide direction towards materials development.

In single cell tests, flow field geometry was found to be strongly influential on Best of Class MEA rated power performance. It is possible that stack flow fields will need to be optimized to take advantage of the high performance capability of NSTF MEAs, and/or NSTF MEAs will need to be optimized to allow decreased sensitivity to flow field geometry.

In stack testing, baseline project MEAs demonstrated very good operational robustness for load transients, validating the project “electrode-extrinsic” approach. While improved, it is likely that the operational robustness of NSTF MEAs remains below that of optimized dispersed electrode MEAs. It remains unclear if the improved NSTF MEA robustness is sufficient for end-use applications for automotive or other applications. Studies to evaluate this are needed, and would provide insight into additional work needed. Alternative approaches, including modification to the intrinsic wettability and pore structure of NSTF electrodes may ultimately be needed. Such work is currently underway at 3M.

Task 7 – Project Management

Task Overview

Task 7 incorporates overall project management tasks, including project-related meetings, correspondence between team members, and report generation.

3M will be primarily responsible to prepare the technical and financial reporting. 3M will provide reports and other deliverables in accordance with the Federal Assistance Reporting Checklist following the instructions therein.

Towards the goal of optimizing the MEA, 3M will generate, collect, and analyze fuel cell testing data. 3M will provide appropriate representative data to the National Renewable Energy Laboratory using data templates as agreed to between 3M and NREL.

3M will participate in the DOE Hydrogen Program Annual Merit Review and prepare and present detailed briefings of plans, progress, and results of the technical effort to DOE personnel, as requested by DOE. 3M will also participate in Fuel Cell Tech Team meetings as requested by DOE.

Subtask High Level Work Summary

N/A

Task Key Results

Team Management

The initial project team consisted of General Motors, Michigan Technological University, and Lawrence Berkeley National Laboratory. The project team was later expanded to include Johns Hopkins University, Oak Ridge National Laboratory, and Los Alamos National Laboratory. Freudenberg FCCT and Argonne National Laboratory were collaborators.

One overall group meeting was held in Sept. ’12, coincident with the project kickoff. Due to the large differences in subcontractor work tasks, meeting between the entire project team were expected to be non-productive. Most subcontractors worked primarily with 3M directly, but significant collaboration was necessary and encouraged between 3M, Michigan Tech, and LBL in Task 3.

Project Reorganization

During the first project year, a major shift in the project plan occurred. On Oct. 5th, 2012, General Motors publicly announced that it would be closing its Honeoye Falls, NY fuel cell research facility. The work GM was to conduct under this project was to primarily have occurred at the Honeoye Falls facility. GM informed 3M that due to this change, it would not have the resources necessary to execute the extensive collaborative MEA integration efforts between the two companies, including significant work under Tasks 1, 5, and 6 (Stack Testing). 3M assumed a significant amount of the single cell testing required to execute the development plan, and LANL was also added to provide additional durability testing capability. A major concern for the project was the uncertainty of whether GM would be able to execute stack testing, including the project deliverable short stack. 3M did not have access to relevant automotive stack hardware and dedicated stack testing engineers required to execute the work.

After numerous negotiations between 3M, GM, and DOE, a plan was formulated that GM would build and evaluate short stacks if certain robustness metrics were first demonstrated in single cell at 3M.

Reporting

3M provided all required quarterly reports (16), including technical and financial information.

3M prepared a project summary report at the project mid-point, to support the project Go decision after BP1.

3M provided four annual progress reports.

3M prepared and delivered 15 presentations (total) to DOE program managers, the USCAR Fuel Cell Tech Team, and at the DOE Annual Merit Review.

Fuel Cell Data Analysis

3M fabricated, evaluated, and analyzed in excess of 1,013 individual MEAs at the primary St. Paul site during the course of the project. MEA test data was analyzed largely with custom automated analysis software. A large majority of the MEAs were integrated into larger comparative analyses.

Durability Data Reporting

For a majority of the project, durability testing consisted predominantly of evaluation of candidate components under ASTs and H_2/Air load cycling under specialized and accelerated) diagnostic testing aimed to identify degradation mechanisms. Such accelerated data was not deemed appropriate to share with NREL for MEA durability projections. Limited data was provided to NREL (Kurtz). In the final project year, non-accelerated load cycle data taken with relevant conditions was generated with the final project BOC MEAs, but facility issues resulted in premature failures of 2 of 3 MEAs, and may have damaged the final remaining MEA. Due to the low statistical sampling size (1 MEA), the data was not provided to NREL.

Project Deliverable

The project deliverable was delivery of short stack containing Final Best of Class MEA to DOE-approved evaluation site. In 2015, the stack evaluation partner (GM) informed 3M that it would not be able to provide a stack outside of GM due to proprietary concerns. 3M and GM requested that DOE recognize GM as a DOE-approved site, and was verbally approved by the program manager (D. Papageorgopoulos).

Two 29-cell short stacks containing numerous project Best of Class MEAs were built and evaluated at GM for performance and operational robustness, which met the project deliverable.

Subtask Conclusions

N/A

Future Directions

N/A

Task 8 – Relative Cost/Mfg. Assessment

Task Overview

In Task 8, 3M will provide relative cost savings data of the downselected MEA relative to current baseline MEA using existing models for MEA cost at ~500k/year volume.

Subtask High Level Work Summary

The final project BOC MEA was analyzed for performance in differential cell mode. The data was used to generate a performance and cost model by Argonne National Laboratory and Strategic Analysis, Inc.

Task Key Results

As a matter of policy, 3M does not disclose product cost information. In lieu of a 3M estimate which may disclose sensitive information, 3M conducted numerous experiments over the project in support of providing data towards development of performance and cost models by Argonne National Laboratories and Strategic Analysis, Inc.

Over the course of the project, 3M provided MEA performance data to our collaborators for (at least) the 2012 (Sept.) BOC MEA, the 2013 (March) BOC MEA, and 2014 MEA data, and the final project 2015 (Sept.) BOC MEA.

The 2015(Sept.) BOC MEA data was generated in differential cell mode, and was fully implemented into the aforementioned performance and cost models. Data was generated with the same pilot-scale produced MEA component lots provided to General Motors for stack testing, described in the Task 6 section.

BOC MEA Performance Evaluation (Differential Cell)

March and Sept. (2015) Best of Class MEAs were evaluated under a variety of test conditions (Table 24) suggested by ANL to establish a performance model, ultimately used to generate a cost model. As discussed in Subtask 4.2, a significant development effort to establish reliable and accurate differential cell testing methodologies was conducted.

Tests were conducted in a differential cell, to minimize data inaccuracy due to down-the-channel effects. A 50cm^2 active area MEA was installed in a 50cm^2 test cell with FF2 cathode, and a 1 mil polyimide sheet with 5cm^2 aperture was placed between the CCM cathode and cathode GDL to define a 5cm^2 active area.

At least 13 sets of conditions were run (5-6 individual test conditions per set). Prior to each condition set, the cell was thermal cycled 3 times in reversed orientation, then thermal cycled 3 times with normal orientation, and then performance under a baseline condition was measured. For each individual test condition, the cell was first thermal cycled once and then two polarization curves at the specific test conditions were taken, one potential controlled down to 0.30V and a second which was current controlled to 1.5-2.0A/cm^2 (or until ~0.55V was reached), during which HFR was measured.

Table 24. Best of Class Differential Cell Test

Series 1. Pressure Effect						
Case	P	T	RH	$X(O_2)$	Air Flow Rate	Fuel Flow Rate
	atm	^0C	%	%	%	%
1.1	1.0	80	100	100, 21, 10, 6, 2, 1	100	100
1.2	1.5	80	100	100, 21, 10, 6, 2, 1	100	100
1.3	2.0	80	100	100, 21, 10, 6, 2, 1	100	100
1.4	2.5	80	100	100, 21, 10, 6, 2, 1	100	100
1.5	3.0	80	100	100, 21, 10, 6, 2, 1	100	100

Series 2. Temperature Effect						
Case	P	T	RH	$X(O_2)$	Air Flow Rate	Fuel Flow Rate
	atm	^0C	%	%	%	%
2.1	1.5	90	100	100, 21, 10	100	100
2.2	1.5	80	100	100, 21, 10	100	100
2.3	1.5	70	100	100, 21, 10	100	100
2.4	1.5	60	100	100, 21, 10	100	100
2.5	1.5	45	100	100, 21, 10	100	100

Series 3. Water Activity Effect						
Case	P	T	RH	$X(O_2)$	Air Flow Rate	Fuel Flow Rate
	atm	^0C	%	%	%	%
3.1	1.5	80	200	100, 21, 10	100	100
3.2	1.5	80	150	100, 21, 10	100	100
3.3	1.5	80	125	100, 21, 10	100	100
3.4	1.5	80	100	100, 21, 10	100	100
3.5	1.5	80	75	100, 21, 10	100	100
3.6	1.5	80	50	100, 21, 10	100	100
3.7	1.5	80	30	100, 21, 10	100	100

Series 4. Flow Rate Effect						
Case	P	T	RH	$X(O_2)$	Air Flow Rate	Fuel Flow Rate
	atm	^0C	%	%	%	%
4.1	1.5	80	100	21	100, 50,25,10	100,50,25,10
4.2	1.5	80	55	21	100,50,25,10	100,50,25,10

Series 5. Anode Water Activity Effect, 21% $X(O_2)$						
Case	P	T	RH_c	RH_a	Air Flow Rate	Fuel Flow Rate
	atm	^0C	%	%	%	%
5.1	1.5	80	100	125,100,75,50,30	100	100
5.2	1.5	80	55	125,100,75,50,30	100	100

Conditions	
	Air Flow Rate: 3 slpm for 12.25 cm^2 active area
	Hydrogen Flow Rate: 1 slpm for 12.25 cm^2 active area

Figure 204 summarizes basic performance trends v. operating conditions for several of the test series. Performance was sensitive to O_2 concentration, total reactant pressure, RH, and cell temperature, generally in line with expectation.

In O_2 concentration testing, the limiting current densities decreased for > 5 down to ca. 0.2A/cm^2 as the concentration decreased from 100% to 1% oxygen. The relatively high limiting current

densities were surprising, considering the relatively large amount of Ni contamination into the PFSA PEM from the PtNi cathode.

In RH sensitivity testing, performance improved slightly with slight subsaturation, and performance loss with 30% RH was only ca. 30% at 0.40V. Performance loss at 150% RH was measurable but modest.

Performance was relatively insensitive to temperature between 60-90°C, with a < 50% loss in limiting current density at 45C.

For all testing, the OCV was surprisingly low (ca. 0.90V). The low OCV was ultimately determined to be due to an artifact associated with the differential cell 5cm^2 active area definition method. In essence, the crossover and electronic shorting parasitic currents were from the entire 50cm^2 MEA. This is discussed in the Subtask 4.2 section.

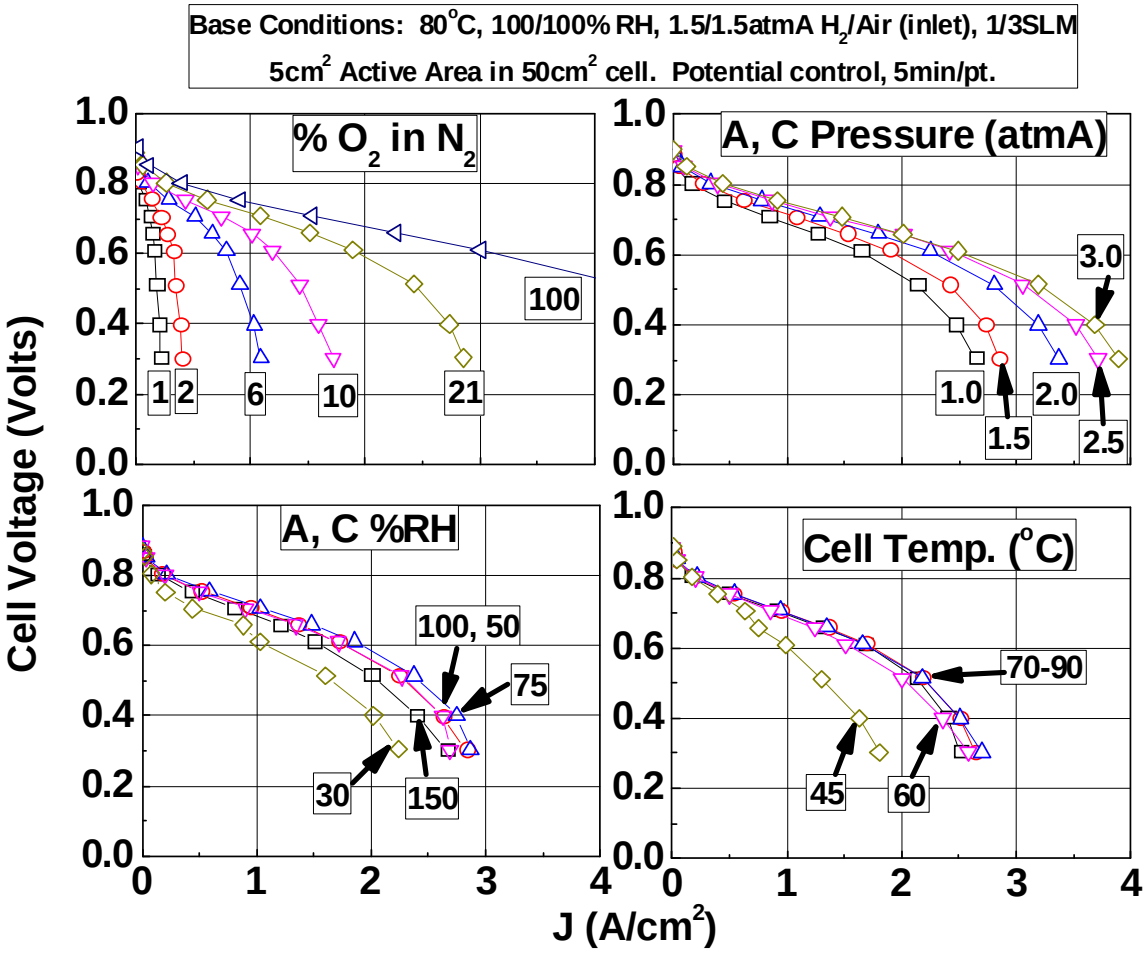

Figure 204. Summary of Performance Sensitivity to [O_2], P, RH, and Cell Temp.

Figure 205 compares H_2/Air performance of the differential cell to 50cm^2 non-differential cells with 2015(Sept.) BOC MEAs. Excellent agreement is observed between the non-differential and differential cell between 0.2 and 2A/cm^2, suggesting that our differential cell testing and assembly method is consistent with our larger cell datasets.

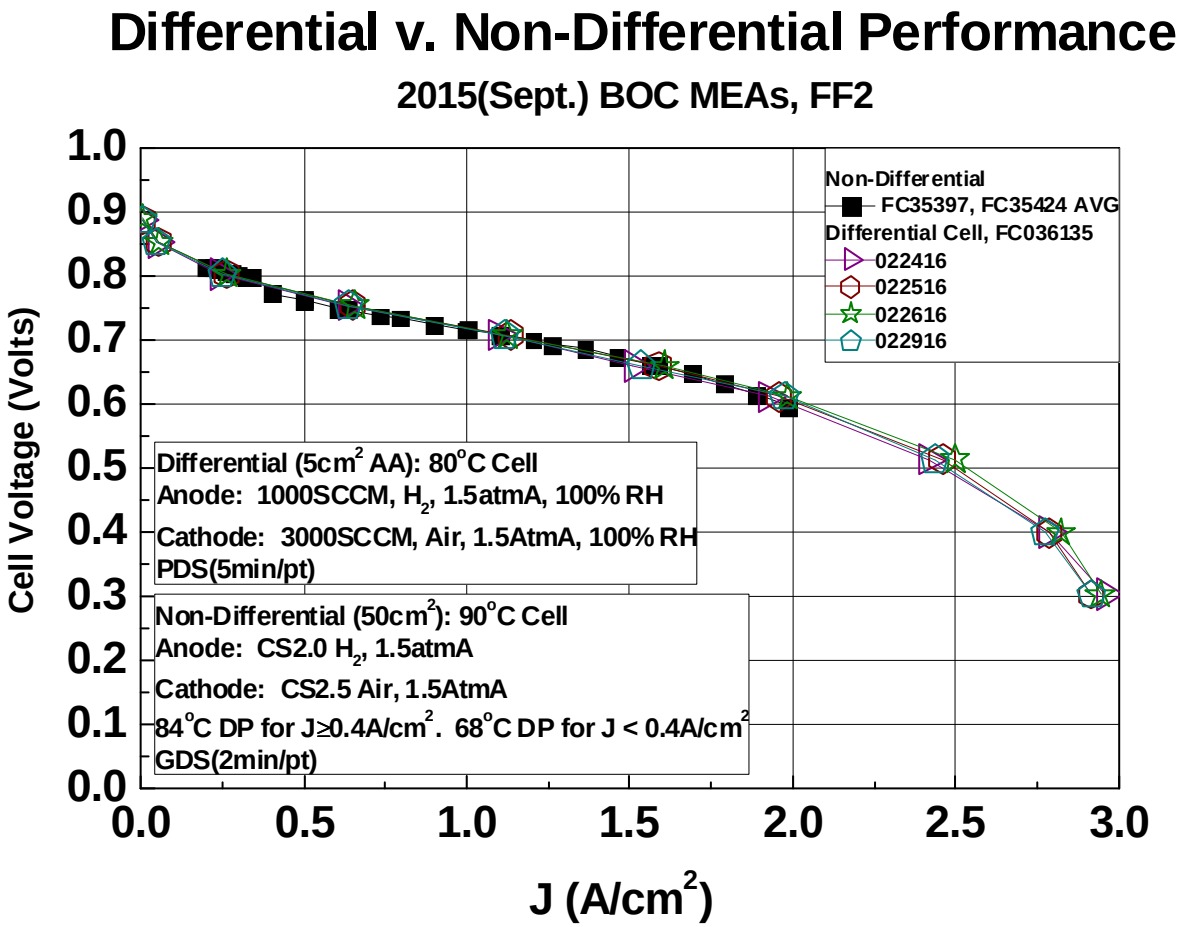

Figure 205. Comparison of Differential Cell to Non-Differential Cell Under 1.5atmA H_2/Air Testing

During the course of testing, the MEA performance degraded modestly. Testing was conducted over a ca. 6 week period, with about 800 hours of total MEA operating time at test completion. Table 16 summarizes the mass activity and specific area for several BOC and BOC-like MEAs in differential and non-differential format, including the MEA used for the above testing, FC036135. On average, the mass activity of differential and non-differential BOC MEAs was ca. 0.38A/mg and did not depend upon build type. However, FC036135's mass activity at BOL was much lower than average, only 0.26A/mg. At the testing "mid-point", the mass activity was unchanged. At the end of test, the mass activity had decreased to 0.21A/mg.

Table 25. Specific Area, Mass Activity of Several Differential and non-Differential BOC and BOC-like MEAs, Compared to FC036135 Differential Cell

	n MEAs	Specific Area (m^2/g)	Mass Activity (A/mg)
$5cm^2$ differential	10	22±2.6	0.38±0.064
$50cm^2$ non-differential	4	18±2.5	0.38±0.058
FC036135, BOL (Jan. 29)	1	24	0.26
FC036135, Mid (Mar. 3)	1	18	0.26
FC036135, EOT (April 4)	1	21	0.21

The lower than typical BOL mass activity of FC36135 was not realized until well into execution of the testing process. Due to timing constraints, 3M decided to complete the requested testing

with this MEA. It is possible that testing with a differential cell BOC MEA with more typical activity would result in further improved performance, but this was not evaluated.
Figure 206 summarizes performances at several pressures near either beginning or end of test, ca. 700 hours of actual test time. The decay extent was found to be a function of pressure, with relatively larger losses at or near ambient pressure and minimal loss at 3atmA. At 0.1A/cm^2, the performance loss at 1.5atmA was 20mV and at 3.0atmA the loss was 13mV. HFR was found to decrease slightly over the test.

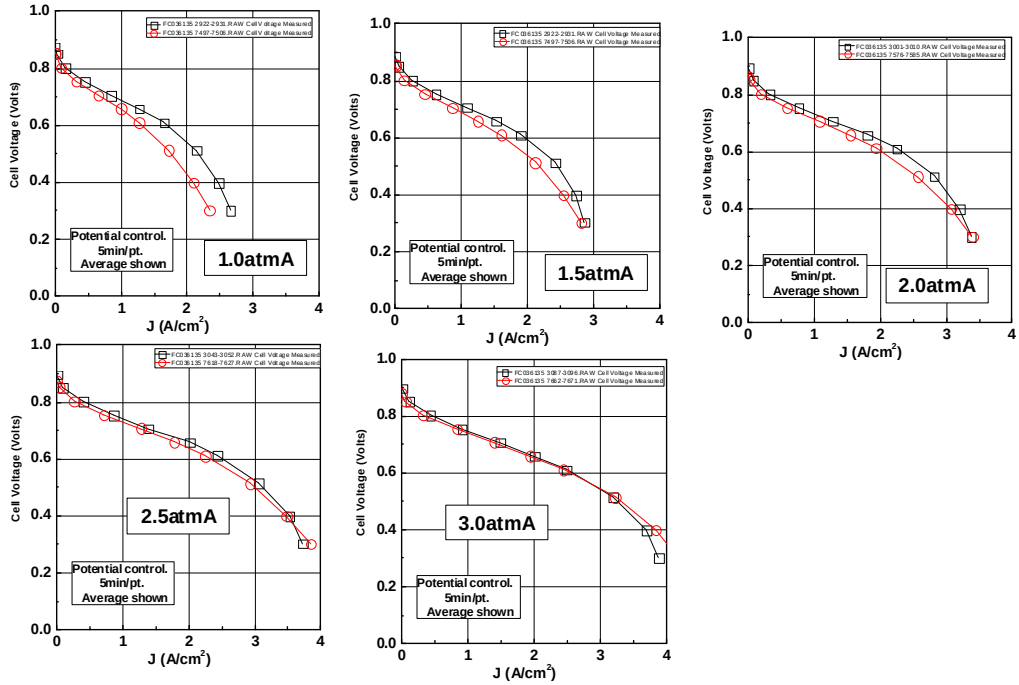

Figure 206. Initial and Final Performance Under Test 1 (21% O_2, various P).

Performance Modeling at ANL (from 2016 AMR)

Testing data was provided to ANL as it was generated, typically on a weekly basis. ANL incorporated the data into an MEA performance model and results were reported at the DOE Hydrogen and Fuel Cells Program 2016 Annual Merit Review (FC017, Ahluwalia). The relevant slides are incorporated as Figure 207-Figure 212.

The modeling consisted of evaluation of catalyst activity, mass transport overpotentials, and RH sensitivity. The modeled mass activity was ca. 0.38A/mg, similar to that typically obtained with BOC MEAs in differential cell and non-differential cell (Figure 208). Modeled limiting current densities ranged from ca. 2.8 to ca. 4.0A/cm^2 as the O_2 pressure increased from ca. 0.15 to ca. 0.50 atmA, and depended on total pressure (Figure 209). Sensitivity to RH was found to be modest at 80°C cell temperature, and optimal performance tended to occur with modest anode or cathode subsaturation (Figure 210).

Dealloyed Pt_3Ni_7 /NSTF Catalyst with Cathode Interlayer (CI)

Collaborating with 3M (FC104) in designing tests on 5-cm^2 active-area differential cells and analyzing data to model performance of full-area (>250 cm^2) cells

- Ternary Anode: $Pt_{68}(CoMn)_{32}$, 0.019 mg_{Pt}/cm^2
- Binary Cathode: Pt_3Ni_7/NSTF, dealloyed (JHU Chemistry), 0.096 mg_{Pt}/cm^2
- Membrane: 3M-S (supported) 725 EW PFSA with additive, 14 μm
- Anode GDL: 3M "X3" (Experimental backing, 3M hydrophobization, MPL)
- Cathode GDL: 3M 2979
- Cathode Interlayer: 3M Type "B", 0.016 mg_{Pt}/cm^2

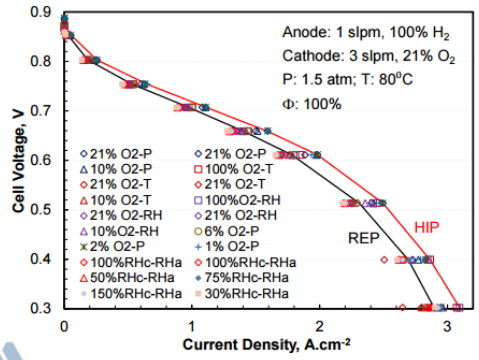

Test Campaign

- 3 TCs (NFAL+RFAL) before each test series, 1 TC before polarization curves
- ~25% decrease in ECSA over ~735 h actual test time, 22.9 to 17.2 m^2/g
- Test space: P: 1-3 bar; T: 45-90°C; X(O_2): 1-21%, 100%; RH(a): 30-100%; RH(c): 30-150%; Q(H_2): 1 slpm; Q(air): 3 slpm
- Performance metrics: HFR, H_2 x-over, mass activity, ECSA, short resistance

*Differential cells have identical build as "Best of Class" (BOC) 50-cm^2 active area cells

12

Figure 207. Test description (from ANL '16 AMR presentation).

ORR Activity of d-Pt_3Ni_7 /NSTF Catalyst with CI

Determined ORR kinetic parameters from IR and crossover corrected cell voltages at low current densities in H_2/O_2 and H_2/air.

- Modeled mass activities of the three catalyst systems are consistent with values measured using the 3M protocol
- Compared to the ternary $Pt_{68}(CoMn)_{32}$/NSTF catalyst, the mass activity of binary d-Pt_3Ni_7/NSTF catalyst with cathode interlayer is 78-144% higher.

Cathode / Anode Catalyst	Membrane	Cathode / Anode Pt Loading	Cathode ECSA	Measured Mass Activity	Modeled Mass Activity	Cell Designation
C: $Pt_{68}(CoMn)_{32}$	20 μm, 835 EW	0.1 mg/cm^2	9.8 m^2/g	180 A/g_{Pt}	190 A/g_{Pt}	19478
A: $Pt_{68}(CoMn)_{32}$		0.05 mg/cm^2				
C: d-Pt_3Ni_7	20 μm, 835 EW	0.125 mg/cm^2	14.5±0.7 m^2/g	330±30 A/g_{Pt}	392 A/g_{Pt}	30086
A: $Pt_{68}(CoMn)_{32}$		0.05 mg/cm^2				
C: d-Pt_3Ni_7 + Cathode Interlayer (CI)	14 μm (S), 725 EW	0.096 + 0.016 (CI) mg/cm^2	22±3 m^2/g	380±60 A/g_{Pt}	334 A/g_{Pt}	36135
A: $Pt_{68}(CoMn)_{32}$		0.019 mg/cm^2				

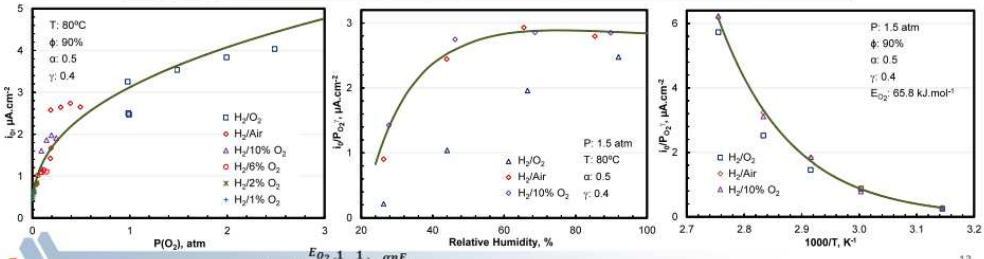

$$i + i_x = i_{0r} P_{O2}^{\gamma} \phi^{\beta} e^{\frac{E_{O_2}}{R}\left(\frac{1}{T} - \frac{1}{T_r}\right)} e^{\frac{\alpha n F}{RT}\eta}$$

13

Figure 208 Mass activity analysis (from ANL '16 AMR presentation).

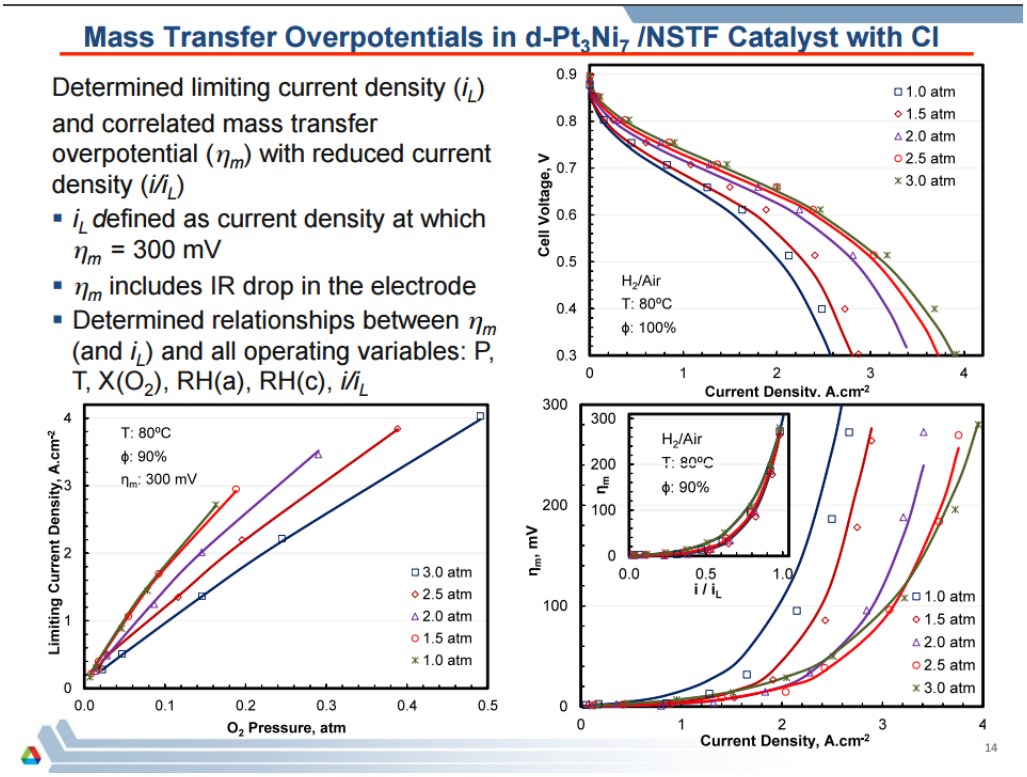

Figure 209. Mass transport analysis (from ANL '16 AMR presentation).

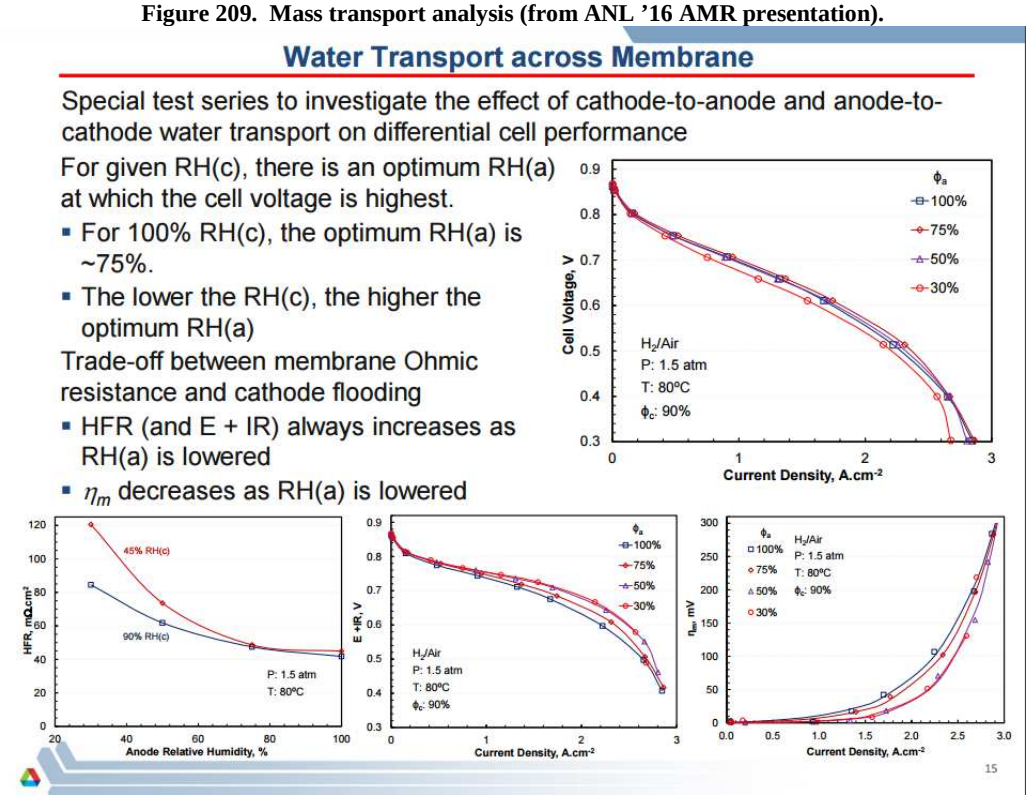

Figure 210. RH sensitivity analysis (from ANL '16 AMR presentation).

Figure 211 summarizes a comparative cost assessment of the modeled ANL fuel cell system with either a baseline ternary NSTF catalyst (PtCoMn) or the project BOC MEA. It is assumed that the estimates are at the typical 500k systems/year estimate used by Strategic Analysis. Direct

MEA cost reductions were not available. As compared to the baseline, the BOC MEA resulted in a modeled **stack** cost reduction of 11, 6, and 5$/kW (28.2, 20.7, and 19.2%) at 1.5, 2.0, and 2.5atm stack operating pressures, respectively. The reduced cost was due in part to decreased PGM content (13%) and absolute power densities increases of 44.2, 29.8, and 25.0% at 1.5, 2.0, and 2.5atm stack operating pressures.

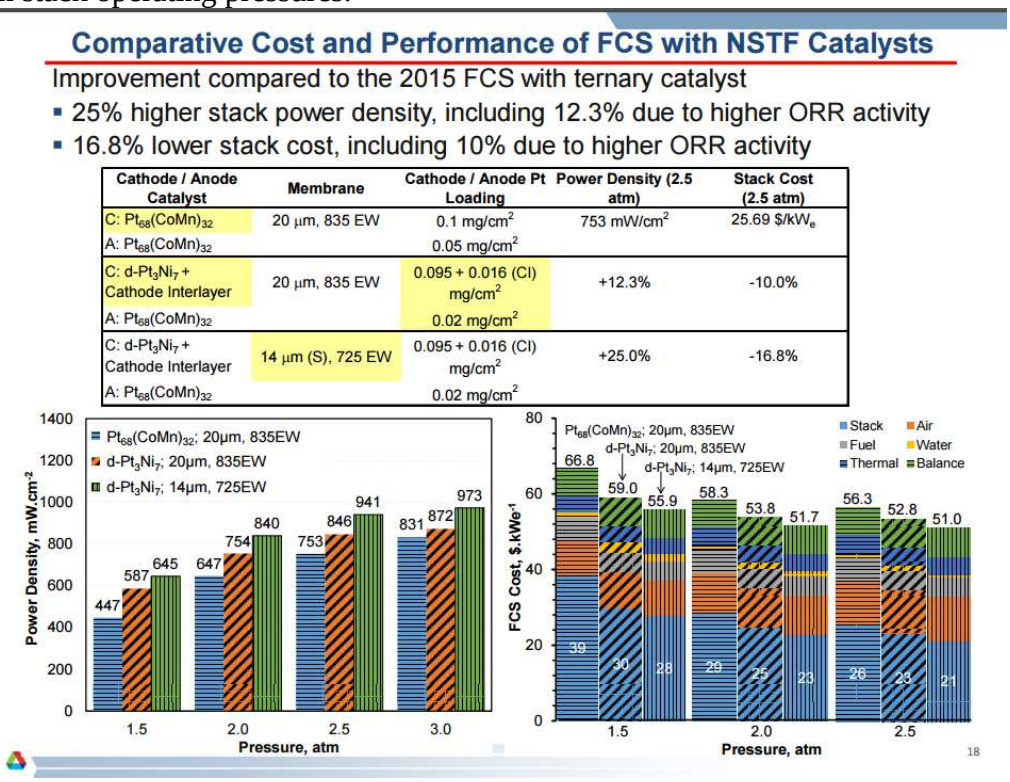

Figure 211. Comparative cost between project baseline and BOC MEAs (from ANL '16 AMR presentation).

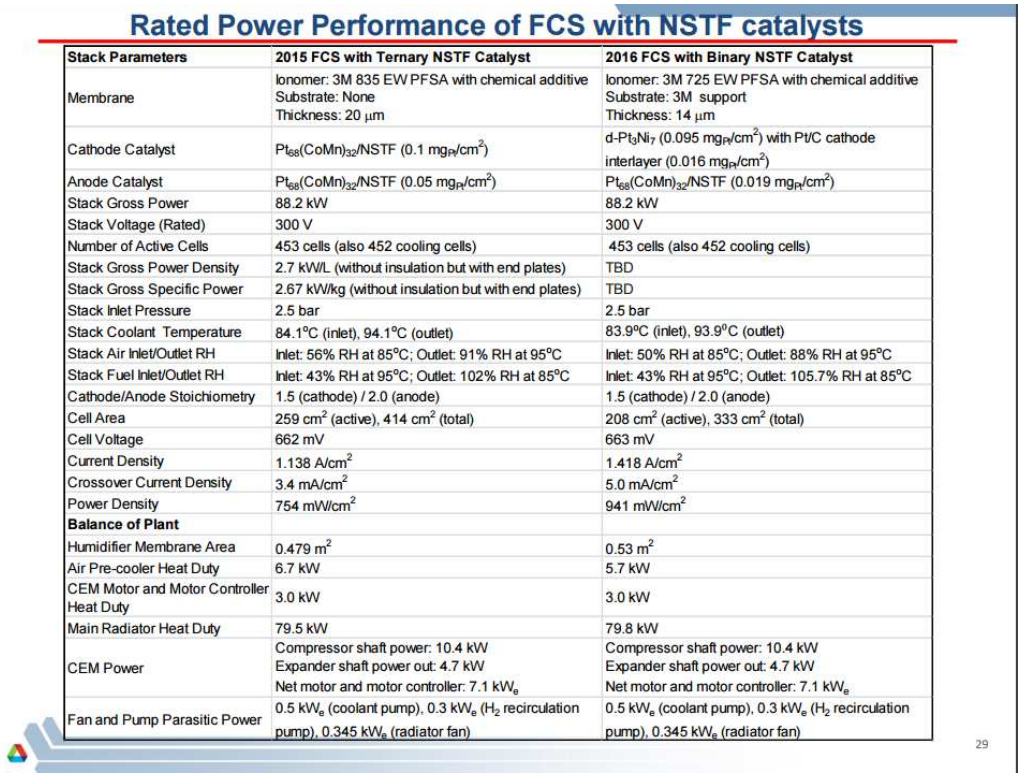

Rated Power Performance of FCS with NSTF catalysts

Stack Parameters	2015 FCS with Ternary NSTF Catalyst	2016 FCS with Binary NSTF Catalyst
Membrane	Ionomer: 3M 835 EW PFSA with chemical additive Substrate: None Thickness: 20 μm	Ionomer: 3M 725 EW PFSA with chemical additive Substrate: 3M support Thickness: 14 μm
Cathode Catalyst	$Pt_{68}(CoMn)_{32}$/NSTF (0.1 mg_{Pt}/cm^2)	d-Pt_3Ni_7 (0.095 mg_{Pt}/cm^2) with Pt/C cathode interlayer (0.016 mg_{Pt}/cm^2)
Anode Catalyst	$Pt_{68}(CoMn)_{32}$/NSTF (0.05 mg_{Pt}/cm^2)	$Pt_{68}(CoMn)_{32}$/NSTF (0.019 mg_{Pt}/cm^2)
Stack Gross Power	88.2 kW	88.2 kW
Stack Voltage (Rated)	300 V	300 V
Number of Active Cells	453 cells (also 452 cooling cells)	453 cells (also 452 cooling cells)
Stack Gross Power Density	2.7 kW/L (without insulation but with end plates)	TBD
Stack Gross Specific Power	2.67 kW/kg (without insulation but with end plates)	TBD
Stack Inlet Pressure	2.5 bar	2.5 bar
Stack Coolant Temperature	84.1°C (inlet), 94.1°C (outlet)	83.9°C (inlet), 93.9°C (outlet)
Stack Air Inlet/Outlet RH	Inlet: 56% RH at 85°C; Outlet: 91% RH at 95°C	Inlet: 50% RH at 85°C; Outlet: 88% RH at 95°C
Stack Fuel Inlet/Outlet RH	Inlet: 43% RH at 95°C; Outlet: 102% RH at 85°C	Inlet: 43% RH at 95°C; Outlet: 105.7% RH at 85°C
Cathode/Anode Stoichiometry	1.5 (cathode) / 2.0 (anode)	1.5 (cathode) / 2.0 (anode)
Cell Area	259 cm^2 (active), 414 cm^2 (total)	208 cm^2 (active), 333 cm^2 (total)
Cell Voltage	662 mV	663 mV
Current Density	1.138 A/cm^2	1.418 A/cm^2
Crossover Current Density	3.4 mA/cm^2	5.0 mA/cm^2
Power Density	754 mW/cm^2	941 mW/cm^2
Balance of Plant		
Humidifier Membrane Area	0.479 m^2	0.53 m^2
Air Pre-cooler Heat Duty	6.7 kW	5.7 kW
CEM Motor and Motor Controller Heat Duty	3.0 kW	3.0 kW
Main Radiator Heat Duty	79.5 kW	79.8 kW
CEM Power	Compressor shaft power: 10.4 kW Expander shaft power out: 4.7 kW Net motor and motor controller: 7.1 kW_e	Compressor shaft power: 10.4 kW Expander shaft power out: 4.7 kW Net motor and motor controller: 7.1 kW_e
Fan and Pump Parasitic Power	0.5 kW_e (coolant pump), 0.3 kW_e (H_2 recirculation pump), 0.345 kW_e (radiator fan)	0.5 kW_e (coolant pump), 0.3 kW_e (H_2 recirculation pump), 0.345 kW_e (radiator fan)

Figure 212. Stack and BOP for FCS (from ANL '16 AMR presentation).

Subtask Conclusions

The project downselected MEA was projected to decrease the cost of automotive stacks by 28.2, 20.7, and 19.2% at 1.5, 2.0, and 2.5atm stack operating pressures, respectively. The estimate is provided from experimental data used to develop performance and MEA cost models at Argonne National Laboratory and Strategic Analysis, Inc., respectively, estimated at 500k systems per year volume.

Future Directions

N/A

Summary

Component Optimization for Performance and Cost Reduction

In Task 1, several improved components were optimized which yielded improved performance and reduced PGM content. The optimization work primarily focused on improvements to the materials and processes of the anode electrode, cathode electrode, and the PEM.

In studies of the anode electrode, minimum anode electrode PGM loadings to obtain acceptable performance ranged from 10-20 $\mu g/cm^2$, being largely dependent upon the specific area of the electrocatalyst. An HOR model revealed that new insight that robustness challenges are possible due to HOR kinetics alone.

Extensive work was conducted to develop annealing and dealloying processes to enable improved activity and H_2/Air performance with PtNi/NSTF cathode electrocatalyst. Annealing was found to modestly increase the mass activity and specific area up to ~ 20% vs. unannealed. While improved, annealed P1 catalyst was not downselected for incorporation into the project best of class MEAs due to increased difficulty in dealloying and reduced startup rate. Dealloying development work resulted in improved performance over baseline. Several dealloying process trials with compositional and electrochemical characterization were conducted, allowing development of a process sensitivity map.

Studies of PFSA PEMs focused on two primary areas. The first primary area was overcoming a material incompatibility of supported 3M PEMs with NSTF electrodes, which resulted in decreased performance and activity. The key factors were identified, and optimized materials and processes were developed which enabled expected performance. The second primary development area was development of a relationship between MEA performance and the PEM effective equivalent weight, which accounted for the ion exchange capacity lost due to transition metal dissolution from the PtNi electrode into the PEM. This relationship was used to set targets for the degree of dealloying needed to achieve high performance in MEA.

Component Optimization for Improved Operational Robustness

In Task 2, optimization work was conducted to improve the operational robustness of NSTF MEAs via anode gas diffusion layers and cathode interlayers. Anode GDL development work largely focused on determination of optimal backing structure, backing hydrophobicity, backing thickness, and microporous layer thickness and composition. The downselected anode GDL resulted in a 2x gain in limiting current density at 40°C over the pre-project baseline. Cathode interlayer development focused on optimization of the interlayer electrocatalyst, including the impacts of carbon support type, heat treatment, and interlayer loading. The key mechanistic insight was identified, that the interlayer performance depends largely on the interlayer Pt surface area. The downselected interlayer, containing $16 \mu g_{Pt}/cm^2$, yielded substantially improved performance for load transients, and was nearly sufficiently durable to maintain robustness after both the DOE Electrocatalyst and Support ASTs. In combination, the downselected anode GDL and cathode interlayer enabled robust operation to as low as 40°C cell temperature, as compared to 70°C minimum with the pre-project baseline material sets.

In Task 3, key insight into the mechanism by which optimized anode GDLs yield improved operational robustness was generated. A key structural factor, density modulation of the backing, was found to qualitatively correlate with experimental MEA results, and modeling results were consistent.

A novel model was developed, which integrated pore network models to characterize transport in the gas diffusion media with an MEA continuum model. The resultant model yielded very good predictive capability against experiment.

New methods of X-ray computed tomography on GDLs were developed and found to be highly insightful into the influences of anode GDL compression, fiber density modulation, and stacked GDLs, all found to be influential on MEA performance. A new method for generating pore size distributions from XCT data was also investigated.

Experiments were conducted to understand how the anode GDL backing, demonstrated to impact low temperature steady state performance, influences MEA water balance. Anode GDLs which enable higher performance have higher apparent limiting water removal rates than low performing anode GDLs. All GDLs evaluated appear to follow a trend that low temperature steady state performance of NSTF MEAs decreases as the limiting anode GDL water removal rate is approached.

Component Optimization for Durability

In Task 5, durability of project components and MEAs were evaluated.

BOC MEA candidate components were evaluated for durability under the DOE chemical durability test, support cycle, and electrocatalyst cycle ASTs. The BOC candidates indicated generally good durability, with most target metrics met or exceeded. The key challenge (under ASTs) was the electrocatalyst cycle stability of dealloyed PtNi, which routinely lost in excess of 65% mass activity with cycling, primarily due to specific activity loss which correlated to additional Ni leaching from the PtNi cathodes. A PtNi stabilization approach was developed outside of the project, but was not able to be implemented with high performance and manufacturability, necessary for the project short stack deliverable.

In extensive studies, rated power durability of baseline NSTF MEAs was found to depend upon several material and operational variables. Performance degradation was accelerated by incorporation of low EW PEMs, lack of PEM decomposition mitigating additive, lower cathode loading, increased operating temperature, and decreased operating potential. A first materials-based approach to improving rated power durability was identified, but performance was insufficient to allow downselection for project BOC MEAs.

A key correlation was identified between H_2/Air performance at 1A/cm^2 and cathode absolute activity from over 53 MEAs and over 200 individual data points. The correlation suggests that cathode activity loss alone may be responsible for rated power loss in NSTF MEAs, and that maintenance of activity above ca. 15mA/cm$^2_{planar}$ may be sufficient to mitigate the effect. The mechanism for why ORR activity influences H_2/Air performance in this manner is not known.

This correlation provides a second materials-based approach for mitigation, namely integration of higher activity, durable electrocatalysts better able to maintain activity above the threshold. Mechanism studies confirmed the hypothesis that rated power loss of NSTF MEAs is due to ORR absolute activity loss, induced by two means, cathode surface area loss and specific activity loss. A correlation was identified between specific activity loss and cumulative cathode F-emission, a measure of PFSA decomposition.

The correlations between H_2/Air performance, ORR activity, and F- emission were used to generate a durability model of NSTF MEAs. The model indicates that with baseline NSTF MEAs, the expected time to 10% voltage loss is approximately 800 hours. To attain the 5000 hour durability target, cathode FER must be reduced by ca. 80% by incorporation of more stable membranes.

The specific root cause mechanism for the ORR specific activity loss with PFSA decomposition is not yet known with certainty, but the hypothesis consistent with all of the experimental results is that PFSA decomposition could conceivably produce water insoluble ionomer fragments which are catalyst poisons, such as long-chain perfluorocarboxylic acids, which adsorb to the cathode catalyst thereby decreasing the activity. Based on the performance decay rates, it is estimated that the generation rate of such contaminants is at least two orders of magnitude less than the F- emission rates.

Performance and Durability of Integrated MEAs

In Task 4, Best of Class component candidates were integrated into MEAs. Over the course of the project, significant gains in absolute performance, specific power, and reduced loading of integrated MEAs were demonstrated in single cell testing. At 90°C cell temperature and 1.5atmA reactant pressures, performance at 0.80V increased 60% and performance at rated power (0.692V) increased 34% while the total loading decreased 13%, resulting in an improvement in specific power of 54% (kW/g). The Q/ΔT target of 1.45kW/°C was achieved. Evaluation of BOC MEA candidates with further reduced PGM loading, as low as $0.105 mg_{PGM}/cm^2$ total, were suggestive that DOE performance and total loading targets are feasible if increased activity cathodes were incorporated.

Numerous integration diagnostic studies were also conducted. One key area of work involved evaluating the impact and mechanism of the required break-in conditioning of BOC MEAs. Studies confirmed that both the NSTF anode and cathode need to be conditioned to enable entitlement performance and operational robustness. The cathode mass activity was found to be obtained very rapidly with standard 3M conditioning protocols, in a few hours or less. The anode conditioning appears to increase the HOR kinetics. Model predictions indicate that HOR overpotential losses of low loaded, low area anode electrodes can be strongly impacted by operating temperature, blocked surface area, and dilution, qualitatively consistent with the observed experimental effects. BOC MEA performance and operational robustness were demonstrably improved with specific anode conditioning. Work to develop more rapid, stack friendly conditioning methods was partially successful. For anode conditioning, use of high potential excursions were effective, either through use of anode CVs or fuel starvation protocols. For cathode conditioning, a previously-determined method found to be effective for PtNi/NSTF cathodes was not effective for the BOC cathode.

The durability of the final project BOC MEAs was assessed by the DOE MEA chemical durability test and a 3M 80°C load/RH cycle test. The BOC MEAs appear to be chemically stable, evidenced by low F- emission rates and steady OCVs > 500 hours for the OCV hold and > than 3000 hours in the load/RH cycle. Voltage degradation rates under load cycling were modest at low current densities but were 3-5x higher than acceptable at 0.8A/cm^2. Loss factors, identified in other work and discussed in the Task 5 section, are known and believed mitigatable.

Stack Evaluation of Integrated MEAs

Stack evaluation of Best of Class MEAs at General Motors in a single 3 cell and two 29-cell short stacks yielded performance below expectation, based on both 3M and GM single cell testing. The BOC MEAs' average cell voltage at 1.2A/cm^2 was below the 3M baseline MEAs' average cell voltage, and only 70% of the GM baseline MEAs' average cell voltage. This contrasts sharply with the 3M results, which show that the BOC MEA yields improved performance over the baseline. GM single cell results were also in contrast to the short stack results, where the 3M Baseline and BOC MEAs yielded similar performances. Several possible factors may be responsible for the low BOC MEA performance and robustness in GM stack testing, including non-optimized test conditions, incompatibility with flow field geometry, and insufficient activation, but none were experimentally confirmed.

A key result is that 3M Baseline MEAs with the project downselect anode GDL and cathode interlayer successfully passed all load transient conditions evaluated, including transients at 30°C stack temperature. This result provides validation of the electrode-extrinsic water management approaches developed within the project in Task 2. The result also indicates that the stack-level operational robustness challenges with the BOC MEAs were likely due to factors specific to that type of MEA, including insufficient or incomplete anode conditioning.

Cost of Integrated MEAs.

In Task 8, extensive experimental performance data with the final project data was generated in differential cell. The resultant data was used to generate an MEA performance model at Argonne National Laboratory, which was then used in support of development of a cost model by Strategic Analysis, Inc. The project downselected MEA was projected to decrease the cost of automotive stacks by 28.2, 20.7, and 19.2% at 1.5, 2.0, and 2.5atm stack operating pressures, respectively.

The cost analysis was conducted with the assumption of achievement of volume sufficient to generate 500k automotive stacks per year. Scalability of component fabrication technology and actual yields are large assumptions in such analyses. The final project MEA components were all generated on pilot scale, continuous processes, providing good early indication of the potential scalability of the approaches used in this project.

Future Directions

While substantial progress was made towards addressing key DOE and technology-specific barriers, additional work is needed to achieve the DOE 2020 targets.

Achievement of the rated power, specific power, and PGM content targets are believed attainable in the nearer-term. The key technical barrier is the project downselected cathode catalyst, PtNi/NSTF dealloyed with a free-corrosion process. Laboratory-scale electrocatalysts show good prospects towards addressing these aspects. Modest increases in activity are feasible with further optimization of electrocatalyst composition, structure, and processing. Improved dealloying methods are needed which can further reduce transition metal content and fully develop nanoporosity are needed. Co-optimizing composition, structure, and process conditions (with scalable processes) to achieve activity and durability is in progress.

While high power was demonstrated in single cells, performance in short stack was substantially below expectation. While several factors are possible, one key factor not explored at stack level was the impact of flow field land and channel geometry. Co-optimization of NSTF MEAs and flow field geometry may be necessary to allow demonstration of entitlement performance at stack level.

Achievement of the DOE Durability with cycling target will require several developments. As discussed in detail in the preceding sections, rated power loss of NSTF MEAs is most likely due to accumulation of water-insoluble PFSA decomposition fragments onto the catalyst surface. The first and closest term improvement is development of a high activity nanoporous NSTF catalyst with sufficient electrocatalyst durability. Sufficient durability of PtNi/NSTF has been shown in the laboratory through incorporation of proprietary additives. Durable, high specific surface area electrocatalysts will have decreased rates of specific activity loss due to decreased rate of fractional surface blockage, assuming constant contaminant generation rates. Development of PEM ionomers which produce the suspected irreversibly-adsorbed contaminants at reduced rates will also be effective at decreasing rated power loss rates. Studies are warranted to attempt to first detect and identify the contaminant species of interest, a potentially difficult and lengthy body of work considering the relatively small levels likely involved (perhaps 10s of nanomole/hour generation rates). Heuristic approaches, such as evaluating numerous experimental ionomers with controlled variations in backbone and sidechain structure, may ultimately be more effective and such work is currently in progress.

Operational robustness of NSTF MEAs has been improved within this project, but it is unclear if the anode GDL and cathode interlayer developed are sufficient to achieve sufficient robustness in end-use applications. The poorer-than-expected performance of the project Best of Class CCMs in stack prevented fair evaluation. Stack testing without such limitation would be warranted to determine the suitability of the project robustness-enhancing materials.

The electrode-extrinsic approaches used within this project allowed the high specific power capability of NSTF electrodes to be retained. Electrode-intrinsic modifications, such as development of hydrophobic pore volume and increasing electrode thickness, are under development at 3M under a ’16 initiated DOE project and already showing improved robustness

over the current project approaches. The key challenge is optimization of the electrode to attain specific power which approaches DOE targets.

Break-in conditioning of NSTF MEAs remains a noteworthy challenge. Work done over the course of this project largely focused on operational approaches to accelerate conditioning rates of the anode and cathode electrodes. While (somewhat) effective, materials-based approaches are ultimately preferred to enable rapid and *method-independent* break-in.

The observed lengthy break-in (> 20 hours typically) is at odds with diagnostic experiments which indicate that NSTF anode and cathode electrocatalysts can be fully conditioned within a few hours, based on analyses of kinetics. The primary relevant hypothesis is that one or more contaminants slowly leach from the PEM at very low levels, which essentially act as surfactants which increase the wettability of the NSTF cathode electrode and/or electrode-GDL interfaces, increasing flooding. Studies are needed to further confirm or refute this hypothesis. If confirmed, experiments to identify the leachants should be feasible. Once identified, ionomer composition and/or processing can be optimized to minimize the extent of leachant generation and to maximize the rate at which it exits the MEA.

Appendix

Publications and Presentations

1. Andrew Steinbach, Project Kickoff Presentation to DOE, Sept. 2012, St. Paul, MN.
2. X. Wang, R. K. Ahluwalia, and A. J. Steinbach, "Kinetics of Hydrogen Oxidation and Hydrogen Evolution Reactions on Nanostructured Thin-Film Platinum Alloy Catalyst", *J. Electrochem. Soc.*, **160**(3) F251-F261 (2013).
3. Project Update Presentation to DOE, Feb. 2013, Golden, CO.
4. Andrew Steinbach, "High Performance, Durable, Low Cost Membrane Electrode Assemblies for Transportation Applications", Presentation FC104, 2013 DOE Annual Merit Review, May 2013, Washington, DC.
5. Andrew Steinbach, Project Review Presentation to DOE, St. Paul, MN, Nov. 2013.
6. A. J. Steinbach and D. M. Peppin, "Polymer Electrolyte Membrane Fuel Cell Active Area Utilization Dependence on Relative Humidity Measured via AC Impedance High Frequency Resistance", *ECS Trans.* **58**(1) 1589-1600 (2013).
7. A. Steinbach, D. van der Vliet, S. Luopa, J. Erlebacher, and D. Cullen, "Dealloying and Annealing Optimization of High Mass Activity Pt_3Ni_7/NSTF ORR Cathodes for PEMFCs", 224th Electrochemical Society Meeting, Abstract #1350, San Francisco, CA, Oct. 2013.
8. A. Steinbach and D. M. Peppin, "PEMFC Active Area Utilization Dependence on Relative Humidity-Measured via AC Impedance High Frequency Resistance", 224th Electrochemical Society Meeting, Abstract #1579, San Francisco, CA, Oct. 2013.
9. A. Kusoglu and A. Z. Weber, "Morphology and Swelling of Perfluorosulfonic-acid (PFSA) Ionomer Thin Films," 224th Electrochemical Society Meeting, Abstract #1283, San Francisco, CA, Oct. 2013.
10. D. A. Cullen. "Optimizing fuel cell materials through electron microscopy and microanalysis", Annual Meeting of the Appalachian Regional Microscopy Society, Raleigh, NC, Nov. 15, 2013.
11. A. Kusoglu, A. Hexemer, and A. Weber, "Interfaces, Bulk, and Confinement in Nafion," Golden Gate Polymer Forum, San Francisco (invited), 2013.
12. P. K. Das, A. Santamaria, and A. Z. Weber, "Understanding liquid water and gas-diffusion layers," Grove Fuel Cell Science and Technology Conference, Amsterdam, 2014.
13. Andrew Steinbach, "High Performance, Durable, Low Cost Membrane Electrode Assemblies for Transportation Applications", Presentation FC104, 2014 DOE Annual Merit Review, Washington, DC, June 2014.
14. A Kusoglu, C. Blake, F. Allen, A. Crothers, AZ Weber, *Understanding Conduction and Structure in PFSA Membranes*, 17th Solid State Protonic Conductors, Seoul, Korea, September 14-19, 2014.
15. A.J. Steinbach, project presentation to USCAR Fuel Cell Tech Team, October 15th, 2014 Southfield, MI.
16. V. Konduru, E. F. Medici, and J. S. Allen, *Modeling Thermal Transport in Heterogeneous Porous Media of PEM Fuel Cells Using Pore Network Model*, Trans. of the 226th Electrochemical Society Meeting, October 2014, Cancun, Mexico.
17. A.J. Steinbach and D. van der Vliet, project presentation to DOE, November 4th, 2014, St. Paul, MN.
18. I.V. Zenyuk, A. Santamaria, P.K. Das, A. Steinbach, R. Mukundan, R.L. Borup, A.Z.Weber *Water Management with Thin-Film Catalyst Layers*, CARISMA, South Africa, Dec. 1, 2014.
19. I.V. Zenyuk, D.Y. Parkinson, G. Hwang, A.Z.Weber *Understanding Water Transport in Compressed Gas Diffusion Layers of Polymer-Electrolyte Fuel Cells Using X-ray Computed Tomography*, 2015 MRS Spring Meeting & Exhibit, April 9th, 2015.
20. D. A. Cullen, M. Lopez-Haro, P. Bayle-Guillemaud, L. Guetaz, M. K. Debe, and A. J. Steinbach, *Linking Morphology with Activity in Novel PtNi Nanostructured Thin Film Catalysts*, J. Mat. Chem. A **3** 11660, 2015.
21. I. Zenyuk**,** E. F. Médici, J. S. Allen, and A. Z. Weber, *Coupling Continuum and Pore Network Models in Polymer Electrolyte Fuel Cells*, 7th International Conference on Porous Media, May 2015, Padova, Italy.

22. V. Konduru, J. S. Allen, J. Pharaoh, *Multiscale modeling of water transport in porous transport layers (PTL) of PEM fuel cells using combined pore network and finite volume modeling*, 7th International Conference on Porous Media, May 2015, Padova, Italy.
23. A.J. Steinbach, *High Performance, Durable, Low Cost Membrane Electrode Assemblies for Transportation Applications*, Presentation FC104, 2015 DOE Annual Merit Review, Washington, DC, June 2015.
24. A.J. Steinbach, *High Performance, Durable, Low Cost Membrane Electrode Assemblies for Transportation Applications*, IEA Annex 34 - Fuel Cells for Transportation, June 24th, 2015, Jülich, Germany.
25. R.K. Ahluwalia, X. Wang, and A.J. Steinbach, *Performance of Advanced Automotive Fuel Cell Systems with Heat Rejection Constraint*, J. Power Sources, 2015, submitted.
26. A.J. Steinbach and D. van der Vliet, project presentation to DOE, July 16th, 2015, St. Paul, MN.
27. A. J. Steinbach, "Challenges and Opportunities with 3M Nanostructured Thin Film (NSTF) Ultra-low PGM ORR Electrocatalysts" Challenges towards zero platinum for oxygen reduction, September 15th, 2015, Le Grande Motte, France; *invited*.
28. A. J. Steinbach, D. F. van der Vliet, A. E. Hester, J. Erlebacher, C. Duru, I. Davy, M. Kuznia, and D. A. Cullen, "Recent Progress in Nanostructured Thin Film (NSTF) ORR Electrocatalyst Development for PEM Fuel Cells", 228th Meeting of the Electrochemical Society, October 13th, 2015, Phoenix, AZ USA; *invited*.
29. A. J. Steinbach, D. F. van der Vliet, A. E. Hester, J. Erlebacher, C. Duru, I. Davy, M. Kuznia, and D. A. Cullen, "Recent Progress in Nanostructured Thin Film (NSTF) ORR Electrocatalyst Development for PEM Fuel Cells", *ECS Trans.* 2015 **69**(17): 291-301.
30. I. V. Zenyuk, E. F. Médici, J. S. Allen, and A. Z. Weber, "Coupling Continuum and Pore- Network Models in Polymer-Electrolyte Fuel Cells", European Fuel Cell 2015 – Piero Lunghi Conference, Naples, December 16-18th, 2015.
31. A. J. Steinbach, "High Performance, Durable, Low Cost Membrane Electrode Assemblies for Transportation Applications", Presentation to Fuel Cell Tech Team, February 17th, 2016.
32. R. K. Ahluwalia, X. Wang, and A. J. Steinbach, "Performance of Advanced Automotive Fuel Cell Systems with Heat Rejection Constraint", *J. Power Sources* **309** 178-191 (2016).
33. E. Medici, I.V. Zenyuk, D.Y. Parkinson, A. Z. Weber, J. Allen "Understanding Water Transport in Polymer-Electrolyte Fuel Cells Using Coupled Continuum and Pore-Network Models", *Fuel Cells* (2016). DOI 10.1002/fuce.201500213
34. E. F. Medici and J. S. Allen, "A Quantitative Technique to Compare Experimental Observations and Numerical Simulations of Percolation in Thin Porous Materials", *Transport in Porous Media* (2016). DOI 10.1007/s11242-016-0672-4
35. A.J. Steinbach, Project Review Presentation to DOE, July 2016, St. Paul, MN.
36. A.J. Steinbach, *High Performance, Durable, Low Cost Membrane Electrode Assemblies for Transportation Applications*, Presentation FC104, 2016 DOE Annual Merit Review, Washington, DC, June 2016.
37. Andrew Steinbach, Project Review Presentation to DOE, St. Paul, MN, April 2014.
38. A.J. Steinbach, project presentation to USCAR Fuel Cell Tech Team, Aug 12th, 2015, Southfield, MI.
39. E. F. Medici and J. S. Allen, "Two Phase Flow Pore Network Model Simulations Validation using a Scaling for Percolation in Thin Porous Materials", 8th International Conference on Porous Media, May 2016, Cincinnati, OH.
40. I. V. Zenyuk, E. F. Médici, J. S. Allen, and A. Z. Weber, "Coupling Continuum and Pore- Network Models in Polymer-Electrolyte Fuel Cells", *Int J Hydrogen Energy*, 40 (2015) pp. 16831-16845.

Inventions

None.

Technology Transfer

None.

Acronyms

BOL: Beginning of Life
CCM: Catalyst coated membrane
ECSA: Electrochemical surface area
EW: Equivalent weight (g / mol H+)
GDL: Gas diffusion layer
HOR: Hydrogen oxidation reaction
IL: Interlayer
MEA: Membrane electrode assembly
MPL: Microporous layer
NFAL: Normal flows and leads
NSTF: Nanostructured thin film
ORR: Oxygen reduction reaction
PFIA: Perfluoroimide acid
PFSA: Perfluorosulfonic acid
PGM: Platinum group metal
RFAL: Reversed flows and leads
SEF: Surface enhancement factor (catalyst roughness factor)